DESIGN AND ANALYSIS OF SPACE-TIME AND GALERKIN/LEAST-SQUARES FINITE ELEMENT METHODS FOR FLUID-STRUCTURE INTERACTION IN EXTERIOR DOMAINS

A DISSERTATION
SUBMITTED TO THE DEPARTMENT OF CIVIL ENGINEERING
AND THE COMMITTEE ON GRADUATE STUDIES
OF STANFORD UNIVERSITY
IN PARTIAL FULFILLMENT OF THE REQUIREMENTS
FOR THE DEGREE OF
DOCTOR OF PHILOSOPHY

By
Lonny L. Thompson
April 1994

I certify that I have read this dissertation and that in my opinion it is fully adequate, in scope and in quality, as a dissertation for the degree of Doctor of Philosophy.

Peter M. Pinsky
Associate Professor of Civil Engineering
(Principal Advisor)

I certify that I have read this dissertation and that in my opinion it is fully adequate, in scope and in quality, as a dissertation for the degree of Doctor of Philosophy.

Thomas J.R. Hughes
Professor of Mechanical Engineering

I certify that I have read this dissertation and that in my opinion it is fully adequate, in scope and in quality, as a dissertation for the degree of Doctor of Philosophy.

Joseph B. Keller
Professor of Mathematics and Mechanical Engineering

Approved for the University Committee on Graduate Studies:

To the memory of my loving mother,
Jeannette, Stanford University, Class of 1959.

Abstract

This work is concerned with the design and analysis of new finite element methods for solution of large-scale fluid/structure interaction problems in exterior domains. In particular, the structural acoustics problem involving the interaction of elastic structures submerged in an infinite acoustic fluid and subject to a far-field radiation condition is addressed. Solution methods for both the time-domain and frequency-domain problems are developed which yield substantial improvements in accuracy and efficiency over standard computational procedures.

This presentation is divided into two parts. The first discusses the development and analysis of space-time finite element methods based on a new time-discontinuous Galerkin/least-squares variational formulation for solution of the coupled structural acoustics problem in the time-domain. The methods developed are especially useful for the application of adaptive solution strategies in which unstructured space-time meshes are used to track waves propagating along space-time characteristics. Throughout the development, energy estimates derived for the continuum problem are used as a guide for the design of stable and accurate algorithms. The formulation employs a finite computational fluid domain surrounding the structure and incorporates time-dependent non-reflecting (radiation) boundary conditions on the fluid truncation boundary. For large-scale three-dimensional discretizations the use of accurate radiation boundary conditions is essential to allow the fluid truncation boundary to be placed close to the structure and thereby minimizing the mesh and matrix problem size. In this work, new higher-order accurate time-dependent non-reflecting boundary conditions are developed based on the exact impedance relation through the Dirichlet-to-Neumann (DtN) map in the frequency domain. Time-dependent counterparts are obtained through the use of an inverse Fourier transform procedure. These non-reflecting boundary conditions are incorporated as 'natural' boundary conditions in the space-time variational equation, i.e. they are enforced weakly in both space and time. The implementation of these boundary conditions in a semidiscrete finite element formulation is also presented. An important feature of the space-time formulation is the incorporation of temporal jump operators which allow for finite element interpolations that are discontinuous in time. For additional stability, least-squares operators based on local residuals of the structural acoustics equations including the non-reflecting boundary conditions are incorporated. Optimal error estimates using

functional analysis are predicted and confirmed numerically. Several numerical examples involving transient radiation and scattering of acoustic waves from submerged structures are presented to illustrate the higher-order accuracy of the new methods.

In the second part of this work, a Galerkin/Least-Squares (GLS) finite element method is developed for time-harmonic acoustics in the frequency domain. An important feature of GLS methods is the introduction of a local mesh parameter that may be designed to provide accurate solutions with relatively coarse meshes: in effect extending the range of finite element solutions to higher frequency calculations. In this thesis, a multi-dimensional Fourier analysis is used to select optimal GLS mesh parameters that lead to dramatically improved phase accuracy for waves propagating in multi-dimensions. For the case where the direction of the wave is known, the optimal mesh parameter is obtained explicitly. For general problems where waves are directed in arbitrary directions, an optimal GLS parameter is found which reduces phase error over all possible directions. Several numerical examples are given which demonstrate the superiority of the new methods over the standard Galerkin method. The optimum GLS parameter is given for both linear and quadratic interpolation functions.

In recent years, there has been a resurgence of interest in the use of hierarchical p-version finite element and spectral elements to obtain high-resolution numerical solutions for structural acoustics. In this thesis, it is shown that high-order finite element discretizations display frequency bands where the solutions are harmonic decaying waves. In these so called 'stopping' bands, the solutions are not purely propagating (real wavenumbers) but are attenuated (complex wavenumbers). In order to interpret the solution within the stopping bands, the standard dispersion analysis technique has been extended to include complex wavenumbers. By allowing for complex wavenumbers, a complete characterization of high-order finite element discretizations has been obtained. Three alternatives are considered: (i) hierarchic p-version elements based on Legendre functions, (ii) new hierarchic Fourier elements based on sinusoidal functions, and (iii) spectral elements based on Lagrange interpolation in conjunction with Gauss-Lobatto quadrature. Practical guidelines for phase and amplitude accuracy in terms of the spectral order and the number of elements per wavelength are reported.

Acknowledgements

I would like to express my deepest gratitude to those who have made the achievement of this dissertation possible:

My advisor, Professor Peter M. Pinsky, for sharing his vast experience, providing invaluable guidance throughout the course of this work, and for his continual encouragement in both my research and teaching interests. I look forward to further collaboration in the many years to come.

Professor Thomas J.R. Hughes, for inspiring my interest in space-time finite element methods, for many stimulating discussions, and serving as a member of both my University examination and dissertation reading committee.

Professor Joseph B. Keller, for his continued interest in my research and for sharing invaluable insights into the world of non-reflecting boundary conditions, and also for serving as a member of both my University examination and dissertation reading committee.

Professor Gene H. Golub, for graciously serving as chairperson for my University examination on extremely short notice and offering insightful suggestions on matrix computations.

Professor David M. Barnett, for serving on my University examination committee and encouraging my research in the modeling of wave propagation problems.

Professor Juan C. Simo, for accepting the role of chairperson for my examination committee, and from whom I am indebted for the vast amount of knowledge imparted to me in the area of nonlinear computational mechanics.

Professor Kincho H. Law, for his teaching advice and encouragement and for his efforts in serving on my University examination committee.

Professor Isaac Harari, for his friendship and for introducing me to Galerkin/least-squares technology, from which a large part of this dissertation is based.

Professor Gregory Hulbert, for supplying the initial version of the computer program used in my work on space-time methods.

Dr. Najib Abboud of Weidlinger Associates and Dr. Raja Jasti of Marc Analysis, both of whom served as my mentor in the early stages of my research at Stanford and whos friendship I continue to cherish.

Deepak Datye for his steadfast friendship and excellent advice throughout my entire stay at Stanford. Karl Grosh for his friendship and sharing his insights and experience in structural acoustics.

Guillermo Hauke, Dr. Kenneth E. Jansen, and Dr. Arif Masud, for many stimulating discussions and their friendship and support. James R. Stewart for his friendship and for carefully proofreading portions of this manuscript.

I would also like to thank my friends and colleagues, Dr. Nils Tarnow, Dr. Steven Rifai, and Dr. John Kennedy for sharing their experience in finite element methods. Dr. Francisco Armero, for many stimulating discussions on coupled problems in computational mechanics, and also for reviewing several chapters of this dissertation. Dr. Paul Barbone for his teachings in the area of analytical acoustics and elastodynamics, and Manish Malhotra, Vinay Rao, Narayana Aluru, Krishnakumar Garikipati for their friendship and youthful enthusiasm for the subject of computational mechanics.

My best friends Bob and Rosie, Mark, Laura, Frogge and Fishe.

Finally, I would like to thank my family, Dad, Kris, Loel, Lori, Grandma and Grandpa T. and E., for their love and support throughout the pursuit of my dream.

This research was supported by an Achievement Rewards for College Scientists (ARCS) scholarship and the Office of Naval Research under contracts N00014–89–J–1951, N00014–92–J–1774 and N00014–89–K–0027. This support is gratefully acknowledged.

I would also like to personally thank Drs. Phil Abraham, Louise Couchman, Jeff Main and Albert J. Tucker of the Office of Naval Research for their support and encouragement for my research in the design and analysis of computational methods for structural acoustics.

Contents

List of Tables

List of Figures

Chapter 1

Introduction

This work is concerned with the exterior structural acoustics problem involving the interaction of vibrating structures submerged in an infinite acoustic fluid and requires solution of the coupled wave equation subject to a far-field radiation condition. The acoustic fluid is modeled under the usual assumptions governing the theory of sound waves – a compressible fluid characterized by small time-dependent pressure fluctuations around a reference state. The physical behavior of the coupled structural acoustic problem can be described by the strength of the interaction between the structure and the acoustic fluid. When the density of the fluid is low compared to the structural materials, such as an elastic plate in contact with air, the fluctuating pressure acting on the surface of the vibrating plate is small enough to have a negligible effect on structural vibrations. Consequently, the dynamic response of the structure can be solved independently, as though the structure were vibrating in a vacuum. In contrast, a structure vibrating in contact with a fluid of comparable density, for example a submarine structure submerged in water, experiences acoustic pressure loading comparable to its inertial and elastic forces. The acoustic pressure loading modifies the forces acting on the structure, which in turn modifies the acoustic pressures, resulting in a feedback mechanism between the coupled fluid and structure. In this work, the structural acoustics problem with significant interaction between the structure and acoustic fluid is studied. Given a forcing excitation within the structure and/or an incident sound pressure field from an acoustic source, the primary goal is to solve for the displacement field in the structure or elastic body and the acoustic pressure field in the surrounding fluid.

1.1 Motivation and Critical Issues

Analytical techniques for solving the fully coupled problem with strong fluid loading have used separable expansions, integral transform techniques and methods of asymptotic theory to solve problems such as elastic plates and shells with simple geometries, see for example JUNGER [1975,1986], and CRIGHTON [1989]. While analytical solutions have been invaluable for understanding the complex feedback mechanisms occurring between the interaction of structures and fluids, the difficulties in obtaining solutions for other than the simplest of geometries has stimulated research in computational methods. In this thesis, the goal is to design efficient computational methods which accurately capture the fundamental processes involved in the fluid-structure interaction of realistically complex structures vibrating in contact with an acoustic fluid. The focus is directed towards computational tools for the design of large-scale structures, that is, structures that are large relative to their operating wavelengths. In addition, the numerical methods developed in this work for the exterior structural acoustics problem may be applied to other fluid/structure interaction problems outside the realm of underwater structural acoustics. Examples include aeroacoustics involving interior and exterior noise from aircraft and automobiles, applications in electromagnetics and optical scattering, and soil/structure/wave interaction in dynamics of buildings, dams and offshore platforms.

1.1.1 Frequency-Domain Methods

For linear problems characterized by a relatively small range of frequencies, a time-dependent solution may be obtained indirectly through a sequence of time-harmonic solutions in the frequency domain followed by an inverse Fourier transform. Considerable progress has been made in the development of numerical methods for the time-harmonic exterior structural acoustics problem. The most widely used computational technique for solving the time-harmonic problem is the coupled finite element/boundary element method (FEM/BEM), see e.g. MARIEM AND HAMDI [1987], EVERSTINE AND HENDERSON [1990], JEANS AND MATHEWS [1990]. This approach has the benefit of the *a priori* satisfaction of the radiation condition at infinity and requires only discretization of the wet surface of the structure. However, offsetting this advantage is the fact that the resulting matrix equations are nonsymmetric and fully populated, and become ill-conditioned at characteristic ('forbidden') frequencies associated with the interior Dirichlet problem, see e.g. PIASZCZYK AND KLOSNER [1984], COPLEY [1968]. Numerous remedies to the non-uniqueness problem have been proposed over the years, e.g. SCHENCK [1968], BURTON AND MILLER [1971], MATHEWS [1986], at the expense of a substantial increase in computational expense. As a result of these deficiencies, dynamic solutions of large-scale structures interacting with an acoustic fluid have been limited to low frequency calculations. For a comparison between competing boundary integral formulations, consult AMINI AND HARRIS [1990].

While boundary element methods have traditionally been the numerical method of choice by acousticians, promising new finite element methods have recently been developed and are currently being used with great success to solve a variety of challenging time-harmonic structural acoustics problems. Recent work in this area include the Galerkin/Least-Squares (GLS) finite element formulation originally described in HARARI AND HUGHES [1991a,1991b,1992c] for acoustics and extended for multi-dimensional wave propagation applications in THOMPSON AND PINKSY [1993c,1993d]. The goal of these new methods is to decrease the computational expense required to achieve a desired level of accuracy at any given frequency, thereby allowing for the solution of large-scale structural acoustics problems at higher frequencies.

The central feature of GLS methods is the introduction of local mesh parameters designed to provide accurate solutions with relatively course meshes. Harari and Hughes accomplished this for one-dimensional problems by matching the approximate finite element dispersion relation with the exact dispersion relation. In HARARI AND HUGHES [1992c], the GLS mesh parameter derived in one-dimension is used in the Dirichlet-to-Neumann (DtN) finite element method proposed by KELLER AND GIVOLI [1989], and GIVOLI AND KELLER [1989]. The Dirichlet-to-Neumann method represents the exact impedance of the infinite acoustic fluid exterior to a finite computational domain in the form of a nonlocal (global) radiation boundary condition. Although it was found that the one-dimensional parameter improved the accuracy of the standard Galerkin solution in some two-dimensional example problems, a comprehensive analysis of GLS dispersion characteristics in multi-dimensions was unavailable. In the work of THOMPSON AND PINSKY [1993c,1993d], the selection of the optimal GLS mesh parameter for the multi-dimensional Helmholtz equation governing the acoustic fluid is considered, and leads to elements that exhibit a dramatic improvement in phase accuracy over the standard Galerkin finite element approach.

In the linear case, frequency-domain methods can be used indirectly (e.g., by Fourier or Laplace transform) to solve the time-dependent problem. Still, a direct time integration approach to solution of transient problems is necessary whenever nonlinearities occur and may be advantageous for some classes of linear problems. For example, in problems characterized by broad frequency spectrums, such as short pulse wave propagation, the indirect approach may not be computationally feasible since it requires a large number of solutions in the frequency domain for any reasonably accurate sweep of the problem band width. In the indirect approach, results for several frequencies must be stored and then superimposed to solve the fully transient problem. In practice this limits the application of this approach to cases in which a few hundred frequencies contribute to the solution.

1.1.2 Time-Domain Methods

Methods that solve fluid/structure interaction problems directly in the time domain are an effective alternative to the indirect frequency domain strategy and are often the only viable computational tool available for solving problems involving inelastic behavior and real-time dynamic control and optimization. In the time domain, three main approaches are possible: (i) boundary element methods based on Kirchoff's retarded potential integral formulation, (ii) semi-discrete finite element methods which employ finite difference techniques for integrating in time, and (iii) space-time finite element methods. While any of these methods will be feasible for smaller problems, they will exhibit markedly different efficiency and accuracy characteristics for large-scale simulations.

Boundary element methods based on the direct time integration of Kirchoff's retarded potential boundary integral lead to unsymmetric and dense matrices and, more importantly, can be extremely memory intensive due to the convolution in time required by the time-dependent free-space Green's function used in the kernel of the boundary integral. When used for medium to long time calculations, the boundary integral approach requires storage of a large pool of historical data during the solution process that can quickly become prohibitive when solving large-scale fluid-structure interaction problems. For theoretical developments of the boundary element method for transient wave propagation, see Mansur and Brebbia [1982,1984], and for applications to structural acoustics see e.g. Huang, Everstine and Wang [1977], Neilson et al. [1978], and Lu [1980].

An alternative approach for the direct solution of the exterior structural acoustics problem in the time-domain is to introduce an artificial boundary where time-dependent non-reflecting boundary conditions are applied in order to simulate the radiation condition at infinity. The resulting bounded computational domain is then discretized and solved with a finite element method. The most common finite element technique for the direct solution of the transient problem is based on semidiscretization, in which the spatial domain is discretized using finite elements, producing a system of ordinary differential equations in time, which in turn is discretized using standard finite difference methods such as the Newmark family of time-integrators. Application of the semidiscrete finite element approach to transient structural acoustics incorporating a high-order accurate non-reflecting boundary condition are reported in Pinsky, Thompson and Abboud [1992] and Pinsky and Abboud [1991] for two- and three-dimensional problems, respectively.

While semidiscrete methods are effective for computing smooth (low frequency) responses, and as such, are well suited to structural dynamics, their performance is less satisfactory when solving acoustic wave propagation problems, especially those exhibiting steep gradients in the pressure amplitude or sharp wave fronts typically arising in the complex radiation and scattering fields found in transient structural acoustics problems. Semidiscrete methods which do not possess appropriate numerical damping will give rise to oscillations in the vicinity of the wave front which can pollute the entire solution. On the other hand, semidiscrete algorithms developed within the context of structural dynamics and which possess numerical damping, e.g. the Hilber, Hughes, and Taylor HHT-α algorithm [1977], will generally not adequately capture steep gradients in acoustic wave propagation problems, for examples see Hulbert and Hughes [1989,1990].

In this thesis a space-time finite element method is presented for solution of the coupled structural acoustics problem in exterior domains. The proposed method employs the simultaneous discretization of the spatial and temporal domains and is based on a new time-discontinuous Galerkin formulation for the coupled fluid/structure system. In this approach, the concept of space-time slabs is employed which allow for discretizations that are discontinuous in time. The resulting space-time algorithm naturally possesses beneficial numerical filtering needed to resolve any sharp gradients in the transient response and leads to stable higher-order accurate methods. The order of accuracy of the solution is related to the order of the finite element spatial and temporal basis functions, and can be specified to any accuracy and for general unstructured discretizations in space and time. A key element of the new time-discontinuous Galerkin formulation is the incorporation of least-squares operators based on local residuals of the governing equations for structural acoustics, including the non-reflecting boundary conditions. These least-squares terms add stability without degrading accuracy of the underlying discontinuous Galerkin method. Physically, the effect of these least-squares operators is to further filter out any high-frequency noise associated with discretization of the space-time continuum.

Time-discontinuous Galerkin methods were originally developed for first-order hyperbolic equations in Reed and Hill [1973], Lesaint and Raviart [1974] and has since been successfully applied to first-order systems of equations arising in problems of fluid dynamics and heat conduction, see e.g. Johnson [1986], Shakib, Hughes and Johan [1991a,1991b]. Classical linear structural acoustics equations can be converted to first-order hyperbolic form and these methods are thus immediately applicable. However, in this approach, the coupled state vector consists of structural displacements, velocities and stresses, as well as acoustic pressure and velocity components, which is computationally uneconomical. In this work, it is proposed to eliminate the acoustic velocity vector in terms of a scalar potential, and then formulate the problem in terms of the second-order hyperbolic scalar wave equation governing the acoustic fluid.

Recently, Hughes and Hulbert [1988] and Hulbert [1989,1990] have successfully extended the time-discontinuous Galerkin space-time method to second-order hyperbolic equations in the context of transient elastodynamics. Based on the success of the time-discontinuous method for elastodynamics, it is desirable to extend this technology to the coupled structural acoustics problem involving the second-order wave equation governing acoustics and the equations of elastodynamics for the structure. Although space-time finite element methods based on the time-discontinuous

Galerkin method has considerable potential for the coupled structural acoustics problem, this approach has not yet been explored previously.

In this work, a space-time finite element method is developed for both the structure and the acoustic fluid together with their interaction. For the coupled equations, scalar velocity potential is chosen as the solution variable for the acoustic fluid, while the displacement vector is used for the structure. As a consequence of this choice of variables, the coupled variational equations for the fluid and structure give rise to a globally symmetric form, which in the context of the space-time finite element formulation, enables us to prove through a rigorous functional analysis that the method is unconditionally stable. In this work, the method is termed unconditionally stable if, in the absence of forcing terms but for arbitrary initial conditions, the computed total energy in the system plus the radiation energy absorbed through the artificial boundary is always less than or equal to the total energy at the previous time step, for arbitrary time steps. A mathematical analysis is performed and the method is proved to converge at an optimal rate in a norm stronger than the total structural acoustic energy norm.

As discussed earlier, when the space-time finite element method is used to solve the transient exterior structural acoustics problem, the fluid domain must be truncated at a finite distance from the structure. If accurate time-dependent non-reflecting boundary conditions are applied to this boundary, the finite element model will be able to use fewer fluid elements than otherwise would be possible and considerable cost savings may result. Therefore there is a need for the development of high-order accurate non-reflecting (absorbing) boundary conditions which eliminate or minimize reflection of outgoing waves and that also preserve the data structure of the finite element method. High-order accurate time-dependent non-reflecting boundary conditions have been proposed by several authors. A survey of the field will be given in Chapter 5; other surveys may be found in Givoli [1991] and Abboud [1990].

In general, non-reflecting boundary conditions can be categorized in terms of the local (differential) or nonlocal (integral) spatial and temporal operators appearing in their definition. An example of a family of high-order accurate non-reflecting boundary conditions which are local both in time and space (i.e. differential operators in time and space) is the sequence derived in Bayliss and Turkel [1980] and implemented in a semidiscrete finite element formulation in Pinsky, Thompson and

Abboud [1991,1992]. This sequence of radiation boundary conditions is based on a power series expansion in inverse powers of a non-dimensional wavenumber. Recently Thompson and Pinsky [1993e,f] derived a new sequence of local time-dependent non-reflecting boundary conditions from an inverse Fourier transform of the localized Dirichlet-to-Neumann (DtN) impedance relation in the frequency domain, (Givoli and Keller [1990], Harari [1991a]). In addition, it is shown that through an inverse Fourier transform a local in time counterpart exists for the spatially nonlocal Dirchlet-to-Neumann map given in Keller and Givoli [1989]. Because these new boundary conditions are based on an exact harmonic expansion as opposed to an approximate power series expansion, the first N operators in this sequence are exact for the first N wave harmonics. Further details of the development of these non-reflecting boundary conditions are given in Chapter 5 of this thesis.

As the order of these and other non-reflecting boundary conditions increases they become increasingly difficult to implement in a semidiscrete setting due to the occurrence of high-order time derivatives on the fluid truncation boundary. In this thesis, we indicate how the time-discontinuous Galerkin space-time method provides a natural variational setting for the incorporation of high-order accurate, local in time non-reflecting boundary conditions that allow for the use of standard C^0 continuous finite element interpolations in both space and time variables. Crucial to the stability and convergence of the method is the introduction of consistent temporal jump operators across space-time slabs restricted to the artificial boundary. The specific form of these operators is designed such that continuity of the solution across slabs is weakly enforced in a form consistent with the non-reflecting boundary conditions.

In addition to the advantages cited above, the space-time finite element approach provides a powerful framework for unified and simultaneous spatial and temporal adaptivity of the discretization. This is especially useful in the application of adaptive solution strategies for transient structural acoustics, in which both spatial and temporal enhancement can efficiently capture waves propagating along space-time characteristics. In regions where the solution is smooth, the mesh can be relatively coarse while a finer mesh can be employed near wave fronts. Thus an accurate solution may be obtained without resorting to a uniformly refined (and computationally expensive) mesh. Furthermore, the use of space-time hp-adaptive discretization strategies, where a combination of mesh size refinement/unrefinement (h-adaptivity), and finite element basis enrichment (p-adaptivity), can easily be accommodated.

An important feature of the space-time finite element method is the treatment of the temporal and spatial domains in a unified manner. It is this consistency that allows for a rigorous mathematical analysis to establish *a posteriori* error estimates useful for reliable and efficient adaptive schemes. Recently JOHNSON [1993], obtained some *a posteriori* error estimates based on the discontinuous Galerkin method for second-order hyperbolic equations. The space-time variational framework advocated in this thesis offers great potential for the design and implementation of efficient and accurate local error indicators to drive adaptive strategies for the transient structural acoustics problem incorporating high-order accurate non-reflecting boundaries.

1.2 Overview

In Chapter 2 the coupled system for the exterior structural acoustics problem is described where the governing differential equations for the structure, the acoustic fluid, and their interaction are summarized. An important feature of the development is the choice of scalar velocity potential for the acoustic fluid in conjunction with the displacement vector for the structure as the fundamental variables for the coupled system. As a consequence of this choice of variables the coupled variational equations take on a globally symmetric form, which leads in the discrete case to a positive (stable) matrix system of equations. In the later part of this chapter, a number of important energy estimates for the continuum problem are established. These results play a central role in the analysis of stability and uniqueness for both the continuum and discrete problems and form the basis for the design of the new time-discontinuous Galerkin variational formulation proposed in this thesis.

In Chapter 3 the space-time finite element method for the coupled structural acoustics problem is formulated. The development proceeds by introducing the reader to the concept of space-time finite element technology where the space-time domain is partitioned into space-time slabs. Within each space-time slab, C^0 continuous space-time finite element interpolations are used. Crucial to the development is the use of temporal jump operators between space-time slabs in the time-discontinuous

Galerkin variational equation. The use of temporal jump operators allows for completely unstructured space-time meshes. The formulation employs a finite computational fluid domain surrounding the structure and incorporates an important class of local time-dependent non-reflecting boundary conditions on the fluid truncation boundary. Non-reflecting boundary conditions are incorporated as 'natural' boundary conditions in the space-time variational equation, i.e. they are enforced weakly in both space and time. Galerkin/Least-Squares operators are added to the underlying Galerkin formulation to enhance stability, while maintaining high-order accuracy of the method. The chapter closes with a discussion of the positive form of the coupled matrix equations and issues related to the stability and efficient solution of these equations.

In Chapter 4 a rigorous analysis of the coupled space-time variational formulation is performed to establish the unconditional stability and convergence of the method. A proof of convergence for both the uncoupled and coupled systems is given. Error estimates are confirmed numerically with a one-dimensional canonical example. This chapter concludes with an extension to a mixed two-field formulation incorporating independent finite element interpolations for both pressure and velocity potential variables.

In Chapter 5 new time-dependent non-reflecting boundary conditions are developed for problems in three-dimensions which exactly represent the first N spherical harmonics for outgoing waves. Two alternative sequences are derived; the first involves both time and spatial derivatives (local in time and local in space version), and the second involves time derivatives yet retains a spatial integral (local in time and nonlocal in space version). The first version starts from the exact localization of the acoustic impedance relation (Dirichlet-to-Neumann (DtN) map) in the frequency domain. Time-dependent boundary conditions are then obtained through the application of an inverse Fourier transform. Details for the implementation of these boundary conditions in the space-time formulation are given. In the second version, we show that an inverse Fourier transform exists for the original nonlocal DtN map, allowing for boundary conditions that are nonlocal in space yet retain the important property of locality in time. Several numerical examples involving transient radiation of acoustic waves from geometrically axisymmetric structures are presented to illustrate the accuracy of the non-reflecting boundary conditions when implemented in the space-time formulation.

In Chapter 6 the design and analysis of local in time non-reflecting boundary conditions for the two-dimensional wave equation are considered. In the two-dimensional case it is not possible to obtain local time-dependent boundary conditions that exactly represent outgoing cylindrical wave harmonics. In this case, use is made of an approximation for large frequency, normalized with the radius of the artificial boundary, to obtain a power series expansion of the Dirichlet-to-Neumann map. Following Bayliss and Turkel, a sequence of differential operators are obtained that match the leading terms in this expansion. Time-dependent boundary conditions are obtained through an inverse Fourier transform and implemented in the same procedure as the three-dimensional case. Numerical examples are presented to demonstrate the effectiveness of the time-discontinuous Galerkin space-time method to accurately simulate transient radiation and scattering from a variety of geometrically complex structures.

In Chapter 7 a semidiscrete finite element formulation is developed for the transient structural acoustics problem. Consistent fluid-structure coupling elements are derived to model the interaction between standard C^0 continuum-based shell elements and acoustic fluid elements. For transient solutions that do not exhibit excessive gradients or for time-dependent problems that are driven to steady-state, we demonstrate that the semidiscrete approach can be an effective alternative to the frequency-domain approach. For the exterior problem, local second-order non-reflecting boundary conditions are implemented in the semidiscrete framework.

In Chapter 8 the design and analysis of frequency-domain methods are considered. In particular, a Galerkin/Least-Squares (GLS) finite element method is developed to solve the Helmholtz equation governing the acoustic fluid in the frequency domain. A multi-dimensional Fourier analysis is used to select a GLS mesh parameter that leads to dramatically improved phase accuracy in the solution. For the case where the direction of wave propagation is known, the optimal mesh parameter is evaluated analytically. For general problems where waves are directed in arbitrary directions, an optimum recommendation for the selection of the GLS parameter is provided. Several numerical examples are given and the results compared with those obtained from the standard Galerkin method. The optimum GLS parameter is given for both linear and quadratic interpolation functions. In addition, extensions to three-dimensional elements and Generalized Galerkin/Least-Squares Methods are discussed.

In recent years, there has been a resurgence of interest in the use of hierarchical p-version finite element and spectral elements to obtain high-resolution numerical solutions for structural acoustics. In Chapter 9 it is shown that high-order finite element discretizations display frequency bands where the solutions are harmonic decaying waves. In these so called 'stopping' bands, the solutions are not purely propagating (real wavenumbers) but are attenuated (complex wavenumbers). In this work, the standard dispersion analysis technique is extended to include complex wavenumbers. This complex wavenumber Fourier analysis technique is then used to examine the dispersion and attenuation characteristics of high-order elements. Three alternatives are considered: (i) hierarchic p-version elements based on Legendre functions, (ii) new hierarchic Fourier elements based on sinusoidal functions, and (iii) spectral elements based on Lagrange interpolation in conjunction with Gauss-Lobatto quadrature. Practical guidelines for phase and amplitude accuracy in terms of the spectral order and the number of elements per wavelength are reported.

Finally, in Chapter 10, conclusions are presented and recommendations for future research are given.

Chapter 2

Coupled Problem Statement

In this work, the exterior structural acoustics problem involving solution of the coupled wave equation defined over an infinite domain is transformed to a coupled fluid-structure interaction problem defined over a finite computational domain through the introduction of an artificial fluid truncation boundary. For uniqueness, radiation boundary conditions are prescribed on the fluid truncation boundary in the form of a linear operator which approximates the asymptotic behavior of the solution at infinity. The coupled system for the exterior structural acoustics problem is composed of four distinct components:

(i) the structure,
(ii) the acoustic fluid,
(iii) structure-fluid interface conditions, and
(iv) non-reflecting boundary conditions.

In the following, the governing differential equations for each of the four components are described. After collecting these equations, the strong (local) form of the fluid-structure initial/boundary-value problem is stated for structural acoustics. In the remainder of this chapter, a number of important energy estimates for the coupled problem are derived. These results play a central role in the analysis of stability for both the continuum and discrete problems and form the basis for the design of the space-time finite element methods presented in this thesis.

The coupled fluid-structure system is illustrated in Figure 2.1, and consists of

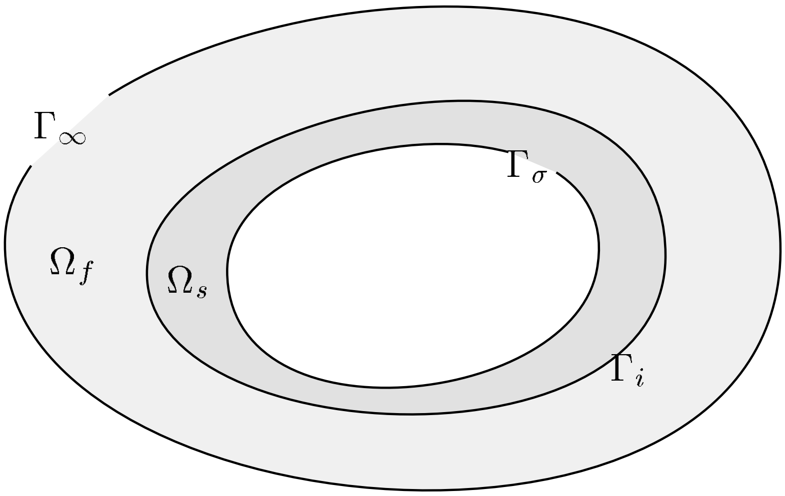

Figure 2.1: Coupled system for the exterior fluid-structure interaction problem, with artificial boundary Γ_∞ enclosing the finite computational domain $\Omega = \Omega_f \cup \Omega_s$.

an artificial truncation boundary Γ_∞ enclosing a finite computational domain Ω. The finite computational domain is composed of the fluid domain Ω_f, which in turn surrounds the structural domain Ω_s such that $\Omega = \Omega_f \cup \Omega_s$. The fluid boundary $\partial\Omega_f$, is divided into a fluid-structure interface boundary Γ_i, and an artificial boundary Γ_∞. The structural boundary $\partial\Omega_s$, is composed of the shared fluid-structure interface boundary Γ_i and a traction boundary Γ_σ. The infinite domain outside the artificial boundary and extending to infinity is denoted by Ω_∞. In this thesis, the domain interior to the elastic body is assumed to be in vacuo, although the inclusion of an interior fluid can be accommodated with no special difficulty. In the following, the equations governing the structure, the acoustic fluid, and their interaction are summarized.

2.1 Governing Equations for Structural Acoustics

The governing equations for the structure are stated for a linear solid continuum without the explicit imposition of kinematic constraints common to structural models such as plates and shells. In this way, full generality of the formulation is maintained in order to accommodate a wide class of shell models into the formulation. The acoustic fluid is modeled under the usual assumptions governing sound wave propagation; a compressible and inviscid fluid linearized about an equilibrium state with constant density and velocity. The fluid is assumed to be homogeneous outside the computational domain Ω_∞, but may be inhomogeneous within Ω_f. In this work the density of the fluid is assumed comparable to the inertial and elastic forces in the structure so that significant interaction exists.

2.2 The Structure

Consider an elastic body occupying the bounded domain $\Omega_s \in \mathbb{R}^d$, where $d = 1$, 2 or 3 is the number of space dimensions. The structural displacement vector is denoted by $\boldsymbol{u}(\boldsymbol{x}, t)$, where $\boldsymbol{x} \in \overline{\Omega}_s := \Omega_s \cup \partial\Omega_s$, and $t \in I =]0, T[$, is the time interval of interest of length $T > 0$. The equations of motion for the structure are governed by the linear momentum balance, which can be stated as,

$$\boxed{\nabla \cdot \boldsymbol{\sigma} \quad = \quad \rho_s \ddot{\boldsymbol{u}} \qquad \text{in} \quad Q_s := \Omega_s \times]0\,,\, T[} \tag{2.1}$$

where $\rho_s = \rho_s(\boldsymbol{x}) > 0$ is the structural density, a superposed dot indicates partial differentiation with respect to time t, and $\boldsymbol{\sigma}$ is the symmetric Cauchy stress tensor which is related to the displacements through the constitutive equation,

$$\boldsymbol{\sigma} \quad = \quad \boldsymbol{C} : \boldsymbol{\varepsilon}[\boldsymbol{u}] \tag{2.2}$$

In this expression, the strain tensor is denoted by $\boldsymbol{\varepsilon}[\boldsymbol{u}] = \nabla^s \boldsymbol{u}$, where $\nabla^s \boldsymbol{u}$ is the symmetric gradient of the displacement vector. The elastic coefficients $\boldsymbol{C} = \boldsymbol{C}(\boldsymbol{x})$ are assumed to satisfy the usual positive-definiteness (pointwise stability) and major and minor symmetry assumptions for an elastic solid continuum. Pointwise stability implies that,

$$C_{ijkl}\varepsilon_{ij}\varepsilon_{kl} \;\geq\; \gamma ||\boldsymbol{\varepsilon}||^2_{\Omega_s} \tag{2.3}$$

for some constant $\gamma > 0$. By the minor symmetries, $\boldsymbol{\sigma}$ is symmetric and depends only upon the symmetric gradient $\nabla^s \boldsymbol{u}$ of the displacement. Under the usual assumption of isotropic materials, the constitutive relation specializes to the generalized Hooke's law:

$$\boldsymbol{\sigma} = \lambda \mathrm{tr}(\boldsymbol{\varepsilon})\mathbf{1} + 2\mu\boldsymbol{\varepsilon} \tag{2.4}$$

where λ and μ are the Lame constants, $\mathrm{tr}(\boldsymbol{\varepsilon})$ is the trace of the strain tensor and $\mathbf{1}$ is the second-order identity tensor. Other constitutive relationships can also be used, for example the visco-elastic relationships described in ABBOUD [1990].

With Γ_σ and Γ_i denoting non-overlapping subregions of $\partial\Omega_s$ such that $\partial\Omega_s = \overline{\Gamma_\sigma \cup \Gamma_i}$, prescribed tractions $\bar{\boldsymbol{t}}$, are enforced through the boundary condition,

$$\boldsymbol{\sigma} \cdot \boldsymbol{n} \quad = \quad \bar{\boldsymbol{t}} \qquad \text{on} \;\; \Upsilon_\sigma := \Gamma_\sigma \times]0\,, T[\tag{2.5}$$

The specification of coupling conditions on the structure-fluid interface Γ_i are discussed later in Section 2.3.3. Here we note that two interface conditions are required: (i) a kinematic interface condition, and (ii) a traction interface condition. Prescribed displacements (i.e. essential boundary conditions) are set to zero for clarity of presentation, although the inclusion of non-homogeneous conditions is straightforward.

2.3 The Acoustic Fluid

The acoustic fluid is modeled under the usual assumptions governing the linearized theory of sound. Under the standard acoustic approximation, the motion of an inviscid, irrotational, and compressible fluid is regarded as a small perturbation from a uniform reference state. Linearizing the conservation equations of compressible inviscid flow around a reference state in which the fluid has a uniform density ρ_0 and is at rest, i.e.

$$\rho_0 = \mathrm{const}\,,\; p_o = \mathrm{const}\,,\; \boldsymbol{v}_0 = 0 \tag{2.6}$$

with products of small quantities neglected, the equations of momentum and of continuity for the acoustic fluid take the form (see e.g. ZAUDERER [1989]):

$$\rho_0 \dot{\boldsymbol{v}} + \nabla p \quad = \quad 0 \tag{2.7}$$

$$\dot{\rho} + \rho_0 \nabla \cdot \boldsymbol{v} \quad = \quad 0 \tag{2.8}$$

where p, ρ, and $\boldsymbol{v}$ denote perturbations of pressure, density and velocity from the reference state. These equations relate the local rates of change of velocity and density to the pressure gradient and to the velocity divergence, respectively. The momentum equation (2.7) expresses the inertial nature of the fluid, while the continuity equation (2.8) expresses the compressibility of the fluid. In this work, the relationship between changes in pressure and density are given by the linearized equation of state, $\dot{p} = c^2 \dot{\rho}$, where $c > 0$ is the speed of sound (velocity of acoustic wave propagation).

2.3.1 First-order hyperbolic form

Combining (2.8) with the equation of state $\dot{p} = c^2 \dot{\rho}$, results in a system of first-order hyperbolic equations in terms of pressure and velocity variables:

$$\rho_0 \dot{\boldsymbol{v}} + \nabla p = 0 \tag{2.9}$$

$$\dot{p} + \rho_0 c^2 \nabla \cdot \boldsymbol{v} = 0 \tag{2.10}$$

Defining the state vector as,

$$\boldsymbol{U} = (p\,,\ v_1\,,\ v_2\,,\ v_3)^T \tag{2.11}$$

where v_i are the velocity components in $\mathbb{R}^3$, these equations can be arranged in standard first-order hyperbolic form as,

$$\boxed{\frac{\partial \boldsymbol{U}}{\partial t} + \sum_{i=1}^{3} \boldsymbol{A}_i \frac{\partial \boldsymbol{U}}{\partial x_i} = 0} \tag{2.12}$$

and $A_i \in \mathbb{R}^{4\times 4}$, $i = 1, \cdots 3$ are sparse unsymmetric matrices for the system in $\mathbb{R}^3$. Considerable progress has been made in the development of stabilized time-discontinuous Galerkin finite elements methods for first-order hyperbolic and parabolic systems; see for example Johnson et al. [1984,1986], Hughes [1987b], Shakib et al. [1991b] and references therein. These methods are immediately applicable to the classical linear acoustics equations written in the first-order form (2.12). However, in this approach, the state vector consists of both pressure and velocity components, requiring a large number of solution variables, which may be computationally uneconomical. Another difficulty with this approach is the coupling between the natural second-order form of the momentum equations governing the structure, and a first-order form for the system of equations describing the acoustic fluid. As a result of the mismatch between the second-order and first-order systems for the structure and fluid respectively, rigorous stability and convergence proofs for the coupled fluid-structure system are difficult (if not impossible) to obtain. In addition, for the exterior problem, incorporation of high-order accurate non-reflecting boundary conditions involving high-order temporal derivatives in a stable and efficient formulation for first-order systems is difficult to achieve.

2.3.2 Second-order hyperbolic form

For these reasons, a more natural approach for the coupled problem is to recast the first-order system of acoustic equations given in (2.12) as a second-order hyperbolic equation in terms of a single scalar variable. The most common choice is to eliminate the velocity in terms of the scalar pressure variable. Taking the divergence of (2.9) and the time derivative of (2.10), and after eliminating the velocity in terms of pressure we obtain the second-order scalar wave equation,

$$\nabla^2 p = a^2 \ddot{p} \tag{2.13}$$

where $a = c^{-1} > 0$ is the slowness and $\nabla^2 = \mathrm{Div}(\mathrm{Grad})$ is the Laplacian operator. Traditional variational (weak) formulations for the coupled structural acoustics problem are based on this second-order hyperbolic wave equation in terms of the scalar acoustic pressure p, together with the equations of elastodynamics in terms of the structural displacement $\boldsymbol{u}$, see e.g. ZIENKIEWICZ [1978] for this approach in the context of the semidiscrete finite element method. While this approach reduces the number of solution variables in the formulation, the use of $\{\boldsymbol{u}\,,\,p\}$ variables leads to an unsymmetric coupled system of equations for the fluid-structure problem. As a result of this lack of symmetry, stability and energy estimates for both the continuum and discrete structural-acoustic problems are difficult to obtain *a priori*.

To eliminate this difficulty for the coupled problem, scalar velocity potential ϕ, is chosen as the solution variable for the acoustic fluid, in conjunction with the displacement vector $\boldsymbol{u}$, for the structure. As a consequence of this choice of variables, the coupled variational equations associated with the fluid-structure interaction problem give rise to a globally symmetric form, which in the context of the space-time finite element formulation, allows for the prove of stability and convergence of the method.

The use of the velocity potential follows directly from the assumption of an irrotational acoustic fluid. Taking the curl of (2.9) and using the fact that the curl of ∇p vanishes, implies,

$$\frac{\partial}{\partial t}(\nabla \times \boldsymbol{v}) = 0 \tag{2.14}$$

This result indicates that the acoustic part of the velocity field is indeed irrotational. Only the irrotational part exhibits the fluctuations associated with sound propagation so that the acoustic velocity $\boldsymbol{v}$, can be written as the gradient of the velocity potential ϕ:

$$\boxed{\boldsymbol{v} = \nabla \phi} \tag{2.15}$$

Substituting (2.15) into (2.9) and (2.10) results in a form involving the Laplacian differential operator,

$$p + \rho_0 \dot{\phi} = 0 \tag{2.16}$$

$$\dot{p} + \rho_0 c^2 \nabla^2 \phi = 0 \tag{2.17}$$

Eliminating the pressure in terms of the velocity potential $\phi(\boldsymbol{x}\,,\,t)$ with $\boldsymbol{x} \in \Omega_f$, gives the desired result,

$$\boxed{\nabla^2 \phi = a^2 \ddot{\phi} \qquad \text{in} \quad Q_f := \Omega_f \times \,]0\,,\,T[} \tag{2.18}$$

This second-order hyperbolic wave equation in terms of the acoustic velocity potential ϕ, is used as the basis for the fluid representation in the variational formulations developed in this thesis. In the presentation to follow, we will show how this choice of variable for the acoustic fluid leads directly to a globally symmetric coupled system from which *a priori* stability and energy estimates are obtained for both the continuum and discrete fluid-structure interaction problem.

2.3.3 Fluid-Structure Coupling

The unique solution to the coupled problem requires two interface conditions between the structure and fluid: (i) a traction boundary condition, and (ii) a kinematic compatibility condition. The traction boundary condition represents the acoustic fluid pressure acting on the structure and is given by,

$$\boxed{\boldsymbol{\sigma} \cdot \boldsymbol{n} \quad = \quad \rho_0 \dot{\phi} \boldsymbol{n} \qquad \text{on} \quad \Upsilon_i := \Gamma_i \times \,]0\,,\, T[} \tag{2.19}$$

where $p = -\rho_0 \dot{\phi}$ and $\boldsymbol{n}$ is the unit outward normal to Ω_s, and inward normal to Ω_f, on Γ_i. The kinematic boundary condition provides for the compatibility of the normal velocity across the fluid-structure interface and is given by,

$$\boxed{\nabla \phi \cdot \boldsymbol{n} \quad = \quad \dot{\boldsymbol{u}} \cdot \boldsymbol{n} \qquad \text{on} \quad \Upsilon_i := \Gamma_i \times \,]0\,,\, T[} \tag{2.20}$$

where $\boldsymbol{v} = \nabla \phi$.

Remark

- When pressure p, is used in place of the velocity potential ϕ, as the basic solution variable for the fluid, the kinematic boundary condition enforcing compatibility of normal velocity is usually replaced with a kinematic condition enforcing compatibility of normal accelerations, i.e.,

  $$\nabla p \cdot \boldsymbol{n} \quad = \quad -\rho_0 \ddot{\boldsymbol{u}} \cdot \boldsymbol{n} \qquad \text{on} \quad \Upsilon_i := \Gamma_i \times \,]0\,,\, T[\tag{2.21}$$

  This condition is in effect the time derivative of (2.20) and is required for a displacement-pressure $\{\boldsymbol{u}\,,\, p\}$ variational formulation where it is incorporated as a Neumann ('natural') boundary condition.

2.3.4 Non-Reflecting Boundary Conditions

The exterior structural acoustics problem typically involves the the radiation and scattering of sound waves emanating from a vibrating structure submerged in an infinite acoustic fluid. When a domain based computational method such as the finite element method is used, the fluid domain must be truncated at a finite distance from the structure. In order to eliminate or minimize reflection of outgoing waves, radiation (non-reflecting) boundary conditions are applied on the fluid truncation boundary. If accurate non-reflecting boundary conditions are used then the fluid truncation boundary can be moved closer to the structure and the finite element model will be able to use fewer elements than otherwise would be possible and considerable cost savings may result.

In this thesis, non-reflecting boundary conditions are imposed on the artificial boundary Γ_∞ in the form of a linear operator $\mathbb{S}_m$, relating Dirichlet data ϕ, to the normal derivative $\nabla\phi \cdot \boldsymbol{n}$, through the mapping,

$$\boxed{\nabla\phi \cdot \boldsymbol{n} \quad = \quad -\mathbb{S}_m \phi \qquad \text{on} \quad \Upsilon_\infty := \Gamma_\infty \times]0, T[} \tag{2.22}$$

This boundary condition approximates the asymptotic behavior of the solution at infinity as described by the Sommerfeld condition, i.e.

$$\lim_{r\to\infty} r^{(d-1)/2} \left(\frac{\partial}{\partial r} + \frac{1}{c}\frac{\partial}{\partial t} \right) \phi = 0 \qquad r + ct = \text{constant} \tag{2.23}$$

where r is the radial distance from the source. This condition asserts that at infinity all waves are outgoing. The non-reflecting boundary condition (2.22) can take several different forms depending on the local (differential) or nonlocal (integral) operators appearing in $\mathbb{S}_m$. The specific definition of the operator $\mathbb{S}_m$ relating Dirichlet to Neumann data is given in Chapters 5 and 6. Here we note that the index m, is related to the order of temporal derivatives appearing in the operator.

For an artificial boundary taken to be a circle in two-dimensions ($d = 2$) or a sphere in three-dimensions ($d = 3$), the obvious choice for $\mathbb{S}_m$ is to use a simple Sommerfeld-like boundary condition on the truncation boundary Γ_∞ of the form,

$$\nabla\phi \cdot \boldsymbol{n} \quad = \quad -\frac{1}{c}\dot{\phi} \qquad \text{on} \quad \Upsilon_\infty := \Gamma_\infty \times]0, T[\tag{2.24}$$

where $\nabla\phi \cdot \boldsymbol{n} = \partial\phi/\partial n$ is the normal derivative on Γ_∞. Restated in terms of the physical variables of pressure, $p = -\rho_0\dot{\phi}$, and velocity $\boldsymbol{v} = \nabla\phi$, this boundary condition becomes,

$$\boldsymbol{v}\cdot\boldsymbol{n} = p/z_o \tag{2.25}$$

where $z_o = \rho_0 c$, is the characteristic impedance for plane-wave propagation. In one-dimension ($d = 1$), this condition is exact not only at infinity, but also at any finite distance r. However, in multi-dimensions ($d = 2, 3$), this boundary condition may produce large spurious reflections, resulting in large errors in the numerical solution, except at very high frequencies or large r where the operator acts as a plane-wave (PW) absorber.

Because of the potential loss of accuracy resulting from the use of (2.24), an improved non-reflecting boundary is needed. A number of high-order accurate non-reflecting boundary conditions are available and will be discussed in detail in Chapters 5 and 6. An example is given here for the first-order accurate boundary condition,

$$\nabla\phi\cdot\boldsymbol{n} \quad = \quad -\frac{1}{R}\phi - \frac{1}{c}\dot{\phi} \qquad \text{on} \quad \Upsilon_\infty := \Gamma_\infty \times]0, T[\tag{2.26}$$

This non-reflecting boundary condition is exact for axially symmetric waves in $\mathbb{R}^3$ and will henceforth be denoted as $\mathbb{S}_1$.

2.4 The Strong Form in the Time-Domain

After collecting the governing equations defined in the preceding sections, the strong (local) form of the fluid-structure initial/boundary-value problem may be stated as:

Given a prescribed traction $\bar{\boldsymbol{t}} : \Gamma_\sigma \times I \mapsto \mathbb{R}^d$ and a source $f : \Omega_f \times I \mapsto \mathbb{R}$,
Find $\boldsymbol{u} : \bar{\Omega}_s \times I \mapsto \mathbb{R}^d$, and $\phi : \bar{\Omega}_f \times I \mapsto \mathbb{R}$, such that

$$\nabla\cdot\boldsymbol{\sigma} - \rho_s\ddot{\boldsymbol{u}} \quad = \quad \boldsymbol{0} \qquad \text{in } Q_s := \Omega_s \times I \tag{2.27}$$

$$\boldsymbol{\sigma} \quad = \quad \boldsymbol{C} : \nabla^s\boldsymbol{u} \qquad \text{in } Q_s := \Omega_s \times I \tag{2.28}$$

$$\nabla^2\phi - a^2\ddot{\phi} \quad = \quad f \qquad \text{in } Q_f := \Omega_f \times I \tag{2.29}$$

$$\boldsymbol{\sigma}\cdot\boldsymbol{n} \quad = \quad \bar{\boldsymbol{t}} \qquad \text{on } \Upsilon_\sigma := \Gamma_\sigma \times I \tag{2.30}$$

$$\boldsymbol{\sigma}\cdot\boldsymbol{n} \quad = \quad \rho_0\dot{\phi}\boldsymbol{n} \qquad \text{on } \Upsilon_i := \Gamma_i \times I \tag{2.31}$$

$$\nabla\phi \cdot \boldsymbol{n} = \dot{\boldsymbol{u}} \cdot \boldsymbol{n} \qquad \text{on } \Upsilon_i := \Gamma_i \times I \tag{2.32}$$

$$\nabla\phi \cdot \boldsymbol{n} = -\mathbb{S}_m \phi \qquad \text{on } \Upsilon_\infty := \Gamma_\infty \times I \tag{2.33}$$

with initial conditions,

$$\boldsymbol{u}(\boldsymbol{x}, 0) = \boldsymbol{u}_o(\boldsymbol{x}) \qquad \text{for } \boldsymbol{x} \in \Omega_s \tag{2.34}$$

$$\dot{\boldsymbol{u}}(\boldsymbol{x}, 0) = \dot{\boldsymbol{u}}_o(\boldsymbol{x}) \qquad \text{for } \boldsymbol{x} \in \Omega_s \tag{2.35}$$

$$\phi(\boldsymbol{x}, 0) = \phi_o(\boldsymbol{x}) \qquad \text{for } \boldsymbol{x} \in \Omega_f \tag{2.36}$$

$$\dot{\phi}(\boldsymbol{x}, 0) = \dot{\phi}_o(\boldsymbol{x}) \qquad \text{for } \boldsymbol{x} \in \Omega_f \tag{2.37}$$

Equations (2.27) – (2.33) together with the initial boundary conditions define a linear coupled system of second-order hyperbolic type due to the positive definite condition on $\boldsymbol{C}$ and $c > 0$. Thus the exterior structural acoustics problem, in its local form, consists of solving the equations of elastodynamics for the displacement field within Ω_s and the scalar wave equation in Ω_f for the acoustic velocity potential field, due to a traction loading, acoustic sources, and initial conditions. In addition, the traction and normal velocity must be continuous across the fluid-structure interface Γ_i, and the velocity potential must satisfy the radiation boundary condition (2.33) on Γ_∞.

2.5 Energy Estimates for the Continuum Problem

In this section we establish some *a priori* estimates for the continuum problem in terms of the energy for the hyperbolic structure-fluid coupled system using structural displacement $\boldsymbol{u}$, and acoustic velocity potential ϕ variables. The study of these important mathematical properties provides a general framework for the design and stability analysis of the proposed space-time finite element algorithm proposed in this thesis.

2.5.1 Energy Identities

In this section an energy identity for the continuum problem is established which relates the total structural and acoustic energies to the radiation energy absorbed through the fluid truncation boundary. Let the solution vector be defined in abstract form as,

$$\boxed{\boldsymbol{\mathcal{X}} := \{\boldsymbol{u}\,,\,\phi\}} \tag{2.38}$$

Then define the total energy for the coupled domain $\Omega = \Omega_s \cup \Omega_f$ by the expression,

$$\boxed{\mathbb{E}(\boldsymbol{\mathcal{X}}) := \mathcal{E}_s(\boldsymbol{u}) + \mathcal{E}_f(\phi)} \tag{2.39}$$

where the total structural energy in terms of the structural displacements is,

$$\mathcal{E}_s(\boldsymbol{u}) := \quad \frac{1}{2}\int_{\Omega_s} [\rho_s \dot{\boldsymbol{u}} \cdot \dot{\boldsymbol{u}} + \boldsymbol{\varepsilon}(\boldsymbol{u}) : \boldsymbol{C} : \boldsymbol{\varepsilon}(\boldsymbol{u})]\ d\Omega \tag{2.40}$$

and the acoustic energy or 'wave energy' in terms of the velocity potential is,

$$\begin{aligned} \mathcal{E}_f(\phi) \quad &:= \quad \frac{1}{2}\int_{\Omega_f} \rho_0[(\frac{p}{\rho_0 c})^2 + \boldsymbol{v}\cdot\boldsymbol{v}]\ d\Omega \\ &= \quad \frac{1}{2}\int_{\Omega_f} \rho_0[a^2(\dot{\phi})^2 + \nabla\phi\cdot\nabla\phi]\ d\Omega \end{aligned} \tag{2.41}$$

The first and second terms in (2.40) are the kinetic and strain energy for the elastic structure respectively. The form of the acoustic energy written in terms of velocity potential is in reverse order: the first term (time derivative squared) and second term (gradient squared) in (2.41) are the potential and kinetic energies respectively. The reverse order of the kinetic and potential energies for $\mathcal{E}_s(\boldsymbol{u})$ and $\mathcal{E}_f(\phi)$ reflect the reciprocal nature of the structure and fluid in an energy sense.

The total energy norm for the coupled system:

An important property of (2.39) is that in the Hilbert space

$$\mathcal{V} = [H^1(\Omega_s)]^d \times H^1(\Omega_f) \tag{2.42}$$

the total energy for the coupled system $\mathbb{E}(\boldsymbol{\mathcal{X}})$ with abstract solution vector $\boldsymbol{\mathcal{X}} \in \mathcal{V}$ defines a natural energy norm on the space $\mathcal{V}$,

$$\boxed{\mathbb{E}(\boldsymbol{\mathcal{X}}) := ||\boldsymbol{\mathcal{X}}||^2_{\mathcal{V}}} \tag{2.43}$$

This result follows directly from the positive definite assumption on $\boldsymbol{C}$ and $c > 0$.

The acoustic intensity:

The acoustic intensity for sound waves is defined as the vector, $\boldsymbol{I} := p\boldsymbol{v}$, where p and $\boldsymbol{v}$ are the acoustic pressure and velocity respectively, see LIGHTHILL [1978]. In terms of the velocity potential the acoustic intensity vector is given by,

$$\boldsymbol{I} = -\rho_0 \dot{\phi} \nabla \phi \tag{2.44}$$

whose component $\boldsymbol{I} \cdot \boldsymbol{n}$ is the rate per unit area at which energy is transmitted in the direction of the unit normal $\boldsymbol{n}$. For the exterior problem, the rate of energy (power) absorbed through the artificial boundary Γ_∞ is then,

$$\mathcal{D}(\phi) := -\int_{\Gamma_\infty} \rho_0 \dot{\phi} \nabla \phi \cdot \boldsymbol{n} \; d\Gamma \tag{2.45}$$

In terms of the absorbing boundary conditions defined through the linear map $\mathbb{S}_m$ we have,

$$\boxed{\mathcal{D}(\phi) = \int_{\Gamma_\infty} \rho_0 \dot{\phi} \mathbb{S}_m \phi \; d\Gamma} \tag{2.46}$$

With these definitions in place, we are in position to prove the following energy estimate for the coupled structural acoustics problem in exterior domains.

Lemma 2.1 (Energy estimate)
Under the conditions of zero sources $f = 0$ in Ω_f, and homogeneous traction boundary conditions $\bar{\boldsymbol{t}} = 0$ on Γ_σ, then the time rate of change of structural acoustic energy in $\Omega = \Omega_s \cup \Omega_f$ is equal to the total rate of transport through the artificial boundary Γ_∞,

i.e.

$$\boxed{\frac{d}{dt}\mathbb{E}(\boldsymbol{\mathcal{X}}) = -\mathcal{D}(\phi), \qquad \forall\; t \geq 0} \tag{2.47}$$

where $\boldsymbol{\mathcal{X}} = \{\boldsymbol{u}\,,\,\phi\}$.

Proof:
The proof of this important result employs integration by parts and provides the key motivation for the space-time finite element formulation proposed in this thesis. Computing the time derivative we have,

$$\begin{aligned} \frac{d}{dt}\mathcal{E}_s(\boldsymbol{u}) &= \int_{\Omega_s} [\rho_s \dot{\boldsymbol{u}} \cdot \ddot{\boldsymbol{u}} \,+\, \boldsymbol{\varepsilon}(\dot{\boldsymbol{u}}) : \boldsymbol{C} : \boldsymbol{\varepsilon}(\boldsymbol{u})]\; d\Omega \\ &= \int_{\Omega_s} [\dot{\boldsymbol{u}} \cdot (\nabla \cdot \boldsymbol{\sigma}) \,+\, \boldsymbol{\varepsilon}(\dot{\boldsymbol{u}}) : \boldsymbol{C} : \boldsymbol{\varepsilon}(\boldsymbol{u})]\; d\Omega \\ &= \int_{\Gamma_i} \rho_0 \dot{\phi}\; \dot{\boldsymbol{u}} \cdot \boldsymbol{n}\; d\Gamma \end{aligned} \tag{2.48}$$

Similarly,

$$\begin{aligned} \frac{d}{dt}\mathcal{E}_f(\phi) &= \int_{\Omega_f} \rho_0 [a^2 \dot{\phi}\,\ddot{\phi} \,+\, \nabla\dot{\phi} \cdot \nabla\phi]\; d\Omega \\ &= \int_{\Omega_f} \rho_0 [\dot{\phi}\,\nabla^2\phi \,+\, \nabla\dot{\phi} \cdot \nabla\phi]\; d\Omega \\ &= -\int_{\Gamma_i} \rho_0 \dot{\phi}\; \dot{\boldsymbol{u}} \cdot \boldsymbol{n}\; d\Gamma - \int_{\Gamma_\infty} \rho_0 \dot{\phi}\; \mathbb{S}_m \phi\; d\Gamma \end{aligned} \tag{2.49}$$

Combining (2.48) and (2.49) gives the desired energy estimate (2.47). □

Remarks

1. It is important to note that by choosing the velocity potential ϕ for the acoustic variable and enforcing the compatibility of normal velocity (2.20) across Γ_i, then the coupling integrals defined on the fluid-structure interface boundary Γ_i, cancel when (2.48) and (2.49) are added together to form (2.47). This is the key property associated with the choice of $\boldsymbol{\mathcal{X}}$ variables and plays an important role in the stability (energy) estimates for the space-time formulation.

If the acoustic pressure is used as the fluid variable, together with the compatibility of normal accelerations (2.21) as required in a coupled variational equation for structural acoustics, then the coupling integrals defined on Γ_i, *will not cancel.* It is this property resulting from the use of $\{\boldsymbol{u}\,,\, p\}$ variables that destroys the inherent symmetry for the coupled structural acoustics system and consequently invalidates the energy estimate given in Lemma 2.1,

2. For the interior (bounded) problem with zero internal sources and homogeneous boundary conditions, energy transport across boundaries is not allowed ($\mathbb{S}_m = 0$), so that $\mathcal{D}(\phi) = 0$, and (2.47) reduces to the familiar result:

$$\frac{d}{dt}\mathbb{E}(\boldsymbol{\mathcal{X}}) = 0 \qquad \forall\, t \geq 0 \tag{2.50}$$

which implies that the total energy within the interior domain Ω is conserved, i.e.

$$\mathbb{E}(\boldsymbol{\mathcal{X}}(t)) = \mathbb{E}(\boldsymbol{\mathcal{X}}(0)) \qquad \forall\, t \geq 0 \tag{2.51}$$

Theorem 2.1 (Energy identity)
At any given time $t > 0$, the energy in $\Omega = \Omega_s \cup \Omega_f$ plus the energy absorbed through the artificial boundary Γ_∞ is equal to the initial energy in the coupled system. i.e.

$$\boxed{\mathcal{E}_s(\boldsymbol{u}(t)) + \mathcal{E}_f(\phi(t)) + \mathcal{R}(\phi(t)) = \mathcal{E}_s(\boldsymbol{u}_0) + \mathcal{E}_f(\phi_0), \qquad \forall\, t \geq 0} \tag{2.52}$$

where

$$\mathcal{R}(\phi(t)) := \int_0^t \mathcal{D}(\phi(\tau))\; d\tau \tag{2.53}$$

is the radiation energy.

Proof: Integrating (2.47) over time,

$$\mathbb{E}(\boldsymbol{\mathcal{X}})\big|_0^t + \int_0^t \mathcal{D}(\phi(\tau))\; d\tau = 0 \tag{2.54}$$

and using definitions (2.40), (2.41) and (2.53) gives,

$$\mathcal{E}_s(\boldsymbol{u}(t)) + \mathcal{E}_f(\phi(t)) + \mathcal{R}(\phi(t)) = \mathcal{E}_s(\boldsymbol{u}(0)) + \mathcal{E}_f(\phi(0)), \qquad \forall\, t \geq 0 \tag{2.55}$$

Using the initial conditions, $\boldsymbol{u}(\boldsymbol{x}\,,\,0) = \boldsymbol{u}_0$ and $\phi(\boldsymbol{x}\,,\,0) = \phi_0$ gives the desired energy identity (2.52). $\square$

This result provides a natural measure of stability for the exterior structural acoustics problem, and will be used to guide the design of the space-time finite element formulation described in the next Chapter.

As a specific example for the energy estimates given in (2.47) and (2.52), consider the first-order non-reflecting boundary condition defined in (2.26). In this case the rate of energy absorbed through the artificial boundary Γ_∞ is given by the surface integral (2.46) with the normal derivative replaced with,

$$-\,\mathbb{S}_1\phi = -\frac{1}{R}\phi - \frac{1}{c}\dot{\phi} \tag{2.56}$$

Defining the following weighted L_2 norms on Γ_∞ as,

$$||\phi||^2_{\Gamma_\infty} \;:=\; \int_{\Gamma_\infty} \rho_0 (\phi)^2 \, d\Gamma \tag{2.57}$$

$$||\dot{\phi}||^2_{\Upsilon_\infty} \;:=\; \int_0^t ||\dot{\phi}||^2_{\Gamma_\infty} \, d\tau \tag{2.58}$$

then with the linear operator $\mathbb{S}_1$ defined in (2.26), the rate of energy transport through the artificial boundary specializes to,

$$\begin{aligned} \mathcal{D}(\phi) &= \frac{1}{R}\int_{\Gamma_\infty} \rho_0\; \dot{\phi}\phi \; d\Gamma \;+\; \frac{1}{c}\int_{\Gamma_\infty} \rho_0\; (\dot{\phi})^2 \; d\Gamma \\ &= \frac{1}{2}\frac{d}{dt} c_0 ||\phi||^2_{\Gamma_\infty} + c_1 ||\dot{\phi}||^2_{\Gamma_\infty} \end{aligned} \tag{2.59}$$

where $c_0 = 1/R$ and $c_1 = 1/c$ are positive constants. An energy identity of the form (2.52) is obtained by integrating (2.59) over time with the result,

$$\boxed{\mathcal{E}_s(\boldsymbol{u}) + \mathcal{E}_f(\phi) = \mathcal{E}_s(\boldsymbol{u}_0) + \mathcal{E}_f(\phi_0) - \frac{1}{2} c_0 ||\phi||^2_{\Gamma_\infty} - c_1 ||\dot{\phi}||^2_{\Upsilon_\infty}} \tag{2.60}$$

This is the stability (energy) estimate for the continuum problem with $\mathbb{S}_1$. It states that the total energy for the structure $\mathcal{E}_s$ and the fluid $\mathcal{E}_f$ at any time $t > 0$ is equal to the total initial energy in the system minus the radiation energy absorbed through the artificial boundary Γ_∞. An analogous result will be derived for the proposed space-time finite element formulation incorporating $\mathbb{S}_1$, see Theorem 4.1.

2.5.2 Uniqueness

A fundamental question pertaining to the exterior structural acoustics problem is whether a solution that satisfies the governing differential equations including the approximate non-reflecting boundary is unique. In this section we show how energy estimates of the form (2.60) can be used to help establish uniqueness of the solution. The question of uniqueness is approached by supposing that two solutions exist and then showing that this assumption leads to a contradiction, see e.g. Zauderer [1989] Chapter 6 and Achenbach [1987] Chapter 3. To prove that the initial/boundary-value problem for the coupled fluid-structure system written in terms of $\boldsymbol{\mathcal{X}} = \{\boldsymbol{u}\,,\,\phi\}$ variables and incorporating the first-order boundary operator $\mathbb{S}_1$, has a unique solution, we show that by assuming two unique solutions exist, given by $\boldsymbol{\mathcal{X}}_1$ and $\boldsymbol{\mathcal{X}}_2$, then it must be concluded that they are identical. Since the problem is linear, by superposition $\boldsymbol{\mathcal{X}} = \boldsymbol{\mathcal{X}}_1 - \boldsymbol{\mathcal{X}}_2$ must be a solution of the homogeneous problem with zero sources, $f = 0$, zero boundary data, $\bar{\boldsymbol{t}} = \boldsymbol{0}$, and zero initial data $\boldsymbol{\mathcal{X}}(0) = \boldsymbol{0}$. As a result, for the homogeneous problem, the energy estimate (2.60) reduces to,

$$\mathcal{E}_s(\boldsymbol{u}) + \mathcal{E}_f(\phi) + \frac{1}{2}c_0||\phi||^2_{\Gamma_\infty} + c_1||\dot{\phi}||^2_{\Upsilon_\infty} = 0 \tag{2.61}$$

Furthermore, both $\mathcal{E}_s(\boldsymbol{u})$ and $\mathcal{E}_f(\phi)$ are positive definite, and since c_0 and c_1 are positive on Γ_∞, the boundary integrals are non-negative as well, hence for (2.61) to hold we conclude,

$$\mathcal{E}_s(\boldsymbol{u}) = \mathcal{E}_f(\phi) = \frac{1}{2}c_0||\phi||^2_{\Gamma_\infty} = c_1||\dot{\phi}||^2_{\Upsilon_\infty} = 0 \tag{2.62}$$

and it follows that, $\boldsymbol{u} = \boldsymbol{0}$ and $\phi = 0$, which implies that the two supposedly different solutions must, in fact, be identical $\boldsymbol{\mathcal{X}}_1 = \boldsymbol{\mathcal{X}}_2$, so that only one solution exists. A remark here is that a crucial property for this proof was the non-negative integrands appearing in the the boundary integrals. Uniqueness proofs for high-order non-reflecting boundary operators $\mathbb{S}_m$ follow similar lines, assuming the non-negative property of the boundary integrals is maintained.

Chapter 3

Design of Space-Time Finite Element Methods for Structural Acoustics

In this chapter space-time finite element methods, based on a time-discontinuous variational formulation for fluid-structure interaction, are developed for the solution of the coupled structural acoustics problem in unbounded domains. Throughout this development, the energy estimates obtained in the preceding Chapter are used as a guide for the design of the proposed space-time algorithms. The formulation employs a finite computational fluid domain surrounding the structure and incorporates high-order accurate radiation boundary conditions on the fluid truncation boundary. Non-reflecting boundary conditions are incorporated as 'natural' boundary conditions in the space-time variational equation, i.e. they are enforced weakly in both space and time. An important ingredient for the success of the proposed space-time finite element method is the incorporation of time-discontinuous jump operators that weakly enforce continuity of the solution between space-time slabs. The specific form of these temporal jump operators are designed such that unconditional stability can be proved *a priori* for general unstructured discretizations in both space and time. An algorithm is termed unconditionally stable if in the absence of forcing terms but for arbitrary initial conditions, the computed total structural acoustic energy plus the radiation energy absorbed through the artificial boundary is always less than or equal to the total energy at the previous time step, for arbitrary step sizes. For additional stability, and to prove convergence, least-squares operators based on local residuals of the Euler-Lagrange equations for the coupled system, including the non-reflecting boundary conditions, are incorporated into the space-time formulation.

3.1 Background

Considerable progress has been made in the development of stabilized space-time finite element methods based on a time-discontinuous Galerkin formulation for problems that can be written as a system of first-order equations. As pointed out in the previous Chapter, classical linear acoustics equations can be converted to first-order hyperbolic form and these methods are thus immediately applicable. However, in this approach, the coupled state vector consists of fluid pressure and velocity components, which is computationally uneconomical.

A more direct approach is to develop space-time finite element methods for structural acoustics based on the natural framework of second-order hyperbolic equations for elastodynamics and the acoustic wave equation. Recently, HUGHES AND HULBERT [1988] and HULBERT AND HUGHES [1990] have successfully generalized time-discontinuous space-time finite element methods developed for first-order systems to the second-order hyperbolic equations of elastodynamics. In this thesis, the formulation is extended to include both the elastic structure and acoustic fluid posed in second-order hyperbolic form together with their interaction. For the coupled equations, scalar velocity potential ϕ is used as the solution variable for the acoustic fluid, while the displacement vector $\boldsymbol{u}$ is used for the structure. As a consequence of this choice of variables, the coupled variational equations for the fluid and structure give rise to a globally symmetric form, which in the context of the space-time finite element formulation, enables us to prove stability and convergence of the method.

3.2 Overview

The proposed space-time finite element method for the solution of the structural acoustics problem proceeds by considering a partitioning of the space-time domain into space-time slabs. Within each space-time slab we employ a time-discontinuous Galerkin approach, which allows for the use of completely unstructured space-time finite element discretizations and eliminates the need for an additional ordinary differential time integrator. By allowing for solutions to be discontinuous in time, the algorithm proceeds by marching sequentially in time. In Section 3.3 we state the trial and weighting spaces needed for the variational formulation and introduce the concept of the discontinuous jump operator which is critical to the stability of the method. In Section 3.4 the coupled variational equation is stated for the structural acoustics problem including the incorporation of an important class of high-order accurate non-reflecting boundary conditions. In Section 3.5 we introduce the concept of Galerkin/least-squares stabilization, in which least-squares operators are added to the basic Galerkin formulation to enhance the stability, while maintaining the accuracy, of the space-time method. Consistency of the proposed method is exposed in Section 3.6 where the weak enforcement of the Euler-Lagrange equations are discussed. In Section 3.8 we finish up this Chapter with a discussion of the positive form of the resulting space-time matrix equations and issues related to the stability and efficient solution of these equations.

3.3 Finite Element Discretization

The development of the space-time finite element method proceeds by considering an ordered partition of the open time interval, $I =]0, T[$, of the form: $0 = t_0 < t_1 < \ldots < t_N = T$. Denoting the nth open time interval,

$$I_n :=]t_n, t_{n+1}[\tag{3.1}$$

with variable time step $\Delta t_n = t_{n+1} - t_n$ we have $I = \left\{ \cup_{n=0}^{N-1} I_n \right\} \cup \{t_1\,,\, t_2\,,\, \ldots, t_{N-1}\}$.

Using this notation,

$$Q_n^s = \Omega_s \times I_n \tag{3.2}$$

$$Q_n^f = \Omega_f \times I_n \tag{3.3}$$

are the nth space-time slabs for the structure and fluid respectively, with boundaries $\Upsilon_n^s = \partial\Omega_s \times I_n$ and $\Upsilon_n^f = \partial\Omega_f \times I_n$. For the nth space-time slab $(n_{el})_n^s$ and $(n_{el})_n^f$ denote the number of space-time finite elements in the subdomains Q_n^s and Q_n^f respectively.

With these definitions, $Q_n^{s^e} \subset Q_n^s$, denotes the interior of the eth element in the structural domain with boundary $\Upsilon_n^{s^e}$. Similarly, $Q_n^{f^e} \subset Q_n^f$, denotes the interior of the eth element in the fluid domain, with boundary $\Upsilon_n^{f^e}$

Figure 3.1 shows an illustration of two consecutive space-time slabs Q_{n-1} and Q_n for the fluid where the superscript is omitted for clarity. Within each space-time element, the trial solution and weighting function are approximated by pth-order polynomials in $\boldsymbol{x}$ and t. These functions are assumed $C^0(Q_n)$ continuous throughout each space-time slab, but are allowed to be discontinuous across the interfaces of the slabs. Assuming the function $\boldsymbol{w}(\boldsymbol{x}\,,\,t)$ to be discontinuous at time t_n, suppressing the argument $\boldsymbol{x}$, the temporal jump operator is defined by,

$$\boxed{[\![\boldsymbol{w}(t_n)]\!] := \boldsymbol{w}(t_n^+) \;-\; \boldsymbol{w}(t_n^-)} \tag{3.4}$$

where

$$\boldsymbol{w}(t_n^{\pm}) = \lim_{\epsilon \to 0\pm} \boldsymbol{w}(t_n + \epsilon)$$

This discontinuity of the finite element functions across space-time slab interfaces, allows for the general use of high-order elements and spectral-type interpolations in both space and time, and provides freedom of changing the spatial discretization from one time step to another.

The collections of finite element interpolation functions are given by the spaces,

Trial structural displacements

$$\mathcal{S}^h = \bigcup_{n=0}^{N-1} \mathcal{S}_n^h\,, \qquad \mathcal{S}_n^h \quad = \quad \left\{ \boldsymbol{u}^h(\boldsymbol{x},t) \middle| \boldsymbol{u}^h \in (C^0(Q_n^s))^d\,,\, \boldsymbol{u}^h\Big|_{Q_n^{s^e}} \in (\mathcal{P}^p(Q_n^{s^e}))^d \right\}$$

Trial fluid potential

$$\mathcal{T}^h = \bigcup_{n=0}^{N-1} \mathcal{T}_n^h\,, \qquad \mathcal{T}_n^h \quad = \quad \left\{ \phi^h(\boldsymbol{x},t) \middle| \phi^h \in C^0(Q_n^f)\,,\, \phi^h\Big|_{Q_n^{f^e}} \in \mathcal{P}^p(Q_n^{f^e}) \right\}$$

where $\mathcal{P}^p$ denotes the space of pth-order polynomials, C^0 denotes the space of continuous functions and d is the number of space dimensions.

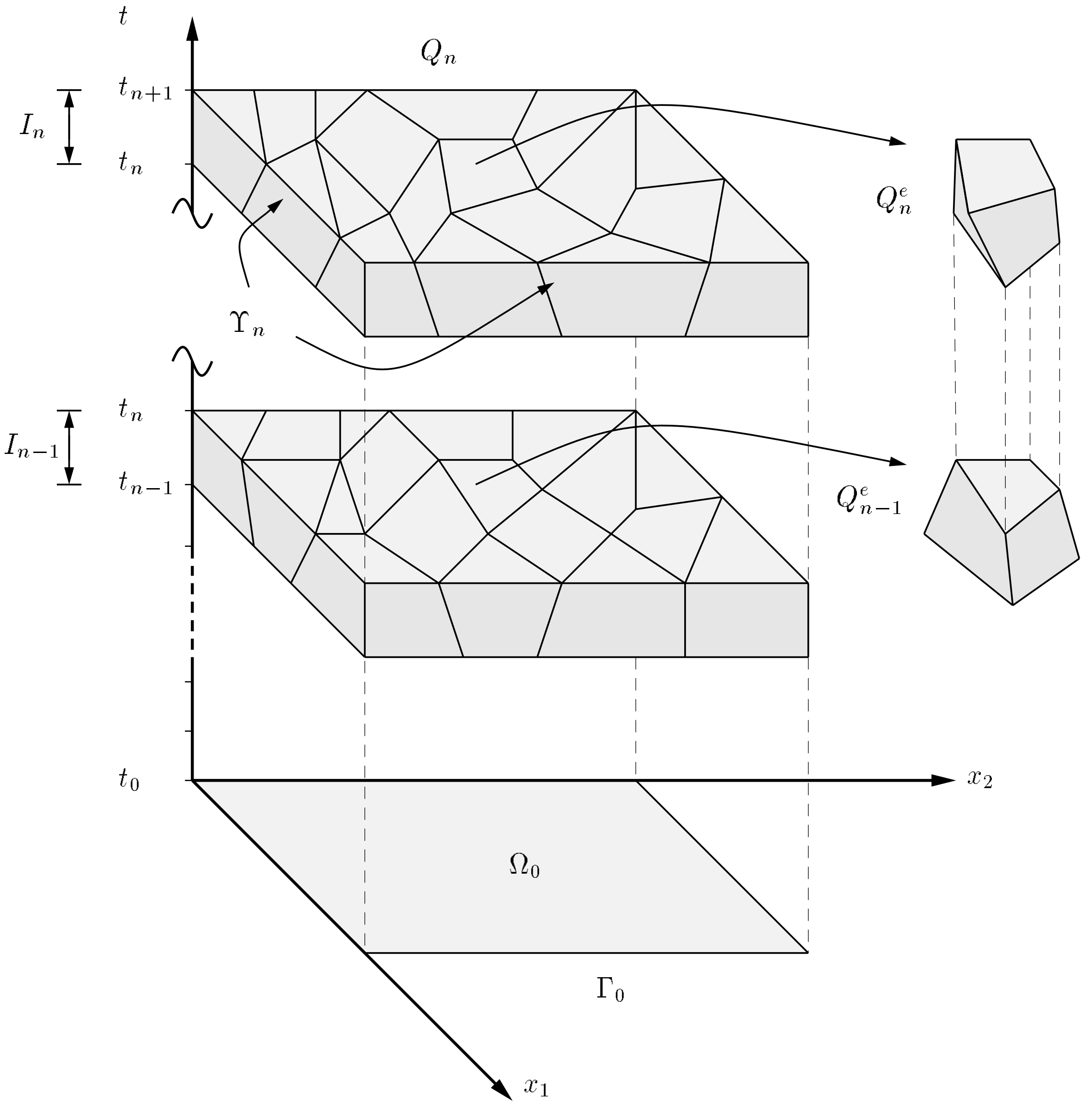

Figure 3.1: Illustration of two consecutive space-time slabs with unstructured finite element meshes in space-time.

As noted earlier, for clarity of presentation, prescribed displacements and prescribed velocity potential boundary conditions were not defined, i.e. essential boundary conditions are omitted. As a result of this assumption, the formulation is simplified in that the trial spaces and weighting spaces are identical, i.e. $\mathcal{S}^h = \mathcal{V}^h$ and $\mathcal{T}^h = \mathcal{W}^h$. Inclusion of essential boundary conditions is straightforward with the usual restrictions placed on the trial and weighting spaces.

3.4 Discontinuous Galerkin Formulation

The space-time variational formulation for the coupled structural acoustics problem is obtained from a weighted residual of the governing equations (2.27)–(2.33) within a space-time slab and incorporates time-discontinuous jump terms across slab interfaces. The specific form of this variational equation is designed such that *a priori* stability and energy estimates analogous to those described in Theorem 2.1 for the continuum problem are obtained for the discrete problem.

Preliminaries:

Before stating the space-time variational equations, it is useful to introduce the following notation.

$$\tilde{Q}_n = \bigcup_{e=1}^{(n_{el})_n} Q_n^e \qquad \text{(element interiors)} \tag{3.5}$$

$$\tilde{\Upsilon}_n = \bigcup_{e=1}^{(n_{el})_n} \Upsilon_n^e - \Upsilon_n \qquad \text{(interior mesh boundaries)} \tag{3.6}$$

Space-time element boundaries which coincide with the artificial boundary $(\Upsilon_\infty)_n = \Gamma_\infty \times I_n$ are denoted, $(\bar{\Upsilon}_\infty)_n^e = \Upsilon_n^e \cap (\Upsilon_\infty)_n$, where the overbar indicates the closure. Using this notation, the interiors of the element boundaries restricted to the artificial boundary are defined as,

$$(\tilde{\Upsilon}_\infty)_n = \bigcup_{e=1}^{(n_{el})_n} (\Upsilon_\infty)_n^e \tag{3.7}$$

Other notations are the following standard inner products,

$$(\boldsymbol{w}^h\,,\,\boldsymbol{u}^h)_{\Omega_s} \quad = \quad \int_{\Omega_s} \boldsymbol{w}^h \cdot \boldsymbol{u}^h \, d\Omega \tag{3.8}$$

$$a(\boldsymbol{w}^h\,,\,\boldsymbol{u}^h)_{\Omega_s} \quad = \quad \int_{\Omega_s} \nabla \boldsymbol{w}^h \cdot \boldsymbol{\sigma}(\nabla \boldsymbol{u}^h)\, d\Omega \tag{3.9}$$

$$(w^h\,,\,\phi^h)_{\Omega_f} \quad = \quad \int_{\Omega} \rho_0 \, w^h \, \phi^h \, d\Omega \tag{3.10}$$

$$(\nabla w^h\,,\,\nabla \phi^h)_{\Omega_f} \quad = \quad \int_{\Omega} \rho_0 \, \nabla w^h \cdot \nabla \phi^h \, d\Omega \tag{3.11}$$

$$(w^h\,,\,\phi^h)_{\Gamma_\infty} \quad = \quad \int_{\Gamma_\infty} \rho_0 \, w^h \, \phi^h \, d\Gamma \tag{3.12}$$

$$(w^h\,,\,\phi^h)_{Q_n^f} \quad = \quad \int_{t_n}^{t_{n+1}} (w^h\,,\,\phi^h)_{\Omega_f} \, dt \tag{3.13}$$

$$(w^h\,,\,\phi^h)_{(\Upsilon_\infty)_n} \quad = \quad \int_{t_n}^{t_{n+1}} (w^h\,,\,\phi^h)_{\Gamma_\infty} \, dt \tag{3.14}$$

$$(w^h\,,\,\phi^h)_{\tilde{Q}_n^f} \quad = \quad \sum_{e=1}^{(n_{el})_n} \int_{Q_n^{f^e}} w^h \phi^h \, dQ \tag{3.15}$$

The strain-energy inner product for the structure is denoted by (3.9) while the kinetic energy inner product for the fluid is denoted by (3.11). Note that inner products for the fluid are weighted by the fluid reference density ρ_0. The meaning of other similar notations may be inferred from these.

3.4.1 Variational Equations

In this section the time-discontinuous Galerkin variational equations for the coupled fluid-structure interaction problem are stated.

Within each space-time slab, $n = 0, 1, ..., N-1$, the object is to find $\boldsymbol{\chi}^h := \{\boldsymbol{u}^h\,,\,\phi^h\} \in \mathcal{S}_n^h \times \mathcal{T}_n^h$, such that $\forall\ \boldsymbol{\psi}^h := \{\boldsymbol{w}^h\,,\,w^h\} \in \mathcal{V}_n^h \times \mathcal{W}_n^h$, the following coupled variational equations are satisfied,

$$B_s(\boldsymbol{w}^h\,,\,\boldsymbol{\chi}^h)_n \quad = \quad L_s(\boldsymbol{w}^h)_n \tag{3.16}$$

$$B_f(w^h\,,\,\boldsymbol{\chi}^h)_n \quad = \quad L_f(w^h)_n \tag{3.17}$$

$$B_s(\boldsymbol{w}^h\,,\,\boldsymbol{\chi}^h)_n \;:=\; E_s(\boldsymbol{w}^h\,,\,\boldsymbol{u}^h)_n \,-\, A(\boldsymbol{w}^h\,,\,\phi^h\boldsymbol{n})_n \tag{3.18}$$

$$B_f(w^h\,,\,\boldsymbol{\chi}^h)_n \;:=\; E_f(w^h\,,\,\phi^h)_n \,+\, A(\boldsymbol{u}^h\,,\,w^h\boldsymbol{n})_n \,+\, E_r(w^h\,,\,\phi^h)_n \tag{3.19}$$

with the following definitions,

$$\begin{aligned} E_s(\boldsymbol{w}^h\,,\,\boldsymbol{u}^h)_n \;:=&\; (\dot{\boldsymbol{w}}^h\,,\,\rho_s\ddot{\boldsymbol{u}}^h)_{Q_n^s} \,+\, a(\dot{\boldsymbol{w}}^h\,,\,\boldsymbol{u}^h)_{Q_n^s} \\ &+\; (\dot{\boldsymbol{w}}^h(t_n^+)\,,\,\rho_s\dot{\boldsymbol{u}}^h(t_n^+))_{\Omega_s} \,+\, a(\boldsymbol{w}^h(t_n^+)\,,\,\boldsymbol{u}^h(t_n^+))_{\Omega_s} \end{aligned} \tag{3.20}$$

$$\begin{aligned} E_f(w^h\,,\,\phi^h)_n \;:=&\; (\dot{w}^h\,,\,a^2\ddot{\phi}^h)_{Q_n^f} \,+\, (\nabla\dot{w}^h\,,\,\nabla\phi^h)_{Q_n^f} \\ &+\; (\dot{w}^h(t_n^+)\,,\,a^2\,\dot{\phi}^h(t_n^+))_{\Omega_f} \,+\, (\nabla w^h(t_n^+)\,,\,\nabla\phi^h(t_n^+))_{\Omega_f} \end{aligned} \tag{3.21}$$

$$A(\boldsymbol{w}^h\,,\,\phi^h\boldsymbol{n})_n \;:=\; (\dot{\boldsymbol{w}}^h\,,\,\rho_0\dot{\phi}^h\boldsymbol{n})_{(\Upsilon_i)_n} \tag{3.22}$$

$$\begin{aligned} L_s(\boldsymbol{w}^h)_n \;:=&\; (\dot{\boldsymbol{w}}^h\,,\,\bar{\boldsymbol{t}})_{(\Upsilon_\sigma)_n} \\ &+\; (\dot{\boldsymbol{w}}^h(t_n^+)\,,\,\rho_s\dot{\boldsymbol{u}}^h(t_n^-))_{\Omega_s} \,+\, a(\boldsymbol{w}^h(t_n^+)\,,\,\boldsymbol{u}^h(t_n^-))_{\Omega_s} \end{aligned} \tag{3.23}$$

$$\begin{aligned} L_f(w^h)_n \;:=&\; (\dot{w}^h\,,\,f)_{Q_n^f} \\ &+\; (\dot{w}^h(t_n^+)\,,\,a^2\,\dot{\phi}^h(t_n^-))_{\Omega_f} \,+\, (\nabla w^h(t_n^+)\,,\,\nabla\phi^h(t_n^-))_{\Omega_f} \end{aligned} \tag{3.24}$$

The operator $E_r(w^h\,,\,\phi^h)_n$, incorporates the time-dependent non-reflecting boundary operators $\mathbb{S}_m$ as natural boundary conditions, i.e., they are enforced weakly through integration over both the artificial boundary Γ_∞ and the time interval I_n. The formal definition of this boundary operator with details for the implementation of the non-reflecting boundary conditions are given in the next section.

In order to guarantee a stable space-time finite element algorithm, the coupled variational equations (3.16) and (3.17) are constructed in a form which is consistent with the energy (stability) estimates given in Lemma 2.1 and Theorem 2.1 The design criteria then is to construct a coupled variational equation such that the natural energy norm emanating from this variational equation satisfies a stability (energy) identity analogous to that obtained for the continuum problem. A key feature is the use of the time derivative (time rate of change) of $\boldsymbol{\psi}^h$, i.e. $\dot{\boldsymbol{\psi}}^h := \{\dot{\boldsymbol{w}}^h\,,\,\dot{w}^h\}$, as the weighting function in the terms evaluated over Q_n in (3.20) and (3.21). With this choice of weighting function, the form of these terms are consistent with the time rate of change of structural acoustic energy defined in (2.47) – (2.49). In the operator $E_s(\cdot\,,\,\cdot)_n$, the terms evaluated over Q_n^s, act to weakly enforce the momentum balance in the structure while in $E_f(\cdot\,,\,\cdot)_n$, the terms evaluated over Q_n^f, act to weakly enforce the scalar wave equation in the fluid within the interior of the nth space-time slab.

The terms evaluated over the structural domain Ω_s in (3.20) and (3.23), together with the terms evaluated over the fluid domain Ω_f in (3.21) and (3.24) act to weakly enforce continuity across space-time slab interfaces. Figure 3.2 illustrates the weak enforcement of the velocity $\boldsymbol{v}^h = \nabla\phi^h$ and pressure $p^h = -\rho_0\dot{\phi}^h$ for the acoustic fluid through the temporal jump operators associated with (3.21) and (3.24), i.e.

$$\boxed{(\dot{w}^h(t_n^+)\,,\,a^2\underbrace{[\![\dot{\phi}^h(t_n)]\!])_{\Omega_f}}_{\text{pressure jump}} + (\nabla w^h(t_n^+)\,,\,\underbrace{[\![\nabla\phi^h(t_n)]\!])_{\Omega_f}}_{\text{velocity jump}}}$$

Similar temporal jump operators associated with (3.20) and (3.23) defined over Ω_s act to weakly enforce structural velocities and stresses across time steps. The specific form of these jump operators are designed such that continuity is weakly enforced via a kinetic and strain energy inner product for the structure and similarly a kinetic and potential energy inner product for the acoustic fluid. These jump conditions are the mechanism by which information is advanced from one space-time slab to the next. Physically, they add a consistent numerical dissipation into the algorithm which helps control any oscillations that may occur in the vicinity of discontinuities or sharp gradients in the solution.

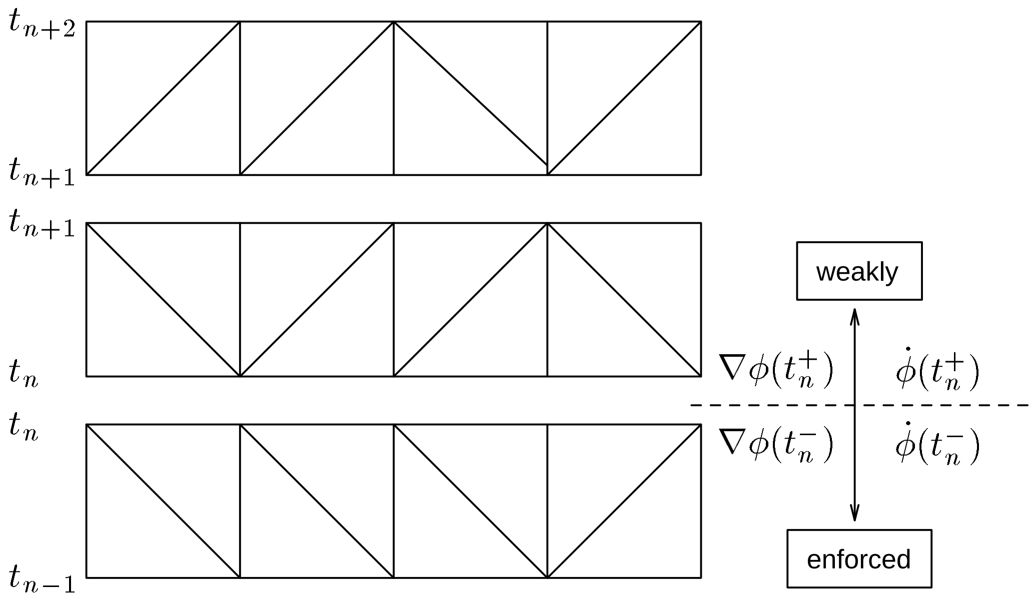

Figure 3.2: Illustration of weak enforcement of velocity $\mathrm{v} = \nabla\phi$ and pressure $p = -\rho_0\dot{\phi}$ for the acoustic fluid across space-time slab interfaces.

Fluid-structure interaction is accomplished through the coupling operators $A(\cdot\,,\,\cdot)_n$ integrated over the fluid-structure interface $(\Upsilon_i)_n = \Gamma_i \times I_n$. These coupling terms appearing in (3.18) and (3.19) weakly enforce the acoustic pressure interface condition (2.5) and continuity of normal velocity condition (2.20), respectively. The fact that the coupling operators in both (3.18) and (3.19) are of the same form; namely (3.22), follows directly from the choice of $\boldsymbol{\mathcal{X}}^h := \{\boldsymbol{u}^h\,,\,\phi^h\}$ for the structure-fluid solution variables and the consistent weighting $\dot{\boldsymbol{\psi}}^h := \{\dot{\boldsymbol{w}}^h\,,\,\dot{w}^h\}$. This global symmetry property of the coupled space-time variational equations facilitates the establishment of stability and convergence proofs for the coupled finite element formulation in a manner similar to that obtained for the continuum problem.

Remarks

1. If pressure is used as the solution variable for the fluid, then the interface boundary condition (2.21) relating the normal pressure gradient to the structural accelerations must be used in place of (2.20). As a result, the coupling terms in the variational equation *will not* be of the same form and would destroy

the global symmetry of the coupled system. As a consequence, it is difficult (if not impossible) to guarantee unconditional stability for unstructured space-time meshes. Recall that a similar difficulty was found for the continuum problem.

2. The method is applied in one space-time slab at a time; data from the end of the previous slab are employed as initial conditions for the current slab. Because the solution is weakly enforced across slab interfaces, the finite element mesh may change from one slab to the next and it is not required that the meshes match across the discrete time levels. This is especially useful for adaptive schemes where the finite element discretization can be refined/unrefined within space-time slabs to track wave fronts as they propagate along space-time characteristics.

3.4.2 Non-Reflecting Boundary Conditions

To allow for a large number of alternative definitions for the non-reflecting boundary conditions, the linear mapping $\mathbb{S}_m\phi$ defined previously in (2.22) is assumed to take the following general abstract form,

$$\boxed{\mathbb{S}_m\phi = \sum_{j=0}^{m} C_j \left[\frac{\partial^j \phi}{\partial t^j}\right] \qquad \text{on} \quad \Upsilon_\infty := \Gamma_\infty \times I_n} \tag{3.25}$$

In this expression, the index m reflects the order of the temporal derivatives appearing in the operator, and $C_j\,,\ j = 0, 1, \ldots m$, are spatial operators that may be local differential operators that couple only adjacent points on the artificial boundary, or nonlocal integral operators that couple all points on the artificial boundary Γ_∞. Specific examples of time-dependent non-reflecting boundary conditions which can be expressed in this general form are discussed in detail in Chapter 5 for problems in $\mathbb{R}^3$, and Chapter 6 for problems in $\mathbb{R}^2$. Here we note that the first-order operator ($m = 1$) defined previously in (2.26) conform to this representation with the spatial operators $C_j\,,\ j = 0, 1$ reducing to $1/R$, and $1/c$.

In general, boundary conditions of the form (3.25) provide increasing accuracy with the order m; however, as the order increases, they become increasingly difficult to implement in a standard semidiscrete finite element setting due to the occurrence

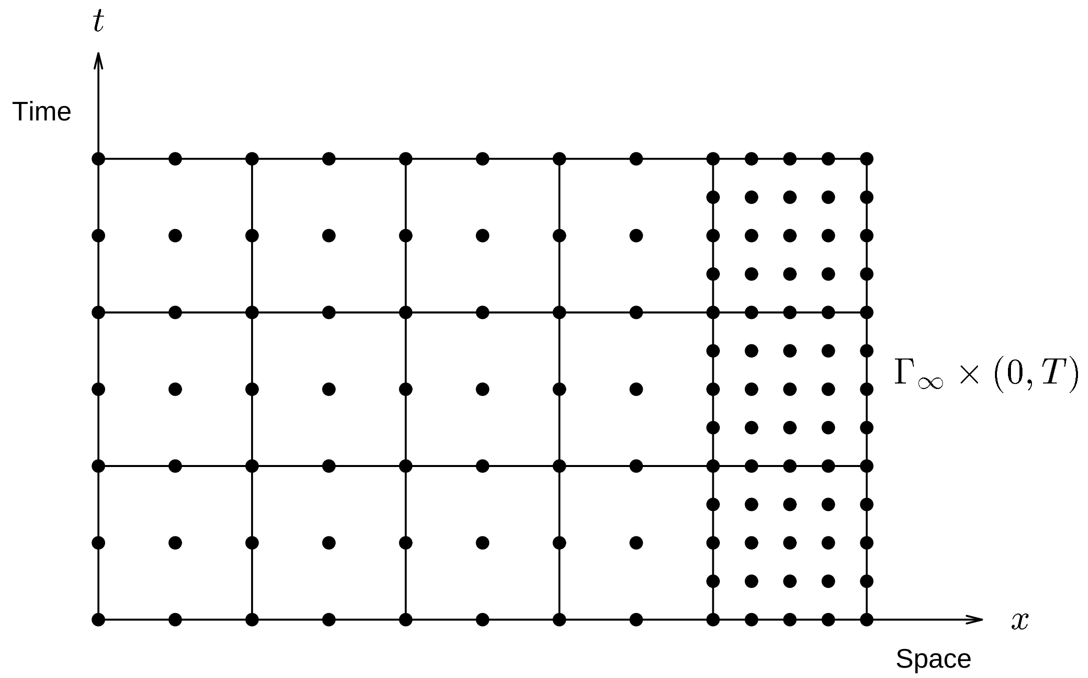

Figure 3.3: Illustration of space-time discretization where the temporal interpolation is increased from biquadratic to biquartic in the region of the non-reflecting boundary $\Gamma_\infty \times]0,T[$.

of high-order time derivatives on the truncation boundary Υ_∞. Semidiscrete methods for second-order hyperbolic wave equations, which discretize the spatial domain with finite elements, lead to a second-order system of ordinary differential equations in time. These ordinary differential equations are then integrated using standard finite difference algorithms such as the Newmark family of time integrators. Since standard semidiscrete algorithms are restricted to integrating up to second-order time derivatives, they are limited to orders $m \leq 2$ only.

Space-time finite element methods, in which the solution is allowed to be discontinuous across space-time slabs places no restriction as to the order m of time derivative appearing in the operator $\mathbb{S}_m$. Since continuity is enforced weakly between time steps, standard C^0 continuous interpolation functions in the time coordinate can be used up to the order dictated by the operator $\mathbb{S}_m$. Figure 3.3 illustrates how the order of the temporal interpolation in the space-time formulation can be increased in the region of the boundary conditions so that temporal accuracy is locally increased to a level required by the boundary condition. It is this special property of the discontinuous Galerkin formulation that provides for the potential to implement (3.25) up to any order desired. It is noted however, that high-order non-reflecting boundary conditions beyond second-order may involve high-order spatial derivatives in C_j, that require increased continuity in the spatial coordinate. In this case special local boundary elements which incorporate high-order continuous spatial basis functions would be needed.

While in principle, it is possible to implement the time dependent operators to any order desired to obtain a greater accuracy, it is difficult to prove *a priori* unconditional stability for orders $m \geq 3$. In the discussion to follow we describe how the time-discontinuous Galerkin space-time method provides a natural variational setting for the incorporation of non-reflecting boundary conditions of the form (3.25), and how under certain conditions on the boundary operators stability and convergence can be proved.

In this work, the class of non-reflecting boundary operators defined in (3.25) are incorporated into the space-time finite element method as 'natural' boundary conditions, i.e., they are enforced weakly in space-time. For boundary operators up to second-order ($m = 2$), the bilinear form $E_r(\cdot\,,\,\cdot)_n$ appearing in the space-time variational equation (3.19), is defined as,

$$
\begin{aligned}
E_r(w^h\,,\,\phi^h)_n \quad &:= \quad (\dot{w}^h\,,\,\mathbb{S}_m\phi^h)_{(\Upsilon_\infty)_n} \\
&+ \quad d_2(\dot{w}^h(t_n^+)\,,\,\underbrace{[\![\dot{\phi}^h(t_n)]\!]}_{\text{jump}})_{\Gamma_\infty} + d_0(w^h(t_n^+)\,,\,\underbrace{[\![\phi^h(t_n)]\!]}_{\text{jump}})_{\Gamma_\infty}
\end{aligned} \tag{3.26}
$$

The term evaluated over $(\Upsilon_\infty)_n := \Gamma_\infty \times I_n$ acts to weakly enforce the non-reflecting boundary condition (3.25) over the time interval $]t_n\,,\,t_{n+1}[$ and Γ_∞. The form of this boundary operator is guided by the definition of the acoustic intensity given in (2.46). Replacing the trial solution with w^h, we have

$$
\begin{aligned}
(\dot{w}^h\,,\,\mathbb{S}_m w^h)_{(\Upsilon_\infty)_n} \quad &= \quad \int_{t_n}^{t_{n+1}} \mathcal{D}(w^h)\;dt \\
&= \quad \int_{t_n}^{t_{n+1}} \int_{\Gamma_\infty} \rho_0 \dot{w}^h \mathbb{S}_m w^h\;d\Gamma\;dt
\end{aligned} \tag{3.27}
$$

Comparing this result to (2.46) we conclude that this term represents an acoustic radiation inner product integrated over the time interval I_n.

As a specific example, consider the first-order, ($m = 1$), non-reflecting boundary condition defined previously in (2.26) and repeated here as,

$$\mathbb{S}_1\phi = C_0\phi + C_1\dot{\phi} \tag{3.28}$$

where the spatial operators reduce to the positive values $C_1 = 1/R$ and $C_2 = 1/c$. For this case, the acoustic radiation operator takes the form,

$$\boxed{(\dot{w}^h\,,\,\mathbb{S}_1\phi^h)_{(\Upsilon_\infty)_n} := \quad d_0(\dot{w}^h\,,\,\phi^h)_{(\Upsilon_\infty)_n} + d_1(\dot{w}^h\,,\,\dot{\phi}^h)_{(\Upsilon_\infty)_n}} \tag{3.29}$$

where the index on the bilinear operators d_1 and d_2 reflects the order of the time derivative appearing on the trial solution. For this simple case, the bilinear operators reduce to,

$$d_0(\dot{w}^h\,,\,\phi^h)_{(\Upsilon_\infty)_n} \quad = \quad \frac{1}{R}\int_{t_n}^{t_{n+1}}\int_{\Gamma_\infty}\rho_0\,\dot{w}^h\,\phi^h\,d\Gamma\,dt \tag{3.30}$$

$$d_1(\dot{w}^h\,,\,\dot{\phi}^h)_{(\Upsilon_\infty)_n} \quad = \quad \frac{1}{c}\int_{t_n}^{t_{n+1}}\int_{\Gamma_\infty}\rho_0\,\dot{w}^h\,\dot{\phi}^h\,d\Gamma\,dt \tag{3.31}$$

Similarly, extending the sequence (3.25) to second-order ($m = 2$),

$$\mathbb{S}_2\phi = C_0\phi + C_1\dot{\phi} + C_2\ddot{\phi} \tag{3.32}$$

the radiation operator reduces to,

$$\boxed{(\dot{w}^h\,,\,\mathbb{S}_2\phi^h)_{(\Upsilon_\infty)_n} := \quad d_0(\dot{w}^h\,,\,\phi^h)_{(\Upsilon_\infty)_n} + d_1(\dot{w}^h\,,\,\dot{\phi}^h)_{(\Upsilon_\infty)_n} + d_2(\dot{w}^h\,,\,\ddot{\phi}^h)_{(\Upsilon_\infty)_n}} \tag{3.33}$$

The form of the bilinear operators d_j depends on the local or non-local character of the spatial operators C_j appearing in (3.25). The index for the operators d_j , $j = 0, 1, 2$, reflects the order of the time derivative on the trial solution appearing in the operator. Specific examples for $\mathbb{S}_2$ will be given in Chapters 5 and 6.

The terms evaluated over the space-time slab interface at the boundary Γ_∞ in (3.26) act to weakly enforce continuity of the trial solution across space-time slab interfaces. The specific form of these operators are designed such that continuity at the artificial boundary Γ_∞ is weakly enforced in a form which is consistent with the radiation boundary term evaluated over $(\Upsilon_\infty)_n$. Thus the form of the consistent temporal jump operators $[\![\phi^h(t_n)]\!]$ and $[\![\dot{\phi}^h(t_n)]\!]$ embedded in the last two terms of (3.26) depend on the form of the spatial derivatives appearing in the bilinear operators $d_0(\cdot\,,\,\cdot)_{\Gamma_\infty}$ and $d_2(\cdot\,,\,\cdot)_{\Gamma_\infty}$. These consistent temporal jump operators are required in order to ensure that the discontinuous Galerkin solution is unconditional stability and are the crucial element that enable generalization of the space-time finite element method to handle exterior domains. Note that no jump operator is needed for the term corresponding to $d_1(\dot{w}^h\,,\,\dot{\phi}^h)_{(\Upsilon_\infty)_n}$. The reason for this becomes clear from the stability analysis described in the next chapter where it is shown that this term naturally leads to a well-defined norm, requiring no additional stabilization.

For the first-order non-reflecting boundary condition defined in (2.26), second-order time derivatives do not appear, and as a result, the term d_2 is not present in the radiation boundary integral. Thus the only consistent jump operator needed is,

$$d_0(w^h(t_n^+)\,,\,[\![\phi^h(t_n)]\!])_{\Gamma_\infty} \quad = \quad \frac{1}{R}\int_{\Gamma_\infty} \rho_0\, w^h(t_n^+)\,,\,[\![\phi^h(t_n)]\!]\; d\Gamma \tag{3.34}$$

Remarks

1. Since the boundary condition $\mathbb{S}_1$ is a local (differential) operator in both space and time, when implemented with standard finite element interpolations with compact support, the boundary integrals couple only degrees-of-freedom in adjacent elements, and the banded sparse data structure of the space-time finite element arrays are preserved. Examples of local non-reflecting boundary conditions of second-order $\mathbb{S}_2$, will be given in Chapters 5 and 6.

2. To facilitate the stability and convergence proofs incorporating non-reflecting boundary conditions, boundary operators are assumed to be spatially non-negative, i.e.,

$$d_j(w^h\,,\,w^h)_{\Gamma_\infty} \geq 0\,, \quad j = 0,1,2 \qquad \forall\, w^h \in \mathcal{W}^h \tag{3.35}$$

Boundary operators which satisfy this positive definite property form an important class of operators. This class of operators also serve as a basic framework for the analysis of other boundary operators, such as those involving unsymmetric terms.

Examining the boundary operators defined in (3.30) and (3.31) for $\mathbb{S}_1$, it is clear that these operators satisfy condition (3.35) explicitly, i.e.

$$d_0(w^h\,,\,w^h)_{\Gamma_\infty} = c_0||w^h||^2_{\Gamma_\infty} \geq 0 \tag{3.36}$$

$$d_1(w^h\,,\,w^h)_{\Gamma_\infty} = c_1||w^h||^2_{\Gamma_\infty} \geq 0 \tag{3.37}$$

where $c_0 = 1/R$ and $c_1 = 1/c$ are positive constants, with notation for the weighted L_2 norm on the boundary,

$$||w^h||^2_{\Gamma_\infty} := \int_{\Gamma_\infty} \rho_0 (w^h)^2 \; d\Gamma \tag{3.38}$$

3.5 Galerkin/Least-Squares Stabilization

In order to enhance the stability of the basic time-discontinuous Galerkin space-time formulation, and to facilitate the proof that the method converges for arbitrary space-time discretizations, local residuals of the governing differential equations in the form of least-squares operators are added to the variational equations. Stabilized methods of this type are referred to as Galerkin/least-squares (GLS) methods. GLS methods were originally developed to improve the stability of numerical solutions for the advection-diffusion equation Hughes, Franca, and Hulbert [1989], and the Euler and Navier-Stokes equations Shakib, Hughes, and Johan [1991]. These ideas have since been extended to second-order hyperbolic equations in the context of elastodynamics in Hughes and Hulbert [1988] and Hulbert and Hughes [1990]. In this section, we extend the use of GLS stabilization to the coupled fluid-structure interaction problem including the incorporation of non-reflecting boundaries. The time-discontinuous Galerkin/least-squares (GLS) formulation for structural acoustics is stated formally as:

Within each space-time slab, $n = 0, 1, ..., N-1$; Find $\boldsymbol{\mathcal{X}}^h := \{\boldsymbol{u}^h\,,\,\phi^h\} \in \mathcal{S}^h_n \times \mathcal{T}^h_n$, such that $\forall\ \boldsymbol{\psi}^h := \{\boldsymbol{w}^h\,,\,w^h\} \in \mathcal{V}_n^h \times \mathcal{W}_n^h$,

$$B^s_{GLS}(\boldsymbol{w}^h\,,\,\boldsymbol{\chi}^h)_n \quad = \quad L^s_{GLS}(\boldsymbol{w}^h)_n \tag{3.39}$$

$$B^f_{GLS}(w^h\,,\,\boldsymbol{\chi}^h)_n \quad = \quad L^f_{GLS}(w^h)_n \tag{3.40}$$

where

$$B^s_{GLS}(\boldsymbol{w}^h\,,\,\boldsymbol{\chi}^h)_n \quad = \quad B_s(\boldsymbol{w}^h\,,\,\boldsymbol{\chi}^h)_n \,+\, B^s_{LS}(\boldsymbol{w}^h\,,\,\boldsymbol{\chi}^h)_n \tag{3.41}$$

$$L^s_{GLS}(\boldsymbol{w}^h)_n \quad = \quad L_s(\boldsymbol{w}^h)_n \,+\, L^s_{LS}(\boldsymbol{w}^h)_n \tag{3.42}$$

similarly,

$$B^f_{GLS}(w^h\,,\,\boldsymbol{\chi}^h)_n \quad = \quad B_f(w^h\,,\,\boldsymbol{\chi}^h)_n \,+\, B^f_{LS}(w^h\,,\,\boldsymbol{\chi}^h)_n \tag{3.43}$$

$$L^f_{GLS}(w^h)_n \quad = \quad L_f(w^h)_n \,+\, L^f_{LS}(w^h)_n \tag{3.44}$$

The least-squares addition to the Galerkin variational equations are defined as:

$$\begin{aligned}
B^s_{LS}(\boldsymbol{w}^h\,,\,\boldsymbol{\chi}^h)_n \quad := \quad & (\mathcal{L}_s\boldsymbol{w}^h\,,\,\rho_s^{-1}\boldsymbol{\tau}\mathcal{L}_s\boldsymbol{u}^h)_{\tilde{Q}^s_n} \\
&+\ ([\![\boldsymbol{\sigma}(\nabla\boldsymbol{w}^h)(\boldsymbol{x})]\!]\cdot\boldsymbol{n}\,,\,\rho_s^{-1}\boldsymbol{s}[\![\boldsymbol{\sigma}(\nabla\boldsymbol{u}^h)(\boldsymbol{x})]\!]\cdot\boldsymbol{n})_{\tilde{\Upsilon}^s_n} \\
&+\ (\boldsymbol{\sigma}(\nabla\boldsymbol{w}^h)\cdot\boldsymbol{n}\,,\,\rho_s^{-1}\boldsymbol{s}\boldsymbol{\sigma}(\nabla\boldsymbol{u}^h)\cdot\boldsymbol{n})_{(\Upsilon_\sigma)_n} \\
&+\ (\mathcal{L}_1\boldsymbol{\psi}^h\,,\,\rho_s^{-1}\boldsymbol{s}\mathcal{L}_1\boldsymbol{\chi}^h)_{(\Upsilon_i)_n}
\end{aligned} \tag{3.45}$$

$$L^s_{LS}(\boldsymbol{w}^h)_n \quad := \quad (\boldsymbol{\sigma}(\nabla\boldsymbol{w}^h)\cdot\boldsymbol{n}\,,\,\rho_s^{-1}\boldsymbol{s}\,\bar{\boldsymbol{t}})_{(\Upsilon_\sigma)_n} \tag{3.46}$$

and

$$\begin{aligned}
B^f_{LS}(w^h\,,\,\boldsymbol{\chi}^h)_n \quad := \quad & (\mathcal{L}_f w^h\,,\,c^2\tau\mathcal{L}_f\phi^h)_{\tilde{Q}^f_n} \\
&+\ (\mathcal{L}_r w^h\,,\,c^2 s\mathcal{L}_r\phi^h)_{(\tilde{\Upsilon}_\infty)_n} \\
&+\ ([\![w^h_{,n}(\boldsymbol{x})]\!]\,,\,c^2 s[\![\phi^h_{,n}(\boldsymbol{x})]\!])_{\tilde{\Upsilon}^f_n}
\end{aligned}$$

$$+ \quad (\mathcal{L}_2 \boldsymbol{\psi}^h \,,\, c^2 s \mathcal{L}_2 \boldsymbol{\chi}^h)_{(\Upsilon_i)_n} \tag{3.47}$$

$$L^f_{LS}(w^h)_n \quad := \quad (\mathcal{L}_f w^h \,,\, c^2 \tau f)_{\tilde{Q}^f_n} \tag{3.48}$$

In the above expressions we define:

$$\mathcal{L}_s \boldsymbol{u}^h \quad := \quad \rho_s \ddot{\boldsymbol{u}}^h - \nabla \cdot \boldsymbol{\sigma}(\nabla \boldsymbol{u}^h) \tag{3.49}$$

$$\mathcal{L}_f \phi^h \quad := \quad a^2 \ddot{\phi}^h - \nabla^2 \phi^h \tag{3.50}$$

$$\mathcal{L}_r \phi^h \quad := \quad \phi^h_{,n} + \mathbb{S}_m \phi^h \tag{3.51}$$

$$\mathcal{L}_1 \boldsymbol{\chi}^h \quad := \quad \boldsymbol{\sigma}(\nabla \boldsymbol{u}^h) \cdot \boldsymbol{n} - \rho_0 \dot{\phi}^h \boldsymbol{n} \tag{3.52}$$

$$\mathcal{L}_2 \boldsymbol{\chi}^h \quad := \quad \dot{\boldsymbol{u}}^h \cdot \boldsymbol{n} - \phi^h_{,n} \tag{3.53}$$

and the normal derivative is denoted $\phi^h_{,n} = \nabla \phi^h \cdot \boldsymbol{n}$. The scalar parameters τ and s, are local weighting parameters for the fluid equations designed to improve stability without degrading the accuracy of the underlying time-discontinuous Galerkin method. The GLS parameter τ has dimensions of time and can be interpreted as an intrinsic time-scale, while the parameter s has dimensions of inverse speed and is referred to as a slowness scale. Similarly for the structure, $\boldsymbol{\tau}$ and $\boldsymbol{s}$ are intrinsic time scale and slowness matrices respectively; both are of size $d \times d$, Hughes and Hulbert [1988].

From a Fourier analysis of the time-discontinuous method Shakib and Hughes [1991a], it was shown that the Galerkin/least-squares formulation achieves high-order accuracy and eliminates undesirable high frequency response without introducing excessive algorithmic damping in the low frequency regime. The GLS weighting parameters are mesh dependent functions that may vary from element-to-element, and when set to zero, the formulation specializes to the discontinuous Galerkin method. Both slowness and time scale parameters are needed in the convergence proof. However, from an algorithmic point of view, the implementation of the terms involving the slowness parameters involve unconventional and possibly expensive calculations. Numerical experience in Hulbert [1989] and Chapter 4 of this thesis indicate that optimal convergence rates are achieved even with the omission of the slowness parameters, and therefore in practice, these parameters are set to zero, i.e. $s = 0$ and $\boldsymbol{s} = \mathbf{0}$.

Remarks

1. Galerkin/least-squares methods have also been used to enhance the stability and accuracy of solutions to the related reduced wave equation (Helmholtz equation) governing time-harmonic acoustics in the frequency domain, see Harari and Hughes [1991b,1992c], Thompson and Pinsky [1993c,1993d]; details are given in Chapter 8.

2. For numerical solutions exhibiting sharp gradients or discontinuities due to shocks, nonlinear discontinuity capturing operators are available to help further control oscillations that may occur in the solution, Hulbert [1992]. However, for the majority of linear structural acoustics problems, numerical experience has indicated that the added expense resulting from a nonlinear solve as required from the use of these discontinuity capturing operators is not justified.

3.6 Euler-Lagrange equations

Weak enforcement of the governing Euler-Lagrange equations for the structure is exposed by integrating (3.39) by parts to yield the following weighted residual expression,

$$\begin{aligned}
0 \quad &= \quad B^s_{GLS}(\boldsymbol{w}^h\,,\,\boldsymbol{\chi}^h)_n \;-\; L^s_{GLS}(\boldsymbol{w}^h)_n \\
&= \quad (\dot{\boldsymbol{w}}^h + \rho_s^{-1}\boldsymbol{\tau}\mathcal{L}_s\boldsymbol{w}^h\,,\,\boldsymbol{r}^h_s)_{\tilde{Q}^s_n} \\
&\quad + \quad (\dot{\boldsymbol{w}}^h + \rho_s^{-1}\boldsymbol{s}\boldsymbol{\sigma}(\nabla\boldsymbol{w}^h)\cdot\boldsymbol{n}\,,\,\boldsymbol{\sigma}(\nabla\boldsymbol{u}^h)\cdot\boldsymbol{n} - \bar{\boldsymbol{t}})_{(\Upsilon_\sigma)_n} \\
&\quad + \quad (\dot{\boldsymbol{w}}^h + \rho_s^{-1}\boldsymbol{s}[\![\boldsymbol{\sigma}(\nabla\boldsymbol{w}^h)(\boldsymbol{x})]\!]\cdot\boldsymbol{n}\,,\,[\![\boldsymbol{\sigma}(\nabla\boldsymbol{u}^h)(\boldsymbol{x})]\!]\cdot\boldsymbol{n})_{(\tilde{\Upsilon}^s)_n} \\
&\quad + \quad (\dot{\boldsymbol{w}}^h + \rho_s^{-1}\boldsymbol{s}\mathcal{L}_1\boldsymbol{\psi}\,,\,\boldsymbol{r}^h_1)_{(\Upsilon_i)_n} \\
&\quad + \quad (\dot{\boldsymbol{w}}^h(t_n^+)\,,\,[\![\dot{\boldsymbol{u}}^h(t_n)]\!])_{\Omega_s}
\end{aligned}$$

$$+ \quad a(\boldsymbol{w}^h(t_n^+)\,,\,[\![\boldsymbol{u}^h(t_n)]\!])_{\Omega_s} \tag{3.54}$$

where

$$\begin{aligned} \boldsymbol{r}_s^h &= \boldsymbol{\mathcal{L}}_s \boldsymbol{u}^h \quad \text{(equation of motion)} \\ \boldsymbol{r}_1^h &= \boldsymbol{\mathcal{L}}_1 \boldsymbol{\mathcal{X}}^h \quad \text{(coupling boundary condition)} \end{aligned} \tag{3.55}$$

The second line in (3.54) describes the weak enforcement of the momentum balance residual $\boldsymbol{r}_s^h$, for the structure within a space-time slab; the third line acts to weakly enforce the prescribed traction at the boundary Γ_σ; while the terms in line four define the weak enforcement of the traction continuity across element boundaries. This term arises from integration-by-parts over the spatial domain. Line five describes the weak enforcement of the traction coupling boundary condition $\boldsymbol{r}_1^h$, at the interface between the structure and the fluid. The last two lines in (3.54) show how continuity between space-time slab interfaces is weakly enforced via a total structural energy inner product.

Similarly for the fluid, integrating (3.40) by parts yields,

$$\begin{aligned} 0 &= B^f_{GLS}(w^h\,,\,\boldsymbol{\mathcal{X}}^h)_n - L^f_{GLS}(w^h)_n \\ &= (\dot{w}^h + \tau c^2 \boldsymbol{\mathcal{L}}_f w^h\,,\,r_f^h)_{\tilde{Q}_n^f} \\ &+ (\dot{w}^h + s c^2 \boldsymbol{\mathcal{L}}_r w^h\,,\,r_\infty^h)_{(\tilde{\Upsilon}_\infty)_n} \\ &+ (\dot{w}^h + s c^2 [\![w^h_{,n}(\boldsymbol{x})]\!]\,,\,[\![\phi^h_{,n}(\boldsymbol{x})]\!])_{(\tilde{\Upsilon}^f)_n} \\ &+ (\dot{w}^h + s c^2 \boldsymbol{\mathcal{L}}_2 \boldsymbol{\psi}\,,\,r_2^h)_{(\Upsilon_i)_n} \\ &+ (\dot{w}^h(t_n^+)\,,\,a^2\,[\![\dot{\phi}^h(t_n)]\!])_{\Omega_f} \\ &+ (\nabla w^h(t_n^+)\,,\,[\![\nabla \phi^h(t_n)]\!])_{\Omega_f} \\ &+ d_2(\dot{w}^h(t_n^+)\,,\,[\![\dot{\phi}^h(t_n)]\!])_{\Gamma_\infty} \\ &+ d_0(w^h(t_n^+)\,,\,[\![\phi^h(t_n)]\!])_{\Gamma_\infty} \end{aligned} \tag{3.56}$$

where

$$\begin{aligned} r_f^h &= \mathcal{L}_f \phi^h - f && \text{(wave equation)} \\ r_\infty^h &= \mathcal{L}_r \phi^h && \text{(radiation boundary condition)} \\ r_2^h &= \mathcal{L}_2 \boldsymbol{\chi}^h && \text{(coupling boundary condition)} \end{aligned} \tag{3.57}$$

The second line in (3.56) describes the weak enforcement of the wave equation r_f^h, over the space-time slab; the third line acts to weakly enforce the non-reflecting boundary conditions r_∞^h, at the artificial boundary; while the terms in line four define the weak enforcement of the gradient continuity in space. This term arises from integration-by-parts over the space-time domain. The notation $[\![\phi_{,n}^h(\boldsymbol{x})]\!] = \phi_{,n}^h(\boldsymbol{x}^+ \,,\, t) - \phi_{,n}^h(\boldsymbol{x}^- \,,\, t)$ is defined as the spatial jump in the gradient across element boundaries. Line five describes the weak enforcement of the kinematic coupling boundary condition r_2^h at the interface between the fluid and the structure.

The last four lines in (3.56) show how continuity of the solution is weakly enforced across space-time slabs through the temporal jump operators. Within the domain Ω_f, continuity is weakly enforced via a total acoustic energy inner product. At the artificial boundary Γ_∞, continuity is weakly enforced via the radiation boundary operators $d_2(\cdot\,,\,\cdot)_{\Gamma_\infty}$ and $d_0(\cdot\,,\,\cdot)_{\Gamma_\infty}$. These additional operators are needed in order to ensure stability and are the crucial element that enable generalization of the time-discontinuous space-time finite element method to handle non-reflecting boundary conditions. In Chapter 6, an example is given which demonstrates how the solution may become unstable if these jump terms are not included on Γ_∞.

3.7 Consistency

From (3.54) and (3.56), it follows that a sufficiently smooth exact solution $\boldsymbol{\chi} := (\boldsymbol{u}\,,\,\phi)$, to the initial/boundary-value problem (2.27)–(2.33), satisfies the coupled GLS variational equations:

$$B_{GLS}^s(\boldsymbol{w}^h\,,\,\boldsymbol{\chi})_n = L_{GLS}^s(\boldsymbol{w}^h)_n \tag{3.58}$$

$$B_{GLS}^f(w^h\,,\,\boldsymbol{\chi})_n = L_{GLS}^f(w^h)_n \tag{3.59}$$

$\forall\,\boldsymbol{\psi} := \{\boldsymbol{w}^h\,,\, w^h\} \in \mathcal{V}_n^h \times \mathcal{W}_n^h$ and $n = 0, 1, ..., N-1$. Thus the error in the finite element solution is orthogonal with respect to the operators,

$$B^s_{GLS}(\boldsymbol{w}^h\,,\, \boldsymbol{E})_n = 0 \tag{3.60}$$

$$B^f_{GLS}(w^h\,,\, \boldsymbol{E})_n = 0 \tag{3.61}$$

where $\boldsymbol{E} = \boldsymbol{\chi}^h - \boldsymbol{\chi}$ is the error; in components $\boldsymbol{E} = \{\boldsymbol{u}^h - \boldsymbol{u}\,,\, \phi^h - \phi\}$. This consistency condition is necessary for maintaining optimal convergence rates for higher-order finite element space-time interpolations. Clearly the time-discontinuous Galerkin formulation with $(\boldsymbol{\tau} = 0, \boldsymbol{s} = 0)$ and/or $(\tau = 0\,, s = 0)$ also satisfies a consistency condition.

3.8 Space-Time Matrix Equations

The space-time matrix equations are obtained by introducing space-time approximations for the structural displacement $\boldsymbol{u}^h$, and acoustic velocity potential ϕ^h,

$$\begin{aligned} \boldsymbol{u}^h(\boldsymbol{x}, t) &= \boldsymbol{N}^e_s(\boldsymbol{x}, t)\, \boldsymbol{d}^e \quad \in \quad \boldsymbol{C}^0(\Omega_s \times I_n) \\ \phi^h(\boldsymbol{x}, t) &= \boldsymbol{N}^e_f(\boldsymbol{x}, t)\, \boldsymbol{\phi}^e \quad \in \quad C^0(\Omega_f \times I_n) \end{aligned}$$

where $\boldsymbol{N}^e_s(\boldsymbol{x}, t) \in Q^s_n$ and $\boldsymbol{N}^e_f(\boldsymbol{x}, t) \in Q^f_n$ are the e^{th} element shape functions for the structure and fluid respectively, and $\boldsymbol{d}^e$ and $\boldsymbol{\phi}^e$ are the element structure displacement and fluid velocity potential solution vectors. Recall that these piecewise element shape functions are C^0 continuous within the space-time slab, but are allowed to be discontinuous across time slabs. Introduction of these approximations into the space-time variational equations (3.39) and (3.40), leads directly to the following coupled system of algebraic equations to be solved in sequence for each time interval $I_n =]t_n\,,\, t_{n+1}[,\;\; n = 0\,,\,1\,,\,\cdots N-1$:

$$\begin{bmatrix} \boldsymbol{K}_s & -\boldsymbol{A} \\ \boldsymbol{A}^T & \boldsymbol{K}_f + \boldsymbol{K}_r \end{bmatrix} \begin{Bmatrix} \boldsymbol{d} \\ \boldsymbol{\phi} \end{Bmatrix} = \begin{Bmatrix} \boldsymbol{f}_s \\ \boldsymbol{f}_f \end{Bmatrix} \tag{3.62}$$

where $\boldsymbol{d}$ and $\boldsymbol{\phi}$ are the global solution vectors for time interval I_n. In the above system, $\boldsymbol{K}_s$ and $\boldsymbol{K}_f$ are the positive matrices emanating from the structural operator

E_s and the fluid operator E_f defined in (3.20) and (3.21) respectively; together with additional least-squares terms. The positive matrix $\boldsymbol{K}_r$ emanates from the positive non-reflecting boundary operators E_r defined in (3.26). The fluid-structure coupling matrix $\boldsymbol{A}$ is given by,

$$\boxed{\boldsymbol{A} \quad = \quad \mathop{\mathbf{A}}_{e=1}^{n_{el}} \int_{t_n}^{t_{n+1}} \int_{\Gamma_i^e} \rho_f \boldsymbol{N}_{s,t}^{eT} \boldsymbol{n} \boldsymbol{N}_{f,t}^e \; d\Gamma^e \; dt} \tag{3.63}$$

where n_{el} is the number of elements in the nth space-time slab, $\mathop{\mathbf{A}}_{e=1}^{n_{el}}$ denotes the assembly operator and the comma with subscript t on the finite element interpolations indicates the time derivative. Note that different space-time interpolations for the fluid domain Q_n^f and the structural domain Q_n^s can be accommodated, allowing possible combinations such as cubic interpolation for the fluid, and quadratic interpolation in the structure.

As a consequence of the choice of $\boldsymbol{\chi}^h := \{\boldsymbol{u}^h \, , \, \phi^h\}$ variables, the matrix equations emanating from the coupled space-time formulation for the structure-fluid interaction problem take on a positive form. This property follows directly from the global symmetry of the coupled variational equations and is intimately related to the stability of the algorithm. The prove of unconditional stability for the coupled system will be given in the next chapter. The algorithm is termed unconditionally stable if, in the absence of forcing terms but for arbitrary initial conditions, then the computed total energy for the system plus the radiation energy absorbed through the artificial boundary is always less than or equal to the total energy at the previous time step for arbitrary step-sizes.

In general, space-time methods give rise to a larger system of equations than those produced by typical semidiscrete methods. In this work, solutions to the numerical examples given in Chapters 5 and 6 were obtained using a direct Crout elimination solver with profile storage and dynamic memory allocation, see Hughes [1987] Chap.11. Profile reduction based on a modified version of the reverse Cuthill-Mckee algorithm was used to minimize storage, (see Algorithm 582 in ACM-Trans. Math. Software, Vol. 8, No. 2.) For larger problems, iterative strategies such as the Generalized Minimum Residual (GMRES) algorithms used by Shakib et al. [1989], and Johan et al. [1991], for matrices arising in computational fluid dynamics may be needed.

In order to decrease the computational cost associated with the use of the space-time method, the coupled system of equations may be cast in predictor-corrector form, where multiple corrector passes would be used to solve a reduced number of equations, Shakib,Hughes, Johan [1991b]. This strategy reduces the system of equations to a sequence of smaller systems within each space-time slab, where iterative strategies may be used for their solution. Hulbert [1989] successfully developed a strategy for generating predictor-multicorrector algorithms for the time-discontinuous Galerkin method for second-order hyperbolic equations; however there is some difficulty extending this idea to the space-time Galerkin/least-squares method in multi-dimensions.

A further strategy for the coupled structural acoustics problem is the use of fractional-step (staggered) solution algorithms. In this approach, a modular computer implementation would be used with separate fluid and structural analyzers interfaced through the coupling terms. The integration process would then be carried out in alternating stages: The solution of either the fluid or the structural system would be advanced first, then the other system would be solved following a time extrapolation of the coupling terms as forcing functions. Previous researchers have used staggered schemes for structural acoustics in the context of Galerkin semidiscrete finite element methods using acoustic pressure and structural displacement variables, see Park and Felippa [1989]. However, do to the somewhat 'ad hoc' coupling used in these formulations, standard staggered methods are only conditionally stable, and additional stabilizing terms are typically required in an attempt to 'patch-up' the deficiencies in these methods. It is anticipated that as a result of the firm mathematical framework inherent in the time-discontinuous Galerkin finite element method presented in this work, a staggered (fractional-step) space-time method can be obtained which inherits the good stability of the underlying method. Another approach that may prove useful for the solution of the structural acoustics problem is the class of fractional-step procedures developed in Armero [1993]. In any approach to coupling the acoustic fluid and shell structure it is essential that the consistency and stability of the method be maintained.

3.9 Conclusions

In this chapter, a new space-time finite element formulation for transient fluid-structure interaction based on the time-discontinuous Galerkin method for second-order hyperbolic systems, Hughes and Hulbert [1988], has been presented. The method is developed from a space-time variational equation for the coupled problem of structural acoustics in $\boldsymbol{\chi} = \{\boldsymbol{u}\,,\,\phi\}$ variables including the incorporation of a class on high-order non-reflecting boundary conditions. As a consequence of this choice of variables, the coupled variational equations inherit the stability (energy) properties of the continuum problem, which in the context of the coupled space-time finite element equations, leads to a positive matrix form. In the next Chapter, these properties are exploited in a stability analysis where we prove that the proposed space-time method for structural acoustics is unconditionally stable for general unstructured space-time meshes.

Chapter 4

Stability and Convergence Analysis for Fluid-Structure Interaction

For the interior problem, where energy is not allowed to flow through domain boundaries, the rate of change of the total energy in the system is constant. In this case the system is referred to as a 'conservative' system and a natural measure of stability is the total energy in the structure and the fluid, see (2.39). In contrast, for the exterior problem a natural measure of stability in the primary variables $\boldsymbol{\mathcal{X}}$, is the total structural acoustic energy in the finite domain Ω plus the radiation energy absorbed through the artificial boundary Γ_∞. It is the radiation energy loss through Γ_∞ that renders the exterior problem 'nonconservative'. The purpose of this Chapter is to prove through a rigorous analysis that the proposed space-time variational formulation inherits a stability estimate of the form given by Theorem 2.1 for the continuum problem. It is this estimate that leads to the conclusion that the proposed space-time method for the coupled structural acoustics problem with non-reflecting boundary conditions is unconditionally stable and converges at an optimal rate. The method is termed unconditionally stable if in the absence of external forces, and for arbitrary initial conditions within Ω, the total energy together with the radiation energy absorbed through the artificial boundary is always less than or equal to the initial energy in the system.

4.1 Overview

Stability and error estimates for the interior problem, in the context of elastodynamics are given in Hughes and Hulbert [1988]. In this work, the stability and convergence analysis of the time-discontinuous Galerkin/least-squares method for second-order hyperbolic equations is extended to the coupled fluid-structure interaction problem. For the exterior problem, the issue of stability for the non-reflecting boundary conditions must be addressed. In this chapter we prove that the discontinuous Galerkin method, including the non-reflecting boundary conditions, is stable and converges at the optimal rate obtained for the interior problem. In Section 4.3, we prove a series of Lemmas which state the coercivity (positive-definiteness) conditions for the acoustic, radiation, and structural components of the coupled variational equations. Using these results, we then establish an energy decay inequality (stability condition) for the coupled space-time algorithm which is the discrete counterpart to the energy estimate obtained for the continuum problem. In Section 4.4, error estimates are obtained for the uncoupled acoustics problem with non-reflecting boundary conditions. A simple one-dimensional numerical example is performed to verify these energy and error estimates. In order to evaluate the purely temporal behavior of the time-discontinuous Galerkin method, a Fourier transformed second-order ordinary differential equation in time is analyized for stability and convergence. In Section 4.5 we return to the coupled problem, where error estimates are obtained for the coupled fluid-structure system. This chapter concludes in Section 4.6 with an extension to a mixed two-field formulation incorporating independent finite element interpolations for both pressure and velocity potential variables.

4.2 Preliminaries

Before proceeding, it is convenient to sum (3.40) over the time slabs and after rearranging terms we have for the fluid,

$$\boxed{B^f_{GLS}(w^h\,,\,\boldsymbol{\chi}^h) \quad = \quad L^f_{GLS}(w^h)} \tag{4.1}$$

with,

$$B^f_{GLS}(w^h\,,\,\boldsymbol{\chi}^h) \;:=\; E_f(w^h\,,\,\phi^h) + A(\boldsymbol{u}^h\,,\,w^h\boldsymbol{n}) + E_r(w^h\,,\,\phi^h) + \sum_{n=0}^{N-1} B^f_{LS}(w^h\,,\,\boldsymbol{\chi}^h)_n \tag{4.2}$$

and where

$$E_f(w^h\,,\,\phi^h) = E_2(w^h\,,\,\phi^h) + E_0(w^h\,,\,\phi^h) \tag{4.3}$$

$$E_r(w^h\,,\,\phi^h) = D_2(w^h\,,\,\phi^h) + D_1(w^h\,,\,\phi^h) + D_0(w^h\,,\,\phi^h) \tag{4.4}$$

and

$$E_2(w^h\,,\,\phi^h) = \sum_{n=0}^{N-1}(\dot{w}^h\,,\,a^2\ddot{\phi}^h)_{Q^f_n} + \sum_{n=1}^{N-1}(\dot{w}^h(t_n^+)\,,\,a^2\,[\![\dot{\phi}^h(t_n)]\!])_{\Omega_f} + (\dot{w}^h(0^+)\,,\,a^2\,\dot{\phi}^h(0^+))_{\Omega_f} \tag{4.5}$$

$$E_0(w^h\,,\,\phi^h) = \sum_{n=0}^{N-1}(\nabla\dot{w}^h\,,\,\nabla\phi^h)_{Q^f_n} + \sum_{n=1}^{N-1}(\nabla w^h(t_n^+)\,,\,[\![\nabla\phi^h(t_n)]\!])_{\Omega_f} + (\nabla w^h(0^+)\,,\,\nabla\phi^h(0^+))_{\Omega_f} \tag{4.6}$$

$$D_2(w^h\,,\,\phi^h) = \sum_{n=0}^{N-1} d_2(\dot{w}^h\,,\,\ddot{\phi}^h)_{(\Upsilon_\infty)_n} + \sum_{n=1}^{N-1} d_2(\dot{w}^h(t_n^+)\,,\,[\![\dot{\phi}^h(t_n)]\!])_{\Gamma_\infty} + d_2(\dot{w}^h(0^+)\,,\,\dot{\phi}^h(0^+))_{\Gamma_\infty} \tag{4.7}$$

$$D_0(w^h\,,\,\phi^h) = \sum_{n=0}^{N-1} d_0(\dot{w}^h\,,\,\phi^h)_{(\Upsilon_\infty)_n} + \sum_{n=1}^{N-1} d_0(w^h(t_n^+)\,,\,[\![\phi^h(t_n)]\!])_{\Gamma_\infty} + d_0(w^h(0^+)\,,\,\phi^h(0^+))_{\Gamma_\infty} \tag{4.8}$$

$$D_1(w^h\,,\,\phi^h) = \sum_{n=0}^{N-1} d_1(\dot{w}^h\,,\,\dot{\phi}^h)_{(\Upsilon_\infty)_n} \tag{4.9}$$

$$A(\boldsymbol{u}^h\,,\,w^h) \;=\; \sum_{n=0}^{N-1}(\dot{\boldsymbol{u}}^h\,,\,\rho_0\,\dot{w}^h\boldsymbol{n})_{(\Upsilon_i)_n} \tag{4.10}$$

with

$$\begin{aligned} L^f_{GLS}(w^h) \;&=\; \sum_{n=0}^{N-1}\Big\{(\dot{w}^h\,,\,f)_{Q^f_n} + L^f_{LS}(w^h)_n\Big\} \\ &+\; (\dot{w}^h(0^+)\,,\,a^2\,\dot{\phi}_0)_{\Omega_f} + (\nabla w^h(0^+)\,,\,\nabla\phi_0)_{\Omega_f} \end{aligned} \tag{4.11}$$

Similarly for the structure, summing (3.39) over the time slabs, we obtain:

$$\boxed{B^s_{GLS}(\boldsymbol{w}^h\,,\,\boldsymbol{\chi}^h) \;=\; L^s_{GLS}(\boldsymbol{w}^h)} \tag{4.12}$$

where

$$B^s_{GLS}(\boldsymbol{w}^h\,,\,\boldsymbol{\chi}^h) \;=\; E_s(\boldsymbol{w}^h\,,\,\boldsymbol{u}^h) - A(\boldsymbol{w}^h\,,\,\phi^h\boldsymbol{n}) + \sum_{n=0}^{N-1}B^s_{LS}(\boldsymbol{w}^h\,,\,\boldsymbol{\chi}^h)_n \tag{4.13}$$

and

$$\begin{aligned} E_s(\boldsymbol{w}^h\,,\,\boldsymbol{u}^h) \;&=\; \sum_{n=0}^{N-1}(\dot{\boldsymbol{w}}^h\,,\,\rho_s\ddot{\boldsymbol{u}}^h)_{Q^s_n} \\ &+\; \sum_{n=1}^{N-1}(\dot{\boldsymbol{w}}^h(t_n^+)\,,\,\rho_s[\![\dot{\boldsymbol{u}}^h(t_n)]\!])_{\Omega_s} + (\dot{\boldsymbol{w}}^h(0^+)\,,\,\rho_s\dot{\boldsymbol{u}}^h(0^+))_{\Omega_s} \\ &+\; \sum_{n=0}^{N-1}a(\dot{\boldsymbol{w}}^h\,,\,\boldsymbol{u}^h)_{Q^s_n} \\ &+\; \sum_{n=1}^{N-1}a(\boldsymbol{w}^h(t_n^+)\,,\,[\![\boldsymbol{u}^h(t_n)]\!])_{\Omega_s} + a(\boldsymbol{w}^h(0^+)\,,\,\boldsymbol{u}^h(0^+))_{\Omega_s} \end{aligned} \tag{4.14}$$

$$\begin{aligned} L^s_{GLS}(\boldsymbol{w}^h) \;&=\; \sum_{n=0}^{N-1}\Big\{(\dot{\boldsymbol{w}}^h\,,\,\bar{\boldsymbol{t}})_{(\Upsilon_\sigma)_n} + L^s_{LS}(\boldsymbol{w}^h)_n\Big\} \\ &+\; (\dot{\boldsymbol{w}}^h(0^+)\,,\,\rho_s\dot{\boldsymbol{u}}_0)_{\Omega_s} + a(\boldsymbol{w}^h(0^+)\,,\,\boldsymbol{u}_0)_{\Omega_s} \end{aligned} \tag{4.15}$$

From (3.60) and (3.61) it follows that for a sufficiently smooth exact solution $\boldsymbol{\mathcal{X}}$, the appropriate consistency conditions for (4.1) and (4.12) are respectively,

$$B^f_{GLS}(w^h\,,\,\boldsymbol{\mathcal{X}}^h - \boldsymbol{\mathcal{X}}) \quad = \quad 0 \tag{4.16}$$

$$B^s_{GLS}(\boldsymbol{w}^h\,,\,\boldsymbol{\mathcal{X}}^h - \boldsymbol{\mathcal{X}}) \quad = \quad 0 \tag{4.17}$$

4.3 Stability

In this section we prove the unconditional stability for both the time-discontinuous Galerkin and GLS methods for the coupled structural acoustics problem incorporating non-reflecting boundary conditions. An algorithm is termed unconditional stable if in the absence of forcing terms but for arbitrary initial conditions, the computed total structural acoustic energy plus the radiation energy absorbed through the artificial boundary is always bounded from above by the initial energy in the system. In the subsequent analysis, the notation $(\cdot\,,\,\cdot)_{\Omega_s}$ denotes the $L_2(\Omega_s)$ inner product defined over the structural domain with natural norm $||\cdot||_{\Omega_s}$. For the fluid, $(\cdot\,,\,\cdot)_{\Omega_f}$ denotes the weighted $L_2(\Omega_f)$ inner product with weighting equal to the reference density ρ_0. An important inequality that will be used often is,

$$|(u,v)| \leq \frac{1}{2}\,(\frac{1}{\epsilon}||u||^2 + \epsilon||v||^2) \qquad \forall\,\epsilon > 0 \tag{4.18}$$

Lemma 4.1 (Total Acoustic Energy)

$$\boxed{E_f(w^h\,,\,w^h) \quad = \quad |||w^h|||_f^2} \tag{4.19}$$

where

$$|||w^h|||_f^2 := \quad \mathcal{E}_f(w^h(0^+)) \,+\, \sum_{n=1}^{N-1} \mathcal{E}_f([\![w^h(t_n)]\!]) \,+\, \mathcal{E}_f(w^h(T^-)) \tag{4.20}$$

and for linear acoustics, the total energy within the domain Ω_f is defined as in (2.41):

$$\mathcal{E}_f(w) \quad = \quad \frac{1}{2}\,||a\dot{w}||^2_{\Omega_f} \,+\, \frac{1}{2}\,||\nabla w||^2_{\Omega_f} \tag{4.21}$$

This is the coercivity condition for the fluid.

Proof:

$$
\begin{aligned}
\sum_{n=0}^{N-1} (\dot{w}^h\,,\,\ddot{w}^h)_{Q_n^f} &= \sum_{n=0}^{N-1} \int_{t_n}^{t_{n+1}} \frac{1}{2}\frac{d}{dt} ||a\dot{w}^h||^2_{\Omega_f}\, dt \\
&= \frac{1}{2}\,||a\dot{w}^h(T^-)||^2_{\Omega_f} - \frac{1}{2}\,||a\dot{w}^h(0^+)||^2_{\Omega_f} \\
&+ \frac{1}{2}\sum_{n=1}^{N-1} \{||a\dot{w}^h(t_n^-)||^2_{\Omega_f} - ||a\dot{w}^h(t_n^+)||^2_{\Omega_f}\} \qquad (4.22)
\end{aligned}
$$

Therefore,

$$
\begin{aligned}
E_2(w^h\,,\,w^h) &= \frac{1}{2}\,||a\dot{w}^h(T^-)||^2_{\Omega_f} + \frac{1}{2}\,||a\dot{w}^h(0^+)||^2_{\Omega_f} \\
&+ \frac{1}{2}\sum_{n=1}^{N-1} \left\{||a\dot{w}^h(t_n^+)||^2_{\Omega_f} - 2(\dot{w}^h(t_n^+)\,,\,a^2\,\dot{w}^h(t_n^-))_{\Omega_f} + ||a\dot{w}^h(t_n^-)||^2_{\Omega_f}\right\} \\
&= \frac{1}{2}\,||a\dot{w}^h(T^-)||^2_{\Omega_f} + \frac{1}{2}\,||a\dot{w}^h(0^+)||^2_{\Omega_f} + \frac{1}{2}\sum_{n=1}^{N-1} ||a[\![\dot{w}^h(t_n)]\!]||^2_{\Omega_f} \qquad (4.23)
\end{aligned}
$$

Similarly,

$$
E_0(w^h\,,\,w^h) = \frac{1}{2}\,||\nabla w^h(T^-)||^2_{\Omega_f} + \frac{1}{2}\,||\nabla w^h(0^+)||^2_{\Omega_f} + \frac{1}{2}\sum_{n=1}^{N-1} ||[\![\nabla w^h(t_n)]\!]||^2_{\Omega_f} \qquad (4.24)
$$

Combining (4.23) and (4.24) and using (4.3) completes the proof. □

Lemma 4.2 (Radiation Energy)
For the exterior problem, assuming the non-reflecting boundary conditions satisfy condition (3.35), then

$$
\boxed{E_r(w^h\,,\,w^h) \quad = \quad |||w^h|||^2_r} \qquad (4.25)
$$

where

$$|||w^h|||_r^2 \;:=\; \sum_{n=0}^{N-1} d_1(\dot{w}^h\,,\,\dot{w}^h)_{(\Upsilon_\infty)_n} + \mathcal{E}_r(w^h(0^+)) + \sum_{n=1}^{N-1} \mathcal{E}_r([\![w^h(t_n)]\!]) + \mathcal{E}_r(w^h(T^-)) \tag{4.26}$$

and the operator $\mathcal{E}_r(\cdot)$ is defined as,

$$\mathcal{E}_r(w) := \frac{1}{2}\, d_2(\dot{w}\,,\,\dot{w})_{\Gamma_\infty} + \frac{1}{2}\, d_0(w\,,\,w)_{\Gamma_\infty} \tag{4.27}$$

This is the coercivity condition for the non-reflecting boundary operators.

Equation (4.26) represents a norm that is stronger than the radiation energy absorbed through the truncation boundary Γ_∞ given by,

$$\begin{aligned}\mathcal{R}(w) &= \int_0^T \int_{\Gamma_\infty} \rho_0 \dot{w} \mathbb{S}_m w \; d\Gamma\; dt \\ &= \mathcal{E}_r(w) + d_1(\dot{w}^h\,,\,\dot{w}^h)_{\Upsilon_\infty}\end{aligned} \tag{4.28}$$

Proof: Proceeding as in Lemma 4.1,

$$\begin{aligned}\sum_{n=0}^{N-1} d_2(\dot{w}^h\,,\,\ddot{w}^h)_{(\Upsilon_\infty)_n} &= \frac{1}{2}\, d_2(\dot{w}^h(T^-)\,,\,\dot{w}^h(T^-))_{\Gamma_\infty} - \frac{1}{2}\, d_2(\dot{w}^h(0^+)\,,\,\dot{w}^h(0^+))_{\Gamma_\infty} \\ &+ \frac{1}{2}\sum_{n=1}^{N-1}\left\{ d_2(\dot{w}^h(t_n^-)\,,\,\dot{w}^h(t_n^-))_{\Gamma_\infty} - d_2(\dot{w}^h(t_n^+)\,,\,\dot{w}^h(t_n^+))_{\Gamma_\infty}\right\}\end{aligned} \tag{4.29}$$

Therefore,

$$\begin{aligned}D_2(w^h\,,\,w^h) &= \frac{1}{2}\, d_2(\dot{w}^h(T^-)\,,\,\dot{w}^h(T^-))_{\Gamma_\infty} + \frac{1}{2}\, d_1(\dot{w}^h(0^+)\,,\,\dot{w}^h(0^+))_{\Gamma_\infty} \\ &+ \frac{1}{2}\sum_{n=1}^{N-1} d_2([\![\dot{w}^h(t_n)]\!]\,,\,[\![\dot{w}^h(t_n)]\!])_{\Gamma_\infty}\end{aligned} \tag{4.30}$$

Similarly,

$$
\begin{aligned}
D_0(w^h\,,\,w^h) \quad &= \quad \frac{1}{2}\,d_0(w^h(T^-)\,,\,w^h(T^-))_{\Gamma_\infty} \;+\; \frac{1}{2}\,d_0(w^h(0^+)\,,\,w^h(0^+))_{\Gamma_\infty} \\
&+ \quad \frac{1}{2}\sum_{n=1}^{N-1} d_0([\![w^h(t_n)]\!]\,,\,[\![w^h(t_n)]\!])_{\Gamma_\infty}
\end{aligned}
\tag{4.31}
$$

Combining (4.30), (4.31) and (4.4) completes the proof. ◻

Lemma 4.3 (Total Structural Energy)

$$
\boxed{E_s(\boldsymbol{w}^h\,,\,\boldsymbol{w}^h) \quad = \quad |||\boldsymbol{w}^h|||_s^2}
\tag{4.32}
$$

where

$$
|||\boldsymbol{w}^h|||_s^2 := \quad \mathcal{E}_s(\boldsymbol{w}^h(0^+)) \;+\; \sum_{n=1}^{N-1} \mathcal{E}_s([\![\boldsymbol{w}^h(t_n)]\!]) \;+\; \mathcal{E}_s(\boldsymbol{w}^h(T^-))
\tag{4.33}
$$

and for elastodynamics, the total energy within the domain Ω_s is defined as in (2.40):

$$
\mathcal{E}_s(\boldsymbol{w}) \quad = \quad \frac{1}{2}\,(\dot{\boldsymbol{w}}\,,\,\rho_s\dot{\boldsymbol{w}})_{\Omega_s} \;+\; \frac{1}{2}\,a(\boldsymbol{w}\,,\,\boldsymbol{w})_{\Omega_s}
\tag{4.34}
$$

This is the coercivity condition for the structure.

The proof of Lemma 4.3 follows the same steps taken to prove Lemma 4.1 and so is omitted.

The norm associated with the coupled fluid-structure system (4.1) and (4.12) is defined by:

$$
\begin{aligned}
|||\boldsymbol{\psi}^h|||^2 \quad &= \quad |||\boldsymbol{w}^h|||_s^2 \;+\; |||w^h|||_f^2 \;+\; |||w^h|||_r^2 \\
&+ \quad \sum_{n=0}^{N-1} \Big\{ (\mathcal{L}_s\boldsymbol{w}^h\,,\,\rho_s^{-1}\boldsymbol{\tau}\mathcal{L}_s\boldsymbol{w}^h)_{\tilde{Q}_n^s} \\
&+ \quad ([\![\boldsymbol{\sigma}(\nabla\boldsymbol{w}^h)(\boldsymbol{x})]\!]\cdot\boldsymbol{n}\,,\,\rho_s^{-1}\boldsymbol{s}[\![\boldsymbol{\sigma}(\nabla\boldsymbol{w}^h)(\boldsymbol{x})]\!]\cdot\boldsymbol{n})_{(\tilde{\Upsilon}_s)_n} \\
&+ \quad (\boldsymbol{\sigma}(\nabla\boldsymbol{w}^h)\cdot\boldsymbol{n}\,,\,\rho_s^{-1}\boldsymbol{s}\boldsymbol{\sigma}(\nabla\boldsymbol{w}^h)\cdot\boldsymbol{n})_{(\Upsilon_\sigma)_n} \\
&+ \quad (\mathcal{L}_1\boldsymbol{\psi}^h\,,\,\rho_s^{-1}\boldsymbol{s}\mathcal{L}_1\boldsymbol{\psi}^h)_{(\Upsilon_i)_n}
\end{aligned}
$$

$$
\begin{aligned}
&+ \quad ||c\tau^{1/2}\mathcal{L}_f w^h||^2_{\tilde{Q}^f_n} + ||cs^{1/2}\mathcal{L}_r w^h||^2_{(\tilde{\Upsilon}_\infty)_n} \\
&+ \quad ||cs^{1/2}[\![w^h_{,n}(\boldsymbol{x})]\!]||^2_{(\tilde{\Upsilon}_f)_n} + (\mathcal{L}_2\boldsymbol{\psi}^h \,,\, c^2 s\mathcal{L}_2\boldsymbol{\psi}^h)_{(\Upsilon_i)_n}\Big\}
\end{aligned} \tag{4.35}
$$

Lemma 4.4 (Stability condition for the coupled system)

$$
\boxed{|||\boldsymbol{\psi}^h|||^2 \quad = \quad B^s_{GLS}(\boldsymbol{w}^h \,,\, \boldsymbol{\psi}^h) + B^f_{GLS}(w^h \,,\, \boldsymbol{\psi}^h)} \tag{4.36}
$$

Proof: The proof follows directly from the superposition of (4.1) and (4.12),

$$
\begin{aligned}
B^s_{GLS}(\boldsymbol{w}^h \,,\, \boldsymbol{\psi}^h) \quad &+ \quad B^f_{GLS}(w^h \,,\, \boldsymbol{\psi}^h) \\
&= \quad E_s(\boldsymbol{w}^h \,,\, \boldsymbol{w}^h) - A(\boldsymbol{w}^h \,,\, w^h\boldsymbol{n}) \\
&+ \quad E_f(w^h \,,\, w^h) + A(\boldsymbol{w}^h \,,\, w^h\boldsymbol{n}) + E_r(w^h \,,\, w^h) \\
&+ \quad \sum_{n=0}^{N-1}\Big\{B^s_{GLS}(\boldsymbol{w}^h \,,\, \boldsymbol{\psi})_n + B^f_{GLS}(w^h \,,\, \boldsymbol{\psi})_n\Big\}
\end{aligned} \tag{4.37}
$$

Using the definitions in Lemmas 4.1 , 4.2 and 4.3, and canceling the coupling terms $A(\cdot\,,\,\cdot)$ completes the proof. The discontinuous Galerkin method ($\boldsymbol{\tau} = 0\,, \boldsymbol{s} = 0$) and/or ($\tau = 0\,,\, s = 0$), also satisfies a coercivity condition. □

Remark

- By the choice of displacement/velocity potential variables $\boldsymbol{\mathcal{X}}^h$, weighting $\dot{\boldsymbol{\psi}}^h$, and weakly enforcing the traction and kinematic interface boundary conditions across $\Gamma_\infty \times I_n$, then the coupling terms $A(\cdot\,,\,\cdot)$, cancel when the structure and the fluid variational equations are added together. Recall that an analogous result occurred in the construction of Lemma 2.1 for the continuum problem. This is the key result which allows for the establishment of a well-defined norm (4.35) for the coupled problem.

In the following, we establish the discrete counterpart to the energy identity obtained in Theorem 2.1 for the continuum problem.

Theorem 4.1 (Energy Estimate)
In the absence of external loading, i.e. $f = 0$ *and* $\bar{\boldsymbol{t}} = 0$, *and assuming the radiation boundary operators satisfy (3.35), then at the end of a time interval the total structural energy, i.e.* $\mathbb{E}(\boldsymbol{\chi}^h(t_n^-))$, *within the computational domain* $\Omega = \Omega_s \cup \Omega_f$, *plus the radiation energy absorbed through the artificial boundary* Γ_∞, *i.e.* $\mathcal{R}(\phi^h(t_n^-))$, *is bounded above by the initial energy in the system, i.e.,* $\mathbb{E}(\boldsymbol{\chi}_0)$.

Proof: With $f = 0$ and $\bar{\boldsymbol{t}} = 0$,

$$\begin{aligned}
L^s_{GLS}(\boldsymbol{u}^h) + L^f_{GLS}(\phi^h) \quad &= \quad (\dot{\boldsymbol{u}}^h(0^+)\,,\,\rho_s\dot{\boldsymbol{u}}_0)_{\Omega_s} + a(\boldsymbol{u}^h(0^+)\,,\,\boldsymbol{u}_0)_{\Omega_s} \\
&+ \quad (\dot{\phi}^h(0^+)\,,\,a^2\,\dot{\phi}_0)_{\Omega_f} + (\nabla\phi^h(0^+)\,,\,\nabla\phi_0)_{\Omega_f} \\
&\leq \quad |(\dot{\boldsymbol{u}}^h(0^+)\,,\,\rho_s\dot{\boldsymbol{u}}_0)_{\Omega_s} + a(\boldsymbol{u}^h(0^+)\,,\,\boldsymbol{u}_0)_{\Omega_s} \\
&+ \quad (\dot{\phi}^h(0^+)\,,\,a^2\,\dot{\phi}_0)_{\Omega_f} + (\nabla\phi^h(0^+)\,,\,\nabla\phi_0)_{\Omega_f}| \\
&\leq \quad \frac{1}{2}\,(\dot{\boldsymbol{u}}^h(0^+)\,,\,\rho_s\dot{\boldsymbol{u}}^h(0^+))_{\Omega_s} + \frac{1}{2}\,(\dot{\boldsymbol{u}}_0\,,\,\rho_s\dot{\boldsymbol{u}}_0)_{\Omega_s} \\
&+ \quad \frac{1}{2}\,a(\boldsymbol{u}^h(0^+)\,,\,\boldsymbol{u}^h(0^+))_{\Omega_s} + \frac{1}{2}\,a(\boldsymbol{u}_0\,,\,\boldsymbol{u}_0)_{\Omega_s} \\
&+ \quad \frac{1}{2}\,||a\dot{\phi}^h(0^+)||^2_{\Omega_f} + \frac{1}{2}\,||a\dot{\phi}_0||^2_{\Omega_f} \\
&+ \quad \frac{1}{2}\,||\nabla\phi^h(0^+)||^2_{\Omega_f} + \frac{1}{2}\,||\nabla\phi_0||^2_{\Omega_f} \\
&= \quad \mathcal{E}_s(\boldsymbol{u}^h(0^+)) + \mathcal{E}_s(\boldsymbol{u}_0) \\
&+ \quad \mathcal{E}_f(\phi^h(0^+)) + \mathcal{E}_f(\phi_0)
\end{aligned} \tag{4.38}$$

where $\mathcal{E}_s(\boldsymbol{u}_0)$ and $\mathcal{E}_f(\phi_0)$ denote the initial total energy in the domains Ω_s and Ω_f respectively. Adding (4.1) and (4.12), and using Lemma 4.4 and the definition of $|||\boldsymbol{\psi}^h|||^2$ results in the energy estimate,

$$\mathcal{E}_s(\boldsymbol{u}^h(T^-)) + \mathcal{E}_f(\phi^h(T^-)) + \mathcal{R}(\phi^h(T^-)) \leq \mathcal{E}_s(\boldsymbol{u}_0) + \mathcal{E}_f(\phi_0) \tag{4.39}$$

Since T is arbitrary,

$$\boxed{\mathbb{E}(\boldsymbol{\chi}^h(t_n^-)) + \mathcal{R}(\phi^h(t_n^-)) \leq \mathbb{E}(\boldsymbol{\chi}_0), \quad n = 0, 1, 2, \ldots, N-1} \tag{4.40}$$

where,

$$\mathbb{E}(\boldsymbol{\chi}^h(t_n^-)) \;:=\; \mathcal{E}_s(\boldsymbol{u}^h(t_n^-)) + \mathcal{E}_f(\phi^h(t_n^-)) \tag{4.41}$$

$$\mathbb{E}(\boldsymbol{\chi}_0) \;:=\; \mathcal{E}_s(\boldsymbol{u}_0) + \mathcal{E}_f(\phi_0) \tag{4.42}$$

and $\mathcal{R}(\phi^h(t_n^-))$ is defined as in (4.28). Equation (4.40) also holds for the time-discontinuous Galerkin method where ($\boldsymbol{\tau} = 0\,, \boldsymbol{s} = 0$) and/or ($\tau = s = 0$). □

This result is the algorithmic counterpart to the energy identity derived for the continuum problem and stated in Theorem 2.1. The energy decay inequality in (4.40) states that the total energy in the fluid-structure system, plus the energy transported through the radiation boundary, is always less than, or equal to the initial energy in the system, which implies that *the space-time formulation is unconditionally stable.*

Corollary 4.1 (Energy decay inequality for the interior problem)
For the interior (bounded) problem, energy transport across boundaries is not allowed so that $\mathcal{R} = 0$, *and (4.40) reduces to,*

$$\boxed{\mathbb{E}(\boldsymbol{\chi}^h(t_n^-)) \leq \mathbb{E}(\boldsymbol{\chi}_0), \quad n = 0, 1, 2, \ldots, N-1} \tag{4.43}$$

The result implies that the algorithm is dissipative. As discussed earlier, it is this numerical dissipation which helps control (damp) unwanted oscillations that may occur near discontinuities in the solution.

Corollary 4.2 (Energy decay inequality for acoustics)
For the uncoupled problem of linear acoustics, with zero sources, $f = 0$, *and 'rigid' boundary conditions, i.e.* $\dot{\boldsymbol{u}}^h = \boldsymbol{0}$, *then (4.40) reduces to,*

$$\boxed{\mathcal{E}_f(\phi^h(t_n^-)) + \mathcal{R}(\phi^h(t_n^-)) \leq \mathcal{E}_f(\phi_0), \quad n = 0, 1, 2, \ldots, N-1} \tag{4.44}$$

As a specific example of the energy estimate (4.40), consider the first-order $\mathbb{S}_1$, non-reflecting boundary condition defined in (2.26). In this case the radiation energy (4.28) reduces to,

$$\begin{aligned} \mathcal{R}(\phi^h) &= \frac{1}{2} d_0(\phi^h\,,\,\phi^h)_{\Gamma_\infty} \,+\, d_1(\dot{\phi}^h\,,\,\dot{\phi}^h)_{\Upsilon_\infty} \\ &= \frac{1}{2}\, c_0 ||\phi^h||^2_{\Gamma_\infty} + c_1 ||\dot{\phi}^h||^2_{\Upsilon_\infty} \end{aligned} \tag{4.45}$$

where $c_0 = 1/R$ and $c_1 = 1/c$ are positive constants. As a result (4.40) specializes to,

$$\mathbb{E}(\boldsymbol{\mathcal{X}}^h(t_n^-)) \,+\, \frac{1}{2}\, c_0 ||\phi^h||^2_{\Gamma_\infty} + c_1 ||\dot{\phi}^h||^2_{\Upsilon_\infty} \,\le\, \mathbb{E}(\boldsymbol{\mathcal{X}}_0) \tag{4.46}$$

This result is the discrete counterpart to (2.60).

4.4 Error Estimates for Acoustics

Before stating the convergence properties for the coupled fluid-structure system, error estimates for the simplified uncoupled problem of linear acoustics with 'rigid' boundary conditions are derived. To further simplify the analysis, non-reflecting boundary operators are restricted to the first-order $\mathbb{S}_1$ condition defined in (2.26). In this case, second-order time-derivatives do not appear in the radiation boundary condition and the boundary term $d_2(\cdot\,,\,\cdot)$ is omitted. The proof of convergence follows along the same lines as in Hughes and Hulbert [1988], with the additional complication of including the non-reflecting boundary operators for the exterior problem.

For the acoustics problem with 'rigid' boundary conditions, (i.e. $\dot{\boldsymbol{u}}^h \cdot \boldsymbol{n} = 0$ on Γ_∞), the coupling operator $A(\boldsymbol{u}^h\,,\,w^h\boldsymbol{n})$ vanishes and the norm associated with (4.1) reduces to,

$$\begin{aligned} |||w^h|||^2 &= |||w^h|||^2_f \,+\, |||w^h|||^2_r \\ &+ \sum_{n=0}^{N-1} \Big\{ ||c\tau^{1/2}\mathcal{L}_f w^h||^2_{\tilde{Q}^f_n} \,+\, ||cs^{1/2}\mathcal{L}_r w^h||^2_{(\tilde{\Upsilon}_\infty)_n} \\ &+ ||cs^{1/2}[\![w^h_{,n}(\boldsymbol{x})]\!]||^2_{(\tilde{\Upsilon}_f)_n} \,+\, ||cs^{1/2} w^h_{,n}||^2_{(\Upsilon_i)_n} \Big\} \end{aligned} \tag{4.47}$$

The coercivity condition for the uncoupled acoustics problem is,

$$|||w^h|||^2 \quad = \quad B^f_{GLS}(w^h\,,\,w^h) \tag{4.48}$$

where the right-hand-side is defined by (4.1) with $A_n = 0$. The appropriate consistency condition is,

$$B^f_{GLS}(w^h\,,\,e) \quad = \quad 0 \tag{4.49}$$

where $e = \phi^h - \phi$.

Let $\tilde{\phi}^h \in \mathcal{T}^h$ denote an interpolant of ϕ, and let $\eta = \tilde{\phi}^h - \phi$ denote the interpolation error. Then the solution error, $e = \phi^h - \phi$, can be split into the sum

$$e = e^h + \eta \tag{4.50}$$

where

$$e^h = \phi^h - \tilde{\phi}^h \in \mathcal{W}^h \tag{4.51}$$

is the difference between the finite element solution and the interpolant. An appropriate space-time mesh parameter is given by,

$$\boxed{h = \max\{c\Delta t\,,\,\Delta x\}} \tag{4.52}$$

where c is the acoustic wave speed and Δx and Δt are maximum element diameters in space and time, respectively.

Theorem 4.2 (Error Estimates)
Assume τ and s satisfy,

$$c_1 h \quad \leq \quad \tau \quad \leq \quad c_2 h \tag{4.53}$$

$$c_3 \quad \leq \quad s \quad \leq \quad c_4 \tag{4.54}$$

where $c_1\,,\,c_2\,,\,c_3$ and c_4 are positive constants ($c_2 > c_1\,,\,c_4 > c_3$). Assuming the exact solution ϕ to the local acoustics problem with $\mathbb{S}_1$, is smooth in the sense that, $\phi \in H^{p+1}(Q_f)$, then the interpolation error, η, satisfies the following estimates:

$$\sum_{n=0}^{N-1} d_1(\dot{\eta}\,,\,\dot{\eta})_{(\Upsilon_\infty)_n} \quad \leq \quad c(\phi)\, h^{2p-1} \tag{4.55}$$

$$\sum_{n=0}^{N-1} ||a\tau^{-1/2}\dot{\eta}||^2_{Q_n^f} \quad \leq \quad c(\phi)\, h^{2p-1} \tag{4.56}$$

$$\sum_{n=0}^{N-1} ||c\tau^{1/2}\mathcal{L}_f\eta||^2_{\tilde{Q}_n^f} \quad \leq \quad c(\phi)\, h^{2p-1} \tag{4.57}$$

$$\sum_{n=0}^{N-1} ||as^{-1/2}\dot{\eta}||^2_{(\Upsilon_\infty)_n} \quad \leq \quad c(\phi)\, h^{2p-1} \tag{4.58}$$

$$\sum_{n=0}^{N-1} ||cs^{1/2}\mathcal{L}_r\eta||^2_{(\Upsilon_\infty)_n} \quad \leq \quad c(\phi)\, h^{2p-1} \tag{4.59}$$

$$\sum_{n=0}^{N-1} ||as^{-1/2}\dot{\eta}||^2_{\tilde{\Upsilon}_n\cup(\Upsilon_i)_n} \quad \leq \quad c(\phi)\, h^{2p-1} \tag{4.60}$$

$$\sum_{n=0}^{N-1} \left\{ ||cs^{1/2}[\![\eta_{,n}(\boldsymbol{x})]\!]||^2_{\tilde{\Upsilon}_n} + ||cs^{1/2}\eta_{,n}||_{(\Upsilon_i)_n} \right\} \quad \leq \quad c(\phi)\, h^{2p-1} \tag{4.61}$$

$$\mathcal{E}_f(\eta(T^-)) + \mathcal{E}_f(\eta(0^+)) + \sum_{n=1}^{N-1} \left\{ \mathcal{E}_f(\eta(t_n^-)) + \mathcal{E}_f(\eta(t_n^+)) \right\} \leq c(\phi)\, h^{2p-1} \tag{4.62}$$

$$\begin{aligned} & d_0(\eta(T^-)\,,\,\eta(T^-))_{\Gamma_\infty} + d_0(\eta(0^+)\,,\,\eta(0^+))_{\Gamma_\infty} \\ + & \sum_{n=1}^{N-1} \left\{ d_0(\eta(t_n^-)\,,\,\eta(t_n^-))_{\Gamma_\infty} + d_0(\eta(t_n^+)\,,\,\eta(t_n^+))_{\Gamma_\infty} \right\} \leq c(\phi)\, h^{2p-1} \end{aligned} \tag{4.63}$$

where $c(\phi)$ is independent of the mesh parameter h. Then,

$$\boxed{|||e|||^2 \quad \leq \quad c(\phi)\, h^{2p-1}} \tag{4.64}$$

The following Lemmas aid in the proof of Theorem 4.2.

Lemma 4.5

$$\begin{aligned} E_2(e^h\,,\,\eta) \quad &= \quad -\sum_{n=0}^{N-1}(\ddot{e}^h\,,\,a^2\,\dot{\eta})_{Q_n^f} \\ &- \quad \sum_{n=1}^{N-1}([\![\dot{e}^h(t_n)]\!]\,,\,a^2\,\dot{\eta}(t_n^-))_{\Omega_f}\;+\;(\dot{e}^h(T^-)\,,\,a^2\,\dot{\eta}(T^-))_{\Omega_f} \end{aligned} \tag{4.65}$$

$$\begin{aligned} E_0(e^h\,,\,\eta) \quad &= \quad -\sum_{n=0}^{N-1}(\nabla e^h\,,\,\nabla\dot{\eta})_{Q_n^f} \\ &- \quad \sum_{n=1}^{N-1}([\![\nabla e^h(t_n)]\!]\,,\,\nabla\eta(t_n^-))_{\Omega_f}\;+\;(\nabla e^h(T^-)\,,\,\nabla\eta(T^-))_{\Omega_f} \end{aligned} \tag{4.66}$$

$$\begin{aligned} D_0(e^h\,,\,\eta) \quad &= \quad -\sum_{n=0}^{N-1}d_0(e^h\,,\,\dot{\eta})_{(\Upsilon_\infty)_n} \\ &- \quad \sum_{n=1}^{N-1}d_0([\![e^h(t_n)]\!]\,,\,\eta(t_n))_{\Gamma_\infty}\;+\;d_0(e^h(T^-)\,,\,\eta(T^-))_{\Gamma_\infty} \end{aligned} \tag{4.67}$$

Results (4.65),(4.66), and (4.67) follow directly using definitions (4.5), (4.6), and (4.8), and from integration-by-parts in time. □

Lemma 4.6

$$\begin{aligned} &(\ddot{e}^h\,,\,a^2\,\dot{\eta})_{Q_n^f}\;+\;(\nabla e^h\,,\,\nabla\dot{\eta})_{Q_n^f}\;+\;d_0(e^h\,,\,\dot{\eta})_{(\Upsilon_\infty)_n}\;+\;d_1(\dot{e}^h\,,\,\dot{\eta})_{(\Upsilon_\infty)_n} \\ = \quad &(\mathcal{L}_f e^h\,,\,\dot{\eta})_{\tilde{Q}_n^f}\;+\;(\mathcal{L}_r e^h\,,\,\dot{\eta})_{(\Upsilon_\infty)_n}\;+\;([\![e^h_{,n}(\boldsymbol{x})]\!]\,,\,\dot{\eta})_{\tilde{\Upsilon}_n^f}\;+\;(e^h_{,n}\,,\,\dot{\eta})_{(\Upsilon_i)_n} \end{aligned} \tag{4.68}$$

Proof:
By integration-by-parts and the divergence theorem,

$$\begin{aligned} (\nabla e^h\,,\,\nabla\dot{\eta})_{Q_n^f} \quad &= \quad -(\nabla^2 e^h\,,\,\dot{\eta})_{\tilde{Q}_n^f}\;+\;(e^h_{,n}\,,\,\dot{\eta})_{(\Upsilon_\infty)_n} \\ &+ \quad ([\![e^h_{,n}(\boldsymbol{x})]\!]\,,\,\dot{\eta})_{\tilde{\Upsilon}_n^f}\;+\;(e^h_{,n}\,,\,\dot{\eta})_{(\Upsilon_i)_n} \end{aligned} \tag{4.69}$$

Thus

$$
\begin{aligned}
& (\ddot{e}^h\,,\, a^2\,\dot{\eta})_{Q_n^f} \,+\, (\nabla e^h\,,\, \nabla\dot{\eta})_{Q_n^f} \,+\, d_0(e^h\,,\, \dot{\eta})_{(\Upsilon_\infty)_n} \,+\, d_1(\dot{e}^h\,,\, \dot{\eta})_{(\Upsilon_\infty)_n} \\
&\quad = \; (a^2\ddot{e}^h - \nabla^2 e^h\,,\, \dot{\eta})_{\tilde{Q}_n^f} \,+\, (e^h_{,n} + \mathbb{S}_1 e^h\,,\, \dot{\eta})_{(\Upsilon_\infty)_n} \\
&\quad + \; ([\![e^h_{,n}(\boldsymbol{x})]\!]\,,\, \dot{\eta})_{\tilde{\Upsilon}_n^f} \,+\, (e^h_{,n}\,,\, \dot{\eta})_{(\Upsilon_i)_n}
\end{aligned} \tag{4.70}
$$

where use is made of (3.29),(3.30), and (3.31) with the first-order $m = 1$, non-reflecting boundary operator defined as in (2.26), i.e.

$$
\mathbb{S}_1 e^h = \frac{1}{R} e^h + \frac{1}{c}\dot{e}^h \tag{4.71}
$$

Employing the definitions (3.52) and (3.53) completes the proof. □

The following two inequalities are also needed.

$$
\begin{aligned}
& \sum_{n=1}^{N-1} \Big\{ -\,([\![\dot{e}^h(t_n)]\!]\,,\, a^2\,\dot{\eta}(t_n^-))_{\Omega_f} \,-\, ([\![\nabla e^h(t_n)]\!]\,,\, \nabla\eta(t_n^-))_{\Omega_f} \Big\} \\
&\quad + (\dot{e}^h(T^-)\,,\, a^2\,\dot{\eta}(T^-))_{\Omega_f} + (\nabla e^h(T^-)\,,\, \nabla\eta(T^-))_{\Omega_f} \\
&\quad \le \; \frac{1}{2}\Big[\sum_{n=1}^{N-1} \{ \mathcal{E}_f([\![e^h(t_n)]\!]) \,+\, 4\mathcal{E}_f(\eta(t_n^-)) \} \\
&\quad + \; \mathcal{E}_f(e^h(T^-)) + 4\mathcal{E}_f(\eta(T^-)) \Big]
\end{aligned} \tag{4.72}
$$

Similarly,

$$
\begin{aligned}
& -\sum_{n=1}^{N-1} d_0([\![e^h(t_n)]\!]\,,\, \eta(t_n^-))_{\Gamma_\infty} \,+\, d_0(e^h(T^-)\,,\, \eta(T^-))_{\Gamma_\infty} \\
& \le \; \frac{1}{2}\Big[\sum_{n=1}^{N-1} \Big\{ \frac{1}{2} d_0([\![e^h(t_n)]\!]\,,\, [\![e^h(t_n)]\!])_{\Gamma_\infty} \,+\, 2\,d_0(\eta(t_n^-)\,,\, \eta(t_n^-))_{\Gamma_\infty} \Big\} \\
& + \; \frac{1}{2} d_0(e^h(T^-)\,,\, e^h(T^-))_{\Gamma_\infty} \,+\, 2\,d_0(\eta(T^-)\,,\, \eta(T^-))_{\Gamma_\infty} \Big]
\end{aligned} \tag{4.73}
$$

Results (4.72) and (4.73) follow directly from repeated use of inequality (4.18). The proof of Theorem 4.2 proceeds as follows,

$$
\begin{aligned}
|||e^h|||^2 &= B^f_{GLS}(e^h\,,\,e^h) \qquad \text{(by the coercivity condition, (4.48))} \\
&= B^f_{GLS}(e^h\,,\,e-\eta) \qquad \text{(by (4.50))} \\
&= -B^f_{GLS}(e^h\,,\,\eta) \qquad \text{(by the consistency condition, (4.49))} \\
&\leq \left|B^f_{GLS}(e^h\,,\,\eta)\right| \\
&= \Big| E_2(e^h\,,\,\eta) + E_0(e^h\,,\,\eta) + D_1(e^h\,,\,\eta) + D_0(e^h\,,\,\eta) \\
&\quad + \sum_{n=0}^{N-1} \Big\{ (\mathcal{L}_f e^h\,,\,c^2\tau\mathcal{L}_f\eta)_{\tilde{Q}^f_n} + (\mathcal{L}_r e^h\,,\,c^2 s\mathcal{L}_r\eta)_{(\tilde{\Upsilon}_\infty)_n} \\
&\quad + ([\![e^h_{,n}(\boldsymbol{x})]\!]\,,\,c^2 s[\![\eta_{,n}(\boldsymbol{x})]\!])_{\tilde{\Upsilon}^f_n} + (e^h_{,n}\,,\,c^2 s\eta_{,n})_{(\Upsilon_i)_n} \Big\} \Big| \\
&\qquad\qquad \text{(by definition of } B^f_{GLS}, (4.3)\ -(4.9)) \\
&= \Big| \sum_{n=0}^{N-1} \Big\{ -(\mathcal{L}_f e^h\,,\,\dot{\eta})_{\tilde{Q}^f_n} + (\mathcal{L}_f e^h\,,\,c^2\tau\mathcal{L}_f\eta)_{\tilde{Q}^f_n} \\
&\quad - (\mathcal{L}_r e^h\,,\,\dot{\eta})_{(\Upsilon_\infty)_n} + (\mathcal{L}_r e^h\,,\,c^2 s\mathcal{L}_r\eta)_{(\Upsilon_\infty)_n} + 2d_1(\dot{e}^h\,,\,\dot{\eta})_{(\Upsilon_\infty)_n} \\
&\quad - ([\![e^h_{,n}(\boldsymbol{x})]\!]\,,\,\dot{\eta})_{\tilde{\Upsilon}^f_n} - (e^h_{,n}\,,\,\dot{\eta})_{(\Upsilon_i)_n} \\
&\quad + ([\![e^h_{,n}(\boldsymbol{x})]\!]\,,\,c^2 s[\![\eta_{,n}(\boldsymbol{x})]\!])_{\tilde{\Upsilon}^f_n} + (e^h_{,n}\,,\,c^2 s\eta_{,n})_{(\Upsilon_i)_n} \Big\} \\
&\quad + \sum_{n=1}^{N-1} \Big\{ -([\![\dot{e}^h(t_n)]\!]\,,\,a^2\,\dot{\eta}(t_n^-))_{\Omega_f} - ([\![\nabla e^h(t_n)]\!]\,,\,\nabla\eta(t_n^-))_{\Omega_f} \Big\} \\
&\quad + (\dot{e}^h(T^-)\,,\,a^2\,\dot{\eta}(T^-))_{\Omega_f} + (\nabla e^h(T^-)\,,\,\nabla\eta(T^-))_{\Omega_f} \\
&\quad - \sum_{n=1}^{N-1} d_0([\![e^h(t_n)]\!]\,,\,\eta(t_n^-))_{\Gamma_\infty} + d_0(e^h(T^-)\,,\,\eta(T^-))_{\Gamma_\infty} \Big| \\
&\qquad\qquad \text{(by Lemmas 4.5 and 4.6)} \\
&\leq \sum_{n=0}^{N-1} \Big\{ \frac{1}{4}\,||c\tau^{1/2}\mathcal{L}_f e^h||^2_{\tilde{Q}^f_n} + ||a\tau^{-1/2}\dot{\eta}||^2_{\tilde{Q}^f_n}
\end{aligned}
$$

$$
\begin{aligned}
&+ \quad \frac{1}{4}\,||c\tau^{1/2}\mathcal{L}_f e^h||^2_{\tilde{Q}^f_n} \,+\, ||c\tau^{1/2}\mathcal{L}_f \eta||^2_{\tilde{Q}^f_n} \\
&+ \quad \frac{1}{4}\,||cs^{1/2}\mathcal{L}_r e^h||^2_{(\Upsilon_\infty)_n} \,+\, ||as^{-1/2}\dot{\eta}||^2_{(\Upsilon_\infty)_n} \\
&+ \quad \frac{1}{4}\,||cs^{1/2}\mathcal{L}_r e^h||^2_{(\Upsilon_\infty)_n} \,+\, ||cs^{1/2}\mathcal{L}_r \eta||^2_{(\Upsilon_\infty)_n} \\
&+ \quad \frac{1}{2}\,d_1(\dot{e}^h\,,\,\dot{e}^h)_{(\Upsilon_\infty)_n} \,+\, 2d_1(\dot{\eta}\,,\,\dot{\eta})_{(\Upsilon_\infty)_n} \\
&+ \quad \frac{1}{4}\,||cs^{1/2}[\![e^h_{,n}(\boldsymbol{x})]\!]||^2_{\tilde{\Upsilon}^f_n} \,+\, ||as^{-1/2}\dot{\eta}||^2_{\tilde{\Upsilon}^f_n} \\
&+ \quad \frac{1}{4}\,||cs^{1/2}e^h_{,n}||^2_{(\Upsilon_i)_n} \,+\, ||as^{-1/2}\dot{\eta}||^2_{(\Upsilon_i)_n} \\
&+ \quad \frac{1}{4}\,||cs^{1/2}[\![e^h_{,n}(\boldsymbol{x})]\!]||^2_{\tilde{\Upsilon}^f_n} \,+\, ||cs^{1/2}[\![\eta_{,n}(\boldsymbol{x})]\!]||^2_{\tilde{\Upsilon}^f_n} \\
&+ \quad \frac{1}{4}\,||cs^{1/2}e^h_{,n}||^2_{(\Upsilon_i)_n} \,+\, ||cs^{1/2}\eta_{,n}||^2_{(\Upsilon_i)_n}\Big\} \\
&+ \quad \frac{1}{2}\sum_{n=1}^{N-1}\Big\{\mathcal{E}_f([\![e^h(t_n)]\!]) \,+\, 4\mathcal{E}_f(\eta(t_n^-))\Big\} \\
&+ \quad \frac{1}{2}\,\mathcal{E}_f(e^h(T^-)) \,+\, 2\mathcal{E}_f(\eta(T^-)) \\
&+ \quad \frac{1}{4}\sum_{n=1}^{N-1}\Big\{d_0([\![e^h(t_n)]\!]\,,\,[\![e^h(t_n)]\!])_{\Gamma_\infty} \,+\, 4d_0(\eta(t_n^-)\,,\,\eta(t_n^-))_{\Gamma_\infty}\Big\} \\
&+ \quad \frac{1}{4}\,d_0(e^h(T^-)\,,\,e^h(T^-))_{\Gamma_\infty} \,+\, 4d_0(\eta(T^-)\,,\,\eta(T^-))_{\Gamma_\infty} \\
&\qquad \text{(by (4.18) and results (4.72) and (4.73))}
\end{aligned}
$$

The terms involving e^h may be subsumed by the left-hand side. The interpolation estimates (4.55)–(4.63) then yield

$$|||e^h|||^2 \quad \leq \quad c(\phi)\,h^{2p-1} \tag{4.74}$$

Likewise,

$$|||\eta|||^2 \quad \leq \quad c(\phi)\,h^{2p-1} \tag{4.75}$$

By the triangle inequality,

$$|||e|||^2 \quad \leq \quad 2|||e^h|||^2 + 2|||\eta|||^2 \quad \leq \quad c(\phi)\, h^{2p-1} \tag{4.76}$$

which completes the proof. □

This result indicates that the error as measured in the natural norm (4.48) for the discontinuous GLS solution to the exterior acoustics problem converges at the rate $(2p-1)/2$.

4.4.1 Confirmation of Energy and Error Estimates

To verify the convergence and energy properties of the space-time finite element formulation, the response of a one-dimensional model problem in the semi-infinite interval $0 \leq x < \infty$ was calculated by introducing a truncation boundary $\Gamma_\infty = L$, and imposing an exact non-reflecting boundary condition. Consider the following initial/boundary-value problem,

$$\ddot{\phi} \quad = \quad c^2\, \phi_{,xx} \qquad \text{for } x \in \Omega\,,\, t > 0 \tag{4.77}$$

$$\phi(0,t) \quad = \quad 0, \qquad \phi_{,x}(L,t) = -(1/c)\dot{\phi}(L,t) \tag{4.78}$$

$$\phi(x,0) \quad = \quad \phi_0(x), \qquad \dot{\phi}(x,0) = 0 \tag{4.79}$$

where $\Omega =]0, L[$ and the condition at $x = L$ in (4.78) is the exact 'plane-wave' non-reflecting boundary condition for this one-dimension problem. The initial pulse,

$$\phi_0(x) = \frac{1}{4}\left(1 - \cos\frac{2\pi}{\lambda}(x - x_0)\right)^2 \tag{4.80}$$

is positioned at the distance $x_0 = 2.4$ from the fixed end, with wavelength $\lambda = .8$, and the computational domain is taken as $\Omega =]0, 4[$, i.e. $L = 4$. The domain Ω is discretized uniformly with standard biquadratic interpolations, $Q2$, in space-time, with 3×3 Gaussian quadrature used throughout.

The exact solution is given by D'Alembert. Half of the initial pulse propagates with velocity $c = 1$, in each direction, i.e.

$$\phi(x,t) = \frac{1}{2}[\phi_0(\xi_+) + \phi_0(\xi_-)] \tag{4.81}$$

for $0 \leq \xi_+ \leq \lambda$ and $0 \leq \xi_- \leq \lambda$ where $\xi_+ = x - x_0 - ct$, and $\xi_- = x - x_0 + ct$. At time $t = 0.8$, the wave propagating to the right, $\phi_0(\xi_+)$, reaches the truncation boundary $\Gamma_\infty = L$, and at $t = 1.6$, this wave leaves Ω entirely. At time $t = 2.4$ the wave propagating to the left, $\phi_0(\xi_-)$, reaches the fixed end and is reflected back. At time $t = 7.2$, the reflected wave leaves Ω, resulting in a quiescent solution. The form of ϕ_0 is chosen such that the solution $\phi(x,t)$ has sufficient smoothness (continuity) for the interpolation estimates given in (4.55) - (4.63) to be valid. For ϕ_0 defined in (4.80), and quadratic space-time elements, $p = 2$, the exact solution satisfies the requirement $\phi \in H^3$.

Figure 4.1 shows the numerical solution using the time-discontinuous Galerkin/least-squares algorithm at three representative times. Each space-time slab was discretized with a uniform mesh of 160 $Q2$ elements. The intrinsic time scale used for all computations is,

$$\tau = \frac{\Delta t}{8\sqrt{1 + C^2}} \tag{4.82}$$

where $C = c\Delta t/\Delta x$ is the Courant number. This definition for τ is a generalization of the τ given in Shakib et.al. [1991b]. The effect of the slowness parameter s, has little consequence on the solution to this problem, and as pointed out by Hulbert and Hughes [1990], due to the complications involved with its assembly, this term is omitted in all the computations.

The energy properties of the exact solution are summarized in the following. The total energy within Ω is the sum of the kinetic and potential energies, i.e.

$$\mathcal{E}(\phi(t)) = \frac{1}{2}||a\dot{\phi}||^2_\Omega + \frac{1}{2}||\phi_{,x}||^2_\Omega \tag{4.83}$$

where

$$\begin{aligned} ||a\dot{\phi}||^2_\Omega &= \int_0^L (a\dot{\phi}(x,t))^2 \, dx \\ ||\phi_{,x}||^2_\Omega &= \int_0^L (\phi_{,x}(x,t))^2 \, dx \end{aligned}$$

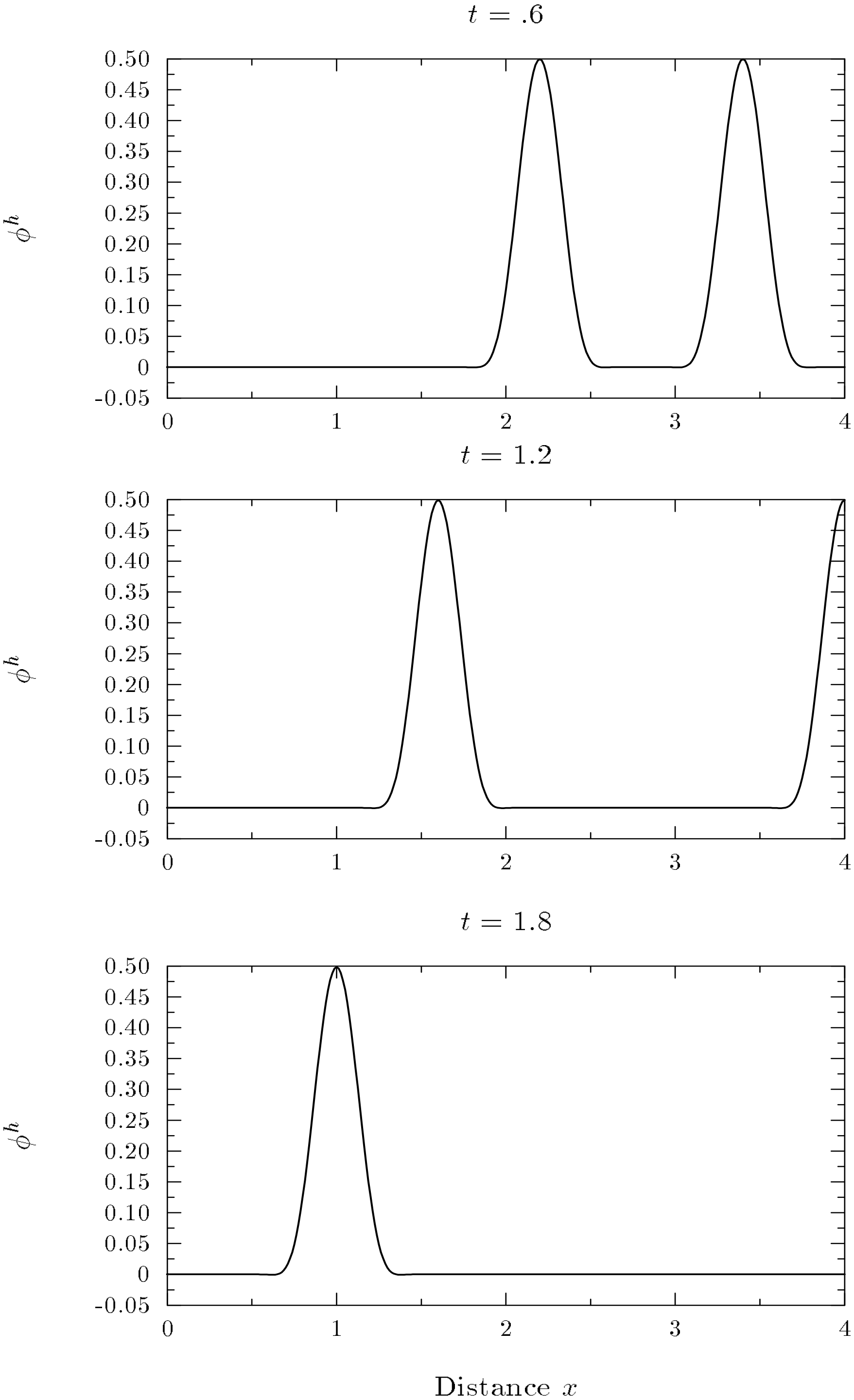

Figure 4.1: One-dimension semi-infinite problem: Numerical solution using time-discontinuous GLS algorithm with 160 $Q2$ elements and a Courant number of $C = 1$. At time $t = .6$ two waves travel in opposite directions. At $t = 1.2$ the wave propagating to the right is absorbed by the non-reflecting boundary located at $x = 4$. At $t = 1.8$ only the left-going wave remains.

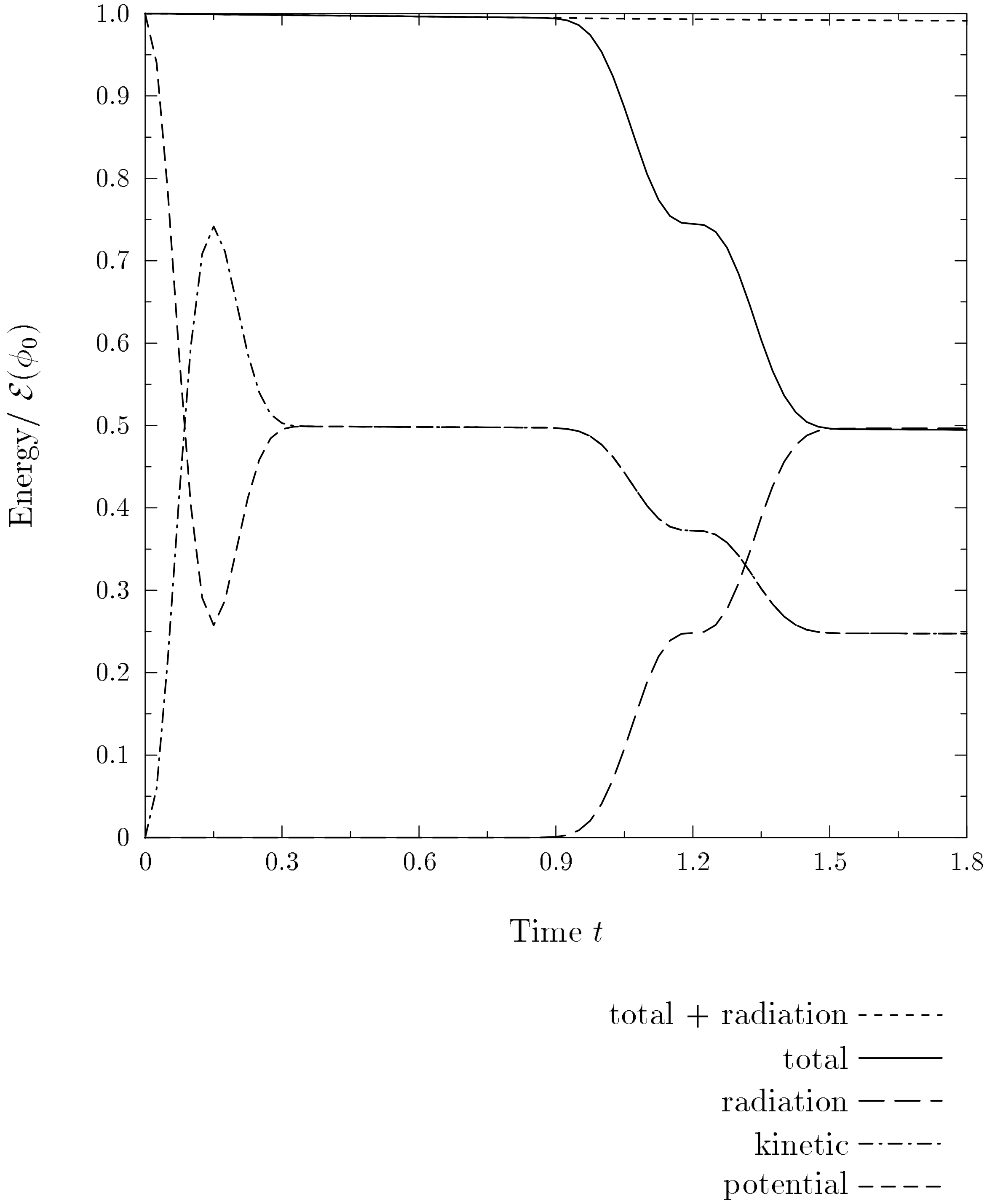

Figure 4.2: Energy calculations using time-discontinuous Galerkin/least-squares algorithm with 160 $Q2$ elements and Courant number $C = 1$. (Total energy = Kinetic energy + Potential energy)

For the initial condition ϕ_0 given in (4.80), $||a\dot{\phi}||_\Omega^2 = ||\phi_{,x}||_\Omega^2$ for $t \geq \lambda/2c$. In addition to the energy in Ω, the power flow, or rate of transfer of energy past the truncation boundary $\Gamma_\infty = L$, is

$$\frac{1}{c}(\dot{\phi}(L,t))^2 \geq 0 \tag{4.84}$$

and it can be shown that the total energy in Ω, plus the energy entering the exterior domain $x > L$, is conserved, i.e.

$$\mathcal{E}(\phi(t)) + \mathcal{R}(\phi(t)) = \mathcal{E}(\phi_0) \tag{4.85}$$

where the radiation energy defined in (4.28) is specialized in one-dimension to,

$$\mathcal{R}(\phi) = \frac{1}{c}\int_0^t (\dot{\phi}(L,\eta))^2 \, d\eta \tag{4.86}$$

Figure 4.2 shows the energy calculations for the time-discontinuous Galerkin/least-squares formulation, with the Courant number set at $C = 1$. At $t = 0$, all the energy is potential, and as the initial pulse begins to propagate, energy is transformed from potential to kinetic. For $t \geq \lambda/2c = 0.4$, the initial pulse has completely separated into a left and right wave, and the space-time finite element solution preserves the equality of the potential and kinetic energies, i.e. $||a\dot{\phi}^h||_\Omega^2 = ||\phi^h_{,x}||_\Omega^2$. At $t = 0.8$, the right going wave reaches $\Gamma_\infty = L$, and the loss in total energy $\mathcal{E}(\phi^h)$ within Ω, is absorbed by the non-reflecting boundary condition as measured by the radiation energy $\mathcal{R}(\phi^h)$. Results confirm that the Galerkin/least-squares method is indeed dissipative, and verifies the energy-decay inequality given in Theorem 4.1, i.e. the total energy plus the radiation energy is bounded above by the initial energy in the computational domain, i.e.

$$\mathcal{E}(\phi^h(t_n^-)) + \mathcal{R}(\phi^h(t_n^-)) \leq \mathcal{E}(\phi_0) \tag{4.87}$$

To study the numerical convergence, the response was calculated for the time interval $0 \leq t \leq T = 1.8$. The convergence rates for the time-discontinuous Galerkin and Galerkin/least-squares formulations are shown in Figure 4.3. Errors were measured in two different norms: $|||\cdot|||_\tau$ denotes the norm, (4.47), with $s = 0$, and $|||\cdot|||_0$ denotes the Galerkin norm, with $\tau = 0$, $s = 0$. Note that the convergence rates are identical for all formulations measured in both norms, and are the same as those predicted by Theorem 4.2. Results for this example show that the Galerkin formulation converges at the same rate as the GLS formulation, with slightly larger errors.

4.4.2 Temporal Stability and Convergence

In order to evaluate the purely temporal behavior of the time-discontinuous Galerkin method, it suffices to consider the Fourier transform of the scalar wave equation from physical space to wavenumber space. Assuming an infinite spatial domain with zero sources, a Fourier synthesis of the wave equation leads to the following second-order ordinary differential equation (ODE).

$$\boxed{\ddot{\phi}(t) + \omega^2 \phi(t) = 0 \qquad t \in]0, T[} \tag{4.88}$$

with initial conditions, $\phi(0) = \phi_0$ and $\dot{\phi}(0) = \dot{\phi}_0$. In the above, $\omega = ck$ is the frequency, c is the wave speed, and k is the wavenumber. The time-discontinuous Galerkin method applied to this ODE is,

$$B_n(w^h\,,\,\phi^h) \quad = \quad L_n(w^h)\,, \qquad n \;=\; 0, 1, ..., N-1 \tag{4.89}$$

where

$$\begin{aligned} B_n(w^h\,,\,\phi^h) \;&:=\; \int_{t_n}^{t_{n+1}} (\dot{w}^h \ddot{\phi}^h + \omega^2 \dot{w}^h \phi^h)\, dt \\ &+\;\; \dot{w}^h(t_n^+)\dot{\phi}^h(t_n^+) + \omega^2 w^h(t_n^+)\phi^h(t_n^+) \end{aligned} \tag{4.90}$$

$$L_n(w^h) \;:=\; \dot{w}^h(t_n^+)\dot{\phi}^h(t_n^-) + \omega^2 w^h(t_n^+)\phi^h(t_n^-) \tag{4.91}$$

Summing (4.89) over the time slabs, we obtain,

$$B(w^h\,,\,\phi^h) \;=\; \sum_{n=0}^{N-1} \int_{t_n}^{t_{n+1}} (\dot{w}^h \ddot{\phi}^h + \omega^2 \dot{w}^h \phi^h)\, dt$$

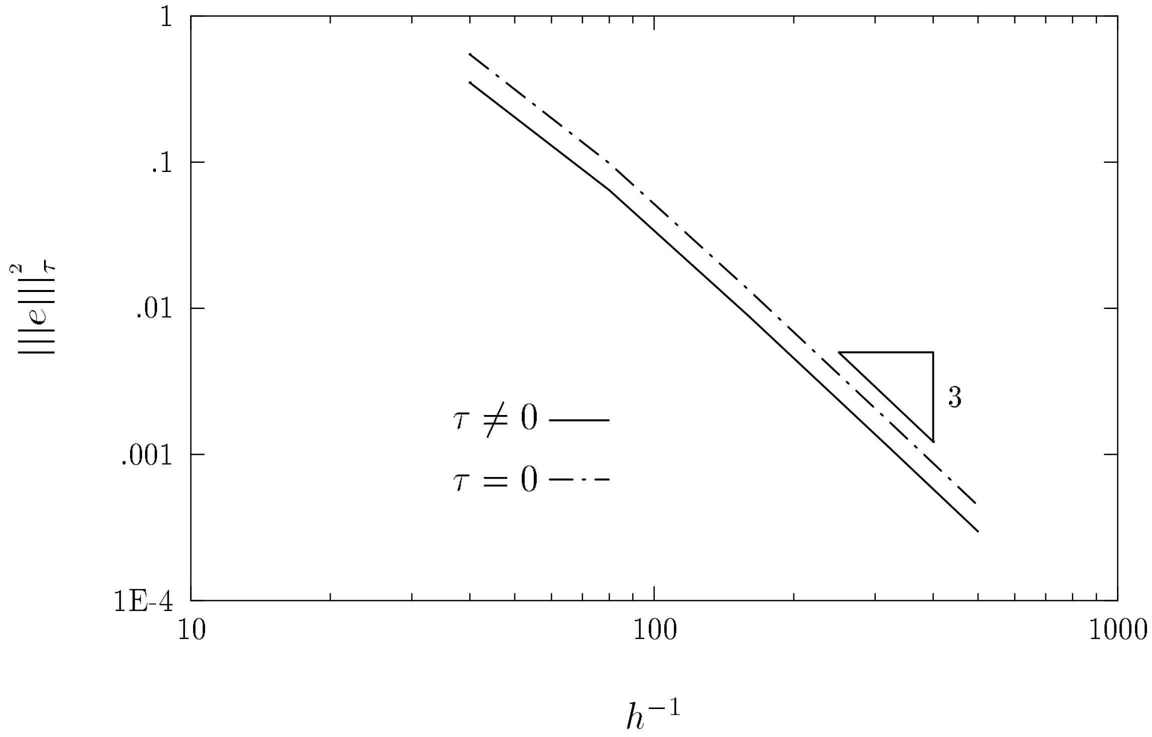

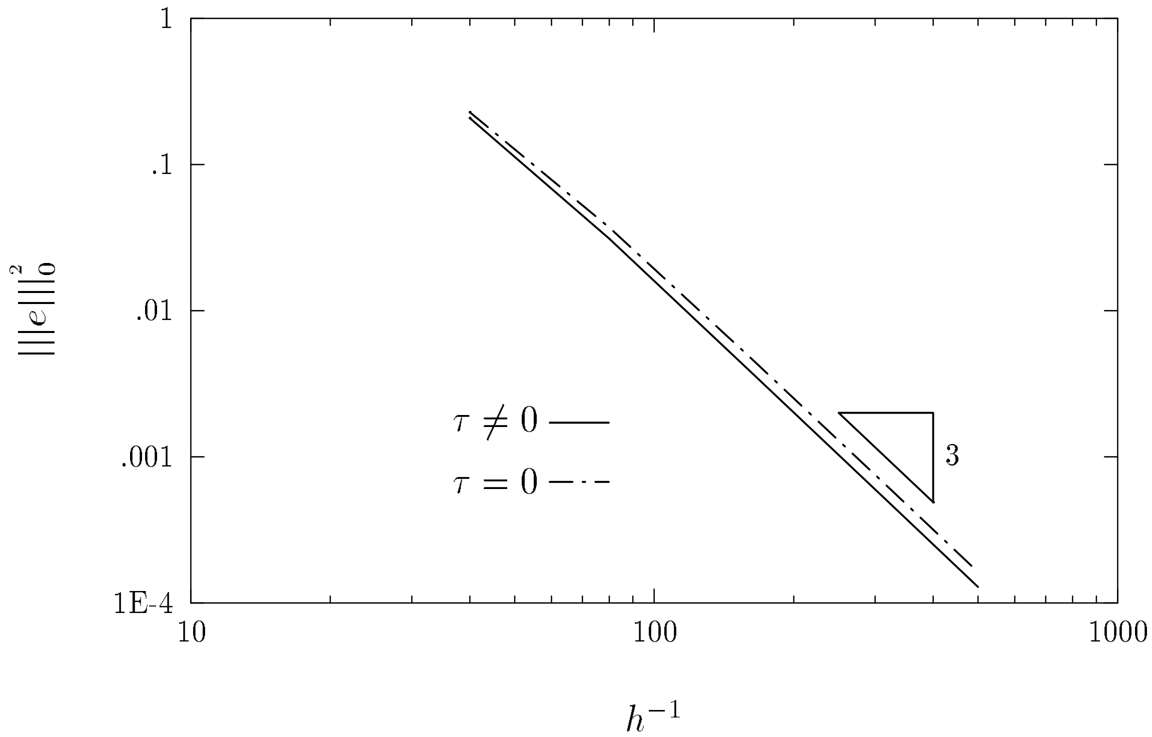

Figure 4.3: Convergence of the numerical error for different formulations employing the $Q2$ element and $C = 1$; h is the length of the element.

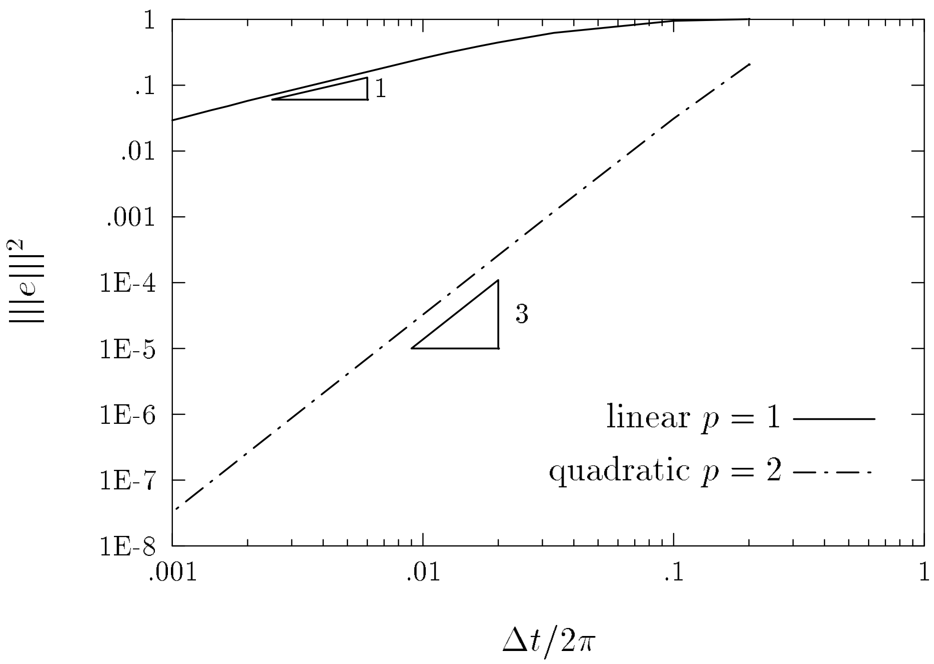

Figure 4.4: Temporal convergence for the time-discontinuous Galerkin formulation applied to a second-order ordinary differential equation in time: Convergence rates employing linear and quadratic interpolation functions.

$$
\begin{aligned}
&+ \sum_{n=1}^{N-1} \left\{ \dot{w}^h(t_n^+)[\![\dot{\phi}^h(t_n)]\!] + \omega^2 w^h(t_n^+)[\![\phi^h(t_n)]\!] \right\} \\
&+ \dot{w}^h(0^+)\dot{\phi}^h(0^+) + \omega^2 w^h(0^+)\phi^h(0^+)
\end{aligned}
\tag{4.92}
$$

The norm associated with (4.92) is defined by:

$$
\begin{aligned}
|||w^h|||^2 \;:=\; & \frac{1}{2}\,\dot{w}^h(T^-)^2 + \frac{1}{2}\,\dot{w}^h(0^+)^2 + \frac{1}{2}\sum_{n=1}^{N-1}[\![\dot{w}^h(t_n)]\!]^2 \\
+ \; & \frac{1}{2}\,w^h(T^-)^2 + \frac{1}{2}\,w^h(0^+)^2 + \frac{1}{2}\sum_{n=1}^{N-1}[\![w^h(t_n)]\!]^2
\end{aligned}
\tag{4.93}
$$

with the coercivity condition:

$$
B(w^h\,,\,w^h) = |||w^h|||^2 \tag{4.94}
$$

Consider the time discretization over the interval $I_n =]t_n\,,\,t_{n+1}[$, with interpolation order p:

$$\phi^h(t) = \sum_{a=1}^{p+1} N_a(t)\phi_a \qquad (4.95)$$

$$w^h(t) = \sum_{a=1}^{p+1} N_a(t)w_a \qquad (4.96)$$

In this expression, $\phi_1 = \phi^h(t_n^+)$ and $\phi_{p+1} = \phi^h(t_{n+1}^-)$ denote unknown discrete values associated with the end point nodes, while the values $\phi_2 \cdots \phi_p$ define a set of internal variables. Substituting these interpolations into (4.89) yields a system of coupled $(p+1)$ equations in $(p+1)$ unknowns $\{\phi_1\,,\, \phi_2 \cdots \phi_{p+1}\}$, which all depend on the solution at the previous time interval, i.e. $\phi^h(t_n^-)$ and $\dot{\phi}^h(t_n^-)$. The solution is obtained in sequence from one time interval to the next, data from the end of the previous time step are employed as initial conditions for the current time interval.

To study the temporal convergence, a numerical solution was obtained using a frequency of $\omega = 1$ and initial data $\phi_0 = 1$ and $\dot{\phi}_0 = 0$. The response was calculated using both linear $p = 1$, and quadratic $p = 2$, interpolation functions. The convergence rates are shown in Figure 4.4 for the time interval $t \in]0\,,\, 6\pi[$. Numerical errors, $e = \phi^h - \phi$, are measured in the natural norm emanating from the time-discontinuous variational equations, i.e. $|||e|||^2$. The slope of the curves indicate a convergence rate of the order $\mathcal{O}(\Delta t^{2p-1})$ as expected.

4.5 Error Estimates for the Coupled Problem

The convergence proof for the coupled fluid-structure problem follows the same basic steps as the uncoupled acoustics problem. As before, only the first-order non-reflecting boundary condition $\mathbb{S}_1$ will be considered. Let $\P\boldsymbol{\mathcal{X}}^h \in \mathcal{S}^h \times \mathcal{T}^h$ denote an interpolant of $\boldsymbol{\mathcal{X}} := \{\boldsymbol{u}\,,\, \phi\}$. Then the error $\boldsymbol{E} = \boldsymbol{\mathcal{X}}^h - \boldsymbol{\mathcal{X}}$, can be written as:

$$\boldsymbol{E} = \boldsymbol{E}^h + \boldsymbol{H} \qquad (4.97)$$

where

$$\boldsymbol{E}^h = (\boldsymbol{\mathcal{X}}^h - \P\boldsymbol{\mathcal{X}}^h) \in \mathcal{V}^h \times \mathcal{W}^h \qquad (4.98)$$

$$\boldsymbol{H} \;=\; \P\boldsymbol{\chi}^h - \boldsymbol{\chi} \quad \text{(interpolation error)} \tag{4.99}$$

In components,

$$\boldsymbol{E} \;=\; \{\boldsymbol{e}\,,\, e\} \tag{4.100}$$

$$\boldsymbol{E}^h \;=\; \{\boldsymbol{e}^h\,,\, e^h\} \tag{4.101}$$

$$\boldsymbol{H} \;=\; \{\boldsymbol{\eta}\,,\, \eta\} \tag{4.102}$$

where $\boldsymbol{e} = \boldsymbol{u}^h - \boldsymbol{u}$ and $e = \phi^h - \phi$. An appropriate space-time mesh parameter for the structural domain Ω_s is given by,

$$h_s = \max\{c_L\Delta t\,,\, \Delta x\} \tag{4.103}$$

where c_L is the dilatational wave speed and Δx and Δt are maximum element diameters in space and time, respectively. For the fluid domain Ω_f,

$$h_f = \max\{c\Delta t\,,\, \Delta x\} \tag{4.104}$$

where c is the acoustic wave speed.

Theorem 4.3 (Error Estimates for the Coupled Problem)
Assume τ and s satisfy the conditions given previously in (4.53) and (4.54). Similarly, assume $\boldsymbol{\tau}$ and $\boldsymbol{s}$ satisfy,

$$c_1 h_s \;\leq\; ||\boldsymbol{\tau}|| \;\leq\; c_2 h_s \tag{4.105}$$

$$c_3 \;\leq\; ||\boldsymbol{s}|| \;\leq\; c_4 \tag{4.106}$$

where c_1, c_2, c_3 and c_4 are positive constants ($c_2 > c_1$, $c_4 > c_3$). Assuming $\boldsymbol{\chi} \in (H^{k+1}(Q_s))^d \times H^{p+1}(Q_f)$, together with standard interpolation estimates for $\boldsymbol{H}$, then

$$|||\boldsymbol{E}|||^2 \;\leq\; c(\boldsymbol{u})\, h_s^{2k-1} \,+\, c(\phi)\, h_f^{2p-1} \tag{4.107}$$

where $c(\boldsymbol{u})$ and $c(\phi)$ are values that are independent of the mesh parameters.

Proof: The proof follows the same basic steps as Theorem 4.2:

$$
\begin{aligned}
|||\boldsymbol{E}^h|||^2 &= B^s_{GLS}(\boldsymbol{e}^h\,,\,\boldsymbol{E}^h)\;+\;B^f_{GLS}(e^h\,,\,\boldsymbol{E}^h) \qquad \text{(by Lemma 4.4)}\\
&= B^s_{GLS}(\boldsymbol{e}^h\,,\,\boldsymbol{E}-\boldsymbol{H})\;+\;B^f_{GLS}(e^h\,,\,\boldsymbol{E}-\boldsymbol{H}) \qquad \text{(by (4.97))}\\
&= -B^s_{GLS}(\boldsymbol{e}^h\,,\,\boldsymbol{H})\;-\;B^f_{GLS}(e^h\,,\,\boldsymbol{H}) \qquad \text{(by (4.16) and (4.17))}\\
&\le \Big|B^s_{GLS}(\boldsymbol{e}^h\,,\,\boldsymbol{H})\;+\;B^f_{GLS}(e^h\,,\,\boldsymbol{H})\Big|\\
&= \Big|E_s(\boldsymbol{e}^h\,,\,\boldsymbol{\eta})\;-\;A(\boldsymbol{e}^h\,,\,\eta\boldsymbol{n})\\
&\quad +\; E_f(e^h\,,\,\eta)\;+\;A(\boldsymbol{\eta}\,,\,e^h\boldsymbol{n})\;+\;E_r(e^h\,,\,\eta)\\
&\quad +\; \sum_{n=0}^{N-1}\Big\{(\mathcal{L}_s\boldsymbol{e}^h\,,\,\rho_s^{-1}\boldsymbol{\tau}\mathcal{L}_s\boldsymbol{\eta})_{\tilde{Q}^s_n}\\
&\quad +\; ([\![\boldsymbol{\sigma}(\nabla\boldsymbol{e}^h)(\boldsymbol{x})]\!]\cdot\boldsymbol{n}\,,\,\rho_s^{-1}\boldsymbol{s}[\![\boldsymbol{\sigma}(\nabla\boldsymbol{\eta})(\boldsymbol{x})]\!]\cdot\boldsymbol{n})_{(\tilde{\Upsilon}_s)_n}\\
&\quad +\; (\boldsymbol{\sigma}(\nabla\boldsymbol{e}^h)\cdot\boldsymbol{n}\,,\,\rho_s^{-1}\boldsymbol{s}\boldsymbol{\sigma}(\nabla\boldsymbol{\eta})\cdot\boldsymbol{n})_{(\Upsilon_\sigma)_n}\\
&\quad +\; (\mathcal{L}_1\boldsymbol{E}^h\,,\,\rho_s^{-1}\boldsymbol{s}\mathcal{L}_1\boldsymbol{H})_{(\Upsilon_i)_n}\\
&\quad +\; (\mathcal{L}_f e^h\,,\,c^2\tau\mathcal{L}_f\eta)_{\tilde{Q}^f_n}\;+\;(\mathcal{L}_r e^h\,,\,c^2 s\mathcal{L}_r\eta)_{(\tilde{\Upsilon}_\infty)_n}\\
&\quad +\; ([\![e^h_{,n}(\boldsymbol{x})]\!]\,,\,c^2 s[\![\eta_{,n}(\boldsymbol{x})]\!])_{\tilde{\Upsilon}^f_n}\;+\;(\mathcal{L}_2\boldsymbol{E}^h\,,\,c^2 s\mathcal{L}_2\boldsymbol{H})_{(\Upsilon_i)_n}\Big|\\
&\qquad\qquad \text{(by definition of } B^s_{GLS} \text{ and } B^f_{GLS})\\
&= \Big|\sum_{n=0}^{N-1}\Big\{-(\mathcal{L}_s\boldsymbol{e}^h\,,\,\dot{\boldsymbol{\eta}})_{\tilde{Q}^s_n}+(\mathcal{L}_s\boldsymbol{e}^h\,,\,\rho_s^{-1}\boldsymbol{\tau}\mathcal{L}_s\boldsymbol{\eta})_{\tilde{Q}^s_n}\\
&\quad -\; ([\![\boldsymbol{\sigma}(\nabla\boldsymbol{e}^h)(\boldsymbol{x})]\!]\cdot\boldsymbol{n}\,,\,\dot{\boldsymbol{\eta}})_{\tilde{\Upsilon}^s_n}\\
&\quad -\; (\boldsymbol{\sigma}(\nabla\boldsymbol{e}^h)\cdot\boldsymbol{n}\,,\,\dot{\boldsymbol{\eta}})_{(\Upsilon_\sigma)_n}\\
&\quad -\; (\mathcal{L}_1\boldsymbol{E}^h\,,\,\dot{\boldsymbol{\eta}})_{(\Upsilon_i)_n}\\
&\quad +\; ([\![\boldsymbol{\sigma}(\nabla\boldsymbol{e}^h)(\boldsymbol{x})]\!]\cdot\boldsymbol{n}\,,\,\rho_s^{-1}\boldsymbol{s}[\![\boldsymbol{\sigma}(\nabla\boldsymbol{\eta})(\boldsymbol{x})]\!]\cdot\boldsymbol{n})_{(\tilde{\Upsilon}_s)_n}
\end{aligned}
$$

$$
\begin{aligned}
&+ \quad (\boldsymbol{\sigma}(\nabla \boldsymbol{e}^h) \cdot \boldsymbol{n} \,,\, \rho_s^{-1} \boldsymbol{s} \boldsymbol{\sigma}(\nabla \boldsymbol{\eta}) \cdot \boldsymbol{n})_{(\Upsilon_\sigma)_n} \\
&+ \quad (\mathcal{L}_1 \boldsymbol{E}^h \,,\, \rho_s^{-1} \boldsymbol{s} \mathcal{L}_1 \boldsymbol{H})_{(\Upsilon_i)_n} \Big\} \\
&\quad\ \sum_{n=0}^{N-1} \Big\{ -(\mathcal{L}_f e^h \,,\, \dot{\eta})_{\tilde{Q}_n^f} + (\mathcal{L}_f e^h \,,\, c^2 \tau \mathcal{L}_f \eta)_{\tilde{Q}_n^f} \\
&- \quad (\mathcal{L}_r e^h \,,\, \dot{\eta})_{(\Upsilon_\infty)_n} + (\mathcal{L}_r e^h \,,\, c^2 s \mathcal{L}_r \eta)_{(\Upsilon_\infty)_n} + 2 d_1 (\dot{e}^h \,,\, \dot{\eta})_{(\Upsilon_\infty)_n} \\
&- \quad ([\![e^h_{,n}(\boldsymbol{x})]\!] \,,\, \dot{\eta})_{\tilde{\Upsilon}_n^f} - (\mathcal{L}_2 \boldsymbol{E}^h \,,\, \dot{\eta})_{(\Upsilon_i)_n} \\
&+ \quad ([\![e^h_{,n}(\boldsymbol{x})]\!] \,,\, c^2 s [\![\eta_{,n}(\boldsymbol{x})]\!])_{\tilde{\Upsilon}_n^f} + (\mathcal{L}_2 \boldsymbol{E}^h \,,\, c^2 s \mathcal{L}_2 \boldsymbol{H})_{(\Upsilon_i)_n} \Big\} \\
&+ \quad \sum_{n=1}^{N-1} \Big\{ -([\![\dot{\boldsymbol{e}}^h(t_n)]\!] \,,\, \rho_s \dot{\boldsymbol{\eta}}(t_n^-))_{\Omega_s} - a([\![\boldsymbol{e}^h(t_n)]\!] \,,\, \boldsymbol{\eta}(t_n^-))_{\Omega_s} \Big\} \\
&+ \quad (\dot{\boldsymbol{e}}^h(T^-) \,,\, \rho_s \dot{\boldsymbol{\eta}}(T^-))_{\Omega_s} + a(\boldsymbol{e}^h(T^-) \,,\, \boldsymbol{\eta}(T^-))_{\Omega_s} \\
&+ \quad \sum_{n=1}^{N-1} \Big\{ -([\![\dot{e}^h(t_n)]\!] \,,\, a^2 \dot{\eta}(t_n^-))_{\Omega_f} - ([\![\nabla e^h(t_n)]\!] \,,\, \nabla \eta(t_n^-))_{\Omega_f} \Big\} \\
&+ \quad (\dot{e}^h(T^-) \,,\, a^2 \dot{\eta}(T^-))_{\Omega_f} + (\nabla e^h(T^-) \,,\, \nabla \eta(T^-))_{\Omega_f} \\
&- \quad \sum_{n=1}^{N-1} d_0([\![e^h(t_n)]\!] \,,\, \eta(t_n^-))_{\Gamma_\infty} + d_0(e^h(T^-) \,,\, \eta(T^-))_{\Gamma_\infty} \Big|
\end{aligned}
$$

(by integration by parts)

$$
\leq \quad \frac{1}{2} |||\boldsymbol{E}^h|||^2 + c(\boldsymbol{u}) h_s^{2k-1} + c(\phi) h_f^{2p-1}
$$

The last lines follows from repeated use of (4.18) and standard interpolation estimates. Subsuming the terms involving $\boldsymbol{E}^h$ to the left-hand-side and from the triangle inequality and the interpolation estimates we have,

$$
|||\boldsymbol{E}|||^2 \quad \leq \quad 2|||\boldsymbol{E}^h|||^2 + 2|||\boldsymbol{H}|||^2 \quad \leq \quad c(\boldsymbol{u})\, h_s^{2k-1} + c(\phi)\, h_f^{2p-1} \tag{4.108}
$$

which completes the proof. □

This result indicates that the error for the coupled system is controlled by the convergence rates in both the structure and the fluid. In other words, for an accurate solution to the coupled fluid-structure problem, discretizations for both the structural domain and the fluid domain must be adequately resolved.

4.6 Two-Field Formulation

In Hughes and Hulbert [1988] an extension of the time-discontinuous Galerkin space-time formulation is given where independent interpolation functions are used for the solution and its time derivative, e.g. for elastodynamics, independent interpolations are used for the displacements and velocities. In this section the single-field formulation described earlier is extended to a two-field formulation incorporating second-order non-reflecting boundary conditions with independent velocity potential and pressure variables. In the following development, only the uncoupled acoustics problem is considered and the superscript indicating fluid terms is omitted for clarity, e.g. $Q_n^f = Q_n$.

The finite element interpolation functions for the two-field formulation are stated in terms of independent trial velocity potential $\phi^h = \phi_1^h$, and trial pressure $p^h = -\rho_0 \phi_2^h$, variables:

Trial velocity potential

$$\mathcal{T}_1^h = \left\{ \phi_1^h \middle| \phi_1^h \in C^0 (\bigcup_{n=0}^{N-1} Q_n) \, , \, \phi_1^h \big|_{Q_n^e} \in \mathcal{P}^k(Q_n^e) \right\}$$

Trial pressure

$$\mathcal{T}_2^h = \left\{ \phi_2^h \middle| \phi_2^h \in C^0 (\bigcup_{n=0}^{N-1} Q_n) \, , \, \phi_2^h \big|_{Q_n^e} \in \mathcal{P}^l(Q_n^e) \right\}$$

For the case of pure Neumann boundary conditions, the trial spaces and weighting spaces are the same, i.e. $\mathcal{T}_1^h = \mathcal{W}_1^h$ and $\mathcal{T}_2^h = \mathcal{W}_2^h$. The statement of the time-discontinuous Galerkn method for the two-field formulation is:

Find $\boldsymbol{U}^h := \{\phi_1^h \, , \, \phi_2^h\} \in \mathcal{T}_1^h \times \mathcal{T}_2^h$, such that $\forall \; \boldsymbol{W}^h := \{w_1^h \, , \, w_2^h\} \in \mathcal{W}_1^h \times \mathcal{W}_2^h$,

$$\boxed{B_n(\boldsymbol{W}^h \, , \boldsymbol{U}^h) = L_n(\boldsymbol{W}^h) \, , \qquad n = 0, 1, ..., N-1} \tag{4.109}$$

with the following definitions,

$$B_n(\boldsymbol{W}^h\,,\boldsymbol{U}^h) \;:=\; E_f(\boldsymbol{W}^h\,,\boldsymbol{U}^h)_n \,+\, E_r(\boldsymbol{W}^h\,,\boldsymbol{U}^h)_n \tag{4.110}$$

$$\begin{aligned} E_f(\boldsymbol{W}^h\,,\boldsymbol{U}^h)_n \;:=\; & (w_2^h\,,a^2\dot{\phi}_2^h)_{Q_n} + (\nabla w_2^h\,,\nabla\phi_1^h)_{Q_n} \\ & + (w_2^h(t_n^+)\,,a^2\,\phi_2^h(t_n^+))_\Omega + (\nabla w_1^h(t_n^+)\,,\nabla\phi_1^h(t_n^+))_\Omega \\ & + (\nabla w_1^h\,,\nabla\mathcal{L}\boldsymbol{U}^h)_{Q_n} \end{aligned} \tag{4.111}$$

$$\begin{aligned} E_r(\boldsymbol{W}^h\,,\boldsymbol{U}^h)_n \;:=\; & d_2(w_2^h\,,\dot{\phi}_2^h)_{(\Upsilon_\infty)_n} + d_1(w_2^h\,,\phi_2^h)_{(\Upsilon_\infty)_n} + d_0(w_2^h\,,\phi_1^h)_{(\Upsilon_\infty)_n} \\ & + d_2(w_2^h(t_n^+)\,,\phi_2^h(t_n^+))_{\Gamma_\infty} + d_0(w_1^h(t_n^+)\,,\phi_1^h(t_n^+))_{\Gamma_\infty} \\ & + d_0(w_1^h\,,\mathcal{L}\boldsymbol{U}^h)_{(\Upsilon_\infty)_n} \end{aligned} \tag{4.112}$$

$$\begin{aligned} L_n(\boldsymbol{W}^h) \;:=\; & (w_2^h\,,f)_{Q_n} \\ & + (w_2^h(t_n^+)\,,a^2\,\phi_2^h(t_n^-))_\Omega + (\nabla w_1^h(t_n^+)\,,\nabla\phi_1^h(t_n^-))_\Omega \\ & + d_2(w_2^h(t_n^+)\,,\phi_2^h(t_n^-))_{\Gamma_\infty} + d_0(w_1^h(t_n^+)\,,\phi_1^h(t_n^-))_{\Gamma_\infty} \end{aligned} \tag{4.113}$$

in which,

$$\boxed{\mathcal{L}\boldsymbol{U}^h \;=\; \dot{\phi}_1^h - \phi_2^h} \tag{4.114}$$

In this formulation the pressures, i.e. $p^h = -\rho_0\phi_2^h$, and velocity potentials, i.e. $\phi^h = \phi_1^h$ are governed by independent interpolations. If we select the pressure space such that, $\mathcal{L}\boldsymbol{U}^h = \dot{\phi}_1^h - \phi_2 = 0$, then the formulation specializes to the single-field formulation presented in Chapter 3.

Since the proofs for stability of the two-field formulation follow nearly identical steps as those used for the single-field formulation, results are presented without proof.

Summing (4.109) over the time slabs we obtain,

$$\boxed{B(\boldsymbol{W}^h\,,\boldsymbol{U}^h) \quad = \quad L(\boldsymbol{W}^h)} \tag{4.115}$$

where

$$\begin{aligned}
B(\boldsymbol{W}^h\,,\boldsymbol{U}^h) \quad = \quad & \sum_{n=0}^{N-1}(w_2^h\,,\,a^2\dot{\phi}_2^h)_{Q_n} \\
+ \quad & \sum_{n=1}^{N-1}(w_2^h(t_n^+)\,,\,a^2\,[\![\phi_2^h(t_n)]\!])_\Omega \,+\, (w_2^h(0^+)\,,\,a^2\,\phi_2^h(0^+))_\Omega \\
+ \quad & \sum_{n=0}^{N-1}\Big\{(\nabla w_2^h\,,\,\nabla\phi_1^h)_{Q_n} \,+\, (\nabla w_1^h\,,\,\nabla\boldsymbol{\mathcal{L}}\boldsymbol{U}^h)_{Q_n}\Big\} \\
+ \quad & \sum_{n=1}^{N-1}(\nabla w_1^h(t_n^+)\,,\,[\![\nabla\phi_1^h(t_n)]\!])_\Omega \,+\, (\nabla w_1^h(0^+)\,,\,\nabla\phi_1^h(0^+))_\Omega \\
+ \quad & \sum_{n=0}^{N-1} d_2(w_2^h\,,\,\dot{\phi}_2^h)_{(\Upsilon_\infty)_n} \\
+ \quad & \sum_{n=1}^{N-1} d_2(w_2^h(t_n^+)\,,\,[\![\phi_2^h(t_n)]\!])_{\Gamma_\infty} \,+\, d_2(w_2^h(0^+)\,,\,\phi_2^h(0^+))_{\Gamma_\infty} \qquad (4.116) \\
+ \quad & \sum_{n=0}^{N-1}\Big\{d_0(w_2^h\,,\,\phi_1^h)_{(\Upsilon_\infty)_n} \,+\, d_0(w_1^h\,,\,\boldsymbol{\mathcal{L}}\boldsymbol{U}^h)_{(\Upsilon_\infty)_n}\Big\} \\
+ \quad & \sum_{n=1}^{N-1} d_0(w_1^h(t_n^+)\,,\,[\![\phi_1^h(t_n)]\!])_{\Gamma_\infty} \,+\, d_0(w_1^h(0^+)\,,\,\phi_1^h(0^+))_{\Gamma_\infty} \\
+ \quad & \sum_{n=0}^{N-1} d_1(w_2^h\,,\,\phi_2^h)_{(\Upsilon_\infty)_n} \qquad (4.117)
\end{aligned}$$

with

$$\begin{aligned}
L(\boldsymbol{W}^h) \quad = \quad & \sum_{n=0}^{N-1}(w_2^h\,,\,f)_{Q_n} \\
+ \quad & (w_2^h(0^+)\,,\,a^2\,\dot{\phi}_0)_\Omega \,+\, (\nabla w_1^h(0^+)\,,\,\nabla\phi_0)_\Omega
\end{aligned} \tag{4.118}$$

The norm associated with (4.115) is defined by:

$$
\begin{aligned}
|||\boldsymbol{W}^h|||^2 \quad := \quad & \mathcal{E}_f(\boldsymbol{W}^h(0^+)) + \sum_{n=1}^{N-1} \mathcal{E}_f([\![\boldsymbol{W}^h(t_n)]\!]) + \mathcal{E}_f(\boldsymbol{W}^h(T^-)) \\
+ \quad & \mathcal{E}_r(\boldsymbol{W}^h(0^+)) + \sum_{n=1}^{N-1} \mathcal{E}_r([\![\boldsymbol{W}^h(t_n)]\!]) + \mathcal{E}_r(\boldsymbol{W}^h(T^-)) \\
+ \quad & \sum_{n=0}^{N-1} d_1(w_2^h\, , \, w_2^h)_{(\Upsilon_\infty)_n}
\end{aligned}
\tag{4.119}
$$

where

$$
\begin{aligned}
\mathcal{E}_f(\boldsymbol{W}^h) \quad &= \quad \frac{1}{2}\, ||a w_2^h||_\Omega^2 + \frac{1}{2}\, ||\nabla w_1^h||_\Omega^2 \\
\mathcal{E}_r(\boldsymbol{W}^h) \quad &= \quad \frac{1}{2}\, d_2(w_2^h\, , \, w_2^h)_{\Gamma_\infty} + \frac{1}{2}\, d_0(w_1^h\, , \, w_1^h)_{\Gamma_\infty}
\end{aligned}
\tag{4.120}
$$

The coercivity condition is:

$$
B(\boldsymbol{W}^h\, , \, \boldsymbol{W}^h) = |||\boldsymbol{W}^h|||^2 \tag{4.121}
$$

For additional stability GLS terms can be appended to (4.109). Convergence proofs for the two-field formulation follow closely the same steps as the proofs for the the single-field formulation. Detailed proofs for the interior problem using the two-field formulation can be found in Hughes and Hulbert [1988]. A two-field formulation for the coupled fluid-structure problem is obtained from a combination of the exterior acoustics variational equation (4.109) and the structural variational equation in Hughes and Hulbert [1988], together with consistent coupling of the interface boundary conditions on Γ_i. Details will be given in a follow-up article to Thompson and Pinsky [1993e].

Chapter 5

Design of Time-Dependent Non-Reflecting Boundary Conditions: The Three-Dimensional Case

As discussed in the introduction to this thesis, numerical methods for solution of the exterior structural acoustics problem may be characterized in terms of the local (differential) or non-local (integral) spatial and temporal operators appearing in the formulation, see Table 5.1. An example of a nonlocal representation for the infinite fluid is the direct time-integration of Kirchhoff's retarded potential boundary integral, see e.g. Mansur and Brebbia [1984], Neilson et al. [1981]. This method leads to unsymmetric and dense matrices and, more importantly, can be extremely memory intensive, typically requiring storage of a large pool of historical data during the solution process. The direct convolution of the DtN map Givoli [1988] is also nonlocal in space and time, requiring convolution over all past time up to the current solution.

Because of the limitations and difficulties noted above there is a need for the development of local in time non-reflecting (absorbing) boundary conditions which eliminate or minimize reflection of outgoing waves and that also preserve the data structure of the finite element method. If accurate non-reflecting boundary conditions are used, then the fluid truncation boundary can be moved closer to the structure.

Table 5.1: Computational methods for representation of unbounded media: Summary of characteristics in terms of applicability (Y) or non-applicability (N) to transient and time-harmonic analysis, and in terms of the local (Y) or nonlocal (N) character of the spatial and temporal dependence.

Methods based on exact representations	Harmonic Analysis	Transient Analysis	Local in Space	Local in Time
Boundary element method	Y	Y	N	N
Dirichlet-to-Neumann map	Y	Y	N	N
Methods based on approximate representations	**Harmonic Analysis**	**Transient Analysis**	**Local in Space**	**Local in Time**
Plane-wave damper	Y	Y	Y	Y
DAA	Y	Y	N	Y
Infinite elements	Y	N	Y	–
Higher-order NRBC	Y	Y	Y	Y

In this case the finite element model will be able to use fewer fluid elements and considerable cost savings will result. Approximate non-reflecting boundary conditions that are local in time (i.e. differential operators in time) have been proposed by several authors. As discussed earlier in Chapter 2, the simplest possible boundary condition takes the form of the Sommerfeld radiation condition at infinity (2.24), repeated here as,

$$\frac{\partial \phi}{\partial n} = -\mathbb{S}_0 \phi, \qquad \text{where} \quad \mathbb{S}_0 := \frac{1}{c}\frac{\partial}{\partial t} \tag{5.1}$$

As noted this operator is sometimes referred to as the 'plane-wave' (PW) damper. The term damper is used to indicate that the operator takes the form of a local 'dashpot' applied to the fluid truncation boundary which absorbs energy leaving the system. The PW-damper was first used by Mindlin and Bleich [1953] to study the response of an elastic shell to a transient shock wave, and later in the context of the semidiscrete finite element method by Zienkewicz [1969,1977]. It can be shown that this simple boundary condition is exact in one-dimension, however in multi-dimensions the performance is known to deteriorate significantly as the position of the artificial boundary approaches the source of radiation, especially in the low-frequency (long wavelength) limit, where the virtual mass (or added mass) approximation of incompressibility is more appropriate, Chertock [1970] .

The doubly asymptotic approximation (DAA) on the other hand, is asymptotically exact in the high-frequency and low-frequency limits and through a consistent matching approximates the exact impedance throughout the intermediate frequency range, GEERS [1971,1978]. The DAA operator essentially matches the local in time PW-damper in the high-frequency limit to the non-local boundary integral representation of the Laplacian operator in the low-frequency limit. A family of DAA's has been derived by the method of matched asymptotic expansions in FELIPPA [1980], and NICOLAS [1989]; though successful implementation to large-scale transient computations involving complex structures seems to be limited to the first member of that family only NEILSON [1981], FELIPPA [1984] and RUZICKA [1989]. As the low-order DAA has difficulty accurately capturing the response over a large range of middle frequencies for complex systems, there is strong motivation to obtain improved non-reflecting boundary conditions that are local in time, and yield highly accurate solutions over a wide range of important frequencies.

High-order accurate non-reflecting boundary conditions that are local in time have been proposed by several authors; complete surveys can be found in GIVOLI [1991] and ABBOUD [1990]. Here we mention the well-known sequence of boundary conditions derived by ENGQUIST AND MAJDA [1977,1979]. In this approach operators of increasing order are obtained using rational approximations to a pseudo-differential operator in the frequency domain. Time-dependent boundary conditions are obtained through an inverse Fourier transform. BAYLISS AND TURKEL [1980,1982], introduced an alternative sequence of local boundary operators derived from a power series (multipole) expansion of the exact solution in negative powers of the radial distance from the source.

In this chapter, new time-dependent non-reflecting boundary conditions are developed for the wave equation in three-dimensions. Two alternative sequences of radiation boundary operators are derived; the first involves both time and spatial derivatives (local in time and local in space version), and the second involves time derivatives yet retains a spatial integral (local in time and nonlocal in space version). The local in time and local in space version starts from the exact localization of the nonlocal impedance relation (DtN map) in the frequency domain (GIVOLI AND KELLER [1990], HARARI [1991a]). Time-dependent boundary conditions are then obtained through the application of an inverse Fourier transform, see Figure 5.1 for

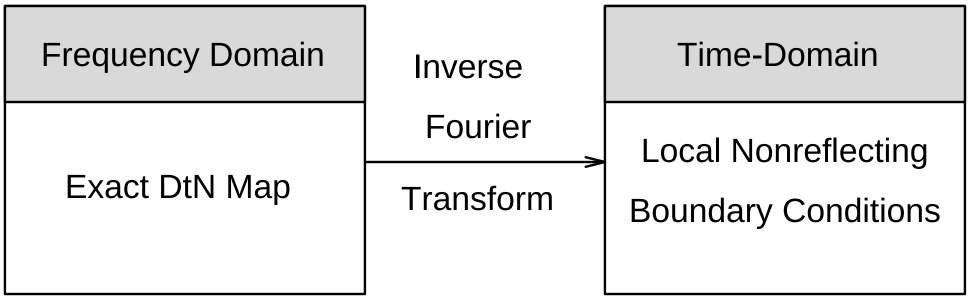

Figure 5.1: Schematic for the development of non-reflecting boundary conditions. Starting in the frequency domain with the exact Dirichlet-to-Neumann (DtN) impedance relation, an inverse Fourier transform is used to obtain the exact local time-dependent counterpart.

a schematic of the procedure. Since these time-dependent boundary conditions follow directly from the exact impedance expressed through the DtN map, the first N operators in this new sequence exactly represent the first N spherical wave harmonics for outgoing waves. In contrast to nonlocal boundary conditions, the proposed local boundary conditions preserve the data structure of the finite element method and require only local storage of historical data during the solution process. In addition, we show that an inverse Fourier transform exists for the frequency dependent Dirichlet-to-Neumann (DtN) map Keller and Givoli [1989], allowing for boundary conditions that are nonlocal in space yet retain the important property of locality in time. The non-reflecting boundary conditions developed in this Chapter are implemented as natural boundary conditions in the time-discontinuous GLS formulation, i.e. they are weakly enforced in both space and time.

5.1 Dirichlet-to-Neumann Map in the Frequency Domain

In order to obtain a sequence of time-dependent non-reflecting boundary conditions which are exact for the first N spherical wave harmonics on the truncation boundary Γ_∞, we start with the Dirichlet-to-Neumann (DtN) map in the frequency domain. The DtN map represents the exact impedance for the infinite acoustic fluid restricted

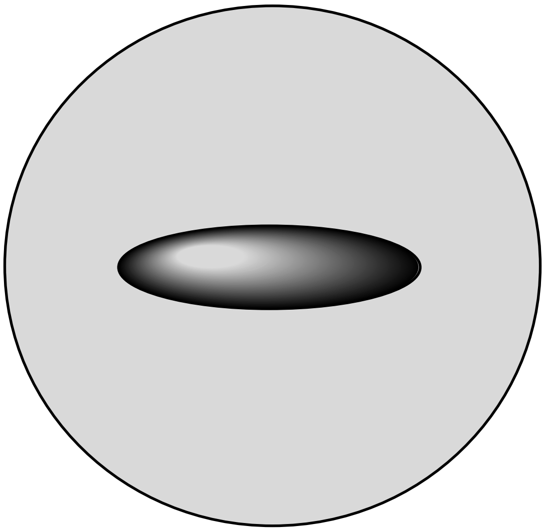

Figure 5.2: Illustration of a finite computational domain enclosed by a spherical artificial boundary of radius R.

to an artificial boundary of separable geometry, e.g. a sphere of radius $r = R$ in $\mathbb{R}^3$, see Figure 5.2. Assuming harmonic time dependence $e^{-i\omega t}$, with frequency $\omega > 0$, the exact non-local Dirichlet-to-Neumann (DtN) boundary condition in the frequency domain can be expressed in terms of an infinite series of spherical wave harmonics, see e.g. Keller and Givoli [1989]:

$$\boxed{\frac{\partial \phi}{\partial n}(R, \theta, \varphi) = \sum_{n=0}^{\infty} z_n \int_{\Gamma_\infty} s_n(\theta, \varphi, \theta', \varphi') \; \phi(R, \theta', \varphi') \; d\Gamma'} \tag{5.2}$$

where the DtN kernels $s_n, \; n = 0, 1, 2, \cdots$ are given by,

$$s_n = \sum_{j=0}^{n}{}' \alpha_{nj} P_n^j(\cos\varphi) P_n^j(\cos\varphi') \cos j(\theta - \theta') \tag{5.3}$$

$$\alpha_{nj} = \frac{(2n+1)(n-j)!}{2\pi R^2 (n+j)!} \tag{5.4}$$

with impedance coefficients,

$$z_n(kR) = \frac{k h_n'(kR)}{h_n(kR)} \tag{5.5}$$

In the above, $k = \omega/c$ is the acoustic wavenumber, $0 \leq \theta < 2\pi$ is the circumferential angle and $0 \leq \varphi < \pi$ is the polar angle for a spherical truncation boundary of radius $r = R$. The differential surface area is $d\Gamma = R^2 \sin\varphi d\theta d\varphi$, P_n^j are associated Legendre functions of the first kind, and h_n are spherical Hankel function of the first kind of order n. The prime on h_n indicates differentiation with respect to its argument, and the prime after the sum indicates that a factor of $1/2$ multiplies the term with $j = 0$. The boundary condition (5.2) can be written in operator form as,

$$\frac{\partial \phi}{\partial n} = -\mathbb{S}\ \phi \qquad \text{on} \ \ \Gamma_\infty \tag{5.6}$$

relating Dirichlet data, ϕ, to Neumann data, $\partial\phi/\partial n$, through the linear mapping $\mathbb{S} : \phi \mapsto \partial\phi/\partial n$. This operator represents the exact impedance of the exterior domain restricted to Γ_∞. The DtN map $\mathbb{S}$, is an integral operator resulting in a nonlocal boundary condition coupling all points on the artificial boundary Γ_∞. When implemented in a finite element method, the matrices emanating from the discretization of this nonlocal boundary condition are fully populated and dense.

Direct time-convolution of the DtN map

The direct time convolution of the DtN map $\mathbb{S}$, is discussed in Givoli [1988] and can be expressed in operator form as,

$$\frac{\partial \phi}{\partial n}(\boldsymbol{x}\,,\,t) = \int_0^t \int_{\Gamma_\infty} s(\boldsymbol{x}\,,\,\boldsymbol{x}'\,,\,t-\tau)\ \phi(\boldsymbol{x}'\,,\,\tau)\ d\Gamma'\ d\tau \tag{5.7}$$

This equation denotes a functional of the values of $\phi(\boldsymbol{x}'\,,\,\tau)$ for $\boldsymbol{x}'$ ranging over Γ_∞ and τ ranging from 0 to t, and expresses both spatial and temporal nonlocality. In other words, the convoluted DtN condition (5.7) indicates that at a given instant in time, the response at every point on the artificial boundary Γ_∞ is coupled with the time histories of all the other points on Γ_∞. Because this boundary condition involves a temporal integral over all past time, numerical solutions can be extremely memory-intensive, typically requiring storage of a large pool of historical data for typical solution times.

5.2 New Exact Time-Dependent Boundary Conditions

In order to circumvent the difficulty of having to solve a temporal convolution integral, two new sequences of time-dependent boundary conditions are derived in this section which replace the temporal integral with local temporal derivatives. This allows for the numerical solution to proceed in succession from one time step to the next with only local storage of data from the previous time step required. Two alternative sequences are derived; the first involves both time and spatial derivatives (local in time and local in space version), and the second involves time derivatives yet retains the spatial integral of the DtN map (local in time and nonlocal in space version).

To obtain exact time-dependent counterparts to the DtN map (5.2) which are local in time, use is made of the special property of spherical Hankel functions which can be represented as the finite series, (Graff [1975]):

$$h_n(kR) = h_0(kR)\left[(-i)^n \sum_{j=0}^{n} \frac{(n+j)!}{j!(n-j)} \left(\frac{-1}{2ikR}\right)^j\right], \quad n = 0, 1, 2, \cdots \tag{5.8}$$

Note that the zero order term $h_0 = \mathrm{e}^{ikR}/(ikR)$ can be taken outside the summation, and this series involves only inverse powers of the nondimensional wavenumber (ikR). As a result, simplified expressions can always be obtained for any order in terms of powers of $(ik)^j$, from which time-dependent counterparts are readily obtained from an inverse Fourier transform. In Chapter 6 it will be shown that a finite series representation for the non-half integer Hankel functions appearing in the two-dimensional case is not possible, and an alternative approach will then be necessary.

5.2.1 Local in time and local in space version

The goal of this section is to derive a sequence of non-reflecting boundary conditions that are local in both time and space, yet retain the desirable property of being exact for the first N outgoing spherical wave harmonics. We thus seek to replace the space-time convolution integral in (5.7) with local temporal and spatial derivatives.

Localization of the DtN map

In Givoli and Keller [1990], a spatially local counterpart to the non-local DtN map $\mathbb{S}$ defined in (5.2), is obtained in the frequency domain. These local boundary conditions inherit the property that they are exact for the first N wave harmonics. The operators were originally proposed for the two-dimensional case, and later extended to three-dimensions in Harari [1991a]. The procedure for constructing these local boundary conditions in the frequency domain is summarized herein. We start by expressing the first N spherical wave harmonics in the truncated DtN map (5.2), in the alternative form,

$$\frac{\partial \phi}{\partial n}(R,\theta,\varphi) = \sum_{n=0}^{N-1} z_n \sum_{j=0}^{n}{}' P_n^j(\cos\varphi)(A_{nj}\cos j\theta + B_{nj}\sin j\theta) \tag{5.9}$$

where the coefficients A_{nj} and B_{nj} involve nonlocal spatial integrals over the artificial boundary. Expressing the solution restricted to Γ_∞, as a finite series of spherical surface harmonics,

$$\phi(R,\theta,\varphi) = \sum_{n=0}^{N-1} \sum_{j=0}^{n}{}' P_n^j(\cos\varphi)(A_{nj}\cos j\theta + B_{nj}\sin j\theta) \tag{5.10}$$

and differentiating with respect to the Laplace-Beltrami operator,

$$\boxed{\Delta_\Gamma \phi := \frac{1}{\sin\varphi}\frac{\partial}{\partial\varphi}\left(\sin\varphi\frac{\partial\phi}{\partial\varphi}\right) + \frac{1}{\sin^2\varphi}\frac{\partial^2\phi}{\partial\theta^2}} \tag{5.11}$$

to the mth power yields,

$$(-\Delta_\Gamma)^m \phi(R,\theta,\varphi) = \sum_{n=0}^{N-1} (n(n+1))^m \sum_{j=0}^{n}{}' P_n^j(\cos\varphi)(A_{nj}\cos j\theta + B_{nj}\sin j\theta) \tag{5.12}$$

Comparing (5.9) and (5.12) suggests expressing the impedance as the finite sum,

$$z_n = \sum_{m=0}^{N-1} (n(n+1))^m \beta_m, \qquad n = 0,1,\cdots,N-1 \tag{5.13}$$

where β_m are obtained by solving this $N \times N$ linear algebraic system. Substituting this expansion into (5.9) and using (5.12), the nonlocal spatial integrals embedded in the coefficients A_{nj} and B_{nj} are replaced with local high-order tangential derivatives $(\Delta_\Gamma)^m$, and the following sequence of local boundary conditions are obtained:

$$\boxed{\frac{\partial \phi}{\partial n} \quad = \quad \sum_{m=0}^{N-1} \beta_m (-\Delta_\Gamma)^m \phi \qquad \text{on} \;\; \Gamma_\infty} \tag{5.14}$$

Since the sequence defined in (5.14) follows directly from the truncated DtN map, the resulting radiation boundary operators are exact for waves consisting of the first N spherical harmonics. In this case, the nonlocal spatial integral has been replaced by a linear map expressed in terms of the differential operator $(\Delta_\Gamma)^m$. For further details see HARARI [1991a]. To obtain the exact time-dependent counterpart to the localized DtN non-reflecting boundary condition (5.14) defined in the frequency domain, use is made of the finite series expansion for spherical Hankel functions given in (5.8). Local in time counterparts are obtained through an inverse Fourier transform. The procedure is explicated by deriving the first three operators in the sequence.

First-order boundary condition

Consider the first operator in the sequence corresponding to $N = 1$; then (5.13) reduces to the simple result $z_0(kR) = \beta_0(kR)$, and the local DtN condition (5.14) specializes to,

$$\frac{\partial \phi}{\partial n} \quad = \quad \frac{k h_0'(kR)}{h_0(kR)} \phi \tag{5.15}$$

For clarity, set $h_n := h_n(kR)$, and use the relations,

$$h_0' = -h_1 \qquad \text{and} \qquad h_1 = \left(\frac{1}{kR} - i \right) \; h_0 \tag{5.16}$$

to obtain a simplified expression for (5.15):

$$\frac{\partial \phi}{\partial n} \quad = \quad \left(ik - \frac{1}{R} \right) \phi \tag{5.17}$$

The time-dependent counterpart to (5.17) is obtained by direct application of the inverse Fourier transform:

$$\phi(\boldsymbol{x}\,,\,t) := \frac{1}{\sqrt{2\pi}} \int_{-\infty}^{\infty} \phi(\boldsymbol{x}\,,\,\omega) e^{-i\omega t}\; d\omega \tag{5.18}$$

In effect, replacing every occurrence of the operator $-ik$ by $\frac{1}{c}\frac{\partial}{\partial t}$ with the result,

$$\boxed{\mathbb{B}_1 \phi := \frac{\partial \phi}{\partial n} + \frac{1}{R}\phi + \frac{1}{c}\dot{\phi} = 0} \tag{5.19}$$

This condition is perfectly absorbing for axially symmetric spherical waves (outgoing wave harmonic $n = 0$).

Second-order boundary condition

For $N = 2$, the system (5.13) yields, $\beta_0 = z_0$ and $\beta_1 = (z_1 - z_0)/2$, so that (5.14) becomes,

$$\frac{\partial \phi}{\partial n} = z_0 \phi + \frac{1}{2}(z_0 - z_1)\Delta_\Gamma \phi \tag{5.20}$$

Clearing the common denominator $h_0 h_1$ we obtain,

$$h_0 h_1 \frac{\partial \phi}{\partial n} = (k h_0' h_1)\phi + \frac{k}{2}(h_0' h_1 - h_1' h_0)\Delta_\Gamma \phi \tag{5.21}$$

Using the recurrence relation,

$$h_n' = h_{n-1} - \left(\frac{n+1}{kR}\right) h_n\,, \qquad n = 1, 2, \cdots \tag{5.22}$$

in conjunction with the starting functions defined in (5.16), and after some algebraic manipulation, we obtain the simplified form,

$$\left(\frac{1}{R} - ik\right)\frac{\partial \phi}{\partial n} \quad = \quad \left(k^2 + \frac{2ik}{R} - \frac{1}{R^2}\right)\phi + \frac{1}{2R^2}\Delta_\Gamma \phi \tag{5.23}$$

Since this expression involves only terms in powers of $(ik)^j$, the inverse Fourier transform is readily obtained with the desired result,

$$\boxed{\mathbb{B}_2\phi := \frac{\partial\phi}{\partial n} + \frac{R}{c}\frac{\partial\dot{\phi}}{\partial n} + \frac{R}{c^2}\ddot{\phi} + \frac{2}{c}\dot{\phi} + \frac{1}{R}\phi - \frac{1}{2R}\Delta_\Gamma\phi = 0} \tag{5.24}$$

This higher-order accurate local boundary condition is perfectly absorbing for the first two spherical wave harmonics of orders $n = 0$ and $n = 1$.

Third-order boundary condition

For $N = 3$, (5.14) becomes,

$$\frac{\partial\phi}{\partial n} = \beta_0\phi - \beta_1\Delta_\Gamma\phi + \beta_2(\Delta_\Gamma)^2\phi \tag{5.25}$$

and the system (5.13) yields the three coefficients,

$$\begin{aligned}
\beta_0 &= z_0 \\
\beta_1 &= (18z_1 - 16z_0 - 2z_2)/24 \\
\beta_2 &= (2z_0 + z_2 - 3z_1)/24
\end{aligned}$$

Using the recurrence relation (5.22), and

$$h_{n+1} = \frac{(2n+1)}{kR}h_n - h_{n-1}\,, \qquad n = 1, 2, \cdots \tag{5.26}$$

in conjunction with the starting functions defined in (5.16), or equivalently (5.8), we obtain the simplified form,

$$\gamma_0\phi_{,n} \;=\; \gamma_1\phi + \gamma_2\Delta_\Gamma\phi + \gamma_3(\Delta_\Gamma)^2\phi \tag{5.27}$$

where the frequency dependent coefficients are

$$\gamma_0 \;=\; 1 - 2ikR - 4(kR)^2/3 + i(kR)^3/3$$

$$
\begin{aligned}
\gamma_1 &= -1/R + 3ik + 10k^2R/3 - 5ik^3R^2/3 - k^4R^3/3 \\
\gamma_2 &= 7/(12R) - ik/2 - k^2R/6 \\
\gamma_2 &= 1/(24R)
\end{aligned}
$$

Since (5.27) involves only terms in powers of $(ik)^j$, the inverse Fourier transform is readily obtained with the desired result,

$$
\begin{aligned}
\mathbb{B}_3\phi \;:=\; & \phi_{,n} + \frac{2R}{c}\phi_{,nt} + \frac{4R^2}{3c^2}\phi_{,ntt} + \frac{R^3}{c^3}\phi_{,nttt} \\
& + \frac{1}{R}\phi + \frac{3}{c}\phi_{,t} + \frac{10R}{3c^2}\phi_{,tt} + \frac{5R^2}{3c^3}\phi_{,ttt} + \frac{R^3}{3c^4}\phi_{,tttt} \\
& - \frac{7}{12R}\Delta_\Gamma\phi - \frac{1}{2c}\Delta_\Gamma\phi_{,t} - \frac{R}{6c^2}\Delta_\Gamma\phi_{,tt} - \frac{1}{24R}(\Delta_\Gamma)^2\phi = 0
\end{aligned}
\tag{5.28}
$$

In this expression an inferior comma denotes differentiation. This higher-order accurate local boundary condition is perfectly absorbing for the first three spherical wave harmonics of orders $n = 0, 1$ and $n = 2$. Expressions for the exact time-dependent local boundary conditions for higher-order modes $N = 4, 5, \cdots$, are obtained using the same procedure as indicated for $N = 1, 2, 3$.

5.2.2 Finite element implementation

Defining the linear operator $\mathbb{S}_m$ as,

$$
\mathbb{B}_m(\phi) := \frac{\partial\phi}{\partial n} + \mathbb{S}_m(\phi) \tag{5.29}
$$

which implies

$$
\frac{\partial\phi}{\partial n} = -\mathbb{S}_m\phi \qquad \text{on } \Gamma_\infty \tag{5.30}
$$

we obtain boundary conditions expressed in the form of (3.25) relating Dirchlet-to-Neumann data through local differential operators. For example, the first three local operators $\mathbb{S}_m$ for m equal to 1,2 and 3 are:

$$
\mathbb{S}_1\phi = \frac{1}{R}\phi + \frac{1}{c}\phi_{,t} \tag{5.31}
$$

$$\mathbb{S}_2\phi = \frac{1}{2R}(2-\Delta_\Gamma)\phi + \frac{1}{c}\left(2 + R\frac{\partial}{\partial r}\right)\phi_{,t} + \frac{R}{c^2}\phi_{,tt} \tag{5.32}$$

$$\begin{aligned} \mathbb{S}_3\phi &= \frac{1}{24R}(24 - 14\Delta_\Gamma - (\Delta_\Gamma)^2)\phi + \frac{1}{2c}\left(6 - \Delta_\Gamma + 4R\frac{\partial}{\partial r}\right)\phi_{,t} \\ &+ \frac{R}{6c^2}\left(20 - \Delta_\Gamma + 8R\frac{\partial}{\partial r}\right)\phi_{,tt} + \frac{R^2}{3c^3}\left(5 + 3R\frac{\partial}{\partial r}\right)\phi_{,ttt} + \frac{R^3}{3c^4}\phi_{,tttt} \end{aligned} \tag{5.33}$$

This sequence of local time-dependent boundary conditions provide increasing accuracy with order N which, however, is also a measure of the difficulty of implementation. In general, the Nth-order condition contains all the even tangential and temporal derivatives up to order $2(N-1)$. For example, for the case $N = 2$, the local time-dependent operator (5.32) contains second-order tangential derivatives embedded in the Laplace-Beltrami operator Δ_Γ and second-order time derivatives. Similarly, for $N = 3$, the local operator (5.33) contains fourth-order tangential derivatives and fourth-order temporal derivatives. As a result of the higher-order time derivatives, these boundary operators become increasingly difficult to implement in a semidiscrete finite element formulation using standard time-integrators such as the Newmark family. A distinct advantage of the time-discontinuous space-time formulation is that it allows the solution at time t_n to be discontinuous across space-time slabs on the truncation boundary $(\Upsilon_\infty)_n := \Gamma_\infty \times I_n$. As a result, standard C^0 continuous finite element interpolation functions in the temporal variable may be used up to the order dictated by the time-derivatives appearing in the boundary operator. For example, for $N = 2$, standard C^0 quadratic Lagrangian interpolation functions can be used to represent the second-order time derivative appearing in (5.32). For this, standard C^0 interpolations can also be used to represent the tangential derivates appearing in the Laplace-Beltrami operator after integrating by parts on Γ_∞.

The sequence of boundary operators defined in (5.31) through (5.33) are incorporated into the space-time finite element formulation as natural boundary conditions, i.e. they are weakly enforced in both time and space. The weak enforcement of $\mathbb{S}_1$ has been described previously in the definition for the acoustic intensity operator given in (3.29) - (3.31). For $\mathbb{S}_2$, the general form of the acoustic intensity operator defined in (3.33), specializes to

$$\begin{aligned} d_0(\dot{w}^h\,,\,\phi^h)_{(\Upsilon_\infty)_n} &= \frac{1}{R}(\dot{w}^h\,,\,\phi^h)_{(\Upsilon_\infty)_n} + \frac{1}{2R}(\dot{w}^h_{,\varphi}\,,\,\phi^h_{,\varphi})_{(\Upsilon_\infty)_n} \\ &+ \frac{1}{2R}(\dot{w}^h_{,\theta}\,,\,\csc^2(\varphi)\,\phi^h_{,\theta})_{(\Upsilon_\infty)_n} \end{aligned} \tag{5.34}$$

$$d_1(\dot{w}^h\,,\,\dot{\phi}^h)_{(\Upsilon_\infty)_n} = \frac{2}{c}(\dot{w}^h\,,\,\dot{\phi}^h)_{(\Upsilon_\infty)_n} + \frac{R}{c}(\dot{w}^h\,,\,\dot{\phi}^h_{,r})_{(\Upsilon_\infty)_n} \tag{5.35}$$

$$d_2(\dot{w}^h\,,\,\ddot{\phi}^h)_{(\Upsilon_\infty)_n} = \frac{R}{c^2}(\dot{w}^h\,,\,\ddot{\phi}^h)_{(\Upsilon_\infty)_n} \tag{5.36}$$

In (5.34), tangential continuity is relaxed on the boundary Γ_∞ through integration by parts:

$$(w\,,\,\Delta_\Gamma \phi)_{\Gamma_\infty} = -(w_{,\varphi}\,,\,\phi_{,\varphi})_{\Gamma_\infty} - (w_{,\theta}\,,\,\csc^2(\varphi)\,\phi_{,\theta})_{\Gamma_\infty} \tag{5.37}$$

Since these boundary operators are local in space and time, the sparse data structure of the finite element arrays is preserved. The locality in time enables the use of only local causal updates from one time step to the next. Thus local boundary conditions of this type have a distinct advantage in computational storage when compared to competing approaches, e.g. Kirchoff's retarded potential representation or the direct convolution of the DtN map (5.7), which involves a temporal integral over all past time and leads to numerical formulations that can be extremely memory-intensive, typically requiring storage of a large pool of historical data.

Temporal continuity across space-time slabs is weakly enforced through the temporal jump operators embedded in the operators $d_2(\cdot\,,\,\cdot)_{\Gamma_\infty}$ and $d_0(\cdot\,,\,\cdot)_{\Gamma_\infty}$, defined in (3.26). For $\mathbb{S}_1$, the consistent jump terms are given in (3.34). For $\mathbb{S}_2$, the consistent jump terms specialize to,

$$\begin{aligned} d_0(w^h(t_n^+)\,,\,[\![\phi^h(t_n)]\!])_{\Gamma_\infty} &= \frac{1}{R}(w^h(t_n^+)\,,\,[\![\phi^h(t_n)]\!])_{\Gamma_\infty} \\ &+ \frac{1}{2R}(w^h_{,\varphi}(t_n^+)\,,\,[\![\phi^h_{,\varphi}(t_n)]\!])_{\Gamma_\infty} \\ &+ \frac{1}{2R}(w^h_{,\theta}(t_n^+)\,,\,\csc^2(\varphi)\,[\![\phi^h_{,\theta}(t_n)]\!])_{\Gamma_\infty} \end{aligned} \tag{5.38}$$

$$d_2(\dot{w}^h(t_n^+)\,,\,[\![\dot{\phi}^h(t_n)]\!])_{\Gamma_\infty} = \frac{R}{c^2}(\dot{w}^h(t_n^+)\,,\,[\![\dot{\phi}^h(t_n)]\!])_{\Gamma_\infty} \tag{5.39}$$

Remarks

1. As discussed in Section 3.4.2, the first-order operator $\mathbb{S}_1$, satisfies the positivity property given in (3.35). The second-order operator $\mathbb{S}_2$, satisfies the positivity property for all terms up to the nonsymmetric operator in the second term of (5.35). As a result, the stability estimate derived earlier in Theorem (4.1), does not strictly hold. While stability is difficult to prove *a priori* through a rigorous functional analysis for this case, extensive numerical studies in Section 5.3 indicate that the operator $\mathbb{S}_2$ is indeed stable for all the numerical examples run to date. These good results suggest that a rigorous proof of stability for this boundary operator should be possible.

2. Because the space-time formulation allows for the use of C^0 interpolations to represent the high-order time derivatives, it is possible to implement the time-dependent operators to any order desired to obtain higher-order accurate non-reflecting boundary conditions. However for operators in the sequence extending beyond $N \geq 3$, the lowest possible order of spatial continuity on the artificial boundary that can be achieved after integration by parts is C^{N-2}. In this case a layer of boundary elements adjacent to Γ_∞, possessing high-order tangential continuity on Γ_∞ are needed. For example, for $N = 3$, C^1 continuous interpolation functions, e.g. Hermite polynomials, are needed to represent the second-order tangential derivatives appearing in the weak enforcement of $\mathbb{S}_3$. It is this potential limitation that motivated the derivation of the local in time and nonlocal in space version of the boundary conditions discussed in the next section, where no requirement on higher-order continuity is present.

3. An interesting observation is that the first-order operator $\mathbb{B}_1$ coincides with the well known spherical damper and is equivalent to the first local boundary condition in the sequence derived by Bayliss and Turkel [1980] and Engquist and Majda [1977]. In addition, we observe that our local boundary condition $\mathbb{B}_2$, which is exact for the first two spherical wave harmonics, coincides with the second-order boundary condition derived by Bayliss and Turkel [1980], after the higher-order radial derivatives in the Bayliss and Turkel sequence are eliminated in favor of high-order tangential derivatives through use of the wave equation in three-dimensions. The equivalence of this second-order

operator holds in both the time-dependent and time-harmonic cases. However for $N \geq 3$, our non-reflecting boundary conditions are different than those of Bayliss and Turkel. Another sequence of time-dependent non-reflecting boundary conditions that is closely related to ours is given in GROTE AND KELLER [1994].

4. An alternative form of the boundary conditions $\mathbb{S}_m$ can be obtained by replacing the high-order temporal derivatives appearing in the operator with high-order radial and tangential derivatives through repeated use of the wave equation written in separable coordinates, e.g. for a sphere in three-dimensions,

$$\frac{\partial^2 \phi}{\partial t^2} = \left(\frac{c}{r}\right)^2 \left[\frac{\partial}{\partial r}\left(r^2 \frac{\partial \phi}{\partial r}\right) + \Delta_\Gamma \phi\right] \tag{5.40}$$

evaluated at $r = R$. However in this approach, the implementation of high-order radial derivatives is not natural to the standard finite element method, and is not recommended.

5.2.3 Local in time and nonlocal in space version

In order to obtain non-reflecting boundary conditions which possess the important property of locality in time, without the requirement of high-order tangential continuity in the Laplace-Beltrami operator $(\Delta_\Gamma)^j$, a local in time counterpart to the spatially nonlocal DtN map (5.2) is derived which exactly represents the first N spherical wave harmonics. This new sequence of boundary conditions retains the nonlocal spatial integral, yet replaces the temporal integral of the time-convoluted DtN map with higher-order local time derivatives. Thus this new sequence of time-dependent boundary conditions has the advantage that when implemented in the space-time formulation, standard C^0 interpolation functions may be used for both the space and time variables.

First-order boundary condition

Consider the first term in the truncated DtN series with $N = 1$, then (5.2) reduces to,

$$\frac{\partial \phi}{\partial n} = z_0 \int_{\Gamma_\infty} \phi \, s_0 \, d\Gamma' \tag{5.41}$$

where $s_0 = 1/(4\pi R^2)$ and $z_0 = kh_0'/h_0$. Using (5.16) and (5.8) and clearing the denominator h_0 gives the alternate form,

$$\frac{\partial \phi}{\partial n} = \left(ik - \frac{1}{R}\right) \int_{\Gamma_\infty} \phi\, s_0 \; d\Gamma' \tag{5.42}$$

Taking the inverse Fourier transform we obtain the local in time but nonlocal in space boundary condition,

$$\mathbb{B}_1 \phi := \frac{\partial \phi}{\partial n} + \int_{\Gamma_\infty} \left(\frac{1}{c}\dot{\phi} + \frac{1}{R}\phi\right) s_0 \; d\Gamma' = 0 \tag{5.43}$$

This condition is perfectly absorbing for axially symmetric spherical waves (outgoing wave harmonic $n = 0$).

Second-order boundary condition

For $N = 2$, the first two terms in the truncated DtN series (5.2) take the form,

$$\frac{\partial \phi}{\partial n} = z_0 \int_{\Gamma_\infty} \phi\, s_0 \; d\Gamma' + z_1 \int_{\Gamma_\infty} \phi\, s_1 \; d\Gamma' \tag{5.44}$$

Using the definition for z_n and relations (5.16),(5.22), (5.8) and clearing the common denominator $h_0 h_1$ we obtain the alternative form,

$$\left(\frac{1}{R} - ik\right) \frac{\partial \phi}{\partial n} = \left(k^2 + \frac{2ik}{R} - \frac{1}{R^2}\right) \int_{\Gamma_\infty} \phi\, s_0 \; d\Gamma' + \left(k^2 + \frac{2ik}{R} - \frac{2}{R^2}\right) \int_{\Gamma_\infty} \phi\, s_1 \; d\Gamma' \tag{5.45}$$

Taking the inverse Fourier transform we arrive at the time-dependent counterpart to (5.45):

$$\begin{aligned} \mathbb{B}_2 \phi := \frac{\partial \phi}{\partial n} + \frac{R}{c}\frac{\partial \dot{\phi}}{\partial n} &+ \int_{\Gamma_\infty} \left(\frac{R}{c^2}\ddot{\phi} + \frac{2}{c}\dot{\phi} + \frac{1}{R}\phi\right) s_0 \; d\Gamma' \\ &+ \int_{\Gamma_\infty} \left(\frac{R}{c^2}\ddot{\phi} + \frac{2}{c}\dot{\phi} + \frac{2}{R}\phi\right) s_1 \; d\Gamma' = 0 \end{aligned} \tag{5.46}$$

where s_0 and s_1 are defined in (5.3). This condition is perfectly absorbing for the first two spherical wave harmonics of order $n = 0$ and $n = 1$.

Third-order boundary condition

For $N = 3$, the first three terms in the truncated DtN series (5.2) are,

$$\frac{\partial \phi}{\partial n} = z_0 \int_{\Gamma_\infty} \phi\, s_0 \; d\Gamma' + z_1 \int_{\Gamma_\infty} \phi\, s_1 \; d\Gamma' + z_2 \int_{\Gamma_\infty} \phi\, s_2 \; d\Gamma' \tag{5.47}$$

Using the definition for z_n, the relations (5.16),(5.22), (5.8) and clearing the common denominator $h_0 h_1 h_2$ we obtain the alternative form,

$$\gamma_0 \frac{\partial \phi}{\partial n} = \gamma_1 \int_{\Gamma_\infty} \phi\, s_0 \; d\Gamma' + \gamma_2 \int_{\Gamma_\infty} \phi\, s_1 \; d\Gamma' + \gamma_3 \int_{\Gamma_\infty} \phi\, s_2 \; d\Gamma' \tag{5.48}$$

where

$$\begin{aligned}
\gamma_0 &= 1 - 2ikR - 4(kR)^2/3 + i(kR)^3/3 \\
\gamma_1 &= -1/R + 3ik + 10k^2R/3 - 5ik^3R^2/3 - k^4R^3/3 \\
\gamma_2 &= -2/R + 4ik + 11k^2R/3 - 5ik^3R^2/3 - k^4R^3/3 \\
\gamma_3 &= -3/R + 6ik + 13k^2R/3 - 5ik^3R^2/3 - k^4R^3/3
\end{aligned}$$

Taking the inverse Fourier transform gives the time-dependent counterpart:

$$\begin{aligned}
\mathbb{B}_3\phi \;:=\; & \phi_{,n} + \frac{2R}{c}\phi_{,nt} + \frac{4R^2}{3c^2}\phi_{,ntt} + \frac{R^3}{3c^3}\phi_{,nttt} && (5.49) \\
+ & \int_{\Gamma_\infty} \left(\frac{R^3}{3c^4}\phi_{,tttt} + \frac{5R^2}{3c^3}\phi_{,ttt} + \frac{10R}{3c^2}\phi_{,tt} + \frac{3}{c}\phi_{,t} + \frac{1}{R}\phi \right) s_0 \; d\Gamma' \\
+ & \int_{\Gamma_\infty} \left(\frac{R^3}{3c^4}\phi_{,tttt} + \frac{5R^2}{3c^3}\phi_{,ttt} + \frac{11R}{3c^2}\phi_{,tt} + \frac{4}{c}\phi_{,t} + \frac{2}{R}\phi \right) s_1 \; d\Gamma' \\
+ & \int_{\Gamma_\infty} \left(\frac{R^3}{3c^4}\phi_{,tttt} + \frac{5R^2}{3c^3}\phi_{,ttt} + \frac{13R}{3c^2}\phi_{,tt} + \frac{6}{c}\phi_{,t} + \frac{3}{R}\phi \right) s_2 \; d\Gamma' = 0 && (5.50)
\end{aligned}$$

where $s_n, \quad n = 0, 1, 2$ are defined in (5.3). This condition is perfectly absorbing for the first three spherical wave harmonics of order $n = 0, 1, 2$. Local in time counterparts for the higher terms, $N \geq 4$, in the truncated DtN series are obtained following the same procedure outlined for $N = 1, 2, 3$. These are nonlocal operators that involve a spatial integral yet retain the important property of locality in time. In general, the boundary operators in this sequence will have higher-order time derivatives up to $2(N-1)$. By expressing the boundary operators in the form,

$$\mathbb{B}_m(\phi) := \frac{\partial \phi}{\partial n} + \mathbb{S}_m(\phi) \tag{5.51}$$

which implies,

$$\frac{\partial \phi}{\partial n} = -\mathbb{S}_m \phi \qquad \text{on} \quad \Gamma_\infty \tag{5.52}$$

the sequence of boundary operators can be implemented as natural boundary conditions in the space-time formulation. The implementation follows a similar procedure to that in Section 5.2.2 where the operator $\mathbb{S}_m$ is weakly enforced through the acoustic intensity operator defined in (3.26).

The advantage of this sequence of operators is that when implemented in the discontinuous space-time finite element formulation, standard C^0 continuous interpolations may be used on $\Gamma_\infty \times I_n$ in both the space and time dimensions. For example, for the third-order operator $\mathbb{B}_3$ defined in (5.50), standard C^0 quartic basis functions in the time dimension and C^0 linear basis functions in the spatial dimension may be used to interpolate the fourth-order temporal and first-order spatial derivatives appearing in the boundary operator. This feature circumvents the need for high-order continuous tangential interpolation functions as required by the local in space version described earlier in Section 5.2.1 for orders $N \geq 3$. It is this special property of the local in time and nonlocal in space version of the non-reflecting boundary conditions, when implemented in the time-discontinuous formulation which offers the greatest potential for implementation of high-order boundary conditions beyond second-order. A closely related sequence can be found in Grote and Keller [1994].

5.3 Numerical Examples

In this section a large number of numerical examples are conducted to demonstrate the effectiveness of the time-discontinuous Galerkin space-time finite element method to accurately model transient acoustic radiation. The problems investigated are primarily designed to assess the performance of the local non-reflecting boundary conditions when implemented in the time-discontinuous Galerkin variational formulation. Only

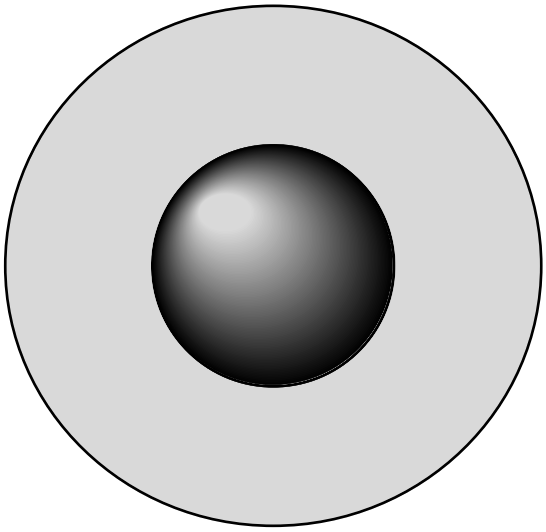

Figure 5.3: Sphere of radius $r = a$ enclosed by a spherical artificial boundary of radius $R = 2a$.

results for the local in time and local in space version of the non-reflecting boundary operators defined in Section 5.2.1 are given. Comparisons are made with the PW-damper $\mathbb{S}_0$ defined in (2.24), and the first-order $\mathbb{S}_1$, and second-order $\mathbb{S}_2$, local boundary conditions defined in (5.31) and (5.32) respectively. For all the numerical results presented, the GLS mesh parameters are set to zero and standard C^0 quadratic finite element shape functions are used in both the time and space dimensions.

All computations were performed on a Sun-SPARCstation 2, in double-precision, and $2 \times 2 \times 2$ Gaussian quadrature for tri-quadratic space-time domain elements and 2×2 quadrature for bi-quadratic space-time boundary elements. To this authors knowledge, this is the first implementation of the time-discontinuous Galerkin space-time finite element method for second-order hyperbolic equations in multidimensions. Numerical results for one-dimensional problems (without non-reflecting boundaries) are reported in Hulbert and Hughes [1989,1990].

5.3.1 Spherical harmonic radiation

In this example, consider the time-dependent radiation from a sphere of radius $r = a$, with a harmonic load distribution of the form,

$$\phi(a, \varphi, t) = P_n(\cos\varphi)\sin\omega t, \qquad \text{for } 0 \leq \varphi < \pi\,, \quad t > 0 \tag{5.53}$$

The exact steady-state solution for this problem is,

$$\phi(r, \varphi, t) = -\mathrm{Imag}\left\{\frac{h_n(kr)}{h_n(ka)} P_n(\cos\varphi)\mathrm{e}^{-i\omega t}\right\} \qquad \text{for } r \geq a \tag{5.54}$$

where P_n are Legendre polynomials of the first kind and h_n are spherical Hankel functions of the first kind of order n. When using a finite element method incorporating approximate non-reflecting boundary conditions on a spherical artificial boundary as illustrated in Figure 5.3, this problem becomes increasingly difficult to solve as the wave harmonic n increases. The spherically symmetric damper $\mathbb{S}_1$ defined in (3.28) or (5.31) is exact for the breathing mode, which corresponds to the harmonic $n = 0$. However, for higher modes, $n = 1, 2, \cdots$ this condition is only approximate. An improved approximation is obtained by using the second-order operator $\mathbb{S}_2$ derived in (5.32). This time-dependent boundary condition is exact for the first two spherical harmonics, $n = 0, 1$.

For this axisymmetric problem, the computational domain is taken as $\Omega = \{a < r < R,\ 0 \leq \varphi < \pi\}$. with the truncation boundary set at $R = 2a$. The resulting bounded domain Ω is discretized with 400 axisymmetric acoustic elements: 10 elements in the radial direction, and 40 elements in the polar direction, see Figure 5.4. As a consequence of the axisymmetric nature of the problem, there is no circumferential dependence on the solution and all terms which depend on the coordinate θ are neglected in the definition of the non-reflecting boundary conditions. In particular, for the local boundary operator $\mathbb{S}_2$ defined in (5.32), the third term in (5.34) and (5.38) are neglected.

A series of transient space-time finite element solutions were obtained for the axisymmetric loading (5.53) with harmonics ranging from $n = 0$ through $n = 4$. A time-increment of $\Delta t = 0.1$ with zero initial conditions on ϕ and $\dot{\phi}$ was used for all the examples in this section. The system starts from rest and is driven towards the steady-state solution with time.

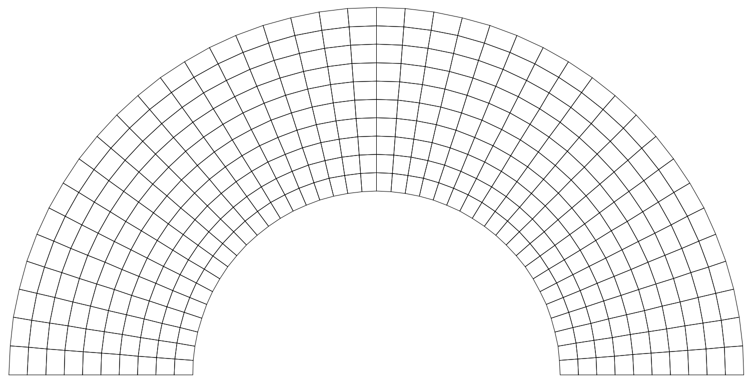

Figure 5.4: Axisymmetric mesh with 400 quadratic elements.

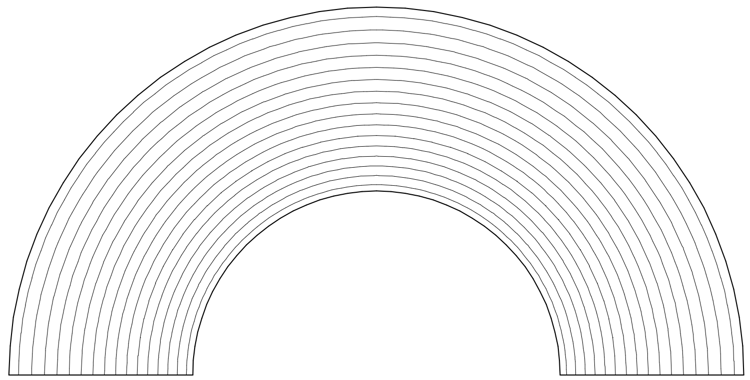

Figure 5.5: Breathing mode ($n = 0$) for a radiating sphere: Solution contours at time $t = 30$ and normalized frequency $ka = 1$.

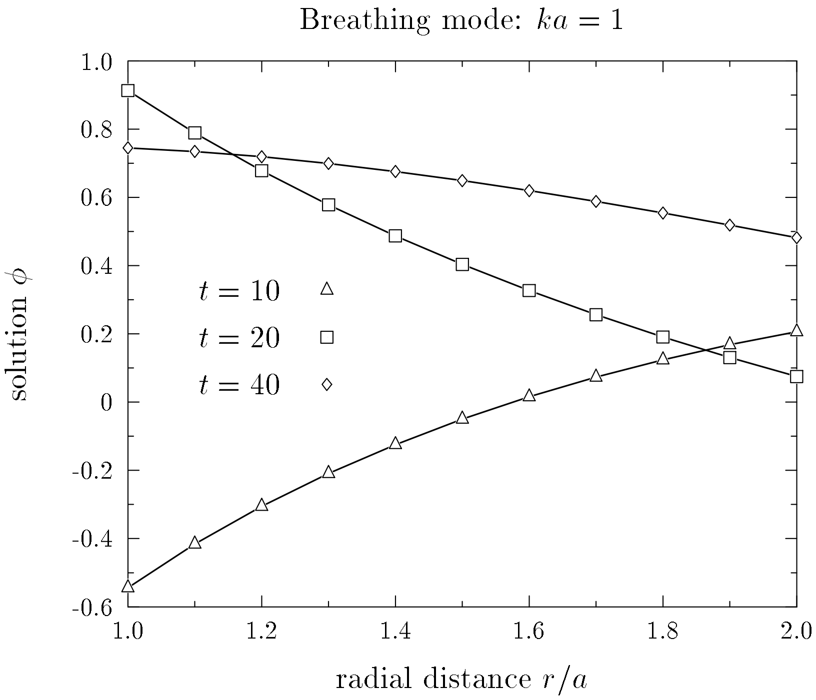

Figure 5.6: Breathing mode ($n = 0$) for a radiating sphere: $ka = 1$. Solution profile using S_1 local boundary condition along the radial distance $a < r < R$, at times $t = 10, 20, 40$.

Harmonic $n = 0$**:**

Before proceeding to more complex radiation patterns we wish to confirm that the spherical operator $\mathbb{S}_1$, is exact for the 'breathing' mode $n = 0$, i.e. for the radiation loading $P_0(\cos\varphi)\sin\omega t$. Figure 5.5 illustrates the contours for the space-time solution at $t = 30$ and a normalized frequency $ka = 1$. Figure 5.6 shows a profile of the time-dependent space-time solution after reaching steady-state in comparison to the exact time-harmonic solution (5.54). The solutions are plotted along the radial coordinate at three sample times: $t = 10, 20, 40$. The solution sample times are such that many spurious reflections between the artificial boundary $r = R$, and the radiating surface at $r = a$, could have occurred. From these results it is clear that the $\mathbb{S}_1$ operator when implemented in the discontinuous Galerkin formulation gives nearly exact solutions for the $n = 0$ spherical harmonic as expected. Numerical results for other values of ka support this conclusion (not shown).

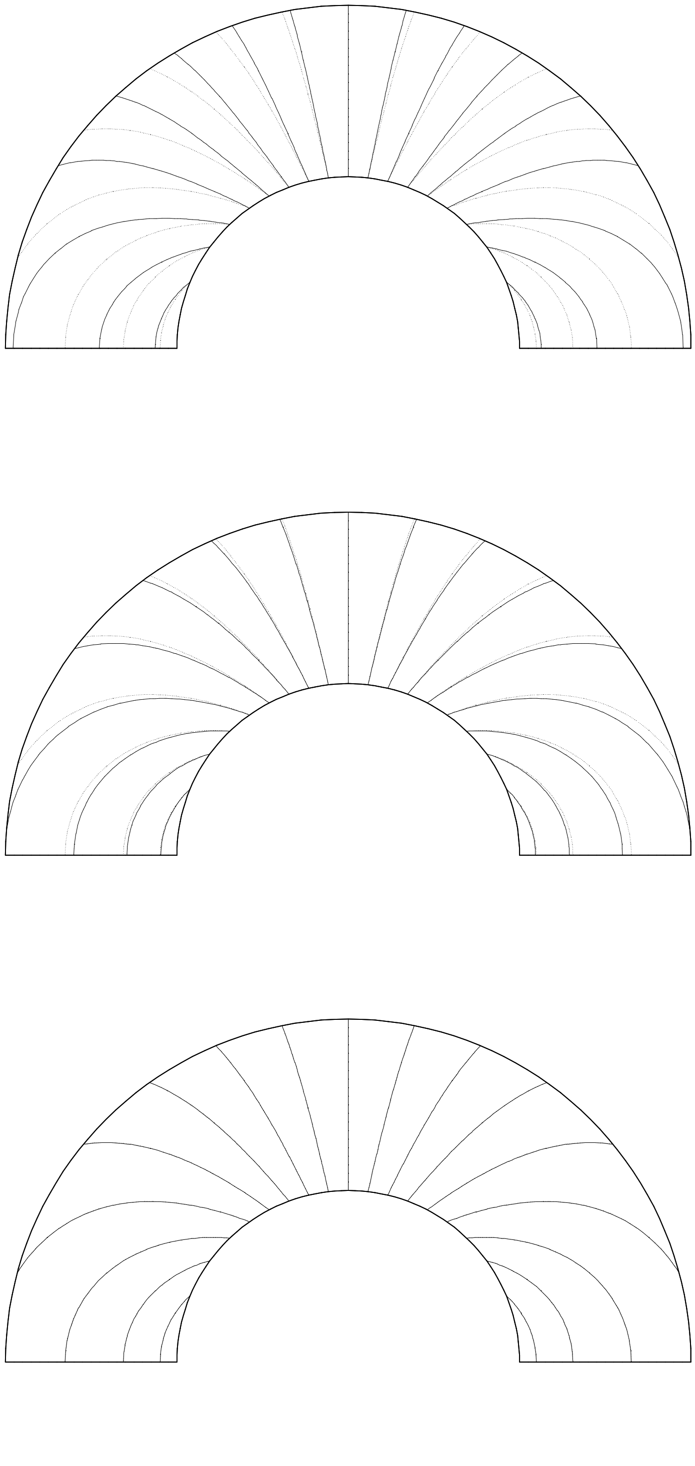

Figure 5.7: Radiation from a sphere with polar harmonic $n = 1$ and normalized frequency $ka = 1$. Contours of space-time solution at $t = 20$ using local boundary conditions, (Top): 'plane-wave' S_0, (Middle): first-order S_1, (Bottom): second-order S_2. (dotted contours denote analytical solution).

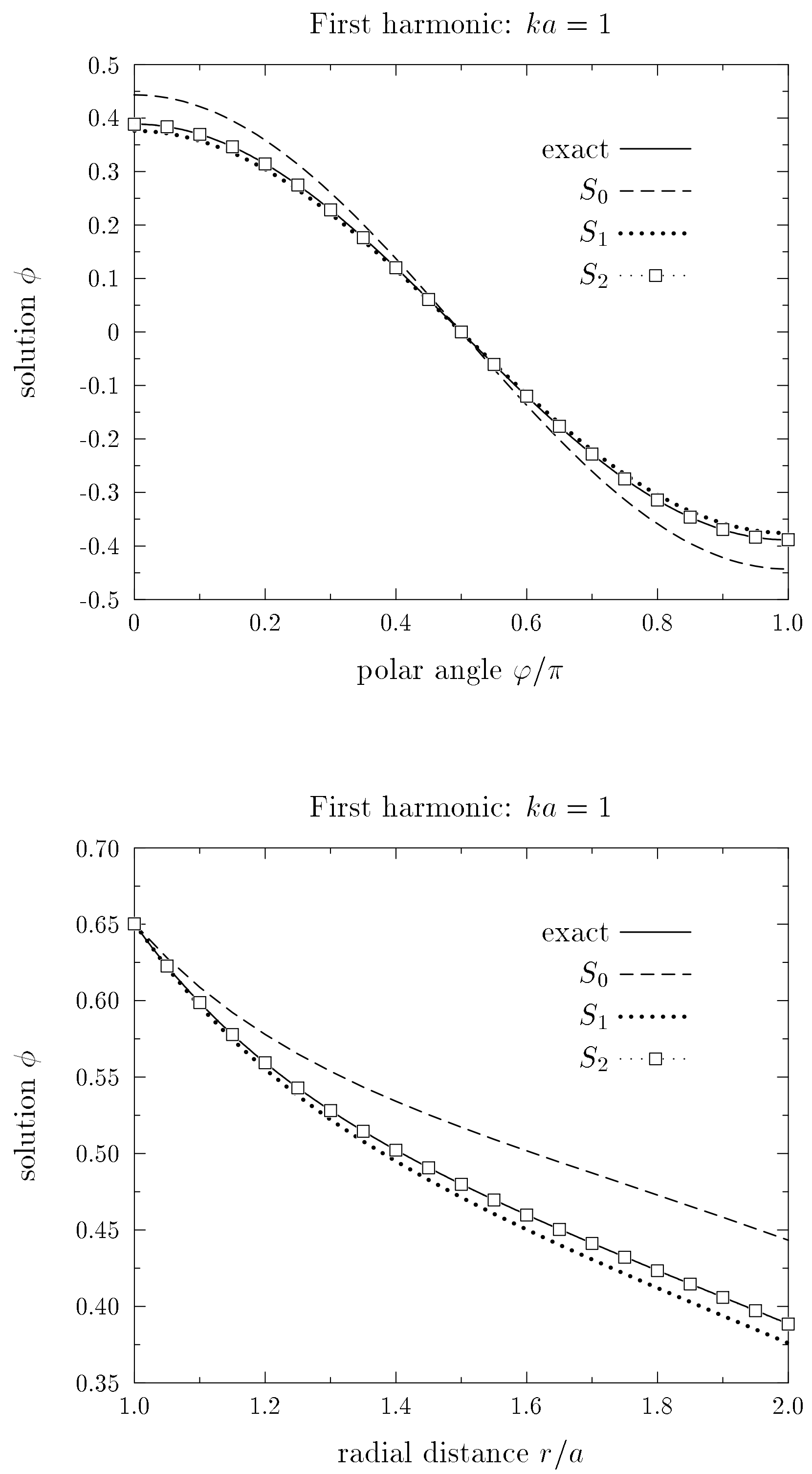

Figure 5.8: Spherical wave harmonic $n = 1$: Results at $t = 20$, comparing the 'plane-wave' S_0, first-order S_1, and second-order S_2 boundary conditions. (Top): Solution profile on the artificial boundary $r = R$. (Bottom): Solution plotted along radial line at $\varphi = 0$.

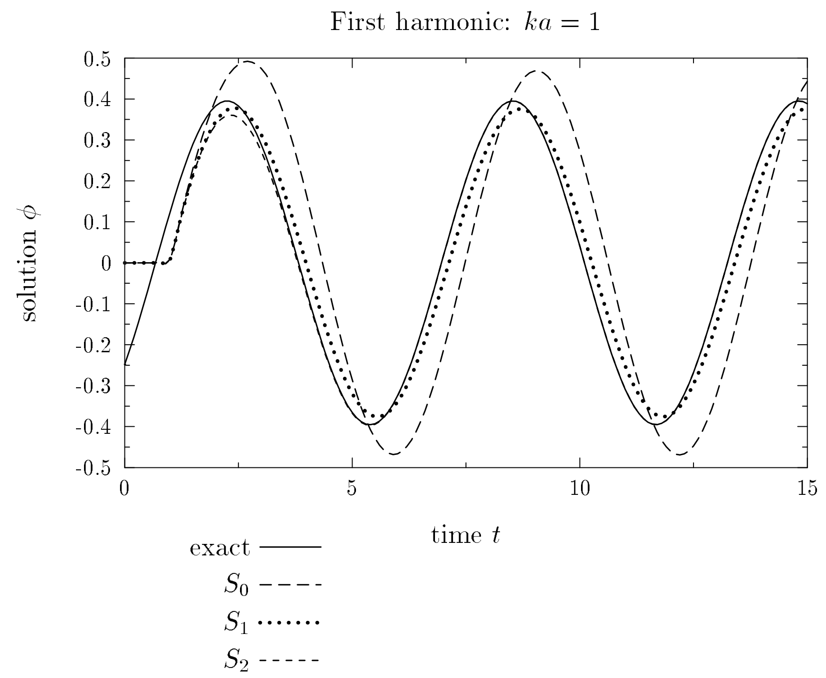

Figure 5.9: Time-dependent solution at a point on the artificial boundary, i.e. $r = R$ and $\varphi = 0$. Results show the transient solution as it is driven to steady-state.

Harmonic $n = 1$**:**

To verify that the second-order boundary operator $\mathbb{S}_2$ is exact for the second wave harmonic, $n = 1$, the numerical solution is obtained for the loading $P_1(\cos\varphi)\sin\omega t$ and $ka = 1$. Figure 5.7 illustrates the contours of the discontinuous Galerkin solution incorporating the local 'plane-wave' boundary operator, $\mathbb{S}_0$, defined in (2.24), and the first-order $\mathbb{S}_1$, and second-order $\mathbb{S}_2$, boundary operators defined in (5.31) and (5.32) respectively, in comparison to the exact steady-state solution. Figure 5.8 shows the solution profile around the artificial boundary at $r = R$, as well as the solution plotted along a radial line located at the polar angle $\varphi = 0$. Figure 5.9 shows the time-dependent solution at a point on the artificial boundary at position $(r, \varphi) = (R, 0)$. Results confirm that the local operator $\mathbb{S}_2$, when implemented in the space-time formulation, give nearly exact solutions for harmonic $n = 1$. The numerical solution using $\mathbb{S}_1$ is somewhat out-of-phase with the exact steady-state solution while the simple 'plane-wave' damper $\mathbb{S}_0$, shows significant errors in both phase and amplitude.

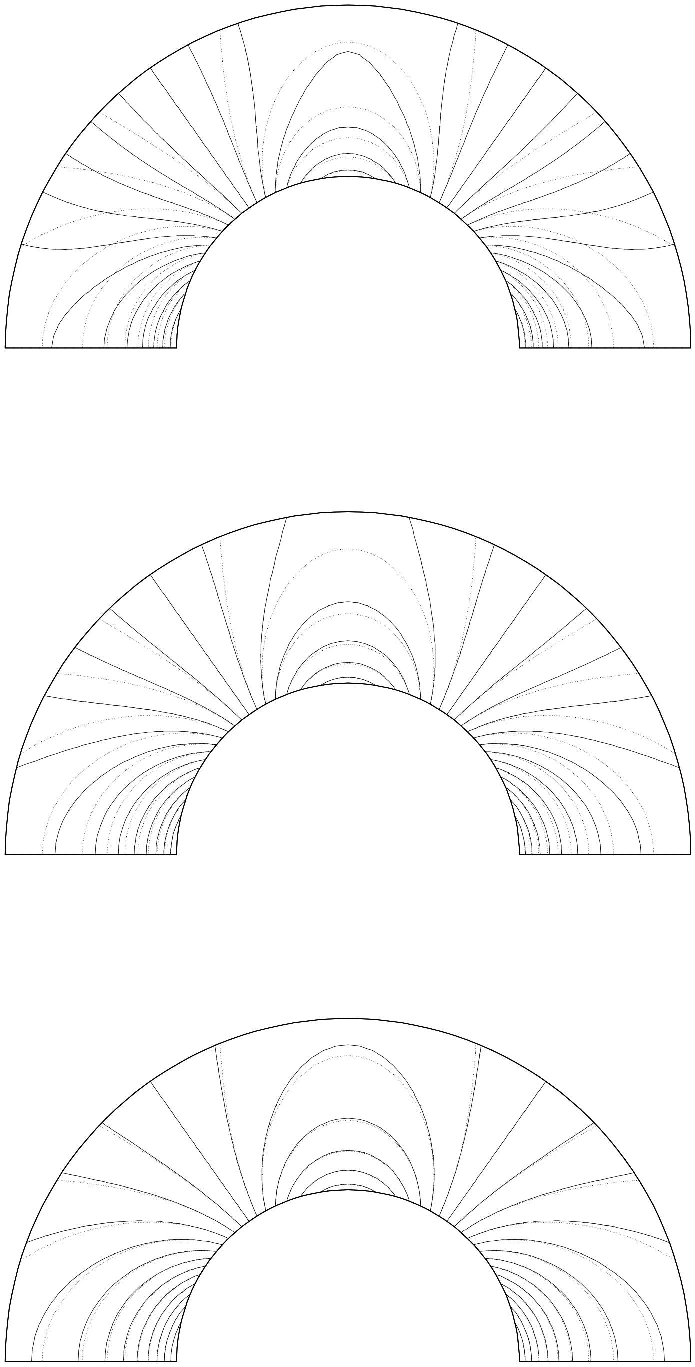

Figure 5.10: Radiation from sphere with polar harmonic $n = 2$ and normalized frequency $ka = 1$. Contours of space-time solution using local boundary conditions, (Top): 'plane-wave' S_0, (Middle): first-order S_1, (Bottom): second-order S_2. (dotted contours denote analytical solution).

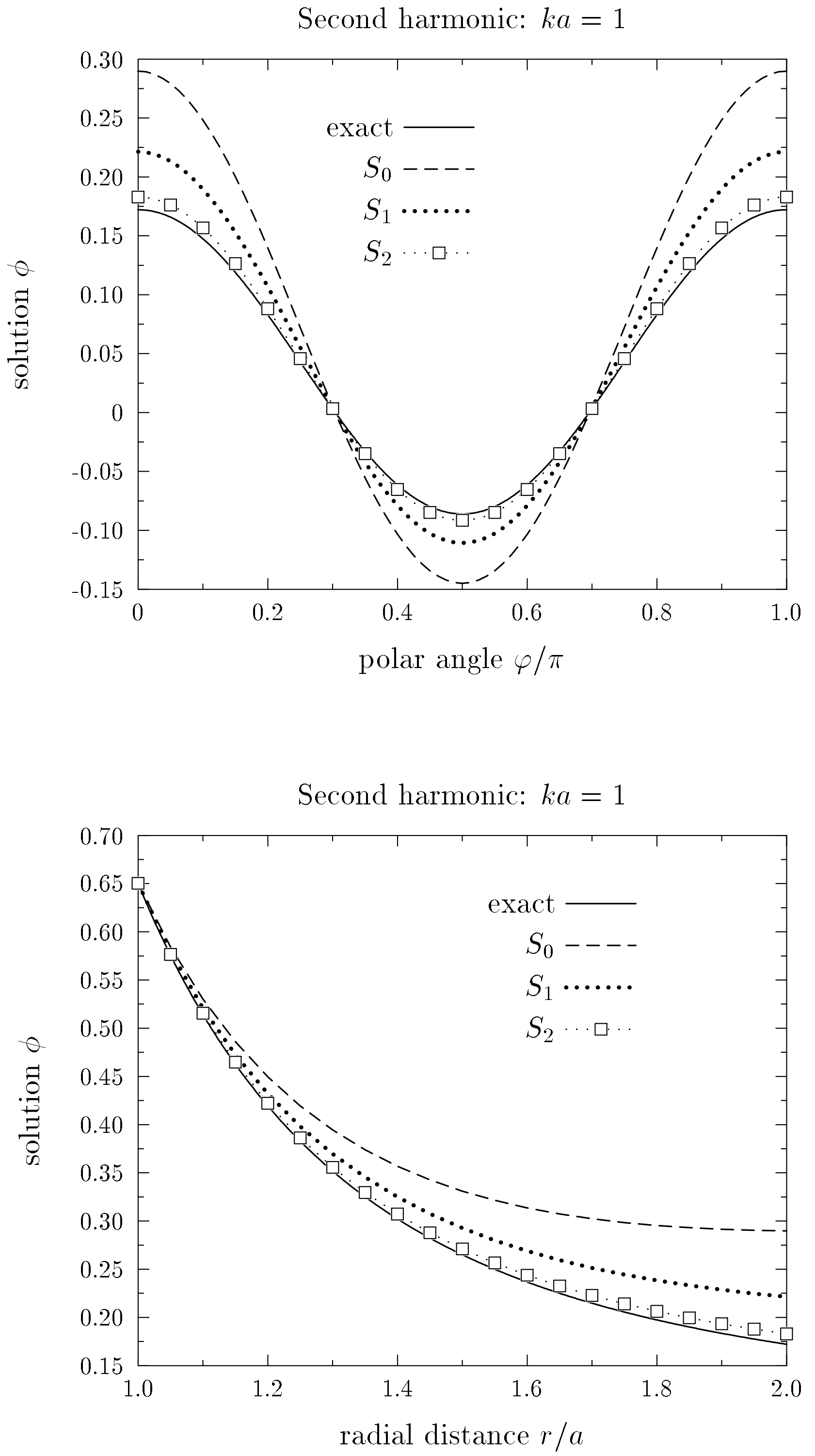

Figure 5.11: Spherical wave harmonic $n = 2$: Results comparing the 'plane-wave' S_0, first-order S_1, and second-order S_2, boundary conditions. (Top): Solution profile on the artificial boundary $r = R$. (Bottom): Solution plotted along radial line at $\varphi = 0$.

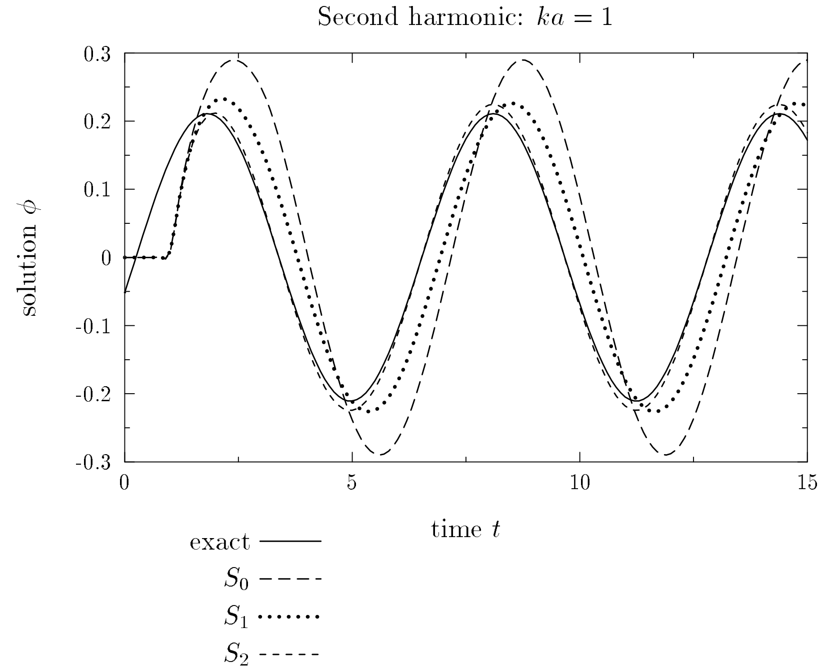

Figure 5.12: Time-dependent solution at a point on the artificial boundary, i.e. $r = R$ and $\varphi = 0$. Results show the transient solution as it is driven to steady-state.

Harmonic $n = 2$**:**

To demonstrate the effectiveness of the second-order operator $\mathbb{S}_2$ to yield accurate numerical solutions for higher modes, we examine harmonic $n = 2$, for a driving frequency given by the nondimensional wavenumber $ka = 1$. Figures 5.10 and 5.11 show a comparison of the space-time solution at time $t = 15$, using the local boundary operators $\mathbb{S}_j$, $j = 0, 1, 2$, The numerical results using the low-order operators $\mathbb{S}_0$ and $\mathbb{S}_1$ show a significant error in the solution, while the solution using $\mathbb{S}_2$ remains relatively accurate with only a small error in amplitude, see Figure 5.12.

Harmonic $n = 3$**:**

Numerical solutions for harmonic loading with $n = 3$, with a driving frequency of $ka = 1$ show significant error for all three local boundary operators tested. However, by increasing the nondimensional wavenumber to $ka = 3$, i.e. by setting the driving frequency to $\omega = 1$ with a wave speed $c = 1/3$, we observe accurate results using the second-order operator $\mathbb{S}_2$. Figures 5.13 through 5.14 show the space-time solution for this frequency. Results using $\mathbb{S}_0$ and $\mathbb{S}_1$ show significant error in the solution. In

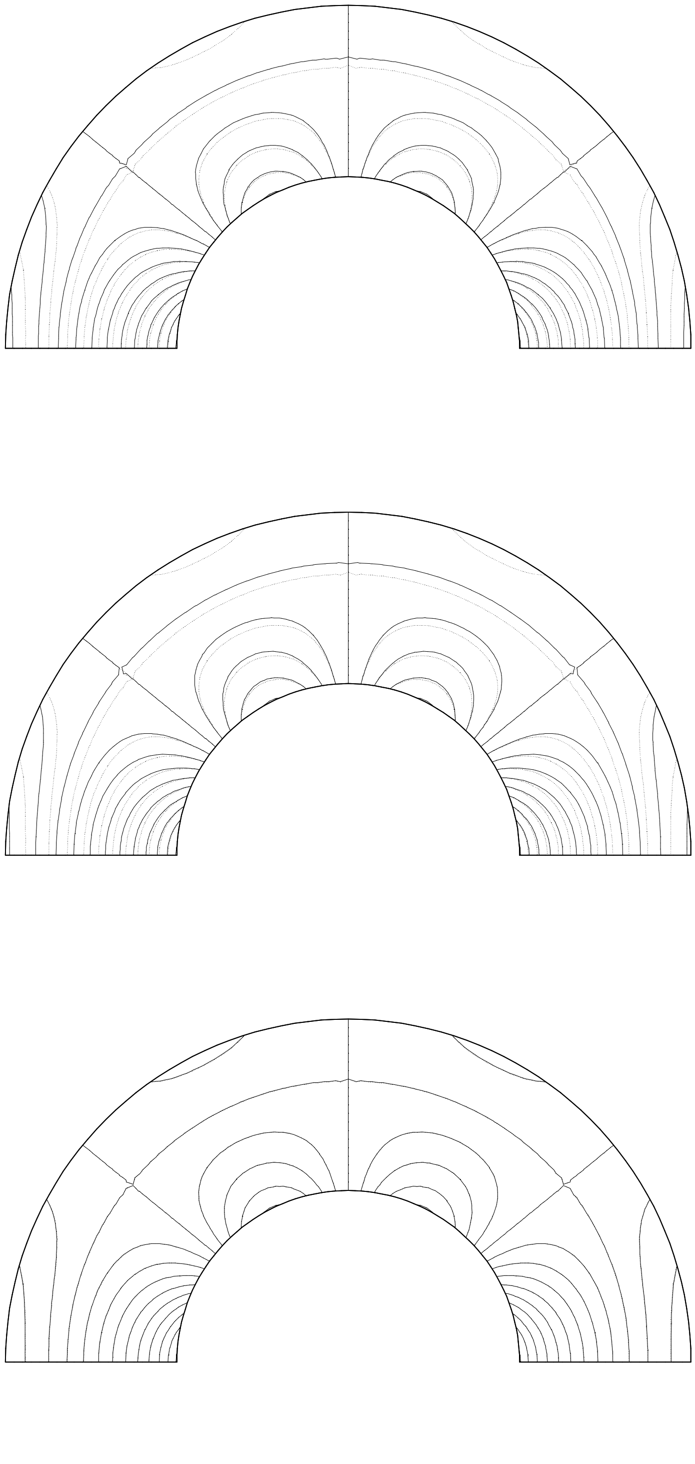

Figure 5.13: Radiation from sphere with polar harmonic $n = 3$ and normalized frequency $ka = 3$. Contours of space-time solution at $t = 20$ using local boundary conditions, (Top): 'plane-wave' S_0, (Middle): first-order S_1, (Bottom): second-order S_2. (dotted contours denote analytical solution).

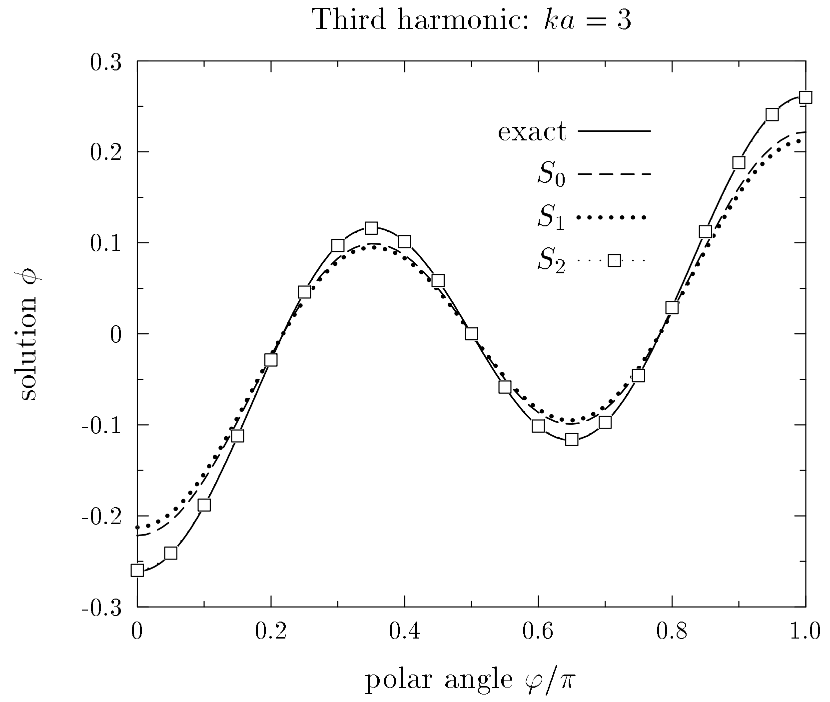

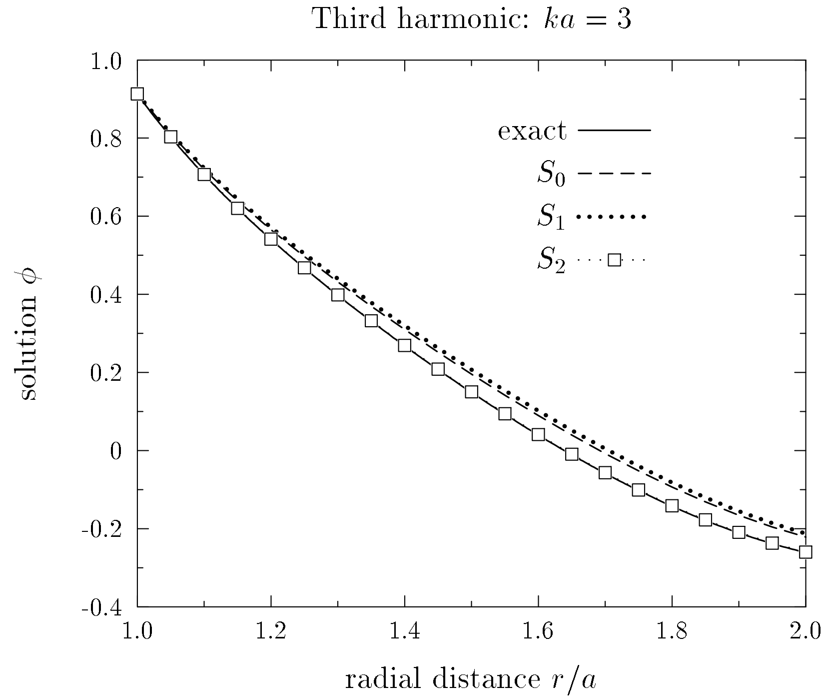

Figure 5.14: Spherical wave harmonic $n = 3$: Results at $t = 20$, comparing the 'plane-wave' S_0, first-order S_1, and second-order S_2 boundary conditions. (Top): Solution profile on the artificial boundary $r = R$. (Bottom): Solution plotted along radial line at $\varphi = 0$.

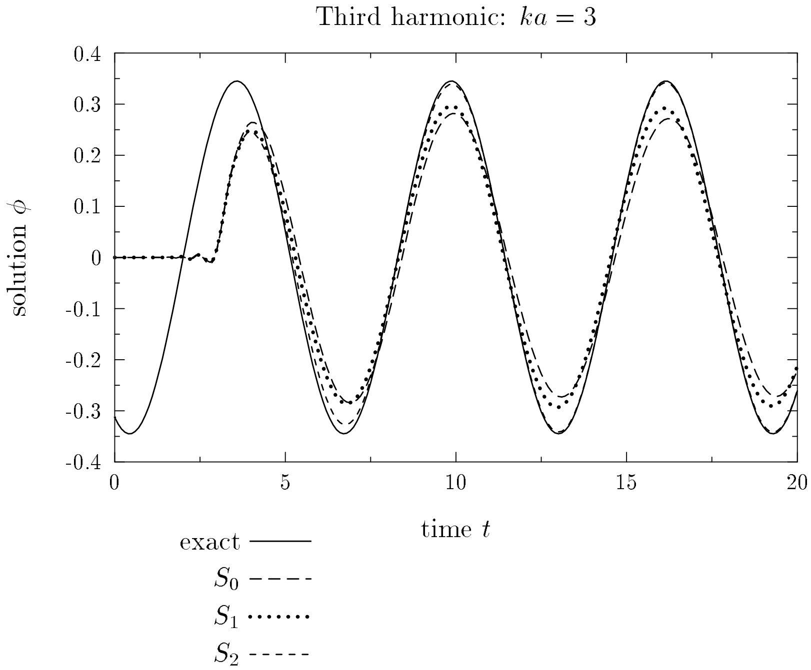

Figure 5.15: Time-dependent solution at a point on the artificial boundary, i.e. $r = R$ and $\varphi = 0$. Results show the transient solution as it is driven to steady-state.

comparison, the solution using $\mathbb{S}_2$ is remarkably accurate; with the numerical and analytical solutions almost indistinguishable.

This example demonstrates an important property of the approximate local boundary conditions: *As the frequency, normalized with respect to the characteristic dimension of the problem increases, the local boundary conditions become increasingly accurate.*

Harmonic $n = 4$:

Figures 5.16 through 5.18 show the solution for the polar harmonic $n = 4$ with a non-dimensional wavenumber $ka = 3$ at time $t = 15$. For this loading, the $\mathbb{S}_2$ local operator is able to maintain an accurate solution, while the solution using the low-order operators $\mathbb{S}_0$ and $\mathbb{S}_1$ have deteriorated significantly. When the harmonic loading is raised to $n = 5$, all three boundary operators tested exhibit large errors in the solution (not shown). In order to obtain accurate solutions for this loading and frequency, the artificial boundary must be moved further away from the sphere, requiring a larger domain, and an increase in computational expense.

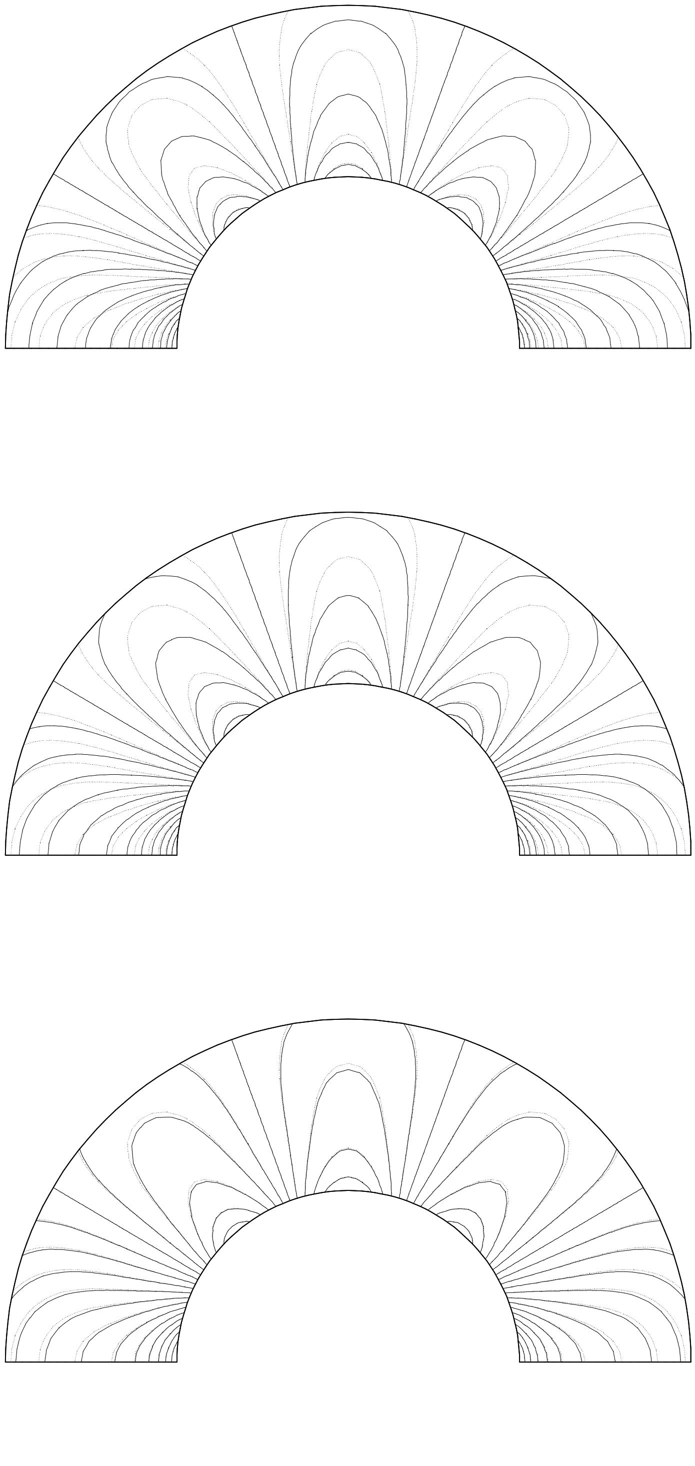

Figure 5.16: Radiation from sphere with polar harmonic $n = 4$ and normalized frequency $ka = 3$. Contours of space-time solution using local boundary conditions, (Top): 'plane-wave' S_0, (Middle): first-order S_1, (Bottom): second-order S_2. (dotted contours denote analytical solution).

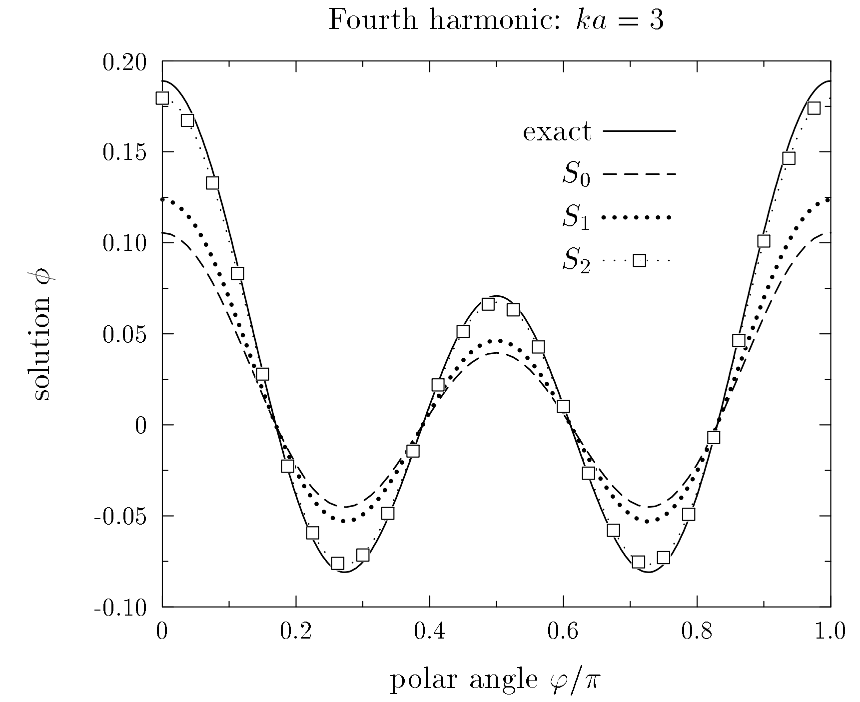

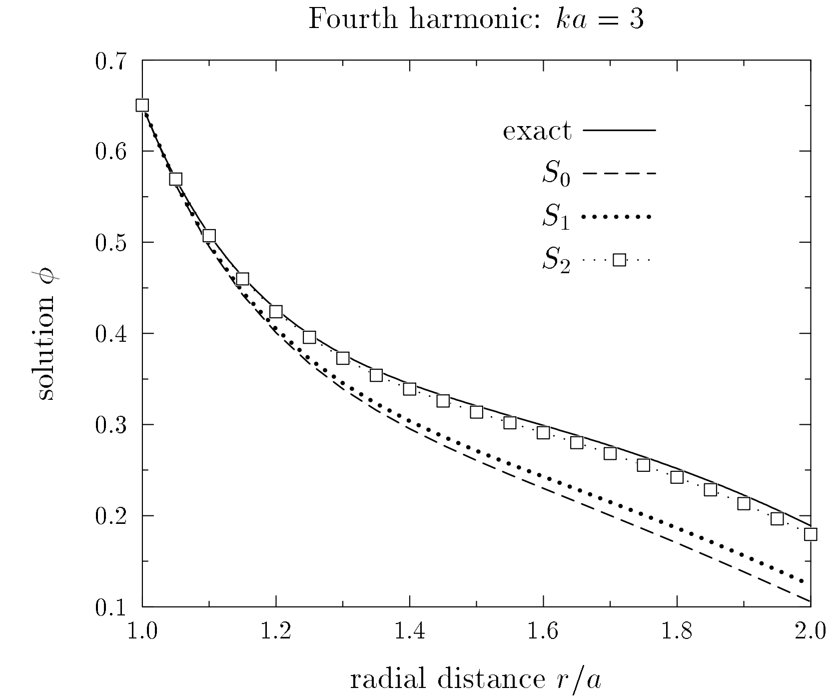

Figure 5.17: Spherical wave harmonic $n = 4$: Results comparing the 'plane-wave' S_0, first-order S_1, and second-order S_2 boundary conditions. (Top): Solution profile on the artificial boundary $r = R$. (Bottom): Solution plotted along radial line at $\varphi = 0$.

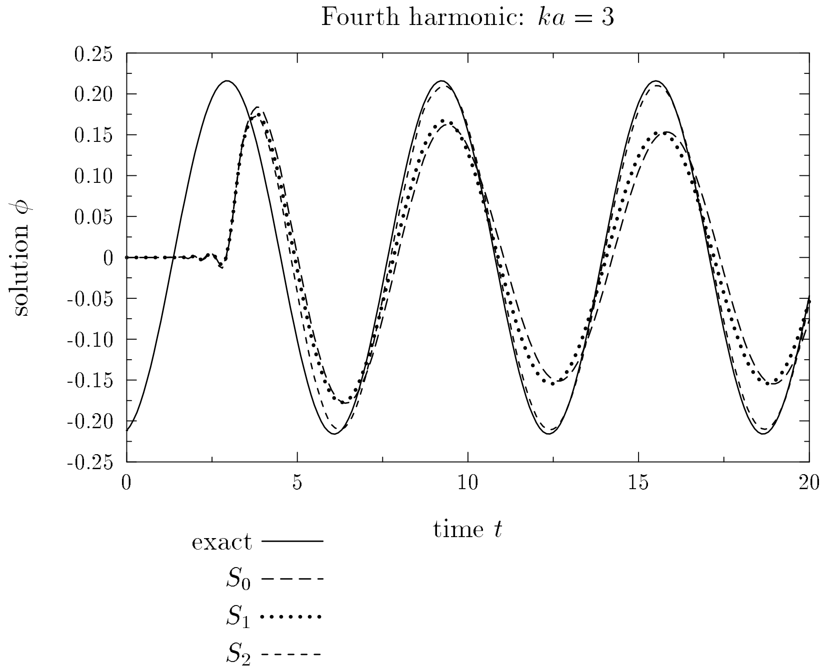

Figure 5.18: Time-dependent solution at a point on the artificial boundary, i.e. $r = R$ and $\varphi = 0$. Results show the transient solution as it is driven to steady-state.

5.3.2 Radiation from a circular piston on a sphere

To study a more complicated problem involving an infinite number of spherical wave harmonics, consider the non-uniform radiation from a circular piston subtending a polar angle $0 \leq \varphi \leq \varphi_p = 13.5^o$ on a submerged sphere of radius $r = a$. The piston has a constant inhomogeneous value $\phi(a,t) = \sin \omega t$ for $t > 0$. Elsewhere on the wet surface, the solution vanishes. The steady-state analytical solution for the velocity potential is,

$$\phi(r,\varphi,t) = -\frac{1}{2}\mathrm{Imag}\left\{\sum_{n=0}^{\infty} \frac{h_n(kr)}{h_n(ka)} \left[P_{n-1}(\cos\varphi_p) - P_{n+1}(\cos\varphi_p)\right] P_n(\cos\varphi)\mathrm{e}^{-i\omega t}\right\} \tag{5.55}$$

This problem gives rise to the interesting feature that as the wave generated at the piston pole $\varphi = 0^o$, travels along longitudes, it is attenuated by a geometrical spreading loss. As the diameter of the sphere increases when compared to a wavelength, the wave field departs more and more from a point source pattern, and in the region opposite the piston pole $\varphi = 180^o$, the amplitude is significantly lower.

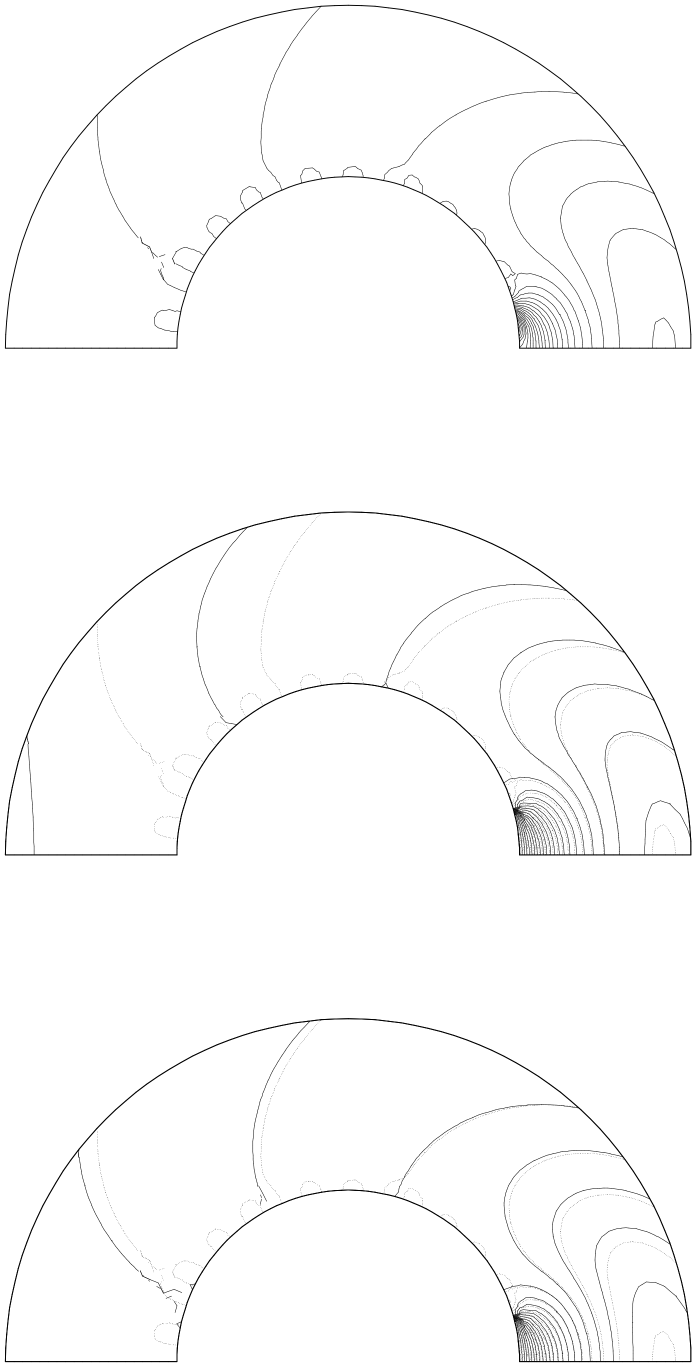

Figure 5.19: Solution contours for radiating piston on a sphere: (Top): Analytic series solution at time $t = 30$ and $ka = 3$. (Middle): Space-time solution with S_1 local boundary condition. (Bottom): Space-time solution with S_2 local boundary condition. (dotted contours denote exact solution)

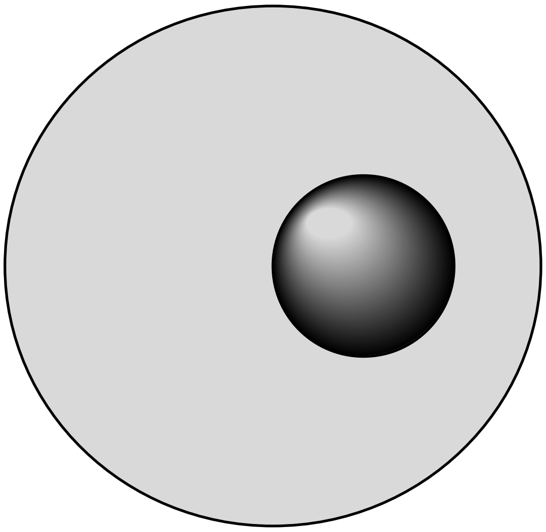

Figure 5.20: Illustration of a spherical radiator of radius a, offset from the center of a spherical artificial boundary of radius $3a$.

In this example, the properties and discretization are unchanged from the previous problem considered. Figure 5.19 (top) shows the contours of the analytical series solution, nodally interpolated with the mesh employed. The low-amplitude oscillations in the vicinity of the wet surface are a product of the difficulty the series solution has in resolving the discontinuity in the loading condition at $\varphi_p = 13.5^o$, and are not relevant to the validation of the numerical results. In Figure 5.19 (middle) and (bottom), results for the space-time solution show a significant improvement in the solution using $\mathbb{S}_2$, in comparison to the solution using $\mathbb{S}_1$. Near the piston pole, both solutions accurately capture the physics of the problem, but as the wave pattern spreads to the backside, the solution using $\mathbb{S}_1$ deteriorates significantly while $\mathbb{S}_2$ maintains an accurate solution throughout the entire computational domain.

5.3.3 Nonconcentric spherical radiator

As the final example in this chapter, consider a sphere of radius $r = a$, pulsating with a uniform sine pulse, $\phi(a,t) = \sin \omega t$ and $\omega = \pi$, during the short time interval $t \in [0, 1]$. Initial conditions are set to zero and the wave speed is $c = 1$. The exact solution to this problem is an outgoing spherical wave of short duration with a $1/r$

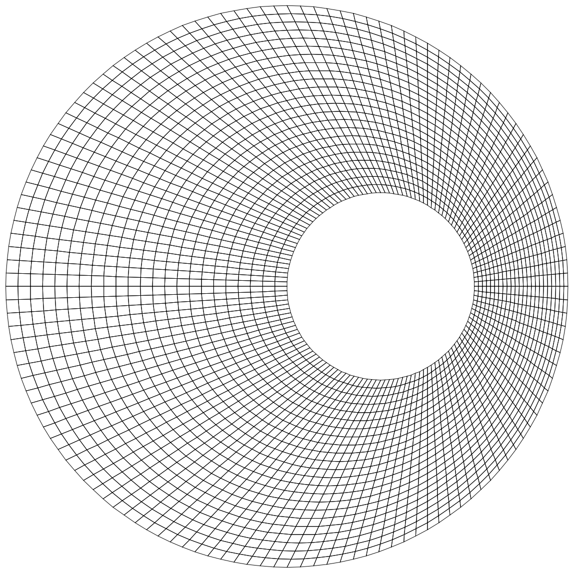

Figure 5.21: Computational domain for a sphere shifted from the center of a spherical non-reflecting boundary. Spatial discretization: Upper half modeled with 1518 axisymmetric elements using quadratic interpolation.

amplitude decay:

$$\phi(r\,,\,t) \quad = \quad \left(\frac{a}{r}\right)\sin\omega(t-\bar{r}/c) \tag{5.56}$$

where $\bar{r} = r - a$ is the radial distance from the spherical radiator and $(t - \bar{r}/c) \in [0, 1]$.

If the radiating sphere is placed concentric with a spherical artificial boundary, as was done in the previous examples of this chapter, then for the uniform radiation field given in (5.56), the problem is trivial in that the first order $\mathbb{S}_1$, and higher order local non-reflecting boundary conditions are all exact. In order to obtain a challenging problem, the radiating sphere is shifted from the center of the spherical artificial boundary Γ_∞, to a nonconcentric position. In this example, the radiating sphere is offset by a distance a, with the radius of Γ_∞ set at $R = 3a$, see Figure 5.20. With this positioning, wave fronts traveling outward along radial lines will strike the artificial boundary at oblique angles. The closer the radiating sphere gets to the edge of Γ_∞, the more acute this angle becomes, making it increasingly difficult for the approximate local boundary conditions to transmit outgoing waves without spurious reflection.

Figure 5.21 shows the computational domain discretized with 1518 axisymmetric elements using quadratic interpolation. Figure 5.22 shows the elevated contours of the time-discontinuous Galerkin solution using the second-order local boundary operator $\mathbb{S}_2$ applied to Γ_∞. In the upper left corner of Figure 5.22, the solution is shown at the end of the initial sine pulse at time $t = 1$. As time progresses, the initial pulse propagates outward from the sphere as a uniform spherical wave pulse of decreasing amplitude. The scales used in the illustrations are normalized at each time step to enhance the visibility of the solution features. After $t = 1$, the spherical pulse begins to pass through the artificial boundary Γ_∞ with negligible reflection. At time $t = 3.5$, as the pulse is just leaving the computational domain, it is noted that the numerical solution displays only insignificant traces of low amplitude reflected waves behind the outgoing wave front. For time steps beyond $t = 4$ (not shown), the low amplitude reflected waves are several orders of magnitude smaller than the amplitude of the physical wave, and are quickly damped out by the numerical dissipation inherent in the time discontinuous Galerkin method. This result illustrates the remarkable performance of the second-order operator $\mathbb{S}_2$ to transmit waves striking the artificial boundary at rather severe angles.

For comparison, this same problem was solved with the low-order boundary operator $\mathbb{S}_1$. Figures 5.23 and 5.24 show the elevated contours at times $t = 2.0$ and $t = 2.5$ respectively, comparing the solution using either $\mathbb{S}_1$ or $\mathbb{S}_2$. The solution using $\mathbb{S}_1$ exhibits significant reflections as the outgoing pulse passes through Γ_∞, as indicated by the elevated contours on the front (right) side of the sphere. In comparison, the solution using $\mathbb{S}_2$ shows no observable reflections from Γ_∞. This conclusion is summarized in Figure 5.25 as a plot of the solution on the artificial boundary Γ_∞ at the axis of symmetry, $\varphi = 0$. The solution using $\mathbb{S}_2$ shows the correct amplitude and phase for the outgoing pulse, and shows no observable reflections behind the wave front. In contrast, the solution using $\mathbb{S}_1$ shows an increase in the maximum amplitude of the outgoing pulse as well as significant reflections, as manifested by the non-zero amplitudes appearing for times $t > 2$.

5.4 Summary and Conclusions

When domain based computational methods are used to model the exterior fluid/structure interaction problem, accurate non-reflecting boundary conditions are required on the artificial truncation boundary. If the form of the non-reflecting boundary condition is over-simplified, for example the simple PW-damper defined in (2.24), spurious reflected waves can be generated at the artificial boundary, which can substantially degrade the accuracy of the numerical solution. In order to minimize the effect of spurious reflections, the computational region can be enlarged so that the artificial boundary is far from the radiator/scatterer, however, this will require an increase in the number of solution variables, with a subsequent increase in computational expense. It is thus preferable to use on Γ_∞ a non-reflecting boundary condition that is sufficiently accurate even when the artificial boundary Γ_∞ is very close to the radiating structure.

In this chapter, new local time-dependent non-reflecting boundary conditions which are exact for the first N spherical wave harmonics have been developed for the three-dimensional wave equation. The development of these boundary conditions begins from the truncated Dirichlet-to-Neumann (DtN) map in the frequency domain. By applying an inverse Fourier transform to the localized form of the DtN map, local time-dependent boundary conditions are obtained. We showed how these local boundary conditions can easily be incorporated into the time-discontinuous variational formulation as natural boundary conditions in both space and time, preserving the banded, sparse date structure of the method.

In addition, we demonstrated that an exact local in time counterpart exists for the spatially nonlocal and frequency dependent DtN non-reflecting boundary condition. This resulted in a sequence of exact boundary conditions that are nonlocal in space yet retain their locality in time. This new sequence of local in time and nonlocal in space nonreflecting boundary conditions allows for the use of C^0 interpolations in both the time and space dimensions. As a result, when implemented in the time-discontinuous finite element formulation, this sequence appears to offer the greatest potential for the implementation of accurate boundary operators beyond second-order.

A favorable feature inherited by the non-reflecting boundary conditions proposed

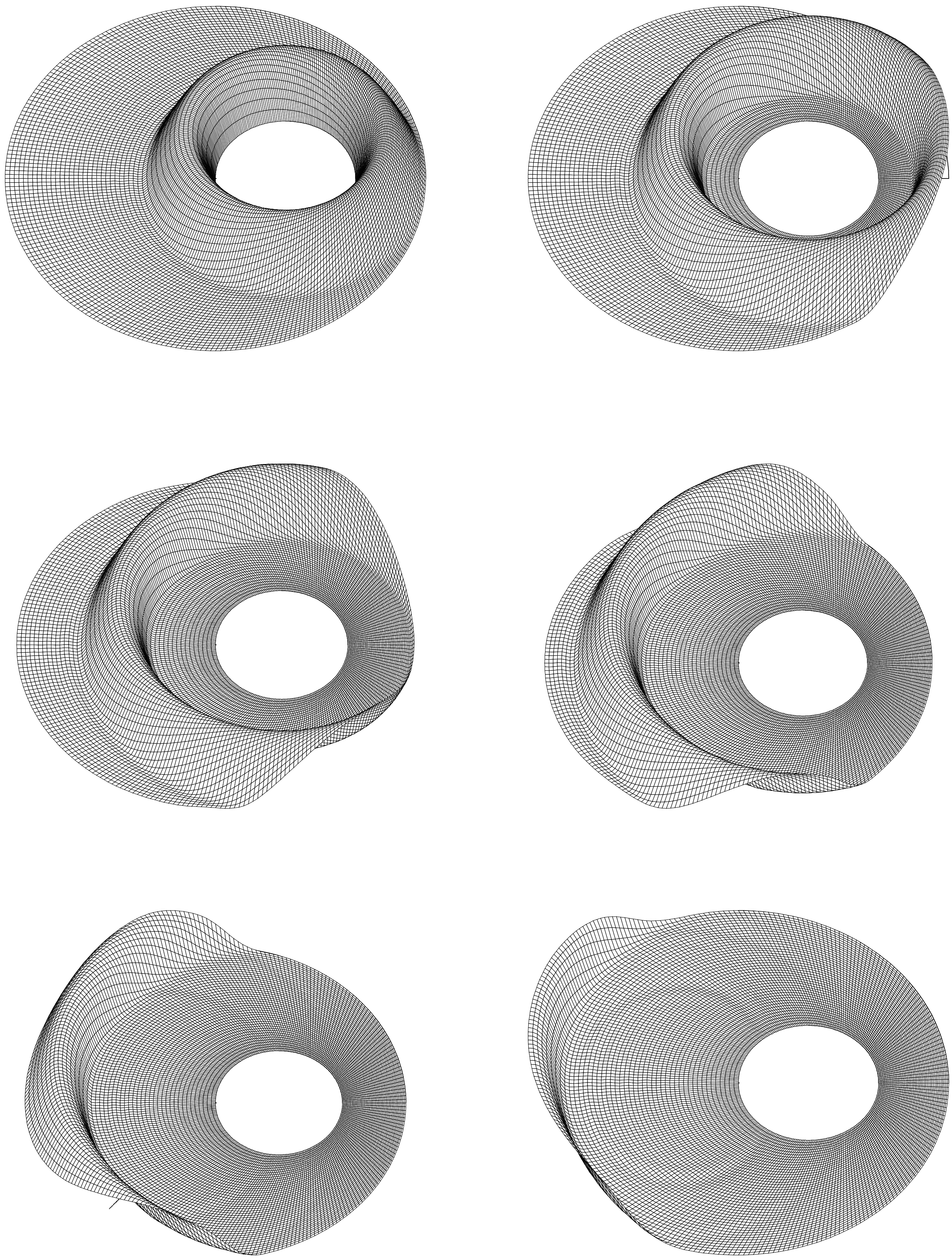

Figure 5.22: Radiation from a nonconcentric sphere. Elevated solution contours shown at the end of the initial pulse at $t = 1$ and later times $t = 1.5$ through $t = 3.5$ in increments of $\Delta t = 0.5$.

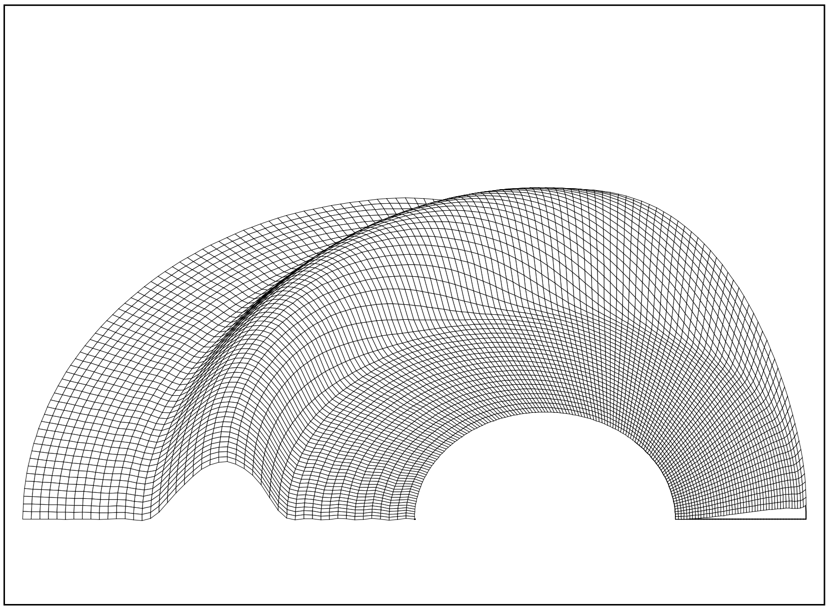

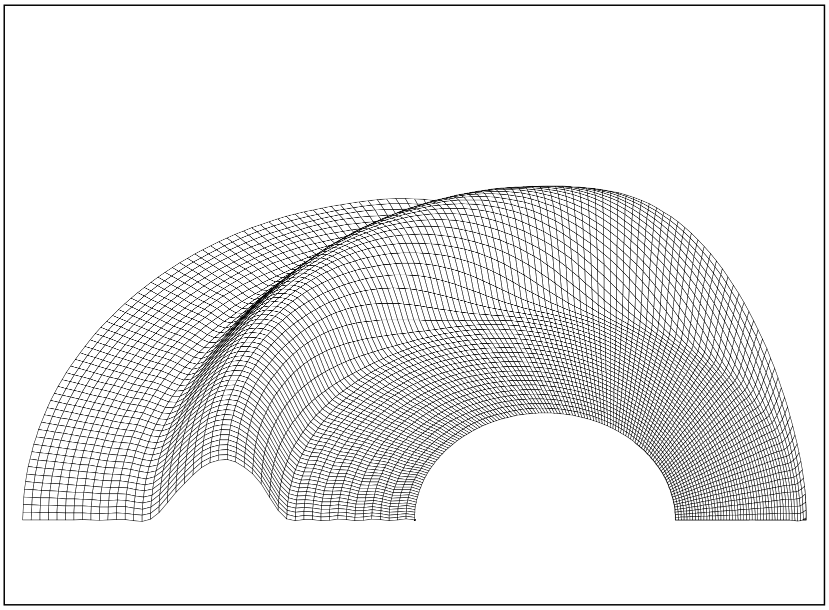

Figure 5.23: Radiation from a nonconcentric sphere. Elevated contours shown at $t = 2.0$. Space-time solution using (top) $\mathbb{S}_1$ local boundary condition. (bottom) $\mathbb{S}_2$ local boundary condition.

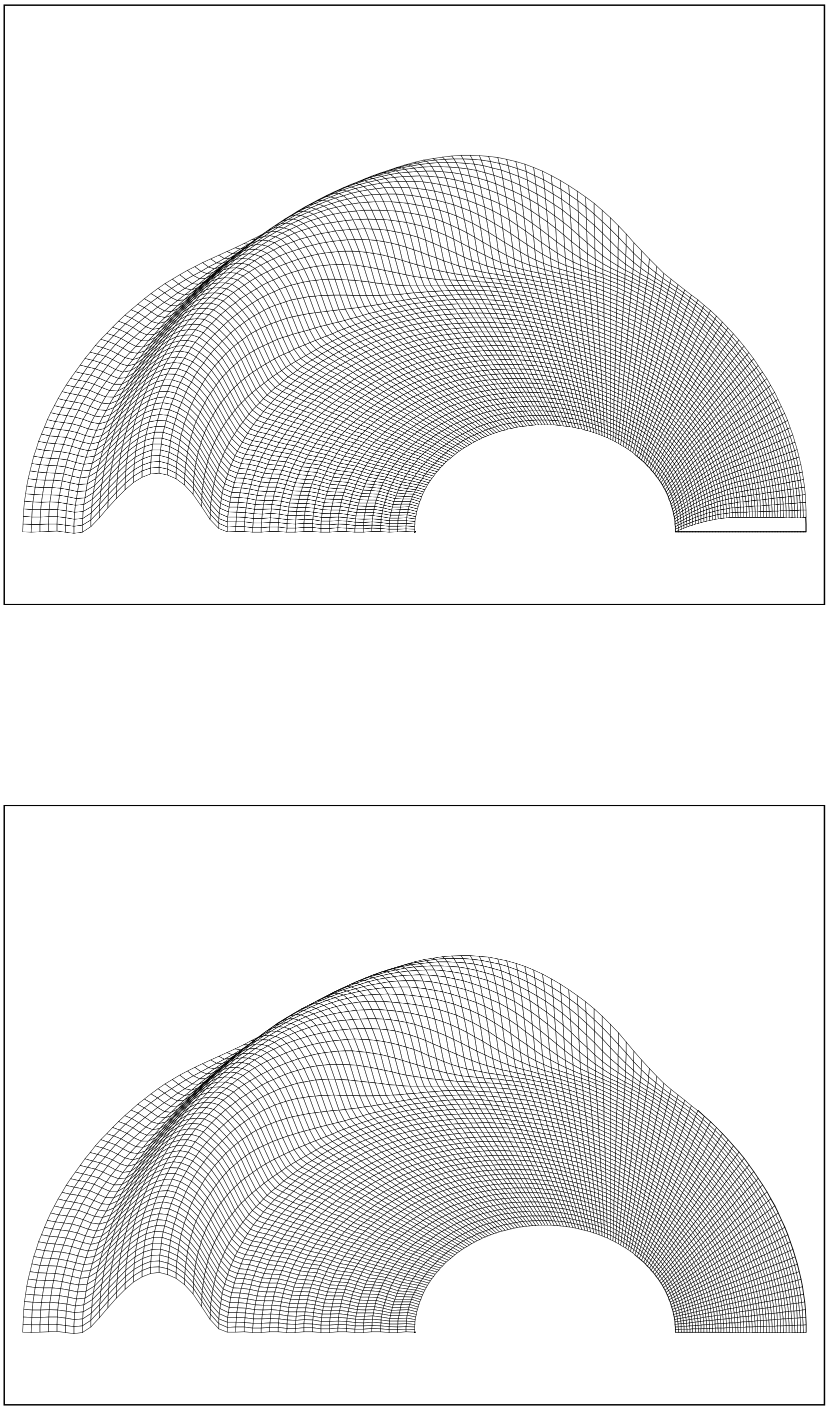

Figure 5.24: Radiation from a nonconcentric sphere. Elevated contours shown at $t = 2.5$. Space-time solution using (top) $\mathbb{S}_1$ local boundary condition. (bottom) $\mathbb{S}_2$ local boundary condition.

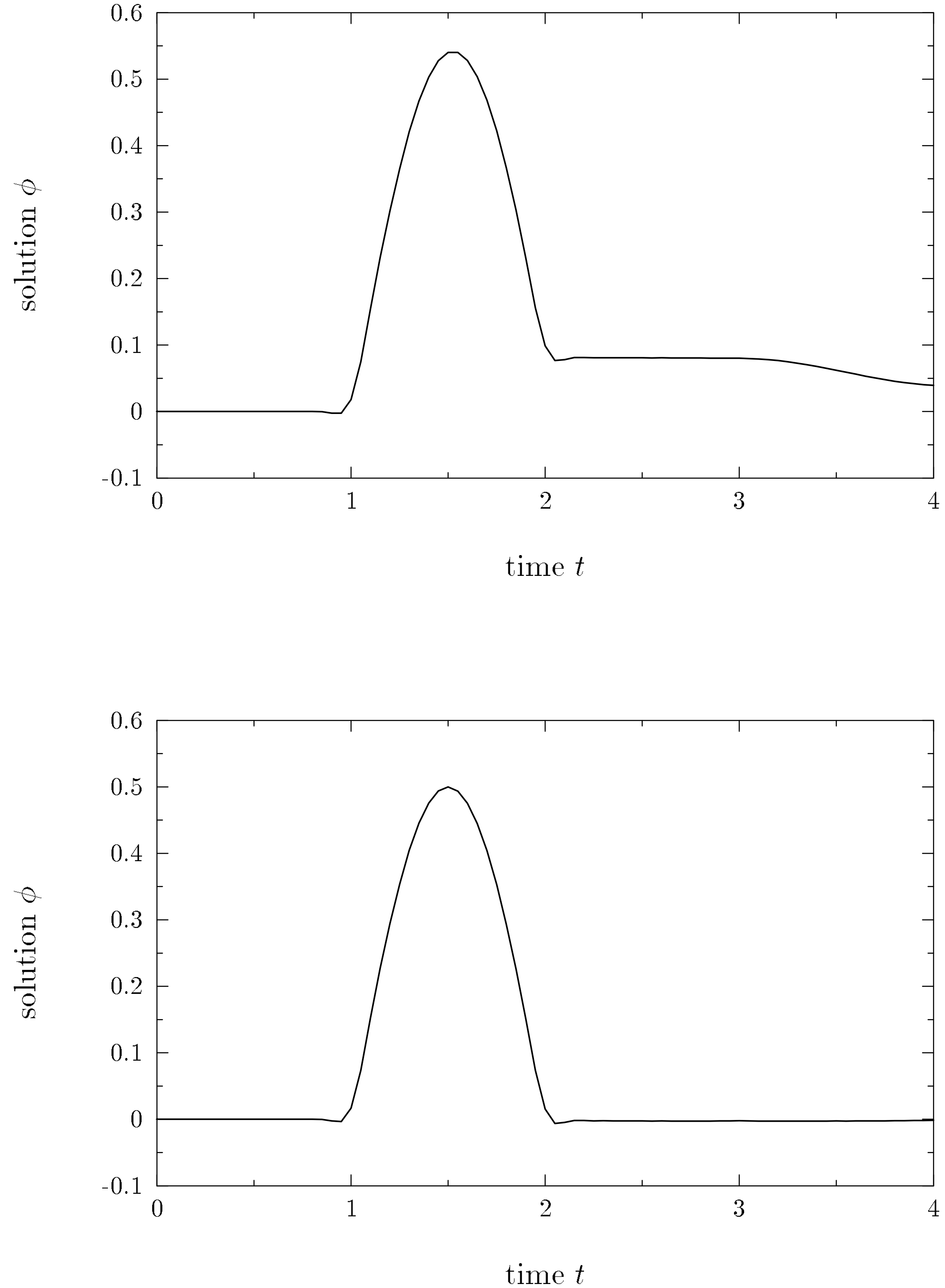

Figure 5.25: Radiation from a nonconcentric sphere: Solution on the artificial boundary Γ_∞, at the axis of symmetry $\varphi = 0$. (top) $\mathbb{S}_1$ local boundary condition. (bottom) $\mathbb{S}_2$ local boundary condition.

in this chapter is that they exactly represent the solution as a series of outgoing spherical wave harmonics. This property plays an important role in the understanding of how individual wave harmonics contribute to the accuracy and stability of the solution as effected by the radial distance of the artificial boundary from the source, and the geometric complexity and frequency content of the outgoing waves. In contrast, a physical understanding of the harmonic contribution to the accuracy and stability of boundary operators based on power series (multipole) expansions, such as the sequence derived by Bayliss and Turkel, is currently lacking.

Numerical solutions for some canonical time-dependent acoustic radiation problems demonstrated the improved accuracy that results from the use of the high-order non-reflecting boundary conditions within the space-time finite element method. In particular, the effects of increasing spherical harmonics n, frequency $\omega = kc$, and the position of the truncation boundary R, on the accuracy of the space-time finite element solution using the local radiation boundary operators was investigated. Results from this study are summarized in the following:

1. The local boundary operators provide increasing accuracy with the order N used in the truncated DtN series.

2. The accuracy depends strongly on the normalized frequency ka, in that the local operators can accurately capture increased wave harmonics as the frequency (wavenumber) is increased relative to the dimension of the radiator/scatterer.

3. The operators are increasingly accurate as the position R of the artificial boundary is moved further away from the radiator/scatterer.

Results from these studies, together with the numerical results obtained from a vibrating piston on a spherical baffle, and the transient radiation from a non-concentric sphere, support the conclusion that the local second-order non-reflecting boundary condition $\mathbb{S}_2$ exhibits superior accuracy when compared to the low-order local boundary conditions $\mathbb{S}_0$ and $\mathbb{S}_1$, with no additional cost. In addition, it has been demonstrated that when implemented in the time-discontinuous Galerkin method, the second-order operator $\mathbb{S}_2$ provides sufficient accuracy for the problems tested. These results suggests that when used with the proper consideration given to the position of the non-reflecting boundary, and the frequency content of the solution, then the local second-order operator provides an economical means to achieve accurate solutions to the transient structural acoustics problem in exterior domains. It remains to be seen what (if any) additional advantage in terms of accuracy and economy can be achieved by the implementation of the third-order operators derived in this chapter.

Chapter 6

Design of Time-Dependent Non-Reflecting Boundary Conditions: The Two-Dimensional Case

In the three-dimensional case, it is always possible to express high-order spherical Hankel functions appearing in the impedance coefficients of the Dirichlet-to-Neumann map in terms of the zero-order spherical Hankel function, see equation (5.8). It is this special property for the three-dimensional case which allows for the derivation of simple expressions for the non-reflecting boundary operators in terms of powers of the wavenumber. As a consequence, an exact inverse Fourier transform was readily obtained to yield time-dependent boundary conditions that are exact for the first N spherical harmonics. Using this procedure, two alternative local in time sequences of non-reflecting boundary conditions were obtained; a local in space version, and a nonlocal in space version.

In contrast, for the two-dimensional case it is not possible to express high-order cylindrical (integer) Hankel functions appearing in the exact Dirichlet-to-Neumann impedance relation solely in terms of the zero-order cylindrical Hankel function. While it is possible to obtain spatially local non-reflecting boundary conditions in the frequency domain that exactly represent the first N cylindrical wave harmonics (Givoli and Keller [1990]), time-dependent counterparts are not readily derived because of the difficulty in obtaining an exact inverse Fourier transform for the two-dimensional Hankel function. However by taking advantage of an asymptotic approximation for the two-dimensional Hankel function for large values of a non-dimensional wavenumber kR, where R is the radial distance to Γ_∞, an approximate localization of the exact impedance relation, i.e. the Dirichlet-to-Neumann mapping, can be obtained which has a simple inverse Fourier transform. The localization process follows by first recasting the exact solution for the exterior problem as a power series expansion, through a recurrence relation for the cylindrical Hankel functions in terms of the zero-order and first-order Hankel functions. By using a far-field approximation for large kR, an approximate asymptotic expansion is constructed in terms of negative powers of the wavenumber and the radial distance to the artificial boundary.

Following Bayliss and Turkel [1980,1982], a sequence of local (differential) operators are then derived which satisfy the first m terms in this asymptotic expansion. This can be considered as a way of matching the first m terms of an approximate solution for outgoing waves on Γ_∞. The operators in this sequence are of progressively higher order and provide increasing accuracy as more terms are matched in the expansion. These boundary operators have an inverse Fourier transform allowing a family of boundary conditions to be defined which are local in space and time.

6.1 Dirichlet-to-Neumann Map in the Frequency Domain

Consider the reduced wave equation (Helmholtz equation) in the exterior domain Ω_∞ with harmonic time dependence $e^{-i\omega t}$, and ω, the angular frequency, is real and positive:

$$\nabla^2\phi + k^2\phi = 0 \qquad \text{in } \Omega_\infty \tag{6.1}$$

$$\phi = \bar{\phi} \qquad \text{on } \Gamma_\infty \tag{6.2}$$

$$\lim_{r\to\infty} \sqrt{r}\left(\frac{\partial\phi}{\partial r} - ik\phi\right) = 0 \tag{6.3}$$

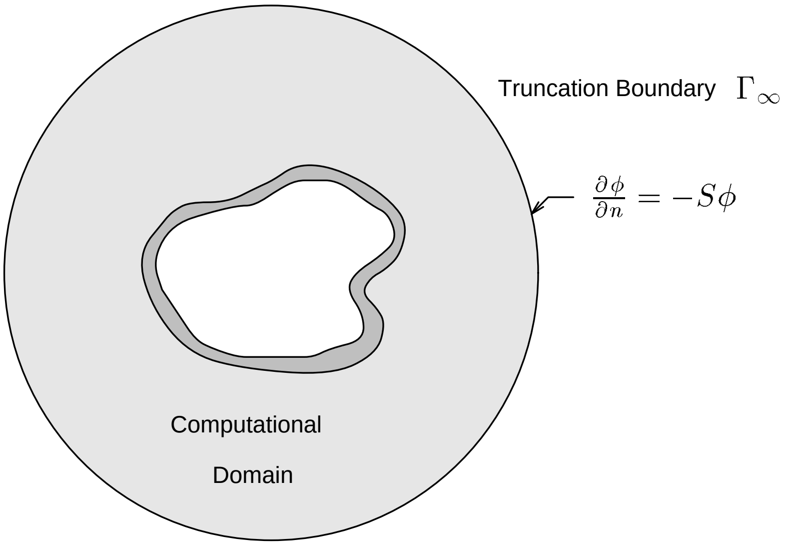

Figure 6.1: Illustration of a circular artificial boundary Γ_∞, enclosing the finite computational domain in $\mathrm{x} \in \mathbb{R}^2$.

where $k = \omega/c \geq 0$ is the acoustic wavenumber and $\bar{\phi}$ is the restriction of ϕ to Γ_∞. Equation (6.3) is the Sommerfeld radiation condition, (Sommerfeld [1964]) for the two-dimensional problem. This condition states that for a unique solution to the exterior problem, all waves at infinity must be outgoing. Restricting the artificial boundary Γ_∞ to be of separable geometry, in this case a circle of radius $r = R$ in two-dimensions (see Figure 6.1), we are able to express the general solution to this problem as an infinite series of cylindrical wave harmonics:

$$\phi(r,\theta) = \sum_{n=0}^{\infty} H_n(kr)(a_n \cos n\theta + b_n \sin n\theta) \qquad r \geq R \tag{6.4}$$

where for outgoing waves, $H_n(kr)$ are cylindrical Hankel functions of the first kind of order n. The function $\bar{\phi}(\theta)$ in (6.2) can be expanded in a Fourier series in the circumferential coordinate θ, and after equating its Fourier coefficients with (6.4) evaluated at $r = R$, i.e. setting $\phi(R,\theta) = \bar{\phi}(\theta)$, we obtain the two-dimensional solution,

$$\phi(r,\theta) = \sum_{n=0}^{\infty} \frac{H_n(kr)}{H_n(kR)} \alpha_n(\theta) \tag{6.5}$$

where

$$\alpha_n(\theta) = \frac{\varepsilon_n}{\pi} \int_0^{2\pi} \cos n(\theta - \theta')\ \phi(R, \theta')\ d\theta'$$

and $\varepsilon_0 = 1/2$ and $\varepsilon_n = 1, n \geq 1$.

Differentiating (6.5) with respect to r evaluated at $r = R$ results in the exact Dirchlet-to-Neumann (DtN) boundary condition in the frequency domain, see Keller and Givoli [1989].

$$\boxed{\frac{\partial \phi}{\partial n}(R, \theta) = \int_0^{2\pi} s_n(\theta - \theta')\ \phi(R, \theta')\ R\ d\theta'} \tag{6.6}$$

where

$$s_n(\theta - \theta') = \frac{\varepsilon_n\ k}{\pi R} \sum_{n=0}^{\infty} \frac{H_n'(kR)}{H_n(kR)} \cos n(\theta - \theta')$$

and $0 \leq \theta < 2\pi$ is the polar angle, and R is the radius of the circular truncation boundary Γ_∞. Eq. (6.6) can be written in operator form as,

$$\frac{\partial \phi}{\partial n} \quad = \quad -\mathbb{S}\ \phi \qquad \text{on } \Gamma_\infty \tag{6.7}$$

which represents a relation between Dirichlet and Neumann data through the linear operator $\mathbb{S}$. The DtN map $\mathbb{S}$, represents the exact impedance for the exterior acoustic fluid restricted to the artificial boundary. Furthermore, the operator $\mathbb{S}$ is an integral operator coupling all points on the artificial boundary Γ_∞, resulting in a nonlocal boundary condition. The direct time-dependent counterpart to this condition involves a convolution integral over time. As a result of the time integral, the boundary condition is nonlocal in time, requiring the storage of a large pool of historical data for long time solutions.

6.2 Local Boundary Operators in the Frequency Domain

For the two-dimensional case, it is not possible to express high-order cylindrical Hankel functions $H_n(kR)$, solely in terms of the zero-order function $H_0(kR)$ as was done for the three-dimensional case; see Watson [1966] for the definition of the cylindrical

Hankel functions $H_n(kR)$ as an infinite series involving the argument kR and the order n. While it is possible to obtain spatially local non-reflecting boundary conditions in the frequency domain that exactly represent the first N cylindrical wave harmonics (Givoli and Keller [1990]), time-dependent counterparts are not readily obtained do to the difficulty in obtaining an exact inverse Fourier transform for the two-dimensional Hankel function. To address this difficulty, we construct approximate boundary conditions which are local in both space and time by expressing the exact solution (6.5) in an alternative form. To this end, we use the recurrence formula for Hankel functions to express $H_n(kr)$ in (6.5) as a linear combination of $H_0(kr)$ and $H_1(kr)$, see Watson [1966]:

$$H_n(kr) = P_n H_0(kr) + Q_n H_1(kr) \tag{6.8}$$

where $P_n(1/kr)$ and $Q_n(1/kr)$ are Lommel's polynomials of degree n in the variable $1/kr$. The polynomials can be obtained recursively as,

$$P_n = \frac{2(n-1)}{kr} P_{n-1} - P_{n-2} \tag{6.9}$$

$$Q_n = \frac{2(n-1)}{kr} Q_{n-1} - Q_{n-2} \tag{6.10}$$

with starting values $P_0 = 1$, $P_1 = 0$, $Q_0 = 0$, $Q_1 = 1$. The resulting expression, namely

$$\phi(r,\theta) = H_0(kr) \sum_{n=0}^{\infty} P_n \frac{\alpha_n(\theta)}{H_n(kR)} + H_1(kr) \sum_{n=0}^{\infty} Q_n \frac{\alpha_n(\theta)}{H_n(kR)} \tag{6.11}$$

can be rearranged to take the form of an asymptotic expansion in $1/kr$:

$$\phi(r,\theta) = H_0(kr) \sum_{j=0}^{\infty} \frac{F_j(\theta)}{(kr)^j} + H_1(kr) \sum_{j=0}^{\infty} \frac{G_j(\theta)}{(kr)^j} \tag{6.12}$$

This series is uniformly and absolutely convergent and can be differentiated termwise with respect to r any number of times, see Karp [1961]. Interestingly, $F_0(\theta)$ contains only even-numbered coefficients, and $G_0(\theta)$ contains only odd ones:

$$F_0(\theta) = \sum_{n=0}^{\infty} \frac{(-1)^{n/2}}{H_n(kR)} \frac{\varepsilon_n}{\pi} \int_0^{2\pi} \cos n(\theta-\theta')\ \phi(R,\theta')\ d\theta' \qquad n = 0, 2, 4, \cdots$$

$$G_0(\theta) \;=\; \sum_{n=1}^{\infty} \frac{(-1)^{(n-1)/2}}{H_n(kR)} \frac{\varepsilon_n}{\pi} \int_0^{2\pi} \cos n(\theta-\theta')\ \phi(R,\theta')\ d\theta' \quad n = 1,3,5,\cdots$$

The coefficients $F_j(\theta)$ and $G_j(\theta)$ can be obtained recursively in terms of F_0 and G_0. They are nonlocal functions, and if evaluated explicitly would lead to an exact boundary condition. Here a method of eliminating this source of non-locality is described.

We first introduce the asymptotic expansion of the Hankel functions, for large kr, see WATSON [1966]:

$$H_n(kr) = (-i)^n \sqrt{\frac{2}{\pi kr}} e^{i(kr-\pi/4)} \left\{ 1 - \frac{(4n^2-1)}{8ikr} + \mathcal{O}\left((kr)^{-2}\right) \right\} \tag{6.13}$$

After substituting this approximation for $H_0(kr)$ and $H_1(kr)$ into (6.12) and accepting an error of the order $\mathcal{O}\left((kr)^{-3/2}\right)$ an approximate asymptotic expansion is obtained:

$$\boxed{\phi(r,\theta) \sim \hat{\phi}(r,\theta) = \sqrt{\frac{2}{\pi kr}} e^{i(kr-\pi/4)} \sum_{j=0}^{\infty} \frac{f_j(\theta)}{(kr)^j}} \tag{6.14}$$

where

$$f_0(\theta) = F_0(\theta) - i\ G_0(\theta) = \sum_{n=0}^{\infty} \frac{(-i)^n}{H_n(kR)} \frac{\varepsilon_n}{\pi} \int_0^{2\pi} \cos n(\theta-\theta')\ \phi(R,\theta')\ d\theta'$$

The coefficients $f_j(\theta)$ can be obtain recursively in terms of f_0.

Following BAYLISS AND TURKEL [1980,1992], a sequence of local differential operators which eliminate the first m nonlocal terms $f_j(\theta)$ in this asymptotic expansion is found. Splitting the asymptotic series (6.14) into two sums and multiplying by $r^{m-1/2}$ throughout, we obtain

$$r^{m-1/2}\hat{\phi} = e^{ikr} \sum_{j=1}^{m} r^{m-j} g_j(\theta) + e^{ikr} \sum_{j=m+1}^{\infty} r^{m-j} g_j(\theta) \tag{6.15}$$

where we have regrouped the coefficients as

$$g_j(\theta) = \sqrt{\frac{2}{\pi}} e^{-i\pi/4} f_{j-1}(\theta) k^{1/2-j}$$

Applying the local differential operator

$$L_o = \frac{\partial}{\partial r} - ik \tag{6.16}$$

to the power of m, i.e. $(L_o)^m$ to both sides of (6.15), the first sum is annihilated. In order to obtain a sequence of operators acting only on $\hat{\phi}$, we write explicitly for $m = 1$ and $m = 2$,

$$\begin{aligned} B_1\hat{\phi} &= L_o^1(r^{1/2}\hat{\phi})/r^{1/2} = (L_o + 1/2r)\hat{\phi} \\ B_2\hat{\phi} &= L_o^2(r^{3/2}\hat{\phi})/r^{3/2} = (L_o + 5/2r)(L_o + 1/2r)\hat{\phi} \end{aligned}$$

By analogy, the local operators are defined recursively as,

$$B_m = \prod_{j=1}^{m} (L_j) = L_m \; L_{m-1} \cdots L_2 \; L_1 \tag{6.17}$$

where

$$L_j = \left(\frac{\partial}{\partial r} - ik + \frac{2j - 3/2}{r} \right), \quad j = 1, 2, \cdots m \tag{6.18}$$

The B_m operator matches the first m terms in the expansion (6.14) with a remainder of order,

$$\begin{aligned} B_m\hat{\phi} &= \prod_{j=1}^{m} (L_j) \cdot \sqrt{\frac{2}{\pi kr}} e^{i(kr - \pi/4)} \sum_{j=1}^{\infty} \frac{f_{j-1}(\theta)}{(kr)^{j-1}} \\ &= \prod_{j=1}^{m} (L_j) \cdot \sqrt{\frac{2}{\pi kr}} e^{i(kr - \pi/4)} \sum_{j=m+1}^{\infty} \frac{f_{j-1}(\theta)}{(kr)^{j-1}} \\ &= \mathcal{O}\left(r^{-m} (kr)^{-m-1/2} \right) \end{aligned} \tag{6.19}$$

Remarks

1. Observe the character of the result (6.19) for fixed kr with increasing m, i.e, $\lim_{m\to\infty} B_m(\phi) = 0$ Thus we define as a hierarchical family of approximate boundary conditions on the artificial boundary,

$$B_m(\phi) := 0 \qquad \text{on} \;\; \Gamma_\infty \tag{6.20}$$

These are higher order boundary conditions on Γ_∞ and provide increasing accuracy with m, allowing in principle the computational region to be reduced to a minimum.

2. The accuracy of these local operators also depends strongly on the parameter kr such that for a fixed r,

$$\lim_{k\to\infty} B_m(\phi) = 0 \tag{6.21}$$

In this way, the B_m operators can be viewed as high frequency approximations of increasing order. From this property the local non-reflecting boundary conditions are increasingly accurate as the frequency (wavenumber) is increased relative to the dimension of the radiator/scatterer.

3. On the other hand, it is expected that the operators will be increasingly accurate as the position of the artificial boundary $r = R$, approaches infinity, i.e.,

$$\lim_{r\to\infty} B_m(\phi) = 0 \tag{6.22}$$

4. The well known plane-wave (PW) differential operator

$$L_o\phi = \left(\frac{\partial}{\partial r} - ik\right)\phi = \mathcal{O}(1/r(kr)^{1/2}) \tag{6.23}$$

is exact in one-dimension, however in higher dimensions, it is generally very inaccurate except at very high frequencies (short wavelength) or at large r. In fact, it can easily be seen that it does not even annihilate the first term in the expansion (6.14).

5. The sequence of operators B_m can be viewed as extensions of the plane-wave approximation. Indeed, we note that the first boundary operator B_1 in the sequence coincides with the cylindrical damper or curved wave approximation.

$$B_1\phi = \left(\frac{\partial}{\partial r} + \frac{1}{2r} - ik\right)\phi \tag{6.24}$$

As $r \to \infty$, the B_1 operator reduces to the PW radiation condition L_o.

6.3 Local Boundary Operators in the Time Domain

Time-dependent operators are obtained by applying an inverse Fourier transform to the time-harmonic operators defined in (6.17). In effect, replacing every occurrence of the operator $-ik$ by $\frac{1}{c}\frac{\partial}{\partial t}$ with the result,

$$\boxed{B_m = \prod_{j=1}^{m} \left(\frac{\partial}{\partial r} + \frac{1}{c}\frac{\partial}{\partial t} + \frac{2j - 3/2}{r} \right)} \tag{6.25}$$

The sequence of operators B_m provides increasing accuracy with m which, however, is also a measure of the difficulty of implementation. The operator B_m involves m^{th} order partial derivatives with respect to r and time t. High order radial partial derivatives are not desirable in the context of finite element analysis because of the implied higher order continuity condition between elements. For $m \geq 2$, the order of differentiation cannot be conveniently reduced to $C^o(\Gamma_\infty)$ by integration-by-parts in the weak form. However, all radial derivatives beyond the first can be eliminated in favor of tangential and time derivatives by the recursive use of the wave equation in polar coordinates:

$$\frac{\partial^2 \phi}{\partial r^2} + \frac{1}{r}\frac{\partial \phi}{\partial r} + \frac{1}{r^2}\Delta_\Gamma \phi - \frac{1}{c^2}\frac{\partial^2 \phi}{\partial t^2} = 0, \tag{6.26}$$

where $\Delta_\Gamma = \partial^2 / \partial \theta^2$ is the Laplace-Beltrami operator in two-dimensions.
For example consider the B_2 operator,

$$B_2 \phi = \frac{\partial^2 \phi}{\partial r^2} + \frac{2}{c}\frac{\partial^2 \phi}{\partial r \partial t} + \frac{1}{c^2}\frac{\partial^2 \phi}{\partial t^2} + \frac{3}{rc}\frac{\partial \phi}{\partial t} + \frac{3}{r}\frac{\partial \phi}{\partial r} + \frac{3\phi}{4r^2} \tag{6.27}$$

$\partial^2 \phi / \partial r^2$ can now be eliminated by use of (6.26), to arrive at a form with only first order radial derivatives.

$$\boxed{B_2 = \frac{1}{r}\frac{\partial}{\partial r} + \frac{1}{c}\frac{\partial^2}{\partial r \partial t} - \left(\frac{1}{2r^2}\right)\Delta_\Gamma + \frac{3}{8r^2} + \frac{3}{2rc}\frac{\partial}{\partial t} + \frac{1}{c^2}\frac{\partial^2}{\partial t^2}} \tag{6.28}$$

Note that the boundary operators are local in both space and time, i.e., they are differential operators. As a consequence, when used in a semidiscrete finite element method, the resulting equations form a mth order system of ordinary differential equations in time. For orders $m \leq 2$, standard time-stepping schemes can be used to solve the resulting system directly, see Chapter 7. However for $m \geq 3$, the boundary operators involve time derivatives up to the mth order, and special time-integrators must be developed. From this observation, it appears that a time-discontinuous space-time formulation may be the only practical way of implementing higher-order boundary conditions of this form beyond second-order.

6.4 Space-Time Finite Element Implementation

After elimination of higher order radial derivatives and restricting the artificial boundary to be a circle, we define the operators $\mathbb{S}_m$ in (2.33) as,

$$B_m(\phi) \equiv \frac{\partial \phi}{\partial n} + \mathbb{S}_m\, \phi \qquad \text{on} \quad \Gamma_\infty \tag{6.29}$$

which implies

$$\nabla \phi \cdot \boldsymbol{n} \quad = \quad -\mathbb{S}_m\, \phi \qquad \text{on} \quad \Gamma_\infty \tag{6.30}$$

which is in the form of a local, (i.e. differential) Dirichlet to Neumann boundary condition through the map $\mathbb{S}_m$. We identify the first two operators $\mathbb{S}_m$ for m equal to 1 and 2 as:

$$\mathbb{S}_1\, \phi \quad = \quad \frac{1}{2R}\phi + \frac{1}{c}\dot{\phi} \tag{6.31}$$

$$\mathbb{S}_2\, \phi \quad = \quad \frac{1}{2R}(3/4 - \frac{\partial^2}{\partial \theta^2})\phi + \frac{3}{2c}\dot{\phi} + \frac{R}{c}\frac{\partial \dot{\phi}}{\partial r} + \frac{R}{c^2}\ddot{\phi} \tag{6.32}$$

These boundary conditions are incorporated into the finite element method as natural boundary conditions, i.e., they are enforced weakly in space-time.

For $\mathbb{S}_2$, the acoustic intensity operator defined in (3.33) specializes to,

$$d_0(\dot{w}^h\,,\, \phi^h)_{(\Upsilon_\infty)_n} \quad = \quad \frac{3}{8R}(\dot{w}^h\,,\, \phi^h)_{(\Upsilon_\infty)_n} + \frac{1}{2R}(\dot{w}^h_{,\theta}\,,\, \phi^h_{,\theta})_{(\Upsilon_\infty)_n} \tag{6.33}$$

$$d_1(\dot{w}^h\,,\, \dot{\phi}^h)_{(\Upsilon_\infty)_n} \quad = \quad \frac{3}{2c}(\dot{w}^h\,,\, \dot{\phi}^h)_{(\Upsilon_\infty)_n} + \frac{R}{c}(\dot{w}^h\,,\, \dot{\phi}^h_{,r})_{(\Upsilon_\infty)_n} \tag{6.34}$$

$$d_2(\dot{w}^h\,,\,\ddot{\phi}^h)_{(\Upsilon_\infty)_n} \quad = \quad \frac{R}{c^2}(\dot{w}^h\,,\,\ddot{\phi}^h)_{(\Upsilon_\infty)_n} \tag{6.35}$$

Continuity requirements due to second-order tangential derivatives $\partial^2/\partial\theta^2$, are relaxed on the artificial boundary Γ_∞, by the use of the identity,

$$(w\,,\,\phi_{,\theta\theta})_{\Gamma_\infty} = -(w_{,\theta}\,,\,\phi_{,\theta})_{\Gamma_\infty} \tag{6.36}$$

Since these boundary operators are local in space and time, they preserve the sparse banded data structure of the finite element arrays. Analogous to the three-dimensional case, the second term in the expression for d_1 contains a spatially nonsymmetric contribution localized to the artificial boundary Γ_∞.

Recall that at Γ_∞, temporal continuity is weakly enforced across space-time slabs through temporal jump operators embedded in the operators $d_2(\cdot\,,\,\cdot)_{\Gamma_\infty}$ and $d_0(\cdot\,,\,\cdot)_{\Gamma_\infty}$, see (3.26). For $\mathbb{S}_2$, the consistent jump terms are,

$$\begin{aligned} d_0(w^h(t_n^+)\,,\,[\![\phi^h(t_n)]\!])_{\Gamma_\infty} \quad &= \quad \frac{3}{8R}(w^h(t_n^+)\,,\,[\![\phi^h(t_n)]\!])_{\Gamma_\infty} \\ &+ \quad \frac{1}{2R}(w^h_{,\theta}(t_n^+)\,,\,[\![\phi^h_{,\theta}(t_n)]\!])_{\Gamma_\infty} \end{aligned} \tag{6.37}$$

$$d_2(\dot{w}^h(t_n^+)\,,\,[\![\dot{\phi}^h(t_n)]\!])_{\Gamma_\infty} \quad = \quad \frac{R}{c^2}(\dot{w}^h(t_n^+)\,,\,[\![\dot{\phi}^h(t_n)]\!])_{\Gamma_\infty} \tag{6.38}$$

6.5 Numerical Examples: Radiation

In this section several two-dimensional numerical examples are solved to demonstrate the effectiveness of the time-discontinuous Galerkin space-time finite element method to accurately model time-dependent acoustic radiation. The problems studied are primarily designed to assess the performance of the two-dimensional, local non-reflecting boundary conditions when implemented in the space-time formulation. For all the numerical results presented, the GLS mesh parameters were set to zero and quadratic space-time finite elements were used throughout.

6.5.1 Circumferential harmonic radiation

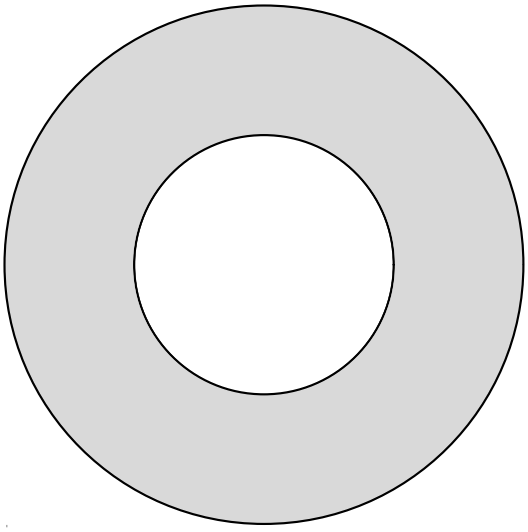

Figure 6.2: Circular cylinder of radius $r = a$, enclosed by a circular artificial boundary of radius $R = 2a$.

In this example we study the uncoupled problem of an infinite circular cylinder of radius $a = 1$, with circumferentially harmonic radiation loading,

$$\phi(a, \theta, t) = \cos n\theta \sin \omega t \qquad \text{for } 0 \leq \theta < 2\pi\,, \quad t > 0 \tag{6.39}$$

The exact steady-state solution for this problem is for $r \geq a$,

$$\phi(r, \theta, t) = -\mathrm{Imag}\left\{ \frac{H_n(kr)}{H_n(ka)} \cos n\theta \mathrm{e}^{-i\omega t} \right\} \tag{6.40}$$

where H_n are cylindrical Hankel functions of the first kind of order n. When using a finite element method incorporating approximate non-reflecting boundary conditions on a circular artificial boundary as illustrated in Figure 6.2, this problem becomes increasingly difficult to solve as the circumferential harmonic n increases. It is expected that as the mode n is increased and the radiation pattern becomes more complex, the higher-order operators $\mathbb{S}_m$ will be increasingly accurate compared to the simple PW damper, denoted $\mathbb{S}_0$.

Taking advantage of the symmetry in this problem, the computational domain is taken as, $\Omega = \{a < r < R,\ 0 \leq \theta < \pi\}$, where the truncation boundary is set at $R = 2a$ and Ω is discretized with 10 elements in the radial direction, and 40 elements

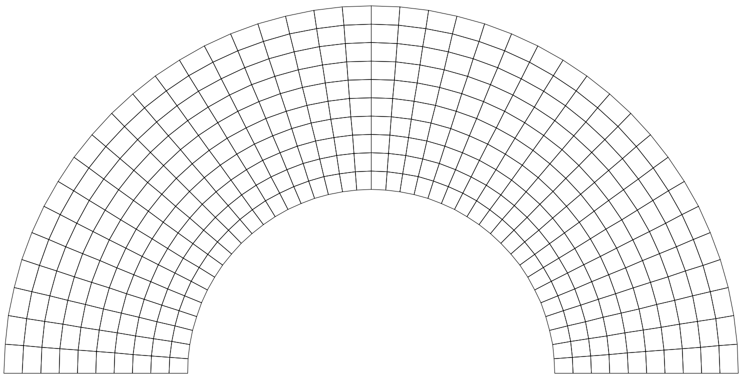

Figure 6.3: Finite element mesh for the radiating circular cylinder: By symmetry, only the upper half is discretized with 400 quadratic elements.

in the polar direction; see Figure 6.3. A series of transient space-time finite element solutions were obtained for this two-dimensional problem using zero initial conditions on ϕ and $\dot{\phi}$ and a time-increment of $\Delta t = 0.1$.

Harmonic $n = 0$:

In order to study the accuracy of the boundary operator $\mathbb{S}_1$ to transmit uniform acoustic radiation, we set $n = 0$, resulting in the 'breathing' mode $\phi(a,t) = \sin \omega t$. An exact local radiation condition on a circular boundary Γ_∞ can be obtained for this simple case of uniform radiation in the frequency domain by setting $n = 0$ in (6.4), differentiating with respect to r and evaluating the result at $r = R$.

$$\frac{\partial \phi}{\partial r} = -k \frac{H_1(kR)}{H_0(kR)} \phi \qquad \text{at} \quad r = R \tag{6.41}$$

As this boundary condition involves the cylindrical Hankel function, its exact time-dependent counterpart cannot be readily obtained. However by using the asymptotic representation of $H_0(kr)$ as $kr \to \infty$ given in (6.13), the asymptotic solution to this

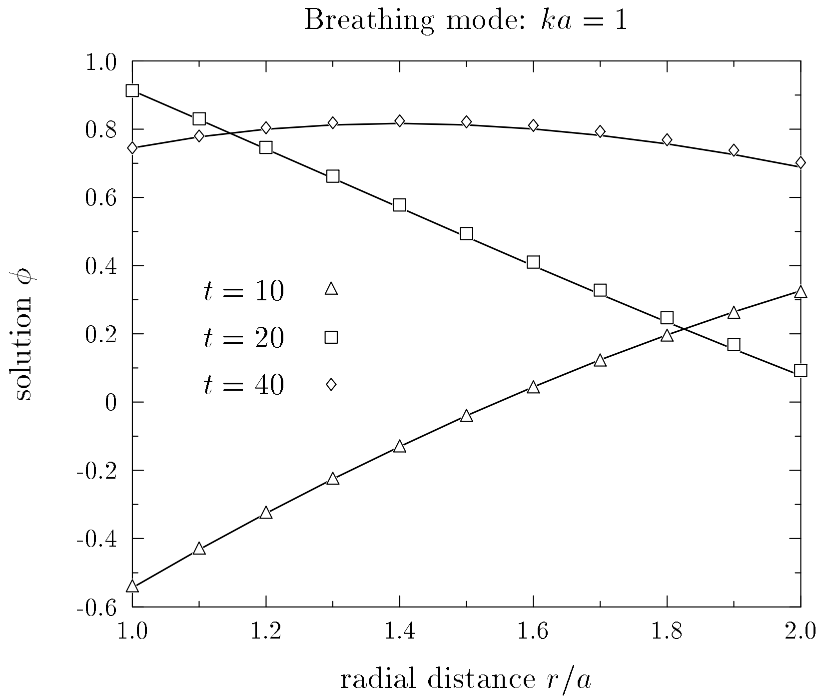

Figure 6.4: Breathing mode ($n = 0$) for circular cylinder with $ka = 1$. Solution using S_1 local boundary condition; profile along the radial distance $a < r < R$, at times $t = 10, 20, 40$.

problem becomes,

$$\phi(r,t) \sim \tilde{\phi} = \frac{1}{H_0(ka)}\sqrt{\frac{2}{\pi kr}}e^{ik((r-\pi/4)-ct)} \qquad \text{for } kr \to \infty \tag{6.42}$$

The nature of the cylindrical wave motion is evident from this asymptotic solution; it reduces to a spreading wave with a $(1/\sqrt{r})$ amplitude decay in the far field, while the wave field near the cylinder is relatively complex. Differentiating with respect to r and taking an inverse Fourier transform we obtain,

$$\frac{\partial\tilde{\phi}}{\partial r} = \left(-\frac{1}{c}\frac{\partial}{\partial t} - \frac{1}{2R}\right)\tilde{\phi} \qquad \text{at } \ r = R \tag{6.43}$$

This local condition is identical to the B_1 operator defined in (6.25) and is asymptotically convergent to the exact solution for large kr:

$$B_1(\tilde{\phi}) = \left(\frac{\partial}{\partial r} + \frac{1}{c}\frac{\partial}{\partial t} + \frac{1}{2r}\right)\tilde{\phi} = 0 \tag{6.44}$$

This conclusion is also valid for any higher order local boundary operator, (B_m, $m \geq 2$), i.e.

$$B_m(\tilde{\phi}) = \prod_{j=2}^{m}(L_j) \cdot B_1(\tilde{\phi}) = \prod_{j=2}^{m}(L_j) \cdot 0 = 0 \qquad \text{for } m \geq 2 \tag{6.45}$$

where the definition of the differential operators L_j are defined in (6.18). We expect the operators (B_m, $m \geq 2$) to add no additional increase in accuracy for this special case involving uniform cylindrical waves.

Figure 6.4 shows the profile of the transient space-time finite element solution for $ka = 1$ along the radial coordinate at three sample times. The solution sample times are chosen such that many spurious reflections between the artificial boundary and the cylinder could have occurred. From these results it is observed that the operator $\mathbb{S}_1$, when implemented in the discontinuous Galerkin formulation gives very accurate solutions for the cylindrical 'breathing' ($n = 0$) mode as expected. As the normalized frequency ka, is increased, it is observed that the solution becomes increasingly accurate.

Harmonic $n = 1$:

In this example, the accuracy of the second-order boundary operator $\mathbb{S}_2$ in transmitting waves corresponding to harmonic $n = 1$, is studied. Figure 6.5 illustrates the contours of the discontinuous Galerkin solution for $ka = 1$ and incorporating the 'plane-wave' boundary operator, denoted $\mathbb{S}_0$, the first-order, $\mathbb{S}_1$ and second-order $\mathbb{S}_2$ boundary operators defined in (6.31) and (6.32). Figure 6.6 shows the solution profile around the artificial boundary and the solution plotted along a radial line located at the angle $\theta = 0$, at time $t = 30$. Results confirm that the local operator $\mathbb{S}_2$, when implemented in the space-time formulation, gives accurate solutions while solutions using either $\mathbb{S}_0$ or $\mathbb{S}_1$ have significant error.

Harmonic $n = 2$:

As the harmonic loading is increased to $n = 2$, the acoustic radiation pattern becomes more complex. For a driving frequency $ka = 1$, significant errors occur in the solution using $\mathbb{S}_0$ or $\mathbb{S}_1$, while the solution using $\mathbb{S}_2$ remains accurate throughout the computational domain, see Figures 6.7 and 6.8 .

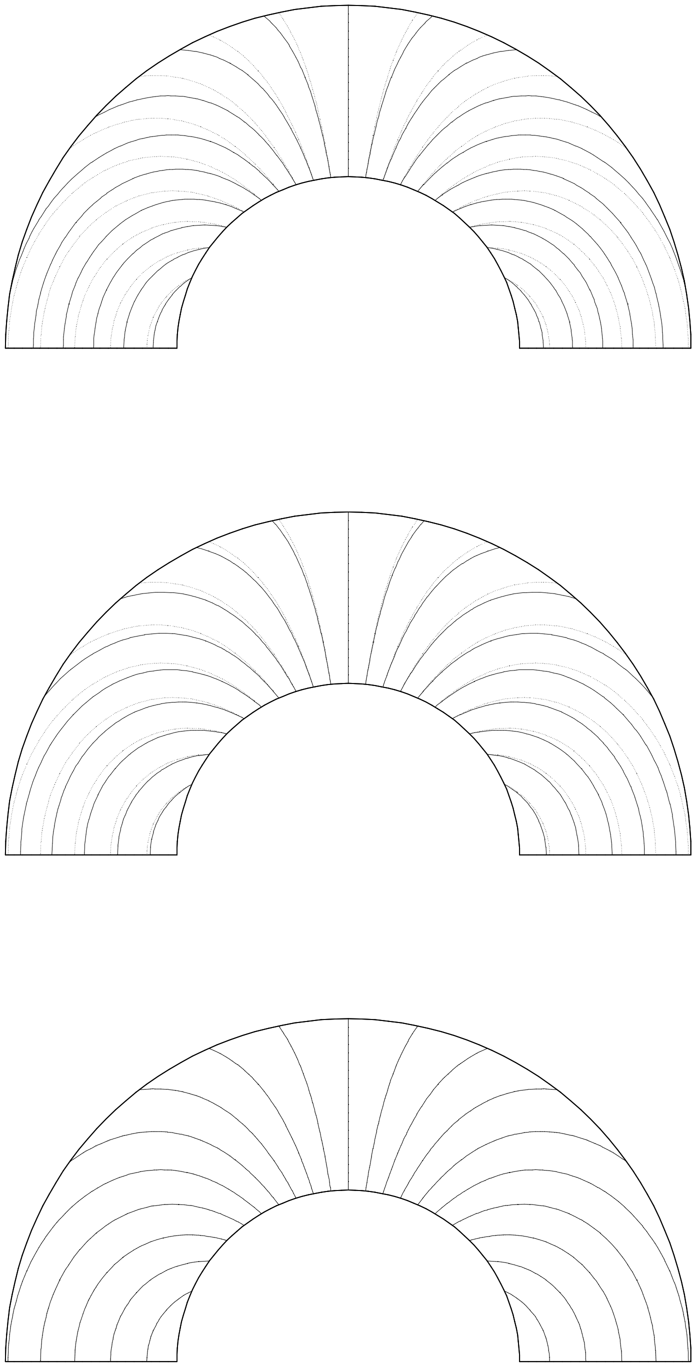

Figure 6.5: Radiation from a circular cylinder with circumferential harmonic $n = 1$, and normalized frequency $ka = 1$. Contours of space-time solution at time $t = 30$, using local boundary conditions, (Top): 'plane-wave' S_0, (Middle): first-order S_1, (Bottom): second-order S_2. (dotted contours denote analytical solution).

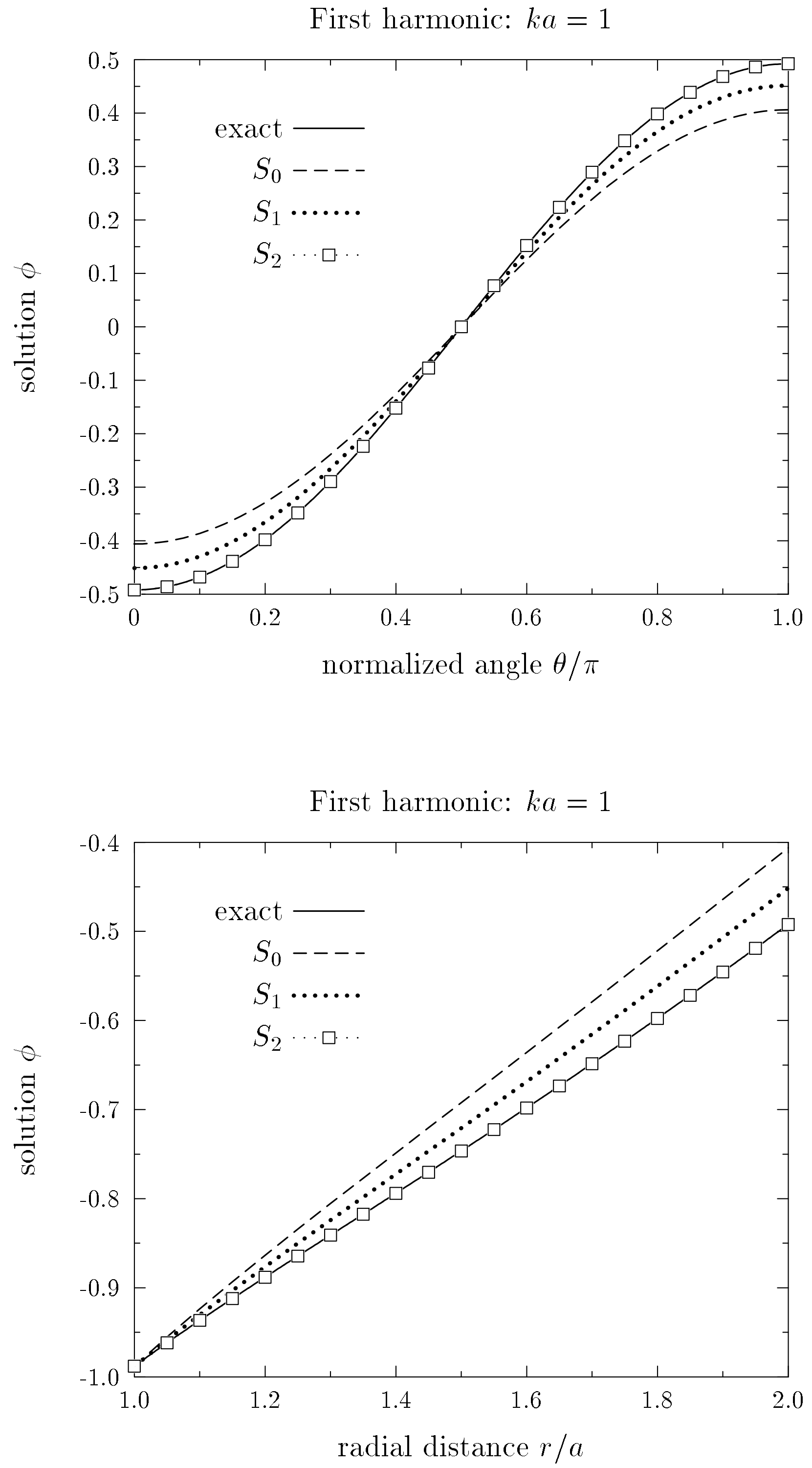

Figure 6.6: Circumferential wave harmonic $n = 1$: Results at $t = 30$, comparing the 'plane-wave' S_0, first-order S_1, and second-order S_2 boundary conditions. (Top): Solution profile on the artificial boundary $r = R$. (Bottom): Solution plotted along radial line at $\theta = 0$.

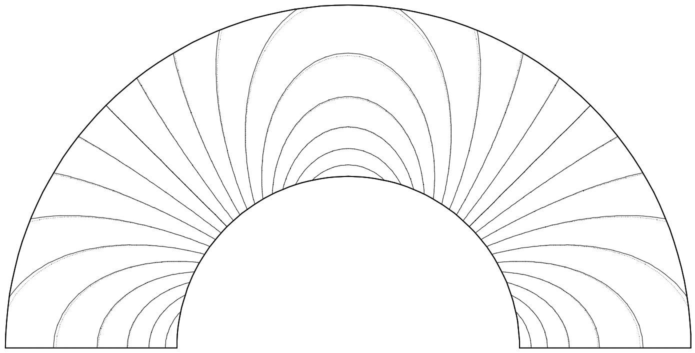

Figure 6.7: Radiation from a circular cylinder with circumferential harmonic $n = 2$, and normalized frequency $ka = 1$. Contours of space-time solution at time $t = 30$, using the second-order S_2 local boundary condition. (dotted contours denote analytical solution).

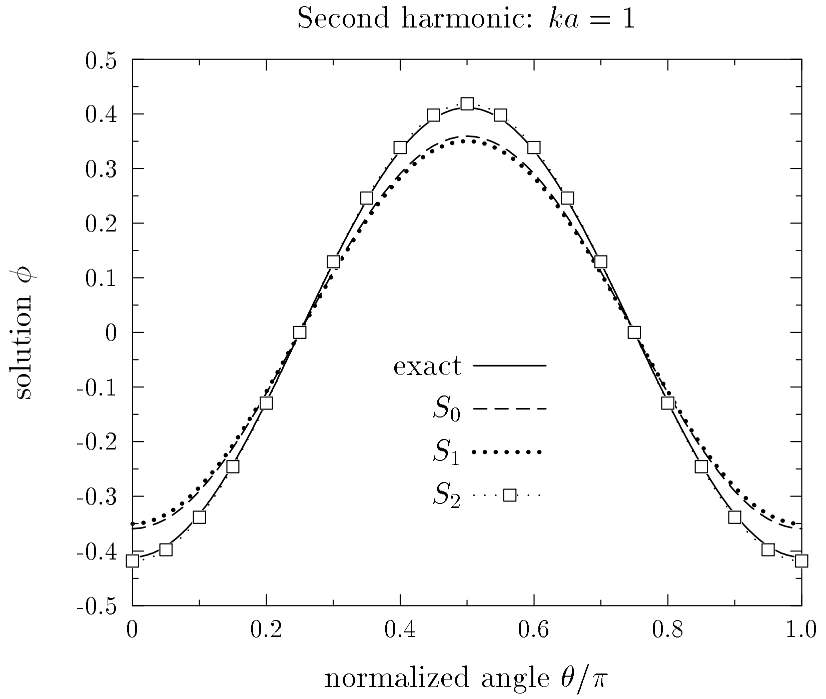

Figure 6.8: Circumferential wave harmonic $n = 2$: Results at $t = 30$, comparing the 'plane-wave' S_0, first-order S_1, and second-order S_2 boundary conditions. Solution profile on the artificial boundary $r = R$.

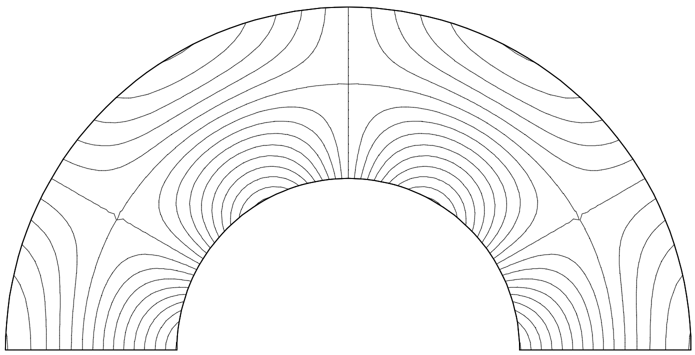

Figure 6.9: Radiation from a circular cylinder with circumferential harmonic $n = 3$, and normalized frequency $ka = 3$. Contours of space-time solution at time $t = 20$, using the second-order S_2 local boundary condition. (dotted contours denote analytical solution).

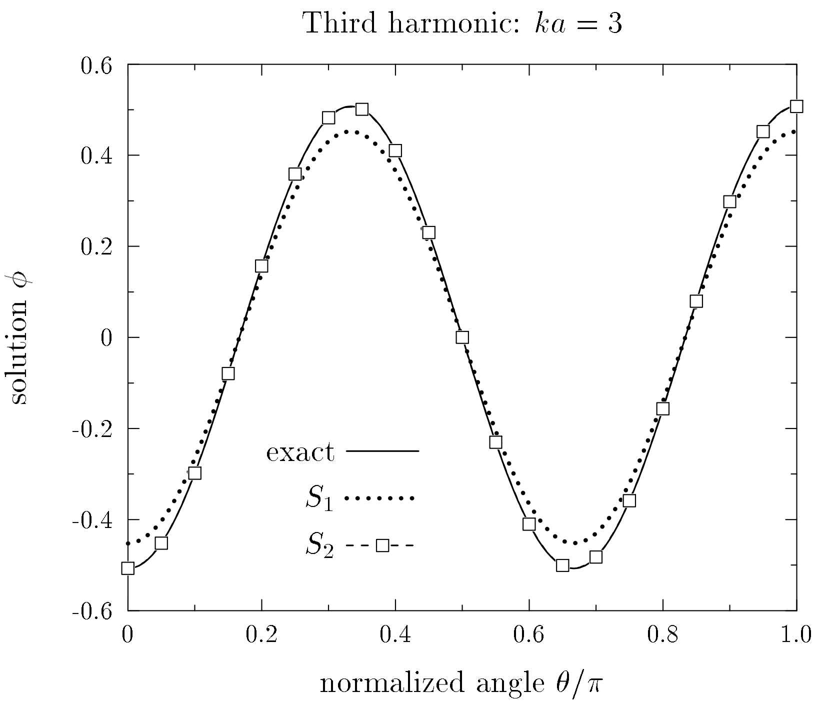

Figure 6.10: Circumferential wave harmonic $n = 3$: Results at $t = 20$, comparing the first-order S_1, and second-order S_2 boundary conditions. Solution profile on the artificial boundary $r = R$.

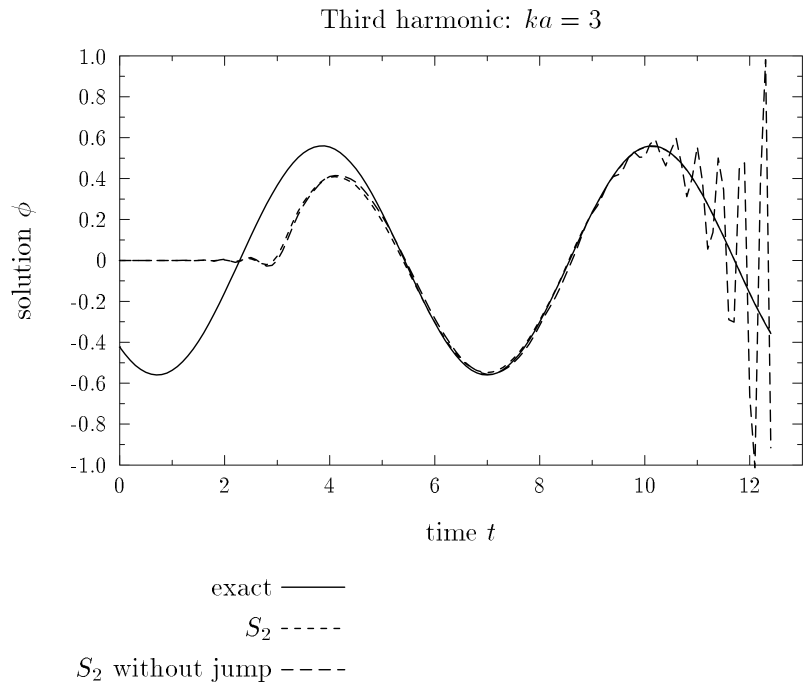

Figure 6.11: Illustration of stability: Radiating circular cylinder with loading $\cos 3\theta \sin \omega t$. Results at the artificial boundary Γ_∞, demonstrate that temporal jump terms are needed on Γ_∞ for stability.

Harmonic $n = 3$:

Numerical solutions for harmonic $n = 3$, with $ka = 1$ show significant error for all three local boundary operators tested. However by increasing the nondimensional wavenumber to $ka = 3$, accurate results are obtained for $\mathbb{S}_2$, see Figures 6.9 and 6.10. Results using $\mathbb{S}_1$ show significant error in the solution, while the solution using $\mathbb{S}_2$ is very accurate; with the numerical and analytical solutions almost indistinguishable. This example demonstrates how for a fixed distance R, and order m, the sequence of local boundary operators become increasingly accurate as the wavenumber is increased.

6.5.2 Illustration of Stability

Figure 6.11 illustrates the need for the weak enforcement of initial data between time slabs on the truncation boundary Γ_∞. The result shows the solution time-history for harmonic $n = 3$, on the truncation boundary at $(r\,,\,\theta) = (R\,,\,0)$. The solid line is the exact time-harmonic solution. When the consistent jump terms defined in (6.37) and

(6.38) are included, the local boundary condition, $\mathbb{S}_2$, displays the correct transient solution for short time, (time less than 6 seconds), and then quickly assumes the exact steady-state solution. When the temporal jump terms are omitted, i.e.

$$\begin{aligned} d_2(\dot{w}^h(t_n^+)\,,\, [\![\dot{\phi}^h(t_n)]\!])_{\Gamma_\infty} &= 0 \\ d_0(w^h(t_n^+)\,,\, [\![\phi^h(t_n)]\!])_{\Gamma_\infty} &= 0 \end{aligned}$$

then the solution quickly becomes unstable, generating large spurious oscillations, leading eventually to overflow. This example demonstrates how these additional operators are needed to ensure a stable solution, and are the key element that enable generalization of the time discontinuous Galerkin method to handle non-reflecting boundary conditions.

6.5.3 Radiation from a line element on a cylinder

To study the performance of the local non-reflecting boundary conditions for a challenging problem involving an infinite number of circumferential harmonics, consider the non-uniform radiation from a line element on an infinite circular cylinder of radius $r = a$, with loading

$$\phi(a, \theta, t) = \sin \omega t, \qquad \text{for } -\theta_p \leq \theta \leq \theta_p, \quad t > 0 \tag{6.46}$$

Elsewhere on the surface $r = a$, the solution vanishes. The steady-state analytical solution for this problem is,

$$\phi(r, \theta, t) = -\text{Imag}\left\{ \sum_{n=0}^{\infty} \frac{H_n(kr)}{H_n(ka)} \left[\frac{\epsilon_n \sin \theta_p}{n\pi} \right] \cos n\theta \, \mathrm{e}^{-i\omega t} \right\} \tag{6.47}$$

where $\epsilon_0 = 1/2$ and $\epsilon_n = 1, n \geq 1$ and H_n are Hankel functions of the first kind of order n. For low values of the normalized wavenumber ka, this solution is relatively uniform in the circumferential direction. The directionality of the solution grows as the wavenumber k is increased, and the solution becomes attenuated at the side of the cylinder opposite the radiating element.

In this example, the properties and discretization are unchanged from the previous problem. Figure 6.12 (top) shows the contours of the analytical series solution with

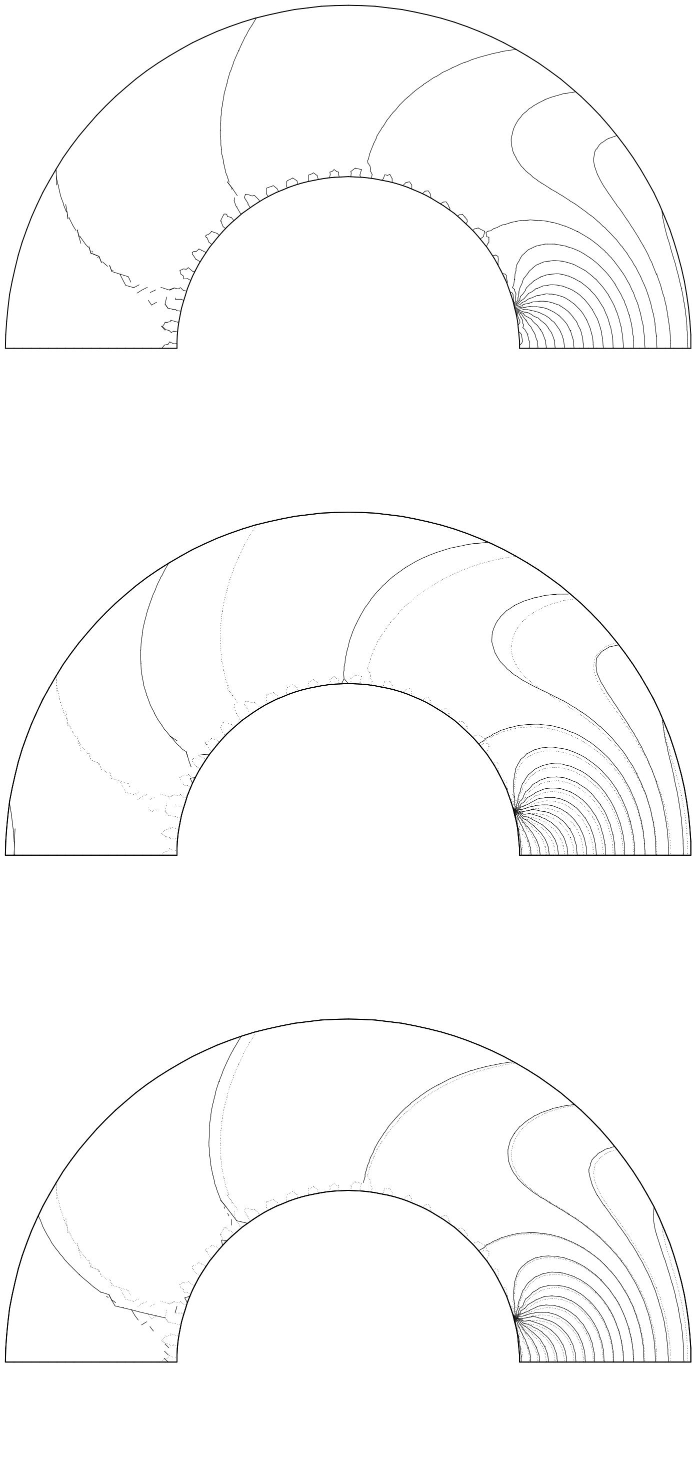

Figure 6.12: Solution contours for radiating element on a circular cylinder: (Top): Analytic series solution (50 terms) at time $t = 30$ and normalized frequency $ka = 3$. Space-time solution with local boundary condition, (Middle): $\mathbb{S}_1$ (Bottom): $\mathbb{S}_2$ (dotted contours denote analytic solution)

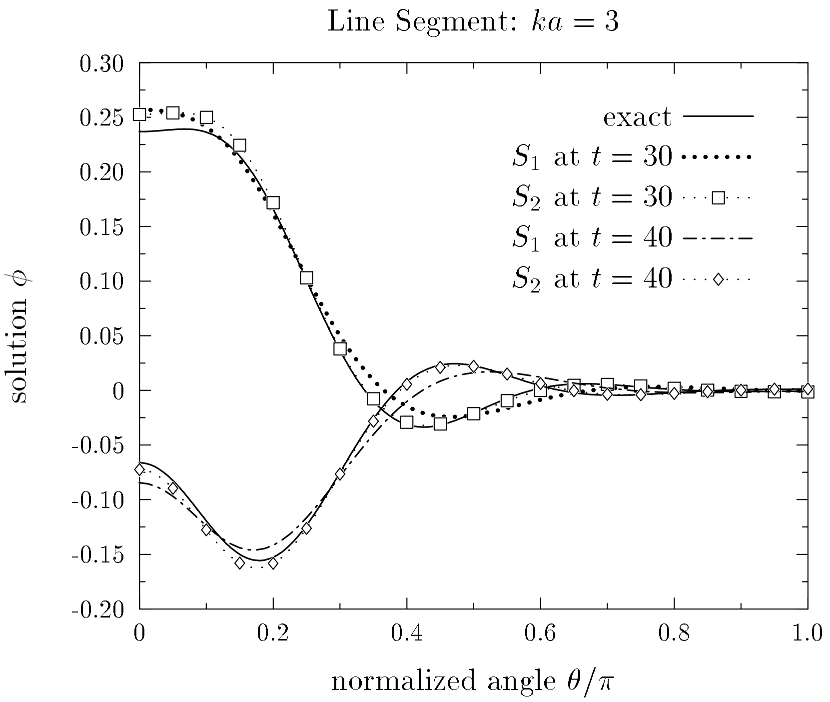

Figure 6.13: Radiating circular cylinder with line segment loading. Solution profile on the artificial boundary $r = R$.

$ka = 3$, nodally interpolated with the mesh employed. The low-amplitude oscillations in the vicinity of the inner boundary are a result of the difficulty the series solution has in resolving the discontinuity in the loading at $\theta_p = 13.5^o$, and are not relevant to the validation of the numerical results. Near $\theta = 0$, solutions using either the boundary condition $\mathbb{S}_1$ or $\mathbb{S}_2$ accurately capture the physics of the problem while as the wave spreads to the backside of the cylinder at $\theta = 180^o$, the solution using $\mathbb{S}_1$ deteriorates significantly while $\mathbb{S}_2$ maintains an accurate solution in this difficult region. These results are quantified in Figure 6.13, as a profile of the solution on Γ_∞ at $r = R$. Results from this and the previous example show the significant improvement in the numerical solution using the second-order operators $\mathbb{S}_2$, in comparison to the numerical solution using the operators $\mathbb{S}_1$ or $\mathbb{S}_0$.

6.6 Numerical Examples: Scattering

In this section numerical simulations of transient scattering from geometrically complex shapes are performed in order to demonstrate the effectiveness of the time-discontinuous Galerkin space-time finite element method to model multi-dimensional wave phenomena. In the following examples, use is made of the second-order local non-reflecting boundary condition $\mathbb{S}_2$ defined in (6.32). GLS mesh parameters are set to zero and quadratic space-time finite elements are used throughout.

6.6.1 Transient scattering from a circular cylinder

For this first example, consider the time-dependent scattering from an infinite circular cylinder of radius $r = a$. In the upper left corner of Figure 6.14 the finite element spatial discretization of the computational domain $\Omega = \{a \leq r \leq R,\, 0 \leq \theta \leq 2\pi\}$ bounded internally by the projection of the infinite circular cylinder, and externally by a circular artificial boundary with radius $R = 3a$ is shown. By symmetry only half the problem is modeled with 1200 quadratic elements. An incident pulse of short duration is generated by an acoustic source positioned midway between the cylinder and the circular artificial boundary, Γ_∞. This example represents a challenging problem where both the incident wave pulse and scattered waves should be transmitted through Γ_∞ with negligible reflection.

For this two-dimensional problem, the second-order local boundary condition defined in (6.32) is prescribed on Γ_∞. The source $f = \delta(x_0, y_0)\sin\omega t$ and $t \in [0\,,\,0.5]$, is positioned inside the computational domain at $(x_0, y_0) = (2a, 0)$, simulating an incident wave during a short time period. Setting the phase speed at $c = 1$ and frequency $\omega = 2\pi$ results in a challenging initial condition. The numerical simulation is continued until just prior to reaching the practical disappearance of the signal from the computational domain.

The numerical simulation at the end of the initial pulse is shown in Figure 6.14 at $t = 0.5$. The subsequent figures show the contours of the scattering phenomena with homogeneous Dirichlet boundary conditions on the cylinder surface $r = a$, i.e. 'release' boundary conditions. The following sequence of events occur:

- At $t = 1.5$ the incident pulse has expanded in a cylindrical wave and has just begun to reflect off the surface of the inner cylinder, while at the artificial boundary, the wave front passes through the boundary with no observable reflection.

- At $t = 2.5$ the incident wave continuous to diffract around the cylinder, creating a backscattered cylindrical wave that moves to the right and passes through the wake of the incident wave.
- At $t = 3.0$ the backscattered wave has just reached the artificial boundary.
- At $t = 4.0$ the backscattered wave is also transmitted through the artificial boundary with no observable reflection.

As a result of the homogeneous Dirichlet boundary conditions, the contours near the wet surface lie parallel to the cylinder outline and the amplitude of the backscattered wave is negative. Figure 6.15(top) shows the transient solution on the artificial boundary at the point $(r\,,\,\theta) = (R\,,\,0)$, for the case of homogeneous Dirichlet ('release') boundary conditions at the inner cylinder. Prior to time $t = 1$, the initial pulse has not reached the boundary Γ_∞ as indicated by the quiescent solution. Upon arrival at time $t = 1$, the solution advances as a sharp pulse with a wake of decaying amplitude. At time $t = 2.5$, the backscattered wave reaches Γ_∞, as indicated by pulse of negative amplitude.

For comparison, Figure 6.15(bottom) shows the transient solution when the boundary condition at the inner cylinder is changed to a homogeneous Neumann condition, i.e. a 'rigid' boundary condition. In this case the backscattered wave takes a positive amplitude.

6.6.2 Transient scattering from a square cylinder

In the next example consider the time-dependent scattering from an infinite square cylinder of dimension $a \times a$. The finite element spatial discretization for this problem is shown in Figure 6.16. By symmetry only the upper half is modeled with 1386 quadratic elements. The source $f = \delta(x_0, y_0)\sin\omega t$ and $t \in [0, 0.5]$, is prescribed with the same data and positioning as the previous example.

The numerical solution at the end of the initial pulse is shown in Figure 6.17 at $t = 0.5$. The sequence of events parallels the previous example: At $t = 1.5$ the incident pulse has expanded in a cylindrical wave and has just reached the vertex of the square

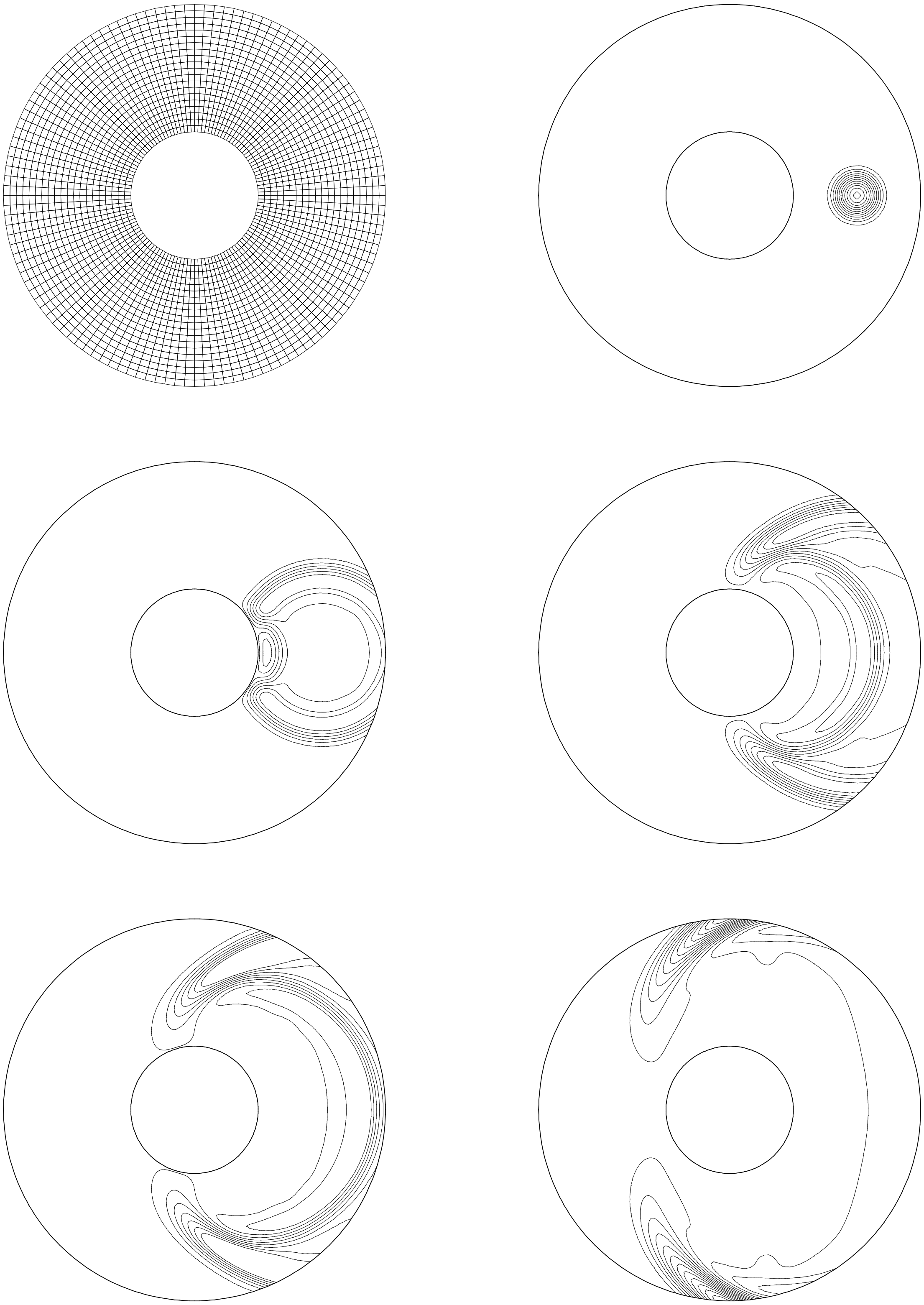

Figure 6.14: Scattering from an infinite circular cylinder due to point source. Solution contours shown at the end of the initial pulse at $t = 0.5$ and later times $t = 1.5$, $t = 2.5$, $t = 3$, and $t = 4$.

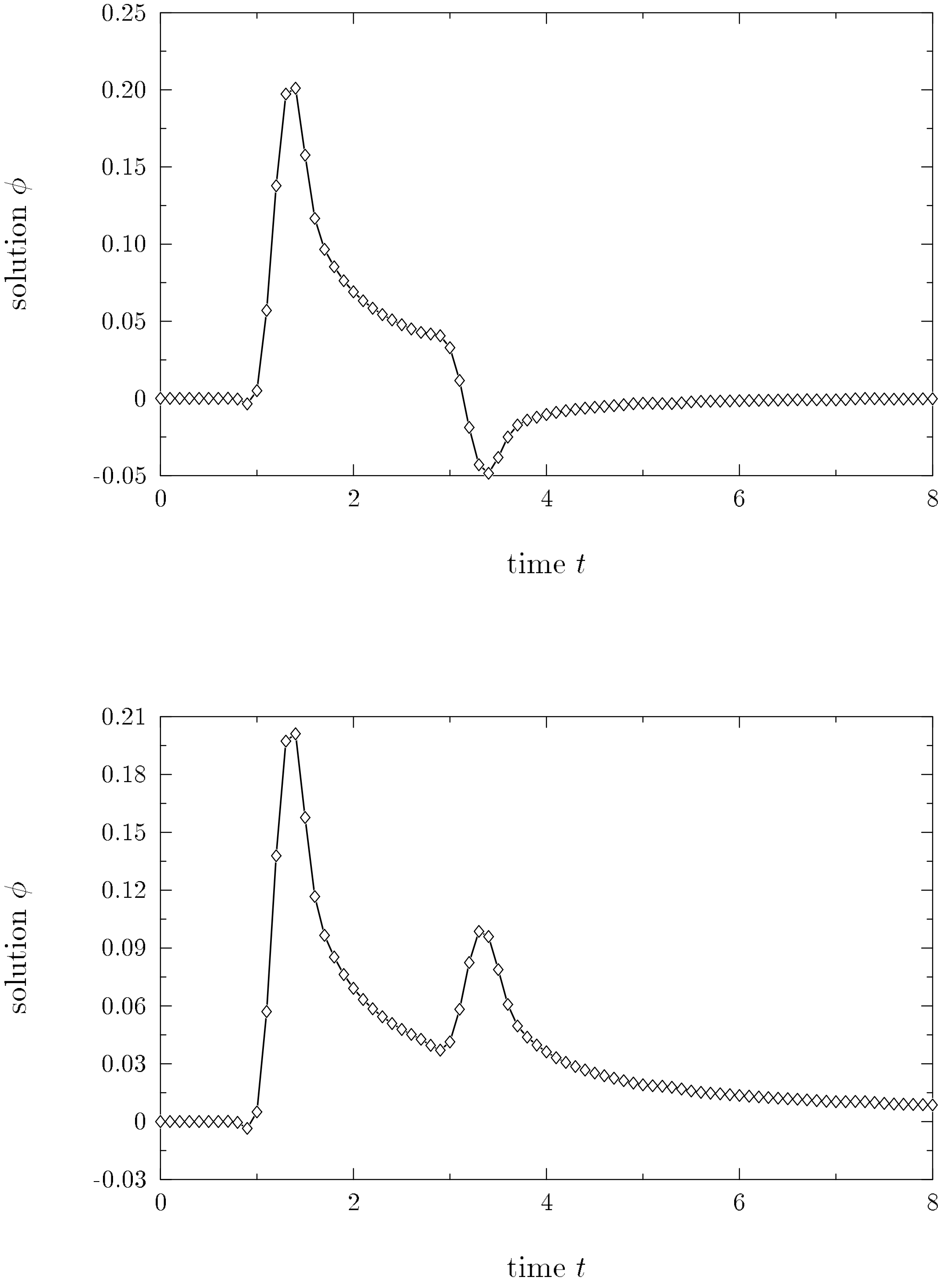

Figure 6.15: Scattering from an infinite circular cylinder: Solution on the artificial boundary Γ_∞, at $\theta = 0$. (top) 'pressure release' cylinder. (bottom) 'rigid' cylinder.

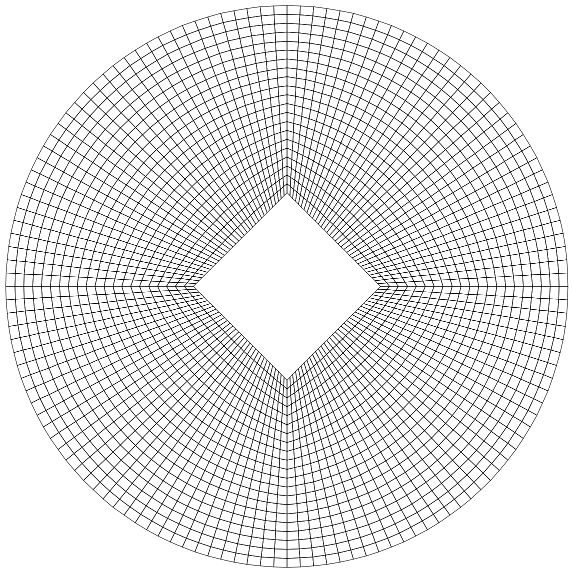

Figure 6.16: Spatial discretization for infinite square cylinder problem: By symmetry only upper half is modeled with 1386 quadratic elements.

scatterer. At $t = 2.5$ through $t = 3.0$ the incident wave has begun to reflect off the 'release' boundary, creating a backscattered wave. As time passes, both the incident and reflected waves are absorbed through the artificial boundary with no observable reflection. Figure 6.18 shows the transient solution on the artificial boundary Γ_∞, at $\theta = 0$, for both 'release' and 'rigid' boundary conditions on the square surface. Comparing these results to those found for the circular cylinder, we find that as a result of increased geometrical spreading, the amplitude of the backscattered wave is reduced while its duration is enlarged. 5

6.6.3 Transient scattering from a cylinder with end caps

Consider the time-dependent scattering from a rigid cylinder with conical-to-spherical end caps and a large length to diameter ratio, $L/d = 6.1$. Figure 6.20 illustrates the finite element spatial discretization of the computational domain. A total of 1600 quadratic elements are used for this example.

For this problem, the source $f = \delta(x_0, y_0)\sin\omega t$ and time $t \in [0, 3]$, is positioned

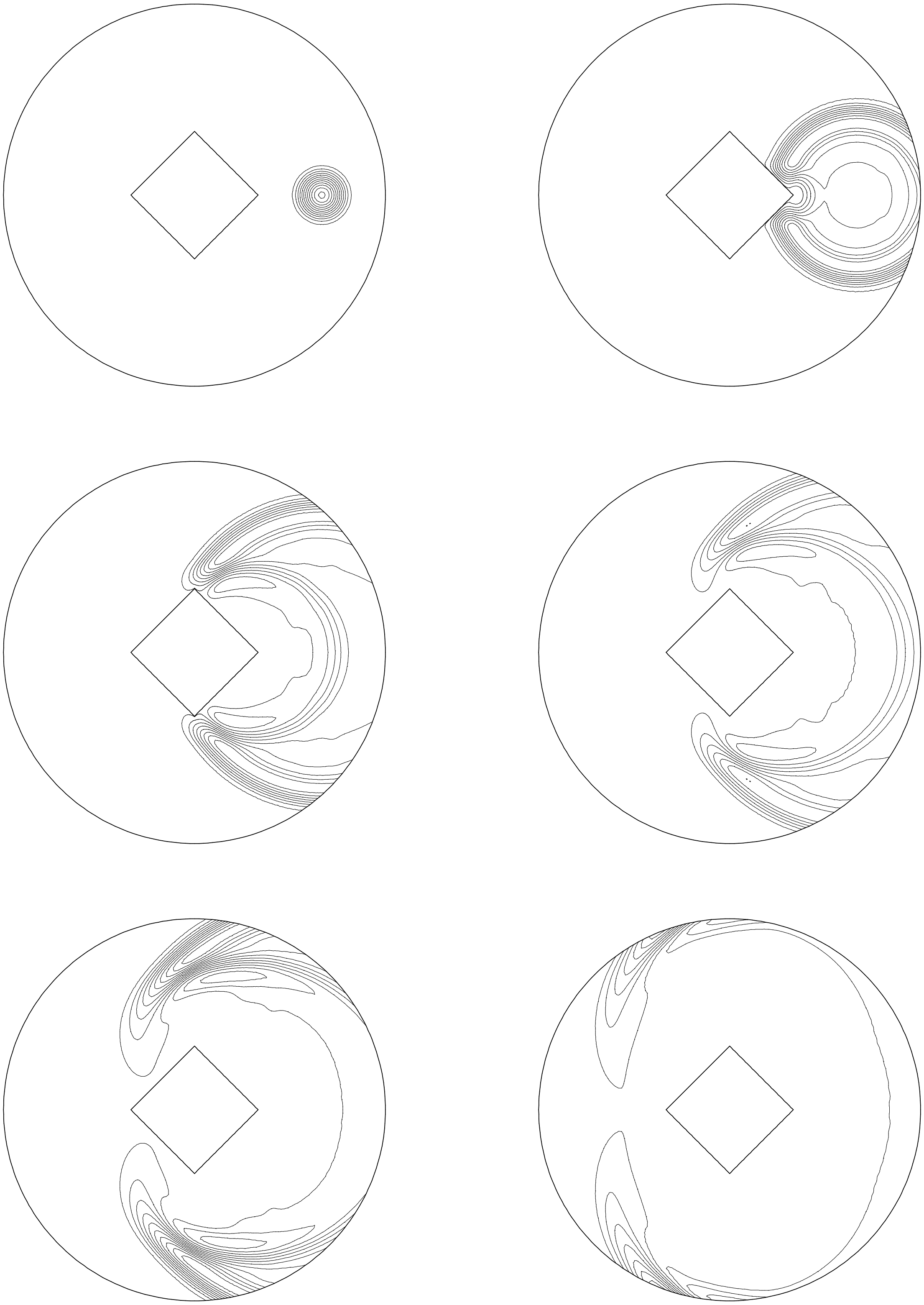

Figure 6.17: Scattering from an infinite square cylinder due to point source. Solution contours shown at the end of the initial pulse at $t = 0.5$ and later times $t = 1.5$, $t = 2.5$, $t = 3.0$, $t = 3.5$ and $t = 4.5$

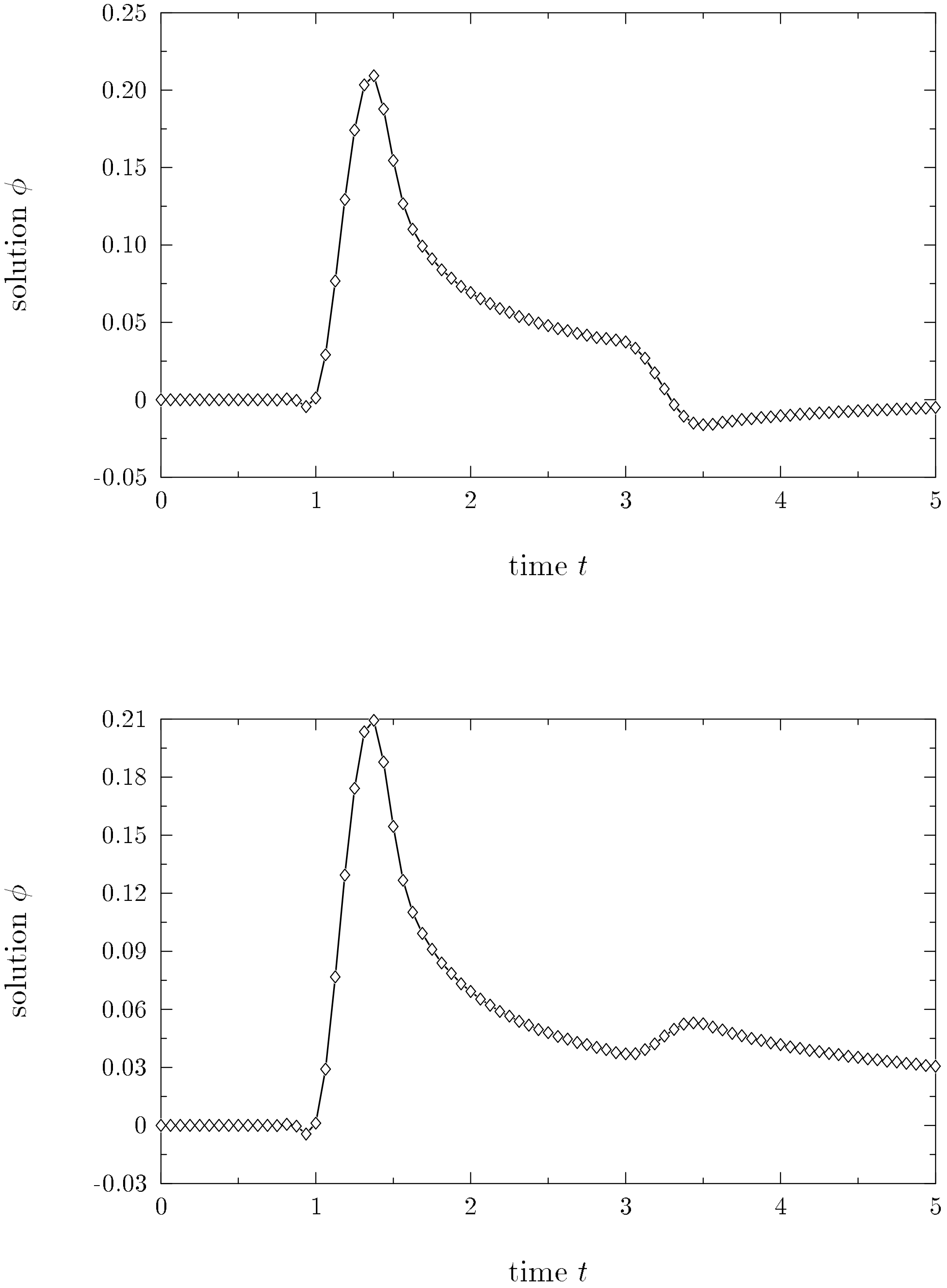

Figure 6.18: Scattering from an infinite square cylinder: Solution on the artificial boundary Γ_∞, at $\theta = 0$. (top) 'release' cylinder. (bottom) 'rigid' cylinder.

inside the computational domain simulating an oblique incident wave during a short time period. The phase speed is set at $c = 1$ with frequency $\omega = \pi/3$. In order to simulate an infinite structural impedance, homogeneous Neumann boundary conditions, i.e. 'rigid' boundary conditions, are prescribed on the cylinder surface. This example represents a challenging problem where the multiple-scales involving the ratio of the wavelength to diameter and length dimension play a critical role in the complexity of the resulting scattered wave field.

The numerical simulation at the end of the initial pulse at $t = 3$ is shown in Figure 6.20. The subsequent figures show the contours of the scattering phenomena as time progresses. The solution is presented in terms of the scalar velocity potential ϕ: Results for other solution variables such as the acoustic pressure $p = -\rho_0 \dot{\phi}$, or the acoustic velocity vector $\boldsymbol{v} = \nabla\phi$, are obtained through simple calculations of the time derivative and gradient of the velocity potential. The following sequence of events occur:

- At $t = 6$ the incident pulse has expanded in a cylindrical wave and has just reached the surface of the rigid cylinder, while at the artificial boundary, the wave front passes through the boundary with negligible reflection.

- At $t = 9$ through $t = 12$, the incident wave has begun to reflect off the cylinder boundary, creating a complicated backscattered wave.

- At $t = 15$, the incident wave begins to scatter into a part that travels along the upper part of the cylinder, and a part that diffracts around the backside. The backscattered wave is seen to transmit through the radiation boundary with no observable reflection.

- At $t = 18$, the incident wave has passed over the cylinder and continues to be absorbed through the non-reflecting boundary. A quiescent state near the right of the cylinder suggests the effectiveness of the local boundary condition in absorbing outgoing waves.

Note that as a result of the prescribed homogeneous Neumann boundary conditions on the cylinder, the amplitude of the reflected wave is positive creating high intensity zones in areas where the incident and backscattered waves coincide.

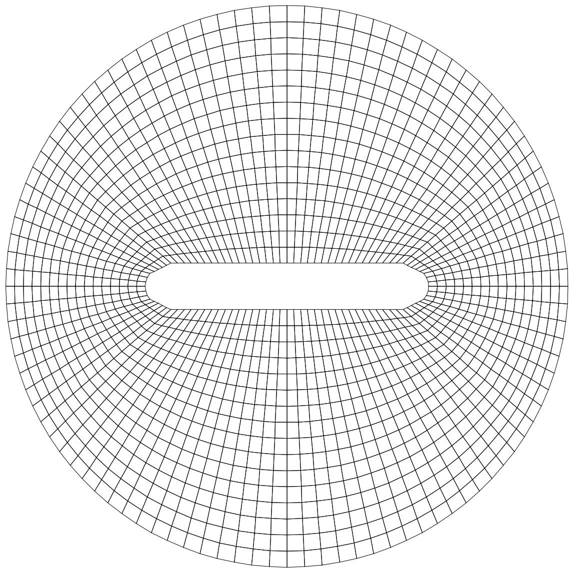

Figure 6.19: Spatial discretization for cylinder with tapered end caps. (1600 quadratic elements)

As a final example, consider the time-dependent scattering from the same cylinder described in Figure 6.19, but now with homogeneous Dirichlet boundary conditions on the wet cylinder surface, i.e. 'release' boundary conditions. The numerical simulation at the end of the initial pulse is shown in Figure 6.21 at $t = 3$. The sequence of events parallels the previous example: At $t = 6$ the incident pulse has expanded in a cylindrical wave and has just reached the boundaries of the cylinder. At $t = 9$ through $t = 12$, the wave has begun to reflect off the 'release' boundary, creating a complicated backscattered wave. As time passes, the originally cylindrical incident wave begins to scatter into a part that travels along the upper part of the cylinder, and a part that diffracts around the backside. The backscattered wave is seen to transmit through the boundary with no observable reflection. Note that as a result of homogeneous Dirichlet boundary conditions, the contours lying near the wet surface are parallel to the cylinder and the amplitude of the backscattered wave is negative.

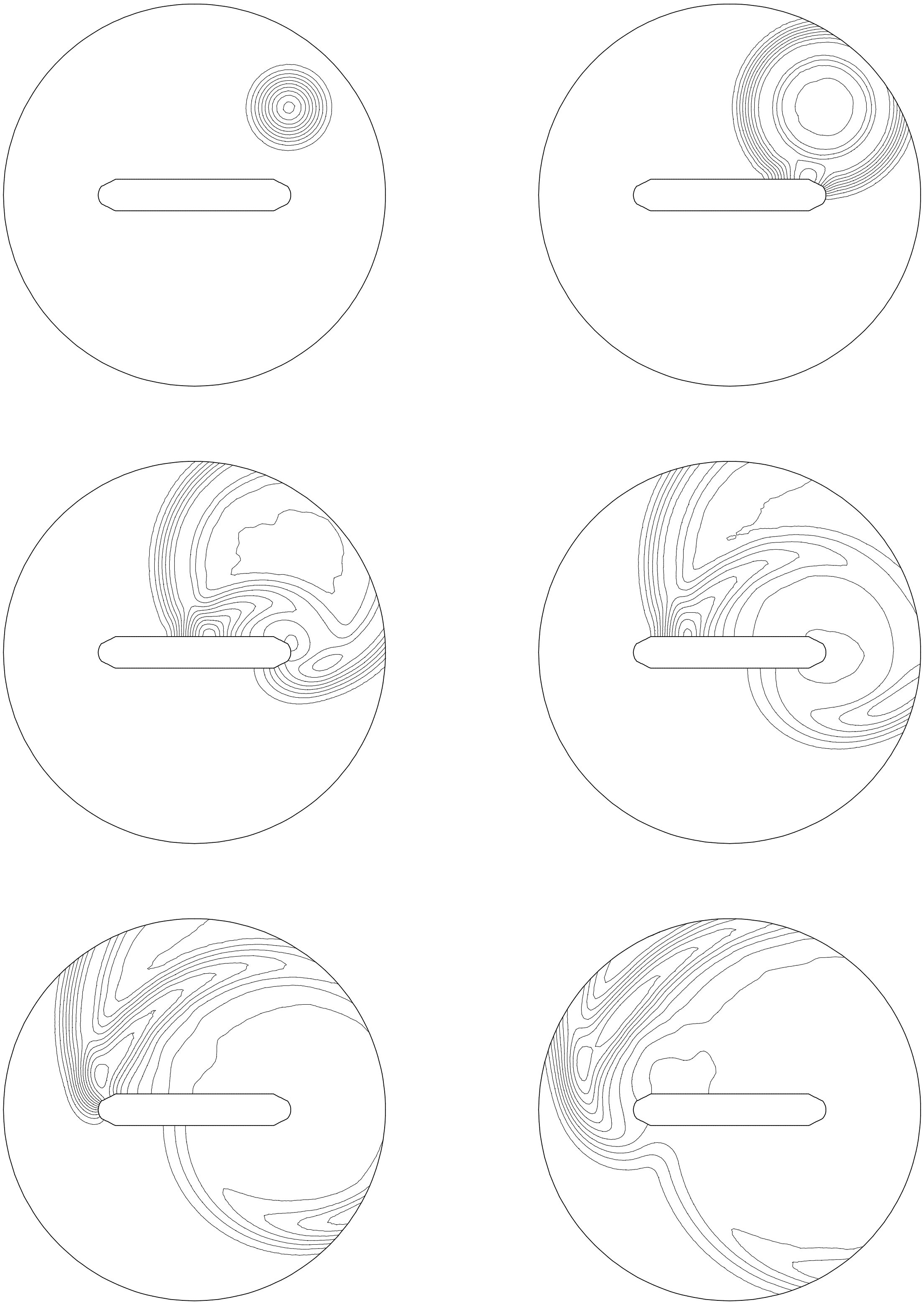

Figure 6.20: Scattering from a 'rigid' cylinder with tapered end caps due to point source. Solution contours shown at the end of the initial pulse at $t = 3$ and later times $t = 6, 9, 12, 15, 18$.

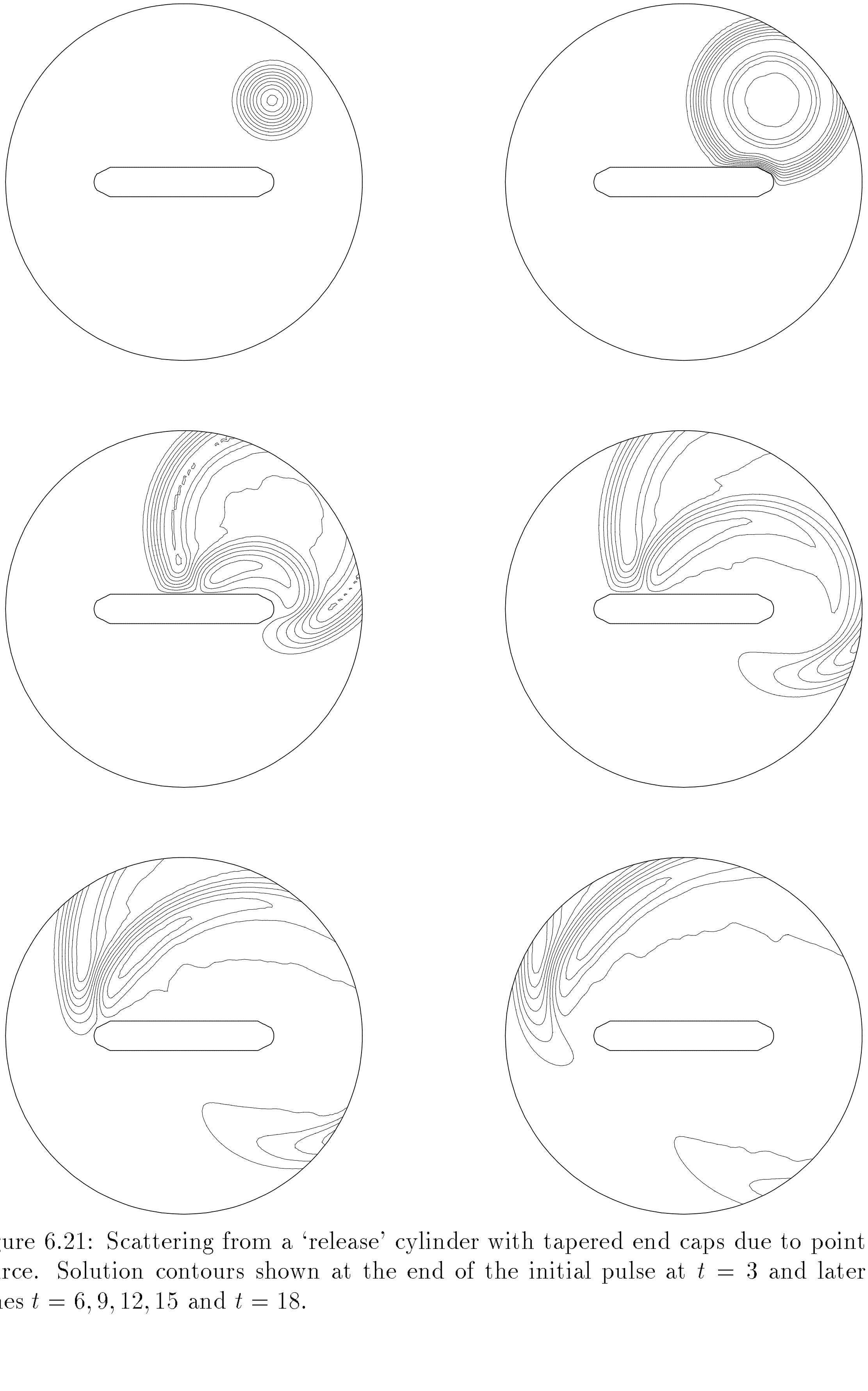

Figure 6.21: Scattering from a 'release' cylinder with tapered end caps due to point source. Solution contours shown at the end of the initial pulse at $t = 3$ and later times $t = 6, 9, 12, 15$ and $t = 18$.

6.7 Summary and Conclusions

For the two-dimensional problem, it is not possible to obtain local time-dependent boundary conditions that exactly represent outgoing cylindrical wave harmonics on the artificial boundary. The difficulty can be traced to the representation of cylindrical Hankel functions appearing in the wave harmonics for the exact solution in the frequency domain. Because of this difficulty, we resort to an approximation to the exact solution for outgoing waves expressed as an asymptotic expansion for large frequency (short wavelength), normalized with the radius of the circular artificial boundary. It has been demonstrated that this radially asymptotic expansion can be obtained starting from the exact Dirichlet-to-Neumann map.

Following Bayliss and Turkel [1980,82] a sequence of differential operators are defined which match the leading terms of the asymptotic approximation to provide local boundary conditions which are of progressively higher order and increasing accuracy. These boundary operators have an inverse Fourier transform allowing a family of boundary conditions that are local in space and time. Since the non-reflecting boundary conditions are local in space and time they preserve the data structure of the space-time finite element method for any order m. After eliminating higher-order radial derivatives through the use of the wave equation, this sequence of non-reflecting boundary conditions can easily be incorporated into the time-discontinuous space-time finite element method.

Numerical results confirm the superiority of the second-order local non-reflecting boundary condition $\mathbb{S}_2$, in comparison to the first-order $\mathbb{S}_1$, and simple 'plane-wave' $\mathbb{S}_0$, operators. The examples in this chapter demonstrate that with proper usage, the second-order non-reflecting boundary condition $\mathbb{S}_2$, when implemented in the space-time finite element method, is sufficiently accurate to capture all the important physics associated with a variety of complicated transient scattering problems.

An area of great potential for space-time finite element methods when solving time-dependent scattering problems, is the development of effective adaptive mesh refinement/unrefinement strategies in both space and time. This is especially important where both temporal and spatial enhancement can occur to track wave fronts as they propagate over large distances and long time intervals. For the examples given in this thesis, the full potential of the discontinuous space-time finite element method was not exploited in that a uniform mesh was fixed at each time step. JOHNSON [1993] and colleagues have recently developed some *a posteriori* error estimates for the discontinuous Galerkin method useful for developing adaptive strategies for the second-order hyperbolic wave equation. Further research efforts are needed to develop efficient and accurate local error indicators to drive the implementation of adaptive strategies for the exterior structural acoustics problem incorporating non-reflecting boundaries. For transient problems where waves propagate throughout the computational domain as a 'local' signal of relatively short duration, e.g. the scattering examples given in the previous section, adaptive methods should be able to reduce solution costs significantly. This may be accomplished by adding extra degrees of freedom in regions local to the signal, and deleting degrees of freedom in areas that are relatively quiescent.

Chapter 7

Semidiscrete Finite Element Formulation

As discussed in the introduction to this thesis, finite element methods for the direct solution of transient problems commonly use the technique of semidiscretization in which the spatial domain is discretized using finite elements, producing a system of ordinary differential equations in time which in turn is discretized using finite difference methods. When semidiscrete methods are used for the exterior structural acoustics problem, high-order nonreflecting boundary conditions must be applied to the artificial boundary surrounding the finite computational domain. As shown in Chapters 5 and 6, high-order accurate non-reflecting boundary conditions typically involve high-order temporal derivates in their definitions. As the order of the non-reflecting boundary conditions increases, they become increasingly difficult to implement in a semidiscrete setting due to the occurrence of high-order time derivatives on the truncation boundary. Standard semidiscrete algorithms for second-order hyperbolic equations such as the Newmark family of time integrators are restricted to integrating up to second-order time derivatives, thus when implemented directly, they are limited to second-order accurate boundary conditions $\mathbb{S}_2$. Furthermore, while semidiscrete methods are effective for computing smooth response, their performance is less satisfactory when solving acoustic wave propagation problems exhibiting steep gradients or sharp wave fronts typically arising in the complex radiation and scattering fields found in transient structural acoustics problems. Nevertheless, for transient problems without excessive gradients in the solution, or for time-dependent problems that are driven to steady-state, semidiscrete finite element methods can be an effective technique.

To demonstrate this, we examine the performance of the second-order $\mathbb{S}_2$ non-reflecting boundary condition described in Chapter 6 in a semidiscrete finite element formulation for the coupled structural acoustics problem. The approach is based on the introduction of an artificial boundary Γ_∞ enclosing a computational domain Ω, which is composed of the fluid domain Ω_f which in turn encloses the structural domain Ω_s. The local boundary operators, which are in a form relating Dirichlet to Neumann data, are imposed on the artificial boundary. Finite element semidiscretization of the coupled problem is accomplished using a scalar velocity potential in the fluid domain and displacements in the structure. The resulting system of ordinary differential equations in time is then integrated using a standard finite difference technique. The use of displacement–velocity potential time-dependent global solution vectors $(\boldsymbol{d}, \boldsymbol{\phi})$ for the coupled fluid-structure fields provides a banded and symmetrically coupled system of ordinary differential equations. The use of a scalar potential has the advantage of the *a priori* satisfaction of irrotationality and a reduction in fluid degrees of freedom when compared to vector representations Bathe and Hahn [1979], Belytschko [1980b] for the fluid variable. The $(\boldsymbol{d}, \boldsymbol{\phi})$ semidiscrete approach was first introduced by Everstine [1980] to correct the problem resulting from the well-known displacement–pressure $(\boldsymbol{d}, \boldsymbol{p})$ formulation Zienkiewicz and Bettess [1978], Gladwell [1966], and Craggs [1971], which results in a non-symmetric system of ordinary equations for the time-dependent case.

7.1 Overview

In Section 7.2, we develop the weak form of the fluid-structure initial boundary-value problem in terms of displacement and velocity potential variables. We also give details on the implementation of second-order non-reflecting boundary conditions in the semidiscrete variational setting. Finite element semidiscrete matrix equations for the coupled system are stated in Section 7.3. Numerical results presented in Section 7.4 illustrate the performance of the two-dimensional time-dependent radiation boundary conditions as affected by frequency, distance from the source of disturbance, and radiation directionality. Accurate results for canonical model problems involving only a single layer of fluid elements have been obtained. Details for the development of consistent fluid-structure coupling elements for the interaction between standard C^0 continuum-based shell elements and acoustic fluid elements are also given in this section. Finally in Section 7.5 conclusions are drawn.

7.2 Coupled Variational Equations

The variational or 'weak' form of the fluid-structure problem corresponding to Eqs. (2.27)–(2.33) may be stated as:

Find $(\boldsymbol{u}\,,\,\phi) \in \mathcal{S} \times \mathcal{T}$, for $t \in [0, T]$ such that $\forall\,(\boldsymbol{w}\,,\,w) \in \mathcal{V} \times \mathcal{W}$,

$$G_s(\boldsymbol{w}\,,\,\boldsymbol{u}) - A(\boldsymbol{w}\,,\,\phi)_{\Gamma_i} \;=\; F_s(\boldsymbol{w}) \tag{7.1}$$

$$G_f(w\,,\,\phi) + A(w\,,\,\boldsymbol{u})_{\Gamma_i} \;=\; F_f(w) \tag{7.2}$$

where the bilinear operators for the structure and fluid are respectively,

$$G_s(\boldsymbol{w}\,,\,\boldsymbol{u}) \;:=\; (\boldsymbol{w}, \ddot{\boldsymbol{u}}) + a_s(\boldsymbol{w}, \boldsymbol{u}) \tag{7.3}$$

$$G_f(w\,,\,\phi) \;:=\; (w, \ddot{\phi}) + a_f(w, \phi) + (w\,,\,\mathbb{S}_m\phi)_{\Gamma_\infty} \tag{7.4}$$

with notation,

$$(\boldsymbol{w}, \ddot{\boldsymbol{u}}) \;=\; \int_{\Omega_s} \rho_s\, \boldsymbol{w} \cdot \ddot{\boldsymbol{u}}\; d\Omega \tag{7.5}$$

$$a_s(\boldsymbol{w}, \boldsymbol{u}) \;=\; \int_{\Omega_s} \nabla\boldsymbol{w} : \boldsymbol{C} : \nabla\boldsymbol{u}\; d\Omega \tag{7.6}$$

$$a_f(w, \phi) \;=\; \int_{\Omega_f} \rho_0\, \nabla w \cdot \nabla\phi\; d\Omega \tag{7.7}$$

$$(w, \ddot{\phi}) \;=\; \int_{\Omega_f} \frac{\rho_0}{c^2}\, w\, \ddot{\phi}\; d\Omega \tag{7.8}$$

$$A(\boldsymbol{w}\,,\,\phi)_{\Gamma_i} \;=\; \int_{\Gamma_i} \rho_0\, \boldsymbol{w} \cdot \boldsymbol{n}\dot{\phi}\; d\Gamma \tag{7.9}$$

$$A(w\,,\,\boldsymbol{u})_{\Gamma_i} \;=\; \int_{\Gamma_i} \rho_0\; w\; \dot{\boldsymbol{u}} \cdot \boldsymbol{n}\; d\Gamma \tag{7.10}$$

$$F_s(\boldsymbol{w}) \;=\; \int_{\Gamma_\sigma} \boldsymbol{w} \cdot \bar{\boldsymbol{t}}\; d\Gamma \tag{7.11}$$

$$F_f(w) \;=\; \int_{\Omega_f} \rho_0\; w\, f\; d\Omega \tag{7.12}$$

$$(w\,,\,\mathbb{S}_m \phi)_{\Gamma_\infty} \;=\; \int_{\Gamma_\infty} \rho_0\; w\; \mathbb{S}_m\; \phi\; d\Gamma \tag{7.13}$$

and where

$$\mathcal{S} \;=\; \left\{ \boldsymbol{u}(\boldsymbol{x}\,,\,\cdot) | \boldsymbol{u} \in (H^1(\Omega_s))^d \right\} \tag{7.14}$$

$$\mathcal{V} \;=\; \left\{ \boldsymbol{w}(\boldsymbol{x}) | \boldsymbol{w} \in (H^1(\Omega_s))^d \right\} \tag{7.15}$$

The definition of the trial and weighting function spaces $\mathcal{T}$ and $\mathcal{W}$ will in general be dependent on the boundary operator index m. Specific examples will be discussed later. Note that the radiation boundary condition is enforced weakly in (7.13), i.e., it is treated as a natural boundary condition. For example the inner product defined on the truncation boundary by Eq. (7.13) becomes for $m = 1$:

$$(w, \mathbb{S}_1\phi)_{\Gamma_\infty} = \mathrm{d}_0(w, \phi)_{\Gamma_\infty} + \mathrm{d}_1(w, \dot{\phi})_{\Gamma_\infty} \tag{7.16}$$

where for the first-order operator defined in (6.31) we have,

$$\mathrm{d}_0(w, \phi)_{\Gamma_\infty} \;=\; \int_{\Gamma_\infty} \frac{\rho_0}{2R} w\, \phi\; d\Gamma$$

$$\mathrm{d}_1(w, \dot{\phi})_{\Gamma_\infty} \;=\; \int_{\Gamma_\infty} \frac{\rho_0}{c} w\; \dot{\phi}\; d\Gamma$$

and for $m = 2$:

$$(w, \mathbb{S}_2\phi)_{\Gamma_\infty} = \mathrm{d}_0(w, \phi) + \mathrm{d}_1(w, \dot{\phi}) + \mathrm{d}_2(w, \ddot{\phi}) \tag{7.17}$$

where for the second-order operator defined in (6.32) we have,

$$
\begin{aligned}
\mathrm{d}_0(w,\phi) &= \int_{\Gamma_\infty} \frac{3\rho_0}{8R} w\,\phi\; d\Gamma + \int_{\Gamma_\infty} \frac{\rho_0}{2R} w,_\theta\; \phi,_\theta\; d\Gamma \\
\mathrm{d}_1(w,\dot{\phi}) &= \int_{\Gamma_\infty} \frac{3\rho_0}{2c} w\,\dot{\phi}\; d\Gamma + \int_{\Gamma_\infty} \frac{\rho_0 R}{c} w\,\dot{\phi},_r\; d\Gamma \\
\mathrm{d}_2(w,\ddot{\phi}) &= \int_{\Gamma_\infty} \frac{\rho_0 R}{c^2} w\,\ddot{\phi}\; d\Gamma
\end{aligned}
$$

In the above, we have used the identity,

$$
\int_{\Gamma_\infty} w \Delta_\Gamma \phi\; d\Gamma = - \int_{\Gamma_\infty} w,_\theta\; \phi,_\theta\; d\Gamma \tag{7.18}
$$

which holds over a closed circular boundary.

Note that the boundary operators are local in both space and time, i.e., they are differential operators. As a consequence, when used as boundary conditions on Γ_∞, the resulting semidiscrete finite element equations are a mth order system of ordinary differential equations in time. For orders $m \leq 2$, standard time-stepping schemes such as the Newmark family of algorithms can be used to solve the transient problem directly. However for $m \geq 3$, the boundary operators involve time derivatives up to mth order, which cannot be handled directly with standard time integration schemes, originally designed for second-order problems. To date, the second-order boundary condition is the highest that has been implemented in a semidiscrete finite element formulation; see Pinsky and Abboud [1990,1991a] for the $\mathbb{R}^3$ case and Pinsky,Thompson, and Abboud [1991b,1992] for the $\mathbb{R}^2$ case.

We emphasize that for the boundary conditions $\mathbb{S}_1$ and $\mathbb{S}_2$, the finite element approximations need only be C^0, i.e. the trial and weighting function spaces are defined as:

$$
\mathcal{T} = \left\{ \phi(\boldsymbol{x},\cdot) | \phi \in H^1(\Omega_f) \right\} \tag{7.19}
$$

$$
\mathcal{W} = \left\{ w(\boldsymbol{x}) | w \in H^1(\Omega_f) \right\} \tag{7.20}
$$

7.3 Semidiscrete Matrix Equations

The semidiscrete matrix equations are obtained by introducing finite element approximations into the variational equations (7.1) and (7.2). Standard spatial element interpolations for the structure displacements $\boldsymbol{u}$ and fluid velocity potential ϕ are expressed by:

$$\begin{aligned} \boldsymbol{u}^h(\boldsymbol{x},t) &= \boldsymbol{N}^e(\boldsymbol{x})\boldsymbol{d}^e(t) && \in \boldsymbol{C}^0(\Omega_s) \\ \phi^h(\boldsymbol{x},t) &= \widetilde{\boldsymbol{N}}^e(\boldsymbol{x})\boldsymbol{\phi}^e(t) && \in C^0(\Omega_f) \end{aligned}$$

where $\boldsymbol{N}^e$ and $\widetilde{\boldsymbol{N}}^e$ are the e^{th} element shape functions for the structure and fluid respectively, and $\boldsymbol{d}^e$ and $\boldsymbol{\phi}^e$ are the time-dependent element structure displacement and fluid velocity potential solution vectors. Introducing these approximations into the variational equations (7.1) and (7.2) and enforcing the conditions of the weak form leads to the following semidiscrete matrix problem:

Given $\boldsymbol{f}_s : (0,T) \mapsto \mathbb{R}^{n_{seq}}$, *and* $\boldsymbol{f}_f : (0,T) \mapsto \mathbb{R}^{n_{feq}}$,
Find $\boldsymbol{d} : (0,T) \mapsto \mathbb{R}^{n_{seq}}$ *and* $\boldsymbol{\phi} : (0,T) \mapsto \mathbb{R}^{n_{feq}}$ *such that,*

$$\begin{bmatrix} \boldsymbol{M}_s & \boldsymbol{0} \\ \boldsymbol{0} & -(\boldsymbol{M}_f + \boldsymbol{D}_2) \end{bmatrix} \begin{Bmatrix} \ddot{\boldsymbol{d}} \\ \ddot{\boldsymbol{\phi}} \end{Bmatrix} + \begin{bmatrix} \boldsymbol{D} & \boldsymbol{A} \\ \boldsymbol{A}^T & -\boldsymbol{D}_1 \end{bmatrix} \begin{Bmatrix} \dot{\boldsymbol{d}} \\ \dot{\boldsymbol{\phi}} \end{Bmatrix}$$

$$+ \begin{bmatrix} \boldsymbol{K}_s & \boldsymbol{0} \\ \boldsymbol{0} & -(\boldsymbol{K}_f + \boldsymbol{D}_0) \end{bmatrix} \begin{Bmatrix} \boldsymbol{d} \\ \boldsymbol{\phi} \end{Bmatrix} = \begin{Bmatrix} \boldsymbol{f}_s \\ \boldsymbol{f}_f \end{Bmatrix} \tag{7.21}$$

where $\boldsymbol{d}$ and $\boldsymbol{\phi}$ are the global solution vectors and,

$$\boldsymbol{K}_s = \boldsymbol{K}_s^T = \mathop{\mathsf{A}}_{e=1}^{n_{el}} \int_{\Omega_s^e} (\nabla \boldsymbol{N}^e)^T \, \overline{\boldsymbol{C}} \, (\nabla \boldsymbol{N}^e) \, d\Omega^e \tag{7.22}$$

$$\boldsymbol{M}_s = \boldsymbol{M}_s^T = \mathop{\mathsf{A}}_{e=1}^{n_{el}} \int_{\Omega_s^e} \rho_s \boldsymbol{N}^{eT} \boldsymbol{N}^e \, d\Omega^e \tag{7.23}$$

$$\boldsymbol{K}_f = \boldsymbol{K}_f^T = \mathop{\mathsf{A}}_{e=1}^{n_{el}} \int_{\Omega_f^e} \rho_0 \left(\nabla \widetilde{\boldsymbol{N}}^e\right)^T \left(\nabla \widetilde{\boldsymbol{N}}^e\right) \, d\Omega^e \tag{7.24}$$

$$\boldsymbol{M}_f = \boldsymbol{M}_f^T = \mathop{\mathsf{A}}_{e=1}^{n_{el}} \int_{\Omega_f^e} \frac{\rho_0}{c^2} \widetilde{\boldsymbol{N}}^{eT} \widetilde{\boldsymbol{N}}^e \, d\Omega^e \tag{7.25}$$

$$\boldsymbol{f}_s = \mathop{\mathsf{A}}_{e=1}^{n_{el}} \int_{\Gamma_\sigma^e} \boldsymbol{N}^{eT} \, \bar{\boldsymbol{t}} \, d\Gamma^e \tag{7.26}$$

$$\boldsymbol{f}_f = \mathop{\mathsf{A}}_{e=1}^{n_{el}} \int_{\Omega_f^e} \rho_0 \widetilde{\boldsymbol{N}}^{eT} \, f \, d\Omega^e \tag{7.27}$$

$$\boldsymbol{A} = \mathop{\mathsf{A}}_{e=1}^{n_{el}} \int_{\Gamma_i^e} -\rho_0 \boldsymbol{N}^{eT} \boldsymbol{n} \widetilde{\boldsymbol{N}}^e \, d\Gamma^e \tag{7.28}$$

$$\boldsymbol{D}_0 = \boldsymbol{D}_0^T = \mathop{\mathsf{A}}_{e=1}^{n_{el}} \int_{\Gamma_\infty^e} \rho_0 \Big[\frac{H_1(m)}{2r} \widetilde{\boldsymbol{N}}^{eT} \widetilde{\boldsymbol{N}}^e \tag{7.29}$$

$$+ \frac{H_2(m)}{2r} \Big(\widetilde{\boldsymbol{N}}_{,\theta}^{eT} \widetilde{\boldsymbol{N}}_{,\theta}^e - \frac{1}{4} \widetilde{\boldsymbol{N}}^{eT} \widetilde{\boldsymbol{N}}^e \Big) \Big] d\Gamma^e \tag{7.30}$$

$$\boldsymbol{D}_1 = \mathop{\mathsf{A}}_{e=1}^{n_{el}} \int_{\Gamma_\infty^e} \frac{\rho_0}{c} (1 + \frac{H_2(m)}{2}) \widetilde{\boldsymbol{N}}^{eT} \widetilde{\boldsymbol{N}}^e \, d\Gamma^e \tag{7.31}$$

$$+ \int_{\Gamma_\infty^e} \frac{\rho_0 r}{c} H_2(m) \widetilde{\boldsymbol{N}}^{eT} \widetilde{\boldsymbol{N}}_{,r}^e \, d\Gamma^e \tag{7.32}$$

$$\boldsymbol{D}_2 = \boldsymbol{D}_2^T = \mathop{\mathsf{A}}_{e=1}^{n_{el}} \int_{\Gamma_\infty^e} \frac{\rho_0 r}{c^2} H_2(m) \widetilde{\boldsymbol{N}}^{eT} \widetilde{\boldsymbol{N}}^e \, d\Gamma^e \tag{7.33}$$

where n_{el} is the number of elements, $\mathop{\mathsf{A}}_{e=1}^{n_{el}}$ denotes the element assembly operator and $H_i(m)$ is a discrete Heavyside function defined such that $H_i(m) = 1$ if m is greater than or equal to i, and zero otherwise. $\boldsymbol{K}_s$ and $\boldsymbol{M}_s$ are the symmetric stiffness and mass matrices respectively for the structure while $\boldsymbol{K}_f$ and $\boldsymbol{M}_s$ are the corresponding stiffness and mass matrices for the acoustic fluid. $\overline{\boldsymbol{C}}$ is the symmetric constitutive matrix for the structure and $\boldsymbol{D}$ is a symmetric structural damping matrix. Fluid-structure interface elements enforce the coupling between the fluid and structure through the $\boldsymbol{A}$ matrix. $\boldsymbol{D}_0$, $\boldsymbol{D}_1$, and $\boldsymbol{D}_2$ are the matrix contributions arising from the non-reflecting boundary conditions. The resulting system of differential equations is symmetric and banded except for the nonsymmetric element matrix contribution $\boldsymbol{D}_1$ arising from the nonsymmetric boundary integral term in d_1 for $m = 2$. Boundary conditions of order $m \geq 3$ have not been implemented. These boundary conditions would lead to the necessity of increased continuity between elements and semidiscrete matrix equations that will include time derivatives up to order m.

Remark

- The displacement–velocity potential $(\boldsymbol{d}, \boldsymbol{\phi})$ system above can easily be reformulated into the well-known displacement–pressure $(\boldsymbol{d}, \boldsymbol{p})$ approach. The velocity potential is eliminated in favor of the pressure by substituting the discrete momentum balance relation $\boldsymbol{p} = -\rho_0 \dot{\boldsymbol{\phi}}$ into the lower partition of (7.21), multiplying through by ρ_0 and differentiating in time. The resulting $(\boldsymbol{d}, \boldsymbol{p})$ matrix problem becomes,

$$\begin{bmatrix} \boldsymbol{M}_s & \boldsymbol{0} \\ \rho_0 \boldsymbol{A}^T & (\boldsymbol{M}_f + \boldsymbol{D}_2) \end{bmatrix} \begin{Bmatrix} \ddot{\boldsymbol{d}} \\ \ddot{\boldsymbol{p}} \end{Bmatrix} + \begin{bmatrix} \boldsymbol{D} & \boldsymbol{0} \\ \boldsymbol{0} & \boldsymbol{D}_1 \end{bmatrix} \begin{Bmatrix} \dot{\boldsymbol{d}} \\ \dot{\boldsymbol{p}} \end{Bmatrix}$$

$$+ \begin{bmatrix} \boldsymbol{K}_s & -\frac{1}{\rho_0}\boldsymbol{A} \\ \boldsymbol{0} & (\boldsymbol{K}_f + \boldsymbol{D}_0) \end{bmatrix} \begin{Bmatrix} \boldsymbol{d} \\ \boldsymbol{p} \end{Bmatrix} = \begin{Bmatrix} \boldsymbol{f}_s \\ \boldsymbol{f}_f \end{Bmatrix} \tag{7.34}$$

  The effect of this reformulation is to move the coupling matrices, $\boldsymbol{A}$, from the extended damping matrix to the extended mass and stiffness matrices. The principle disadvantage of this pressure formulation is the nonsymmetric system of equations that result.

7.3.1 A consistent fluid-structure coupling element

In this section a consistent fluid-structure coupling element is developed for the interaction between standard C^0 continuum-based shell elements and the acoustic elements. Fluid-structure interface finite elements generate the consistent coupling matrix defined by (7.28). These elements serve as a transition between the structure and fluid, having both structural and fluid nodes. The coupling matrix is restated as,

$$\boldsymbol{A} = \mathop{\mathbf{A}}_{e=1}^{n_{el}} (\boldsymbol{A}^e), \qquad \boldsymbol{A}^e = [\boldsymbol{A}^e_{ab}] = \int_{\Gamma^e_i} -\rho_0 \boldsymbol{N}^{eT}_a \boldsymbol{n} \widetilde{\boldsymbol{N}}^e_b \, d\Gamma^e \tag{7.35}$$

In the above and subsequent equations the index a takes values of 1 to n_{esn}, the number of element structural nodes, and b takes values of 1 to n_{efn}, the number of fluid nodes. The total number of nodes per interface element, n_{en}, is the sum of n_{esn} and n_{efn}. Both structural and fluid nodes lie on the interface boundary Γ_i^e.

Specializing to shell kinematics, the displacement vector $\boldsymbol{u}$ is parameterized by the element natural coordinates $(\xi, \eta, \zeta) \in (-1, 1)^3$ and has the following form:

$$\boldsymbol{u}(\xi, \eta, \zeta) = \sum_{a=1}^{n_{esn}} N_a(\xi, \eta)\bar{\boldsymbol{u}}_a + \zeta \sum_{a=1}^{n_{esn}} N_a(\xi, \eta)\frac{t_a}{2}\hat{\boldsymbol{u}}_a \tag{7.36}$$

where $\bar{\boldsymbol{u}}_a$ is the displacement of the element reference surface, $\hat{\boldsymbol{u}}_a$ is the displacement due to the rotation of the shell cross section, and t_a is the thickness at each node. $N_a(\xi, \eta)$ denotes a two-dimensional shape function associated with node a. The vector $\hat{\boldsymbol{u}}_a$ is constructed such that the cross sectional fiber may rotate, but not stretch, viz.,

$$\hat{\boldsymbol{u}}_a = \theta_{a2}\boldsymbol{e}_{a1}^f - \theta_{a1}\boldsymbol{e}_{a2}^f \tag{7.37}$$

The angles θ_{a1} and θ_{a2} represent the rotations of the fiber about the orthonormal basis vectors $\boldsymbol{e}_{a1}^f$ and $\boldsymbol{e}_{a2}^f$, respectively. Further details of the shell kinematics can be found in HUGHES [1987].

An expression for the nodal structural shape function matrix is obtained as,

$$\boldsymbol{u} = \sum_{a=1}^{n_{esn}} \boldsymbol{N}_a\boldsymbol{d}_a \ , \quad \boldsymbol{N}_a = N_a \begin{bmatrix} 1 & 0 & 0 & -z_a e_{a12}^f & z_a e_{a11}^f \\ 0 & 1 & 0 & -z_a e_{a22}^f & z_a e_{a21}^f \\ 0 & 0 & 1 & -z_a e_{a32}^f & z_a e_{a31}^f \end{bmatrix}, \quad \boldsymbol{d}_a = \begin{Bmatrix} \bar{\boldsymbol{u}}_a \\ \theta_{a1} \\ \theta_{a2} \end{Bmatrix} \tag{7.38}$$

where $z_a = \zeta t_a/2$. The fluid nodes have only one velocity potential degree of freedom per node and are interpolated using standard shape functions:

$$\phi = \sum_{b=1}^{n_{efn}} \widetilde{N}_b(\xi, \eta)\phi_b \tag{7.39}$$

Substitution of the shape functions for the shell nodes, $\boldsymbol{N}_a$, and fluid nodes, $\widetilde{N}_b$, into (7.35) results in,

$$\boldsymbol{A}_{ab}^e = \int_{\Gamma_i^e} -\rho_0 N_a \widetilde{N}_b \begin{bmatrix} \boldsymbol{n} \\ -z_a\boldsymbol{e}_{a2}^f \cdot \boldsymbol{n} \\ z_a\boldsymbol{e}_{a1}^f \cdot \boldsymbol{n} \end{bmatrix} d\Gamma^e, \qquad \boldsymbol{n} = \frac{\boldsymbol{e}_\xi \times \boldsymbol{e}_\eta}{\|\boldsymbol{e}_\xi \times \boldsymbol{e}_\eta\|} \tag{7.40}$$

where $\zeta = 1$ at the interface boundary Γ_i^e, $\boldsymbol{n}$ is the unit normal outward from the interface boundary, and $\boldsymbol{e}_\xi$ and $\boldsymbol{e}_\eta$ are unit tangent vectors in the ξ- and η- coordinate directions respectively. Note that different orders of interpolation for the structural nodes vs. the fluid nodes can be accommodated, allowing possible combinations such as quadratic interpolation for shell nodes and cubic interpolation for fluid nodes.

7.4 Numerical Examples

In this section numerical studies are performed to assess the accuracy of the local non-reflecting boundary conditions implemented in a semidiscrete finite element formulation, as effected by the operator order, acoustic wave number, radiation directionality, and distance from the acoustic source. In all the results to follow, the semidiscrete matrix equations are integrated in time using the standard second-order accurate trapezoidal rule. Numerical results are obtained using the simple 'plane-wave' (PW) damper and the first two local boundary operators defined in (6.31) and (6.32), and implemented in (7.16) and (7.17). In the following discussions, the notation for the local operators $\mathbb{S}_1$ and $\mathbb{S}_2$ will be replaced with the notation B_1-damper and B_2-damper to distinguish the semidiscrete implementation of these operators.

7.4.1 Uniform acoustic radiation

Consider the uncoupled problem of an infinite cylindrical radiator of radius $a = 1$, pulsating uniformly with a Dirichlet boundary condition $\phi(a,t) = \phi_o sin\omega t$ for $t > 0$ on the wet surface. The steady-state solution is a circular cylindrical wave given by (6.5) where R is replaced by a, and $n = 0$.

$$\phi(r,t) = -\mathrm{Imag}\left\{ \frac{H_0(kr)}{H_0(ka)}\, \phi_o\, e^{-i\omega t} \right\} \qquad \text{for } r \in [a, +\infty] \tag{7.41}$$

A series of transient finite element solutions were obtained for this problem using zero initial conditions on ϕ and $\dot{\phi}$ and a time increment of $\Delta t = 0.2$. The nondimensional wavenumber is set at $ka = 1$. The artificial boundary is positioned at $R = 6a$ and then reduced to $R = 1.5a$ in order to examine the influence of radial distance on the accuracy of the non-reflecting boundary conditions. Discretization in the radial direction was kept constant with an element dimension of $h^e = 0.5$ in this direction, corresponding to 4π elements per wavelength. Bilinear elements are used throughout and the following definitions employed; Mesh L1: $n = 1$, $R = 1.5$ and Mesh L2: $n = 10$, $R = 6.0$.

Figure 7.1 shows the profiles of the exact and transient finite element solutions in the fluid along a ray at two sample times. The solution sample times are such that many spurious reflections between the truncation boundary and cylinder could have occurred. In Figure 7.1a, results for $R = 6$ and 10 elements in the radial direction indicate that the as expected the B_1 operator is nearly exact. The plane-wave damper (PW) performs well at this value of R. Figure 7.1b shows results for $R = 1.5$ with a single element in the radial direction. The operator B_1 remains accurate whereas the solution accuracy for the plane-wave damper deteriorates significantly. This observation is clear from the time-dependent solution measured on the artificial boundary $r = R$, see Figure 7.2.

7.4.2 Fluid-structure interaction example

Now consider the coupled problem of an elastic infinite cylindrical thin shell submerged in an acoustic fluid, subject to time-harmonic uniform internal pressure loading,

$$p = p_o e^{-i\omega t} \tag{7.42}$$

The governing equation for a cylindrical shell of radius a, submerged in the fluid under plane-strain conditions is

$$(k_s - \omega^2 m_s)u_r = p_o - i\omega\rho_o\phi(a) \tag{7.43}$$

where u_r is the radial displacement of the shell, p_o is the applied pressure, the last term on the right hand side represents fluid pressure loading, and k_s and m_s are the shell stiffness and mass per unit area, respectively, given by:

$$k_s = \frac{Eh}{a^2(1-\nu^2)}, \qquad m_s = \rho_s h \tag{7.44}$$

In the above, E and ν are the Young's modulus and Poisson's ratio for the shell material, h is the thickness and ρ_s is the shell density.

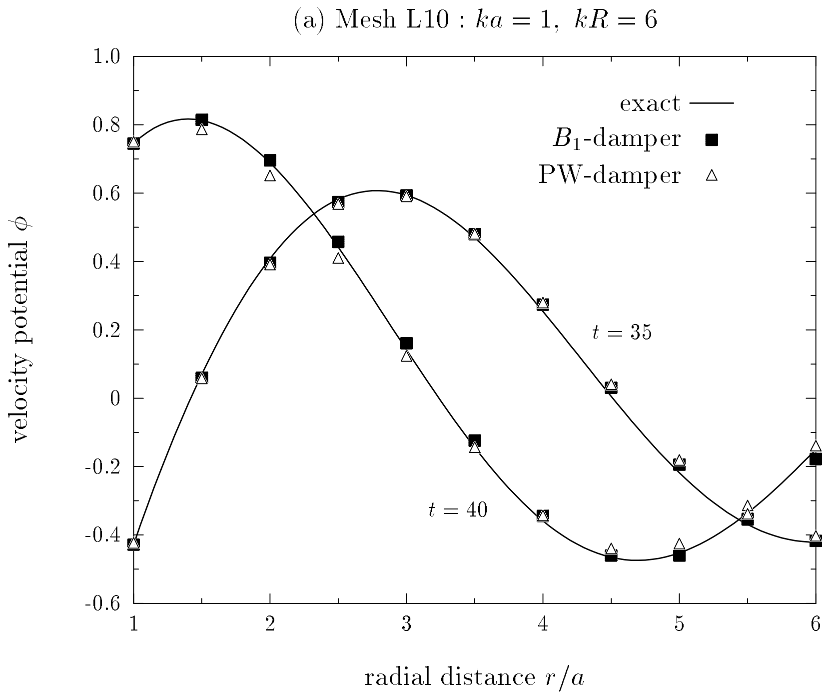

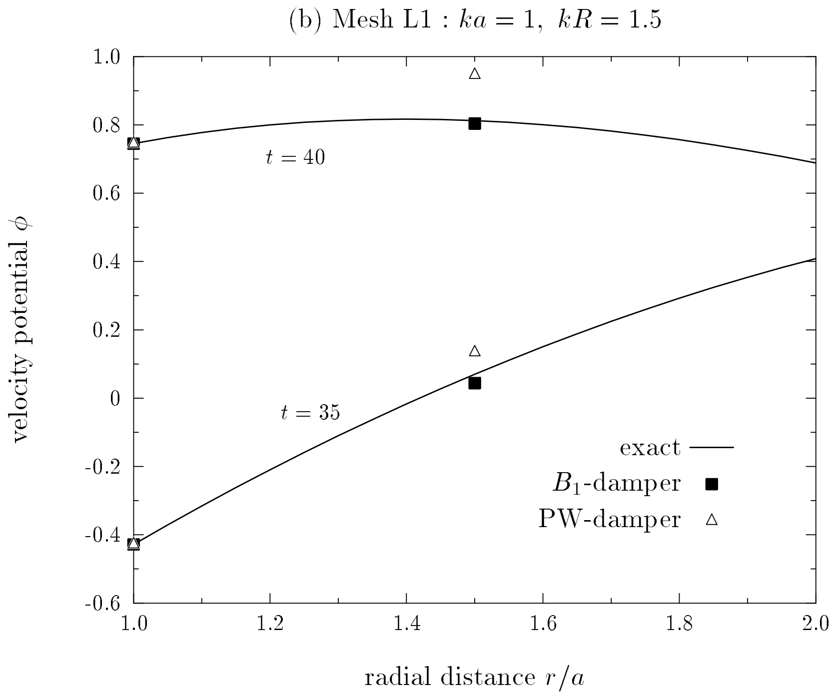

Figure 7.1: Uniformly pulsating cylindrical radiator. Solution profile at time $t = 35$ and $t = 40$: (a) $kR = 6$ (b) $kR = 1.5$.

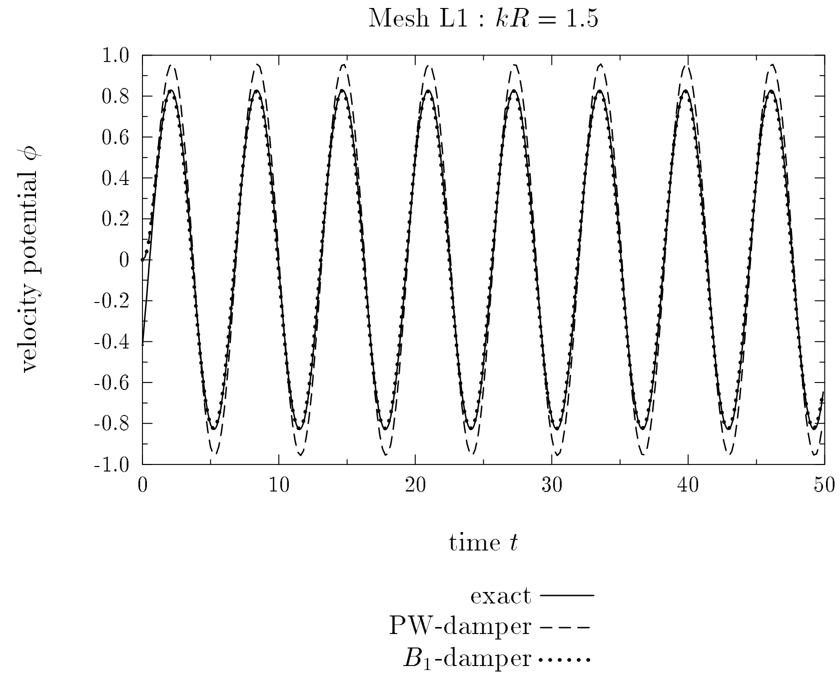

Figure 7.2: Uniformly pulsating cylindrical radiator. Solution at $r = R$.

The exact solution for the velocity potential and shell radial displacement is,

$$\phi(r,t) = ic\frac{H_0(kr)}{H_1(ka)}u_r(t) \tag{7.45}$$

$$u_r(t) = \frac{p_o e^{-i\omega t}}{\left(k_s - \omega^2 m_s - \omega\rho_o c\dfrac{H_0(ka)}{H_1(ka)}\right)} \tag{7.46}$$

A finite element solution of this problem was obtained using the following values. The shell has a radius of $a = 1.0$ and thickness $h = 1/20$. The material properties of the shell are $E = 91. \times 10^6$, $\nu = 0.3$, and $\rho_s = 1000$. The fluid properties are the same as those considered in the previous case with $c = 1.0$ and $\rho_o = 2.0$. The structure is modeled using standard C^0 linear continuum–based shell elements with transverse shear capability. Bilinear Lagrange based shell elements with selectively reduced integration were employed with plane-strain boundary conditions. The consistent fluid-structure coupling element developed earlier in Section 7.3.1 is used to couple the shell to the acoustic fluid elements. Details of the shell formulation can be found in HUGHES [1987]. The fluid discretization is identical to that used previously in the uncoupled case.

The numerical solution obtained using a truncation radius of $R = 6$ and 10 acoustic elements in the radial direction was extremely accurate for all three boundary conditions tested. In this case the exact and numerical solutions were nearly coincident (not shown). Fig. 7.3 compares the analytical solution for radial displacement and the acoustic fluid velocity potential with the finite element solution when the radius to the truncation boundary is reduced to $R = 1.5$ with only a single fluid element in the radial direction. The results are displayed for a point on the fluid-shell interface Γ_i, i.e. at $a = 1$. The operator B_1 is very accurate and performs better than the B_2 and PW operators for this uniform wave problem.

Now consider the same infinite elastic cylindrical shell submerged in an acoustic fluid, subject to a step in internal pressure, $p(a,t) = p_o$ for $t > 0$ and zero initial conditions. The shell properties are the same as those in the previous example except that the Young's modulus is changed to $E = 910.$, such that the shell breathing mode characteristic frequency in vacuum is $\omega_o = \sqrt{k_s/m_s} = 1$ (this choice accentuates the transient character of the solution). The fluid properties are the same as those used previously.

Since an exact solution for this problem is not readily obtainable, we take as a basis for comparison, a numerical solution obtained using an extensive and fine mesh of acoustic elements with a truncation radius of $R = 26$ (this solution is labeled 'infinite mesh' in Figures 7.4 and 7.5). This mesh is large enough that the wave front will not reach the truncation boundary of the computational fluid domain during the analysis time span.

Figure 7.4 shows the solution time history for the structure radial displacement and fluid velocity potential at the structure-fluid interface for the mesh with $R = 6$ having 10 elements in the radial direction. Figure 7.5 shows the results for these solutions obtained with the mesh with $R = 1.5$ and one fluid element in the radial direction. For both meshes, the structure radial displacement is computed accurately for both B_1 and B_2 conditions, Figures 7.4a and 7.5a. Solutions with the PW damper are somewhat inferior at $R = 1.5$.

Figures 7.4b and 7.5b show comparisons of the velocity potential ϕ at the fluid–structure interface as the truncation boundary Γ_∞ is brought closer to the structure.

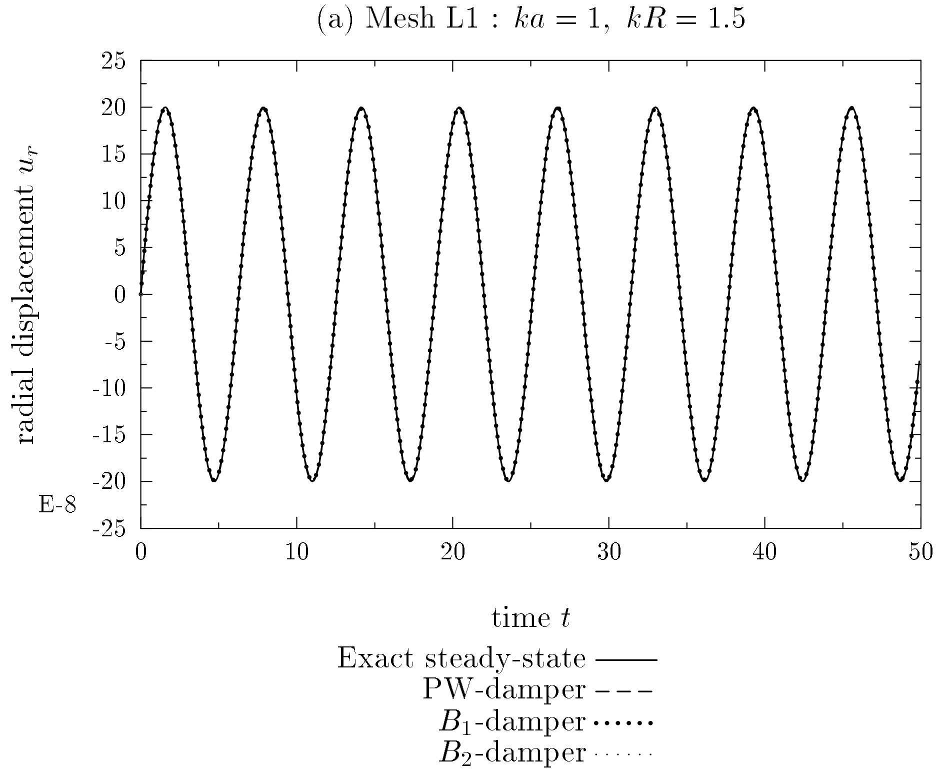

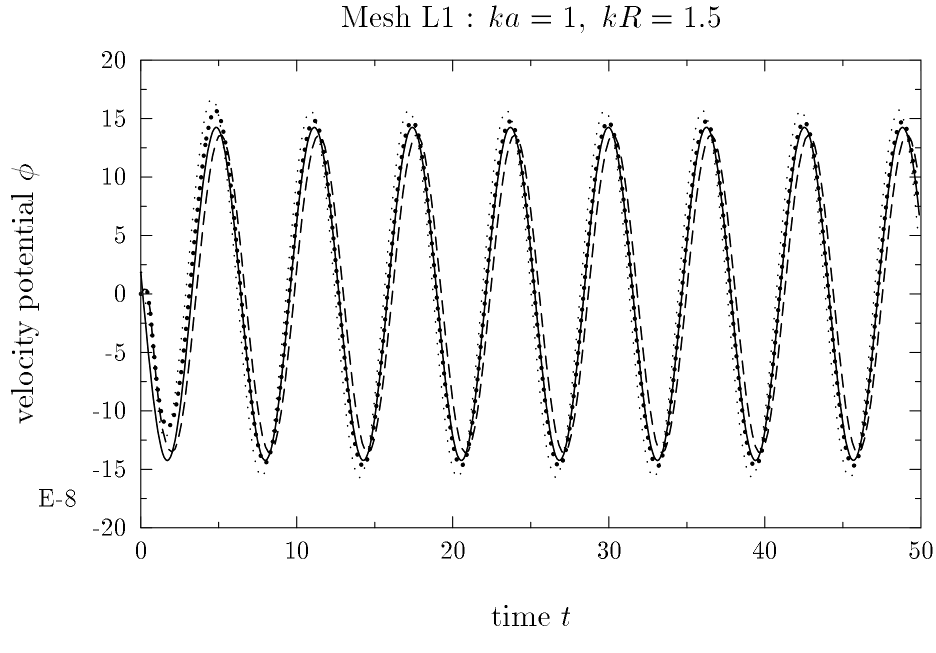

Figure 7.3: Submerged elastic cylinder subject to sinusoidal internal pressure. Solution at the fluid-shell interface for $kR = 1.5$.

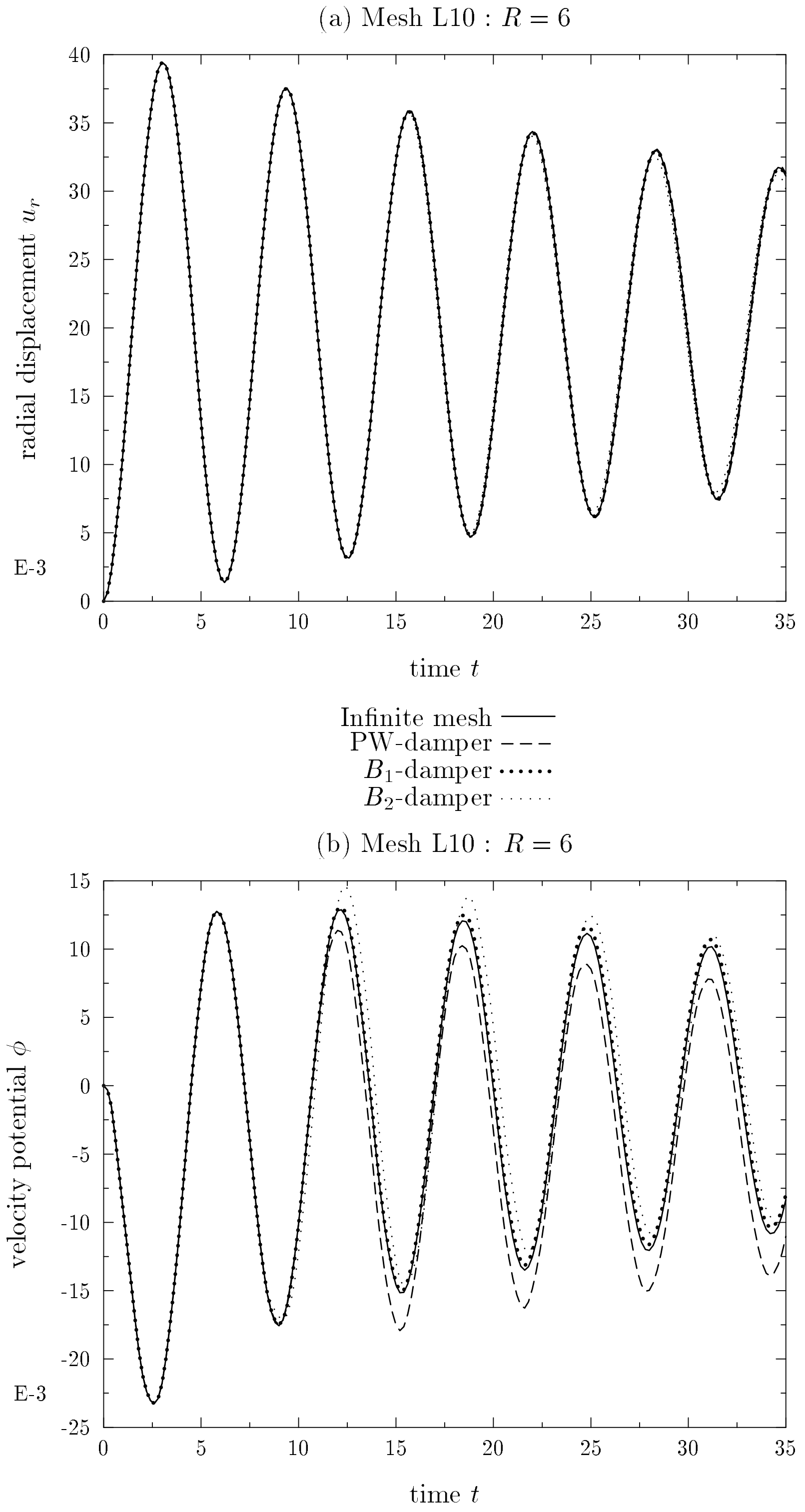

Figure 7.4: Submerged elastic cylinder subject to step in internal pressure. Solution at the fluid-shell interface for $R = 6$. (a) Shell radial displacements.(b) Acoustic fluid velocity potential.

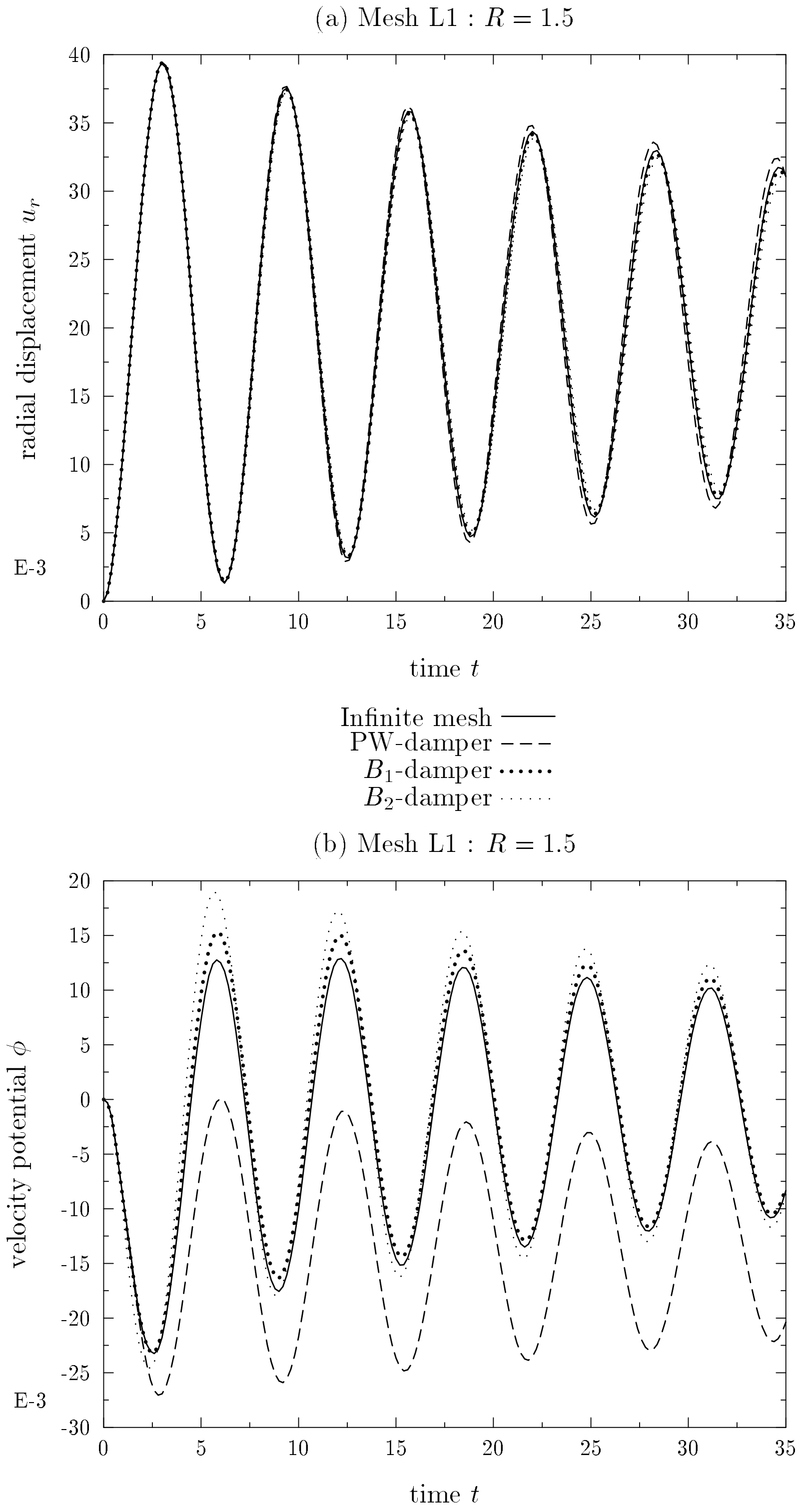

Figure 7.5: Submerged elastic cylinder subject to step in internal pressure. Solution at the fluid-shell interface for $R = 1.5$. (a) Shell radial displacements.(b) Acoustic fluid velocity potential.

It is observed that the transient response is captured accurately by the B_1 operator while the B_2 solution displays some error in the early-time but quickly converges to the coupled fluid-shell breathing mode response predicted by the infinite/finite element mesh solution. The PW damper results exhibit significant spurious reflections as indicated by severe amplitude and phase errors. These results demonstrate that for the simple case of uniform radiation, the B_1 operator performs optimally.

7.4.3 Nonuniform acoustic radiation

It is expected that as the radiation pattern becomes more complex, the higher order operators B_m will be increasingly accurate when compared to the simple PW damper. To investigate the performance of the dampers in transmitting non-uniform acoustic radiation when implemented in a semidiscrete finite element method, the problem of an infinite circular cylindrical radiator with circumferentially harmonic loading $\phi(a,\theta,t) = \phi_o \cos n\theta \sin \omega t$ for $t > 0$ is solved with a time step of $\Delta t = 0.2$ and zero initial conditions. The finite element calculations were based on a uniform fluid mesh of quadratic elements, denoted Mesh Q5, with 5 elements in the radial direction and 10 elements in the circumferential direction (100 elements).

Figure 7.6 shows the solution profile around the artificial boundary as the circumferential mode n ranges from 1 through 5, and $ka = 4$. It is observed that as n is increased, the B_2 operator is able to accurately capture the non-uniform wavefronts in the higher circumferential modes, while the lower order boundary conditions begin to lose accuracy in the higher spatial harmonics, Figure 7.6b. In a second calculation we reduce the nondimensional wavenumber to $ka = 1$. The results for the first three modes are shown in Figure 7.7. In this case, the B_2 condition is clearly superior to the other conditions tested. These numerical results support our earlier conclusions: as we increase the order m of the operator B_m, we increase the order of accuracy and are able to capture progressively more complex radiation patterns.

In Chapter 6 it was noted that for a fixed order m and radius R, as the acoustic wavenumber k is increased, the accuracy of B_m is increased, i.e. $\lim_{k\to\infty} B_m(\phi) = 0$. To examine the effect of increasing wavenumber consider the non-uniform radiation from a cylinder with constant time-harmonic velocity potential $\phi(a,\theta,t) = \phi_o \sin(\omega t)$, prescribed on the arc, $(-\theta_o \leq \theta \leq \theta_o)$. Elsewhere on the wet surface, $\phi(a,\theta,t) = 0$.

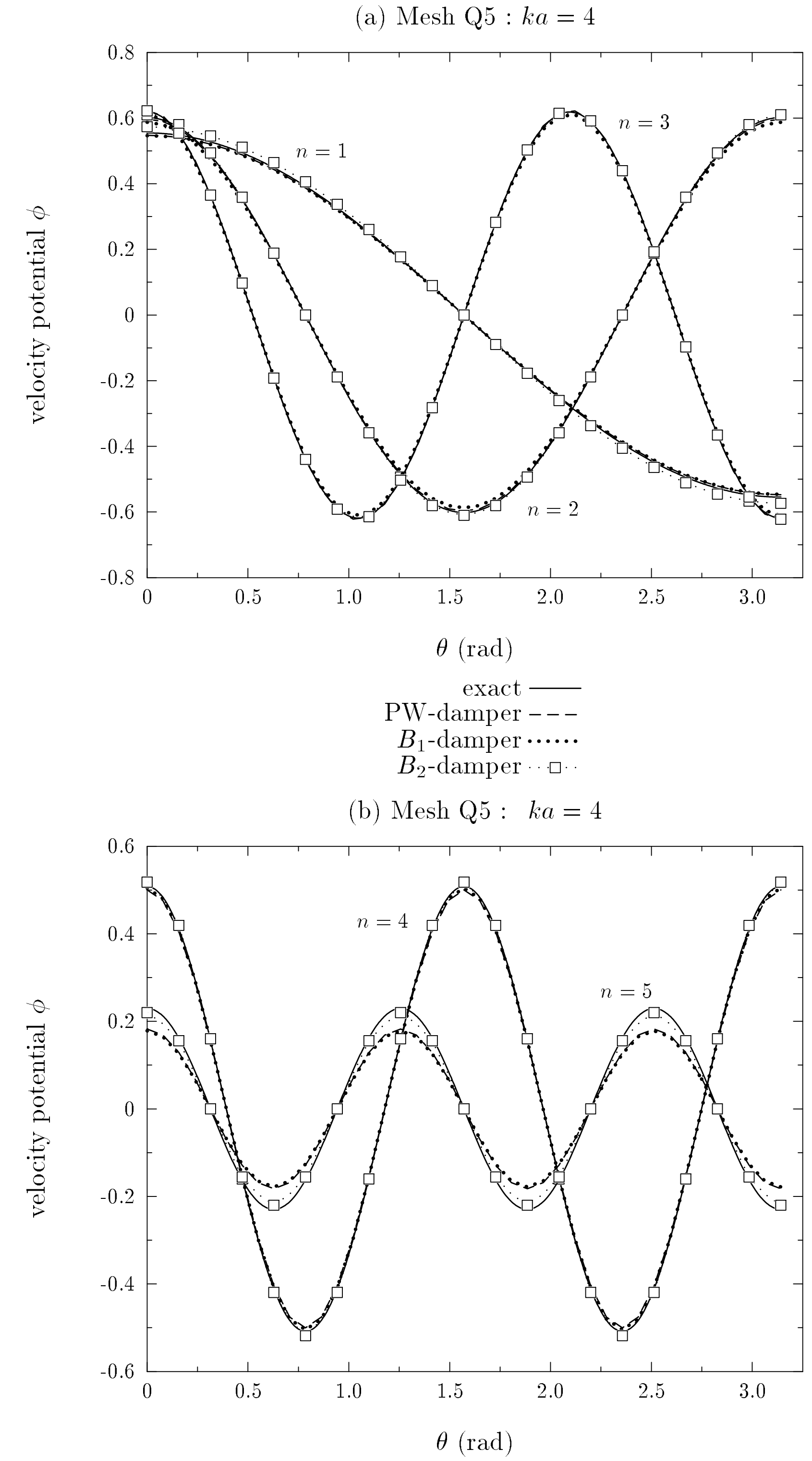

Figure 7.6: Radiating rigid cylinder with $\cos n\theta$ circumferential harmonics of order n, for $ka = 4$. Solution profile on the radiation boundary at time $t = 30$: (a) $n = 1, 2, 3$ (b) $n = 4, 5$.

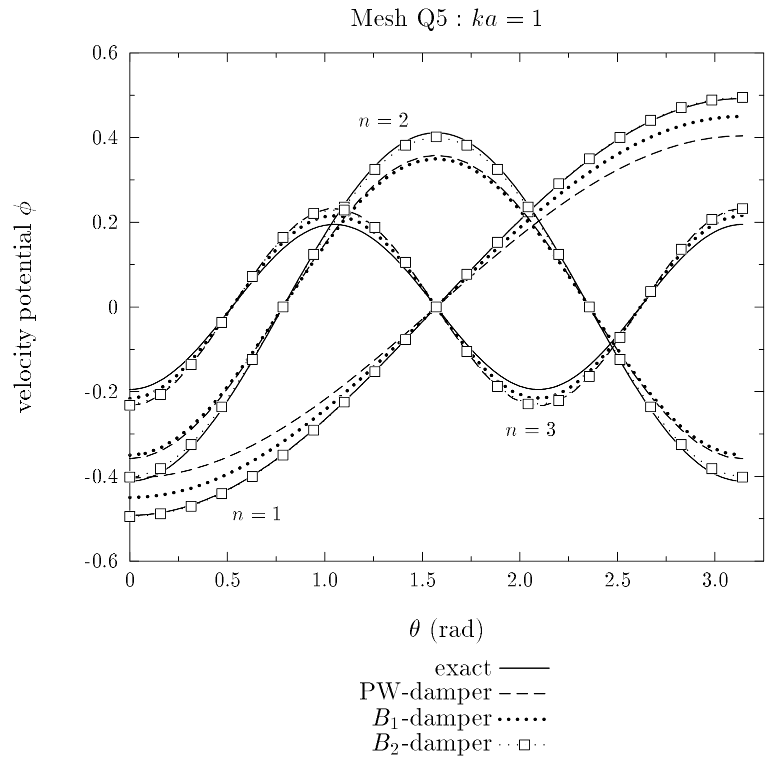

Figure 7.7: Radiating rigid cylinder with $\cos n\theta$ circumferential harmonics of order n, for $ka = 1$. Solution profile on the radiation boundary at time $t = 30$ with $n = 1, 2, 3$.

The problem is solved numerically as a transient semidiscrete problem where the wavenumber is increased from $ka = 1$ through $ka = 6$. The solution profile around the circumference of the radiation boundary is depicted in Figure 7.8 at fixed time $t = 40$. The exact solution is accurately captured by all the dampers throughout the domain for $ka \geq 3$. Note that in the vicinity of the source ($0 \leq \theta \leq \theta_o$), the solution is dominated by the 'breathing' mode defined by $n = 0$. In this region, the B_1-damper is the most accurate. As the backside is approached, the amplitude has been attenuated down to a few percent of the source position and the B_2-damper is the most accurate. Below $ka = 3$, the PW and B_1 dampers begin to lose accuracy, yet the B_2 damper is able to maintain accuracy down to $ka = 1$.

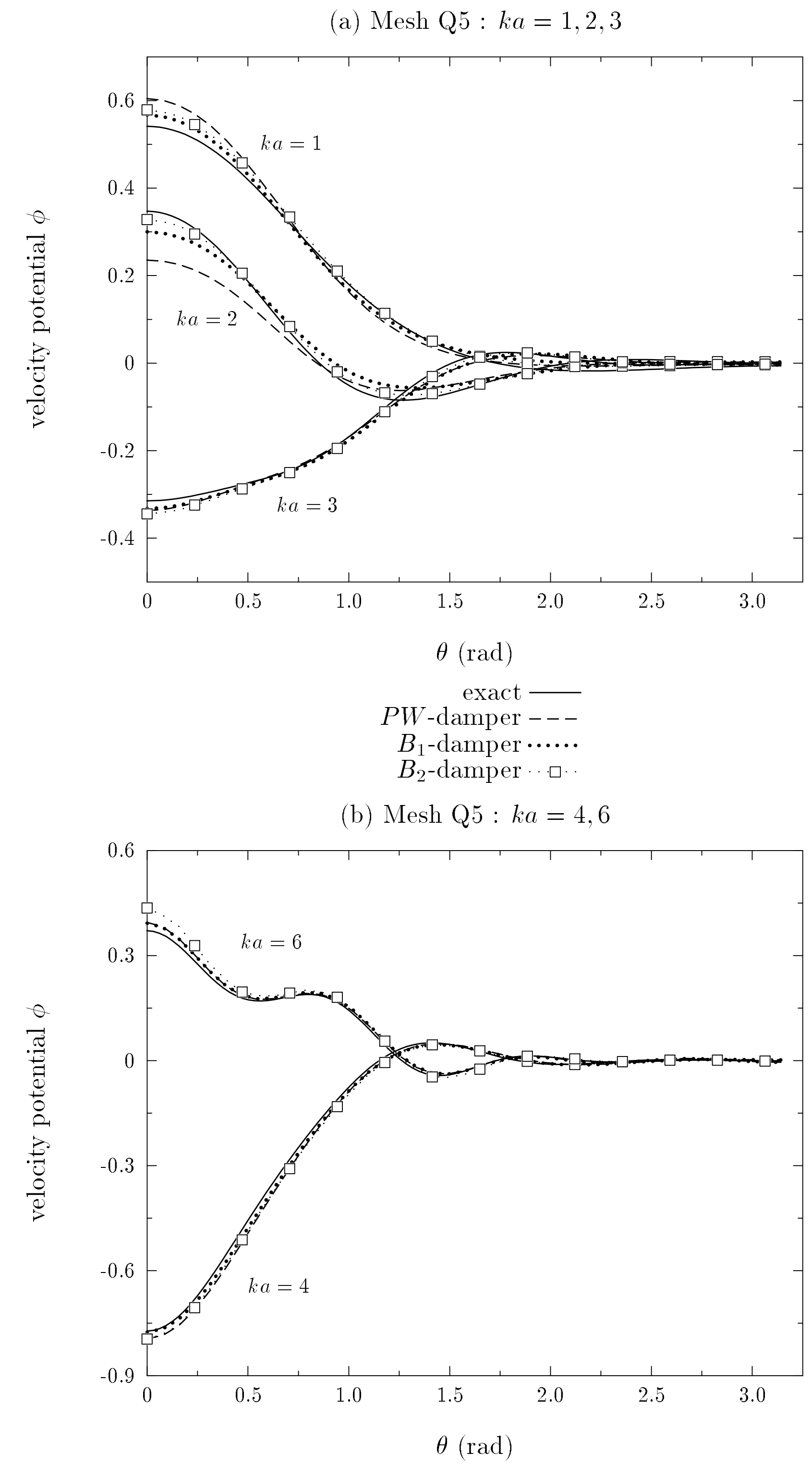

Figure 7.8: Radiation from an element of a cylinder. Solution profile on the radiation boundary at time $t = 40$. (a) $ka = 1, 2, 3$ (b) $ka = 4, 6$.

7.5 Summary and Conclusions

In this chapter the sequence of local radiation boundary operators described in Chapter 6 have been incorporated into a general coupled semidiscrete finite element formulation for transient analysis. Consistent fluid-structure coupling elements are developed for the interaction between standard C^0 continuum-based shell elements and acoustic fluid elements. It has been shown that the local boundary conditions preserve the data structure of the standard finite element method and up to order $m = 2$ are easily incorporated into semidiscrete finite element programs. Boundary conditions of order $m \geq 3$ have not been implemented. These boundary conditions would lead to the necessity of increased continuity between elements and semidiscrete matrix equations that must include time derivatives up to order m. The design of stable time integration algorithms capable of incorporating third order and higher boundary conditions remains an open question. It is this limitation of the semidiscrete approach that motivated the development of the space-time finite element approach for the exterior structural acoustics problem, where their is no intrinsic restriction on the order of time derivative appearing in the governing equations.

Numerical results comparing the performance of the first- and second- order local absorbing boundary conditions in a semidiscrete approach confirm the superiority of B_2 over B_1. Accurate results have been obtained with the B_2 operator using only a single layer of acoustic fluid elements. In the case of uniform radiation, we note for the B_2 operator a slight decrease in accuracy compared to the B_1 operator, which we have shown performs optimally for this case. However, for non-uniform acoustic radiation involving higher order wave harmonics, results indicate that the B_2 condition outperforms the lower-order conditions as expected. Further numerical examples for the semidiscrete approach can be found in Abboud [1990], Pinsky and Abboud [1990,1991a] for three-dimensional problems and Pinsky, Thompson, and Abboud [1991b,1992] for two-dimensional problems.

Chapter 8

Design of Galerkin/Least-Squares Methods in the Frequency Domain

As discussed in the introduction to this thesis, for linear problems characterized by a relatively small range of frequencies, a time-dependent solution to the structural acoustics problem may be obtained indirectly in the frequency domain through a Fourier transform. The Fourier transform $\tilde{f}(\boldsymbol{x}, \omega)$ of a function $f(\boldsymbol{x}, t)$ is defined as,

$$\tilde{f}(\boldsymbol{x}, \omega) := \frac{1}{\sqrt{2\pi}} \int_{-\infty}^{\infty} f(\boldsymbol{x}, t) \mathrm{e}^{i\omega t}\, dt \tag{8.1}$$

where ω is the temporal transform parameter or circular frequency and $i = \sqrt{-1}$. Application of the Fourier transform to the differential equations (2.27) - (2.33) governing structural acoustics leads to the strong (local) form of the boundary value problem in the frequency-domain.

Strong Form of the Time-Harmonic Problem

For a given frequency $\omega > 0$,
Find the displacement vector $\boldsymbol{u}(\boldsymbol{x}, \omega) : \bar{\Omega}_s \mapsto \mathbb{C}^d$, and the acoustic velocity potential $\phi(\boldsymbol{x}, \omega) : \bar{\Omega}_f \mapsto \mathbb{C}$, such that the following differential equations are satisfied:

$$\nabla \cdot \boldsymbol{\sigma} + \rho_s \omega^2 \boldsymbol{u} = \boldsymbol{0} \qquad \text{in } \Omega_s \tag{8.2}$$

$$\boldsymbol{\sigma} = \boldsymbol{C} : \nabla^s \boldsymbol{u} \qquad \text{in } \Omega_s \tag{8.3}$$

$$\nabla^2\phi + k^2\phi = f \qquad \text{in } \Omega_f \tag{8.4}$$

$$\boldsymbol{\sigma}\cdot\boldsymbol{n} = \bar{\boldsymbol{t}} \qquad \text{on } \Gamma_\sigma \tag{8.5}$$

$$\boldsymbol{\sigma}\cdot\boldsymbol{n} = -i\omega\rho_0\phi\boldsymbol{n} \qquad \text{on } \Gamma_i \tag{8.6}$$

$$\nabla\phi\cdot\boldsymbol{n} = -i\omega\boldsymbol{u}\cdot\boldsymbol{n} \qquad \text{on } \Gamma_i \tag{8.7}$$

$$\nabla\phi\cdot\boldsymbol{n} = -\mathbb{S}_m\phi \qquad \text{on } \Gamma_\infty \tag{8.8}$$

In the above, $k = \omega/c$, is the acoustic wavenumber where c is the speed of sound in the fluid medium. The acoustic pressure is calculated simply as $p = i\omega\rho_0\phi$. Equation (8.8) is either a local or nonlocal non-reflecting boundary condition defined through the operator $\mathbb{S}_m$. An alternative is to replace the boundary condition (8.8) with an infinite element, see Burnett [1993].

Time-harmonic acoustic radiation and scattering from complex structures such as submarines can be predicted accurately at the lower and higher ends of the frequency spectrum using existing solution techniques. At high frequencies characterized by normalized frequencies above $ka > 20$, where a is a length scale associated with the geometry, e.g. for an end-capped cylinder, the scale a measures the radius of the cylinder, approximate ray methods based on the geometrical theory of diffraction Keller [1962], can be used effectively. At low frequencies $ka < 10$, standard numerical methods such as the Galerkin finite element method, see for example Zienkiewicz and Bettess [1978], are effective for obtaining accurate solutions. However, as the frequency increases for a fixed mesh size, finite element solutions using the standard Galerkin approach deteriorate in accuracy. A standard rule of thumb is that ten linear elements are needed to accurately resolve a single wavelength. While there is no intrinsic limit on the size of frequency that can be handled using standard finite element methods, i.e. the mesh can always be refined to maintain a specified resolution accuracy; for large frequencies above $ka > 10$, the modeling effort required to satisfy this criteria can be prohibitive. Thus for high frequencies the number of degrees of freedom in a Galerkin finite element model can be overwhelming. A remark here is that the normalized frequency limits stated are only estimates, and may vary somewhat depending on the complexity of the structure and loading.

In this Chapter a simple enhancement of the standard Galerkin method, referred to as the Galerkin/Least-Squares (GLS) method is developed to address the problem of obtaining increased accuracy with a minimum number of degrees of freedom; in effect extending the range of the finite element solutions to higher frequency calculations. The starting point is the equivalent weak form of the time-harmonic boundary value problem defined in (8.2) through (8.8). The weak form can be obtained through a weighted residual statement and integration by parts.

Weak Form of the Time-Harmonic Problem

For a given frequency $\omega > 0$,
Find $(\boldsymbol{u}\,,\,\phi) \in \mathcal{S} \times \mathcal{T}$, such that $\forall\,(\boldsymbol{w}\,,\,w) \in \mathcal{V} \times \mathcal{W}$,

$$G_s(\boldsymbol{w}\,,\,\boldsymbol{u}) + i\omega A(\boldsymbol{w}\,,\,\phi)_{\Gamma_i} \;=\; F_s(\boldsymbol{w}) \tag{8.9}$$

$$G_f(w\,,\,\phi) - i\omega A(w\,,\,\boldsymbol{u})_{\Gamma_i} \;=\; F_f(w) \tag{8.10}$$

where the sesquilinear operators for the structure and fluid are respectively,

$$G_s(\boldsymbol{w}\,,\,\boldsymbol{u}) \;:=\; a_s(\boldsymbol{w},\boldsymbol{u}) - \omega^2(\boldsymbol{w},\boldsymbol{u}) \tag{8.11}$$

$$G_f(w\,,\,\phi) \;:=\; a_f(w,\phi) - k^2(w,\phi) + (w\,,\,\mathbb{S}_m\phi)_{\Gamma_\infty} \tag{8.12}$$

with

$$(\boldsymbol{w},\boldsymbol{u}) \;=\; \int_{\Omega_s} \rho_s\, \boldsymbol{w}\cdot\boldsymbol{u}\; d\Omega \tag{8.13}$$

$$a_s(\boldsymbol{w},\boldsymbol{u}) \;=\; \int_{\Omega_s} \nabla\boldsymbol{w} : \boldsymbol{C} : \nabla\boldsymbol{u}\; d\Omega \tag{8.14}$$

$$a_f(w,\phi) \;=\; \int_{\Omega_f} \rho_0\, \nabla w\cdot\nabla\phi\; d\Omega \tag{8.15}$$

$$(w,\phi) \;=\; \int_{\Omega_f} \rho_0\; w\;\phi\; d\Omega \tag{8.16}$$

$$A(\boldsymbol{w}\,,\,\phi)_{\Gamma_i} \;=\; \int_{\Gamma_i} \rho_0\; \boldsymbol{w}\cdot\boldsymbol{n}\phi\; d\Gamma \tag{8.17}$$

$$A(w\,,\,\boldsymbol{u})_{\Gamma_i} \;=\; \int_{\Gamma_i} \rho_0\; w\;\boldsymbol{u}\cdot\boldsymbol{n}\; d\Gamma \tag{8.18}$$

$$F_s(\boldsymbol{w}) = \int_{\Gamma_\sigma} \boldsymbol{w} \cdot \bar{\boldsymbol{t}} \; d\Gamma \tag{8.19}$$

$$F_f(w) = \int_{\Omega_f} \rho_0 \; w \, f \; d\Omega \tag{8.20}$$

$$(w \, , \, \mathbb{S}_m \phi)_{\Gamma_\infty} = \int_{\Gamma_\infty} \rho_0 \; w \; \mathbb{S}_m \; \phi \; d\Gamma \tag{8.21}$$

and where the trial and weighting function spaces are defined as,

$$\mathcal{S} = \mathcal{V} = \left\{ \boldsymbol{u} | \boldsymbol{u} : \Omega_s \mapsto \mathbb{C}^d, \boldsymbol{u} \in (H^1(\Omega_s))^d \right\} \tag{8.22}$$

$$\mathcal{T} = \mathcal{W} = \left\{ \phi | \phi : \Omega_f \mapsto \mathbb{C}, \phi \in H^1(\Omega_f) \right\} \tag{8.23}$$

Note that this weak form can also be obtained directly from the Fourier transform of the variational equation given in Chapter 7 for the semidiscrete formulation. The Galerkin finite element method is obtained by partitioning the domain into finite elements and by introducing discrete approximations to the trial and weighting functions. After solving for the time-harmonic displacements and acoustic pressures, the time-dependent solution can then be obtained indirectly by a Fast Fourier Transform (FFT) inversion algorithm of the frequency-domain solution. Of course if the dynamic disturbance varies harmonically with time as $e^{-i\omega t}$, i.e. the steady-state problem, or the analyist is only interested in the time-harmonic frequency response, then no such inversion is necessary.

In the Galerkin/Least-Squares (GLS) method, additional terms involving residuals of the governing differential equations are added to the Galerkin variational equation in least-squares form. In this thesis the design of GLS finite element methods for the Helmholtz equation governing the acoustic fluid medium are considered. The ideas presented here can also be extended to the structural response, but will not be addressed here. Applications to one-dimensional structural elements can be found in Grosh and Pinsky [1993b].

8.1 Background

Finite element solutions to the Helmholtz equation have primarily been sought using the standard Galerkin method; for applications see for example, MacCamy and

Marin [1980], Goldstein [1982], Bayliss, Goldstein and Turkel [1985a] and Burnett [1993]. However, it is well known that the numerical phase accuracy of standard Galerkin finite element solutions deteriorate rapidly as the wavenumber, normalized with the element mesh size, is increased, Belytschko and Mullen [1978], Mullen and Belytschko [1982]. This resolution problem arises from the use of piecewise polynomial shape functions to approximate highly oscillatory wave propagation solutions. To obtain an acceptable level of accuracy, more than ten elements per wavelength are required and for large wavenumbers, refining the mesh to maintain this requirement may become prohibitively expensive. Global error estimates for the Galerkin finite element method in terms of the wavenumber and local element size are derived in Bayliss, Goldstein and Turkel [1985b], Aziz, Kellogg and Stephens [1988] and Douglas, Santos, Sheen, and Schreiyer [1993].

Several approaches designed to improve the numerical phase accuracy of the standard Galerkin method have been proposed in recent years. Goldstein [1986] employed a version of the weak element method to the Helmholtz equation where the local solution within each element is approximated by a sum of exponentials. In this approach, continuity at interelement boundaries is enforced weakly for certain functionals of the approximate solution. As reported by Goldstein, for general problems in two-dimensions, the success of this approach has been limited.

Park and Jensen [1989] and Alvin and Park [1991] used discrete Fourier analysis to derive wavenumber dependent modifications to the stiffness and mass matrices arising from standard Galerkin finite element methods. The modified element matrices are designed to minimize dispersion error over a specified frequency–wavenumber window. This approach can be viewed as an extension of previous modifications to Galerkin finite element equations such as diagonal, and higher-order mass approximations, see Goudreau and Taylor[1973] and Fried [1979], but now tailored over a specified range of frequencies. A difficulty of such methods, is that they do not possess a firm mathematical basis for proving stability and convergence. In particular, they do not inherit the consistency inherent in the Galerkin method, an important ingredient for obtaining improved convergence rates with higher-order interpolation functions.

Over the last view years, a new class of residual based finite element formulations has emerged to counteract the stability problems and other numerical pathologies exhibited by the classical Galerkin method. These methods are developed by appending residuals of the Euler-Lagrange equations to the standard Galerkin variational equation. The added residual terms preserve the consistency inherent in the parent Galerkin method. Methods of this type were originally developed by Hughes and Brooks [1979], to improve the stability of numerical solutions for the advection-diffusion equation, and are referred to as 'streamline-upwind/Petrov-Galerkin' (SUPG) methods. For a review of SUPG type methods applied to advective-diffusive systems and fluid flow equations, see Hughes [1987] and Johnson [1986].

These ideas have since been extended by Hughes, Franca and Hulbert [1989], to the concept of Galerkin/Least-Squares (GLS) by appending residuals of the Euler-Lagrange equations in least-squares form to the standard Galerkin formulation. GLS finite element methods have been successfully employed in a wide variety of applications where enhanced stability and accuracy properties are needed, including problems governed by Navier-Stokes and the compressible Euler equations of fluid mechanics, Shakib and Hughes [1991] and the transient structural acoustics problem using the space-time formulation developed in this thesis.

Recently, Harari and Hughes [1991b] have applied GLS technology to the Helmholtz equation for one-dimensional model problems. An important feature of GLS methods is the introduction of a local mesh parameter into the variational equation that may be designed to provide accurate solutions with relatively coarse meshes. Harari and Hughes accomplished this for one-dimensional problems using dispersion analysis. In Harari and Hughes [1992c], the GLS mesh parameter derived in one-dimension is used in the DtN finite element method proposed by Keller and Givoli [1989] for solving the exterior Helmholtz problem. Although it was found that the one-dimensional parameter improved the accuracy of the Galerkin solution in some two-dimensional example problems, a comprehensive analysis of GLS dispersion characteristics in two-dimensions was unavailable.

In this work the selection of the optimal GLS mesh parameter for the multi-dimensional Helmholtz equation is considered, and leads to elements that exhibit improved accuracy. Optimal GLS methods for time-harmonic wave propagation in multi-dimensions were first introduced in Thompson and Pinsky [1993c], with extensions to exterior problems in Thompson and Pinsky [1993d]. Although for any given direction of wave propagation, it is shown in this work that an optimal GLS mesh parameter can be obtained, in general, the direction of wave propagation will not be known *a priori*. To remedy this difficulty, a GLS parameter is found which reduces phase error for all possible wave vector directions over an element. By performing a multi-dimensional Fourier analysis we have been able to characterize the phase accuracy and directional properties of the Galerkin/Least-Squares solution over all wave vector magnitudes and directions. A number of alternative GLS parameters are derived for general numerical integration rules such as Gaussian and Lobatto quadrature and their dispersion characteristics analyzed over the full range of wave vector orientations. Results from this analysis quantify the reduction in phase error achieved using alternative GLS mesh parameters. A number of example problems are numerically solved to verify the accuracy of the GLS method and assess the performance of competing GLS design parameters. Extensions to three-dimensional trilinear elements are discussed as well as alternative methods such as the Generalized Galerkin/Least-Squares (GGLS) method. Extensions to higher-order finite element interpolations is also considered. In particular, an optimal GLS parameter is designed that reduces dispersion for elements with quadratic interpolation functions, together with some approximate GLS mesh parameters useful for efficient computation.

8.2 Overview

In Section 8.3 the Helmholtz equation and its characteristic equation relating frequency and wave vector components in two-dimensions is reviewed. In Section 8.4 the Galerkin/Least-Squares variational equation is given. Difference equations arising from the assembly of a uniform discretization of bilinear elements are derived in Section 8.5. In Section 8.6 a discrete Fourier analysis is performed. Optimal GLS parameters are derived and dispersion curves compared to the standard Galerkin method in Section 8.7. In Section 8.8, numerical examples of both interior and exterior problems are solved. Extensions of the new multi-dimensional GLS mesh parameters to three-dimensions and to Generalized Galerkin/Least-Squares (GGLS) methods are give in Sections 8.9.1 and 8.9.2 respectively. Finally in Section 8.9.3 the application of GLS methods to high-order finite element interpolations is considered.

8.3 The Helmholtz Equation

To illustrate the ideas involved for the selection of optimal Galerkin/Least-Squares mesh parameters in multi-dimensional wave propagation problems, we start with the two-dimensional Helmholtz equation; extensions to three-dimensions is straightforward.

Consider a two-dimensional homogeneous isotropic acoustic medium whose wave speed is c. The wave solution $u(\boldsymbol{x}, t)$ corresponding to a harmonic source vibrating at a given fixed frequency $\omega > 0$ satisfies the scalar wave equation:

$$\nabla^2 \phi(\boldsymbol{x}, t) - \phi_{,tt}(\boldsymbol{x}, t)/c^2 = -f(\boldsymbol{x}) e^{-i\omega t}, \qquad (\boldsymbol{x}, t) \in \Omega \times]0\,,\,T[\tag{8.24}$$

Looking for a solution to (8.24) such that $u(\boldsymbol{x}, t) = \phi(\boldsymbol{x}) e^{-i\omega t}$ we find that ϕ must satisfy the scalar Helmholtz (reduced wave) equation:

$$\mathcal{L}\phi \equiv \nabla^2 \phi + k^2 \phi = -f \qquad \text{in} \;\; \Omega \tag{8.25}$$

where $k = \omega/c > 0$ is the wavenumber with wavelength $2\pi/k$, ∇^2 is the Laplacian differential operator and Ω is the spatial domain of interest.

The Helmholtz equation in $\mathbb{R}^2$ admits the plane-wave propagating solution,

$$\phi(x, y) = e^{i(k_x x + k_y y)} \tag{8.26}$$

where the frequency ω and the wave vector components k_x and k_y are linked by the characteristic equation,

$$\boxed{\left(\frac{\omega h}{c}\right)^2 = (k_x h)^2 + (k_y h)^2} \tag{8.27}$$

and h is a problem dependent characteristic length. This nondispersive relation is satisfied by the directional wave vector components $k_x = k\cos\theta$ and $k_y = k\sin\theta$, where the normal to the plane wave is oriented at angle θ relative to the x-axis.

Alternatively, the characteristic equation (8.27) can be obtained by a two-dimensional

Fourier transform from physical space to wave space through the transform operation,

$$\tilde{F}(k_x, k_y) := \frac{1}{\sqrt{2\pi}} \int_{-\infty}^{\infty} \int_{-\infty}^{\infty} F(x, y) \mathrm{e}^{-i(k_x x + k_y y)} dx dy \tag{8.28}$$

The discrete counterpart to this continuous transform will be used as a tool for the design of improved finite element methods for the solution of the two-dimensional Helmholtz equation.

8.4 Finite Element Formulations

Consider a partition of Ω into finite elements. Let Ω_e be the interior of the eth element, and $\tilde{\Omega} = \bigcup_e \Omega_e$. Let $\mathcal{S}^h \subset H^1(\Omega)$ and $\mathcal{V}^h \subset H^1(\Omega)$ be finite element spaces consisting of continuous piecewise polynomials of order p.

8.4.1 Galerkin

As a point of departure, consider the classical Galerkin method.
Given $k = \omega / c > 0$, *find* $\phi^h \in \mathcal{S}^h$, such that

$$A(w^h, \phi^h) = L(w^h) \qquad \forall w^h \in \mathcal{V}^h \tag{8.29}$$

where

$$A(w^h, \phi^h) \equiv (\nabla w^h, \nabla \phi^h)_\Omega - k^2 (w^h, \phi^h)_\Omega \tag{8.30}$$

$$L(w^h) \equiv (w^h, f)_\Omega \tag{8.31}$$

and $(\cdot, \cdot)_\Omega$ denotes the $L_2(\Omega)$ inner product. The Galerkin formulation is consistent in the sense that ϕ, the exact solution to the Helmholtz equation, satisfies (8.29). For $k^2 > 0$ the operator,

$$A(w^h, w^h) = ||\nabla w^h||^2 - k^2 ||w^h||^2 \qquad \forall w^h \in \mathcal{V}^h \tag{8.32}$$

loses positive-definiteness as the wavenumber increases, resulting in a loss of ellipticity (stability) with increasing wavenumber. This difficulty is especially important when solving large-scale problems with iterative solvers where the condition number of the matrix equations, and hence the convergence rate, depends on the wavenumber, see for example, Bayliss, Goldstein, and Turkel [1983].

8.4.2 Galerkin/Least-Squares

It is well known that the phase accuracy associated with the Galerkin finite element solution degrades as the wavenumber k is increased relative to the mesh parameter h. In order to improve the accuracy characteristics of the standard Galerkin method, a least-squares operator is added to (8.29). This additional operator is constructed from a residual of the governing Helmholtz differential equation evaluated within element interiors.

$$\boxed{A(w^h, \phi^h) + (\tau \mathcal{L} w^h, r^h)_{\tilde{\Omega}} = L(w^h)} \tag{8.33}$$

In this expression, $r^h = \mathcal{L}\phi^h + f$ is the residual, and τ is a local mesh parameter with units of inverse length-squared to be determined from dispersion analysis. If $\tau = 0$, the method reverts to Galerkin. Formally, GLS can be stated as follows:
Find $\phi^h \in \mathcal{S}^h$, such that

$$A_{GLS}(w^h, \phi^h) = L_{GLS}(w^h) \qquad \forall w^h \in \mathcal{V}^h \tag{8.34}$$

where

$$A_{GLS}(w^h, \phi^h) \equiv A(w^h, \phi^h) + \sum_{e=1}^{n_{el}} \int_{\Omega_e} \tau \mathcal{L} w^h \, \mathcal{L}\phi^h \, d\Omega \tag{8.35}$$

$$L_{GLS}(w^h) \equiv L(w^h) - \sum_{e=1}^{n_{el}} \int_{\Omega_e} \tau \mathcal{L} w^h \, f \, d\Omega \tag{8.36}$$

As a result of being a weighted residual method, the error $e = \phi^h - \phi$ is orthogonal $\forall w^h \in \mathcal{V}^h$ with respect to A_{GLS}.

$$A_{GLS}(w^h, e) = 0 \tag{8.37}$$

This consistency condition is an important ingredient in obtaining improved convergence rates with higher-order interpolation. A Fourier synthesis of A_{GLS} from physical space to wavenumber space is used as a tool to determine the optimal τ for two-dimensional applications.

8.4.3 Illustration of fundamental difficulty

The following calculations demonstrates the difficulty Galerkin methods have in resolving time-harmonic waves as the wavenumber is increased relative to the mesh size. Consider the problem of finding the solution $\phi : \bar{\Omega} = \{(x, y) : 0 \leq x \leq L_x, 0 \leq y \leq L_y\} \rightarrow \mathbb{R}$ with an inhomogeneous Dirichlet boundary condition within a waveguide.

$$(\nabla^2 + k^2)\phi(x, y) = 0 \qquad \text{in } \Omega \tag{8.38}$$

$$\phi(0, y) = g_0, \qquad \phi(L_x, y) = 0 \tag{8.39}$$

$$\phi_{,y}(x, 0) = \phi_{,y}(x, L_y) = 0 \tag{8.40}$$

The analytical solution to this problem is characterized by the standing plane-wave representation,

$$\phi(x|k) = g_0 \frac{\sin(k(L_x - x))}{\sin(kL_x)} \tag{8.41}$$

Let $L_x = L_y = L$, and discretize the computational domain with a uniform mesh of $n_{el} = 10 \times 10$ equally spaced bilinear finite elements. It can be verified that the GLS nodal solution to this problem has the same form as the analytical solution but with the physical wavenumber k replaced with a numerical wavenumber k^h. Since this problem is an example of a plane-wave solution directed along x-direction mesh lines, the problem essentially is one-dimensional. In this case the GLS method can be designed to achieve nodal exactness (superconvergence) by choosing an optimal GLS parameter τ such that exact phase is obtained, that is $k^h = k$, Harari and Hughes [1991b].

Figure 8.1 illustrates the elevated contours of the nodally exact GLS solution interpolated with the underlying mesh, for a nondimensional wavenumber $kh = \pi/6$, corresponding to a relatively refined mesh of twelve elements per wavelength. The profile of this solution plotted along the x-axis is shown in Figure 8.2(top). The Galerkin ($\tau = 0$) solution with either consistent ($\epsilon = 1$) or lumped mass ($\epsilon = 0$) approximation is well-resolved as predicted from the finite element dispersion analysis

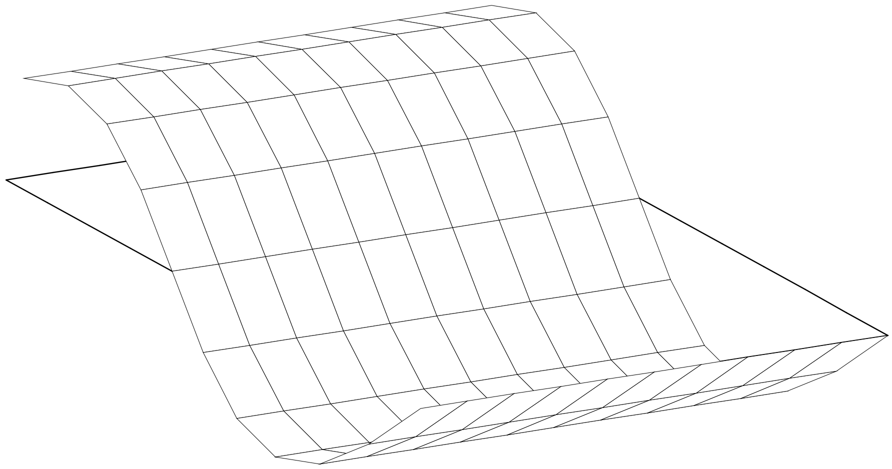

Figure 8.1: Elevated contours of plane-wave solution directed along x-direction mesh lines with $kh = \pi/6$, twelve elements per wavelength.

in the following Sections. Figure 8.2(bottom) illustrates that as the wavenumber is increased to $kh = \pi/3$, corresponding to a coarse mesh of six elements per wavelength, the accuracy of the Galerkin solution deteriorates significantly, while GLS remains nodally exact as designed.

For a uniform mesh of piecewise linear finite elements, then $\nabla^2\phi^h$ is identically zero on element interiors, and with no sources $f = 0$, the method reverts to a modified wavenumber method, i.e.

$$A_{GLS}(w^h, \phi^h) = (\nabla w^h, \nabla \phi^h)_\Omega - \tilde{k}^2(w^h, \phi^h)_\Omega \tag{8.42}$$

where $\tilde{k}^2 \equiv (1-\tau k^2)k^2$. If $f \neq 0$, the GLS method differs from a modified wavenumber approach in that the consistent loading operator for GLS takes the form,

$$L_{GLS}(w^h) = (1 - \tau k^2)L(w^h) \tag{8.43}$$

This distinction is crucial in order to maintain the consistency and accuracy of the GLS formulation. As an illustration of this issue, consider the same problem as above

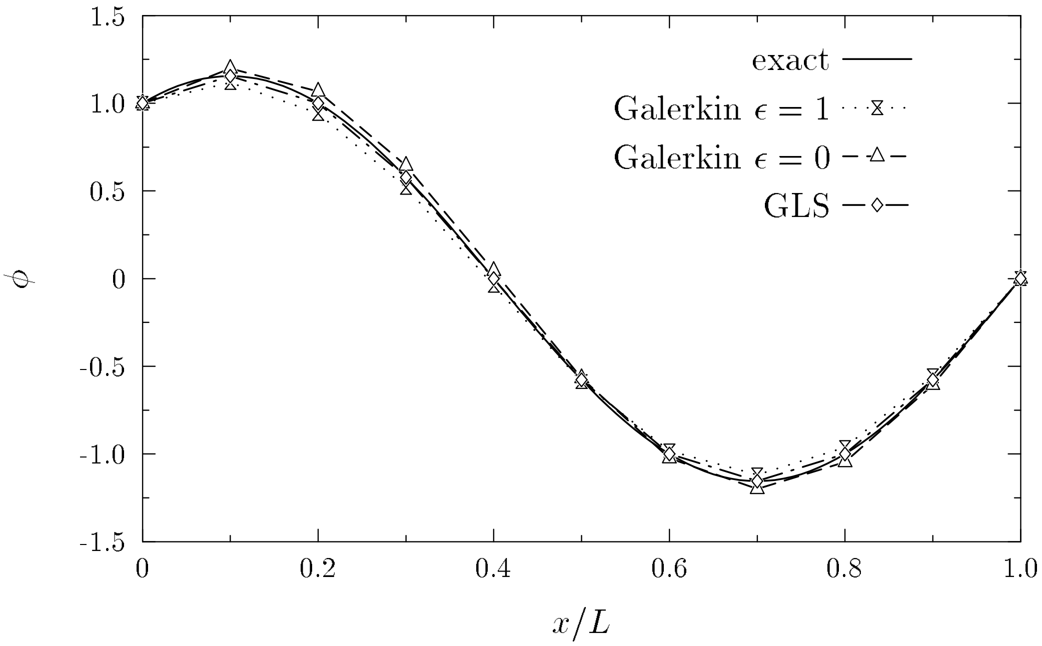

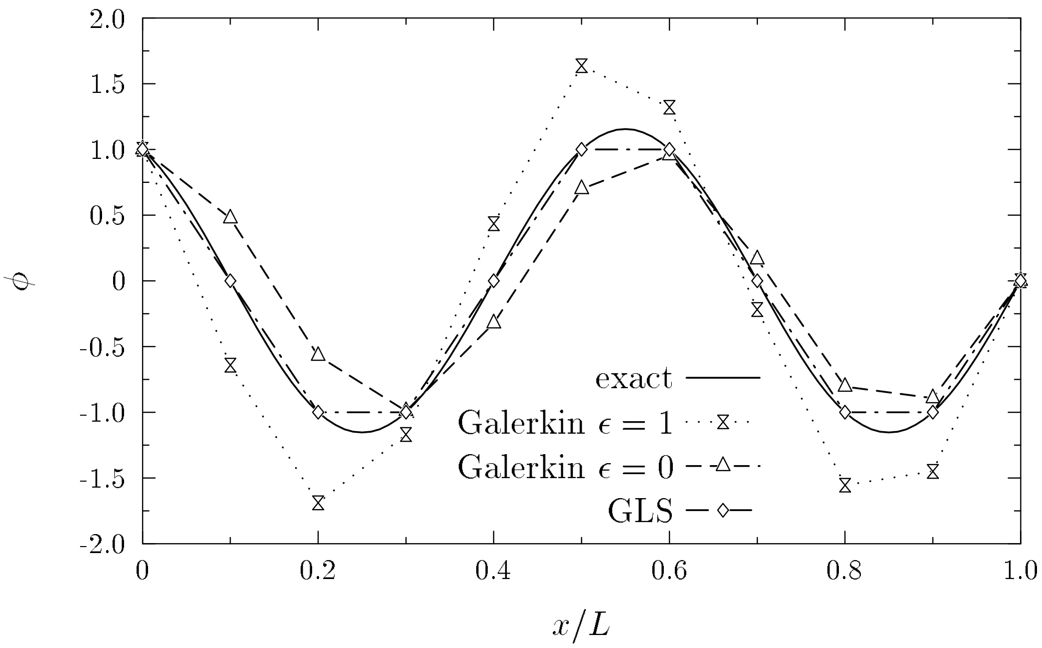

Figure 8.2: Waveguide problem with plane-wave solution directed along x-direction mesh lines with (top) $kh = \pi/6$, twelve elements per wavelength. (bottom) $kh = \pi/3$, six elements per wavelength.

but now with a source loading given by $f = -10\sin(2\pi x/L)$, and a nondimensional wavenumber $kh = \pi/3$ corresponding to six elements per wavelength. Figure 8.3 shows that when source terms are present, i.e. $f \neq 0$, then a modified wavenumber approach becomes inconsistent and as a result loses accuracy. In contrast, the GLS method, with consistent modification of the loading operator maintains nodal exactness by design. To this authors knowledge, this is the first demonstration of this fact for the Helmholtz equation. While for plane-waves traveling along mesh lines it is possible to obtain nodally exact solutions, in multi-dimensional wave propagation problems, this is not generally possible. The goal of this work then is to design an optimal GLS mesh parameter for multi-dimensional waves that minimizes dispersion errors over all possible wave vector orientations.

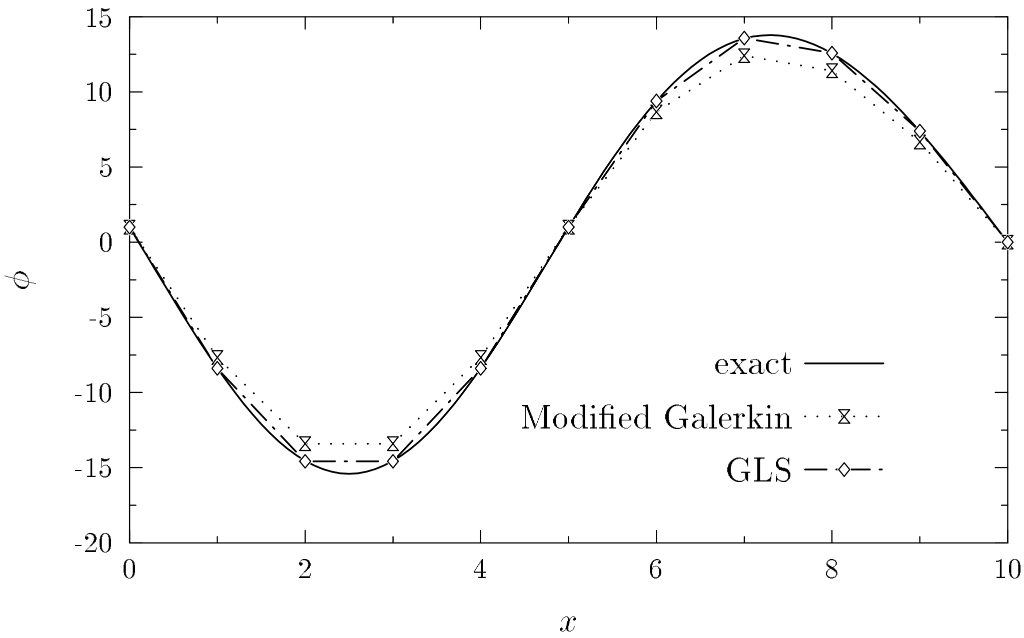

Figure 8.3: Waveguide problem with source term $f = -10\sin(2\pi x/L)$, and $kh = \pi/3$, six elements per wavelength.

8.5 Finite Element Discretization

Consider a uniform mesh of bilinear elements,

$$\mathbb{R}^2_h = \{(x, y) \in \mathbb{R}^2 = (mh_x, nh_y)\,,\,(m, n) \in \mathbb{Z}\} \tag{8.44}$$

with element sides h_x in the x-direction and h_y in the y-direction. In order to expose the directional behavior of the finite element discretization, the approximation of ϕ^h and w^h within each element is defined as the tensor product $\mathcal{P}^1 \times \mathcal{P}^1$ of one-dimensional linear interpolants over the biunit square $(\xi, \eta) \in (-1, 1)^2$:

$$\phi^h(\xi, \eta) = \sum_{k=1}^{2}\sum_{l=1}^{2} L_k(\xi)L_l(\eta)\phi^e_{kl} \tag{8.45}$$

$$w^h(\xi, \eta) = \sum_{i=1}^{2}\sum_{j=1}^{2} L_i(\xi)L_j(\eta)w^e_{ij} \tag{8.46}$$

where $L_i(\xi) = (1 + \xi_i\xi)/2$, $\xi_i = \pm 1$ and $\phi^e_{kl} = \phi^h(\xi_k, \eta_l)$ are the element nodal variables. For a uniform mesh of bilinear elements, all derivatives of order higher that one vanish within element interiors Ω^e, i.e. $\mathcal{L}\phi^h = k^2\phi^h$. When $f = 0$, the GLS local element equations defined in tensor product form are,

$$\sum_k\sum_l \left(S^e_{ijkl} - \gamma k^2 M^e_{ijkl}\right)\phi^e_{kl} = 0 \tag{8.47}$$

The quantity

$$\boxed{\gamma := (1 - \tau k^2)} \tag{8.48}$$

embodies the GLS mesh parameter τ, and the local element stiffness and mass tensors integrated with a (2×2) quadrature rule are defined as,

$$\boldsymbol{S}^e = [S^e_{ijkl}], \qquad S^e_{ijkl} := \frac{1}{h_x^2}A_{ik}B_{jl} + \frac{1}{h_y^2}B_{ik}A_{jl} \tag{8.49}$$

$$\boldsymbol{M}^e = [M^e_{ijkl}], \qquad M^e_{ijkl} := B_{ik}B_{jl}/4 \tag{8.50}$$

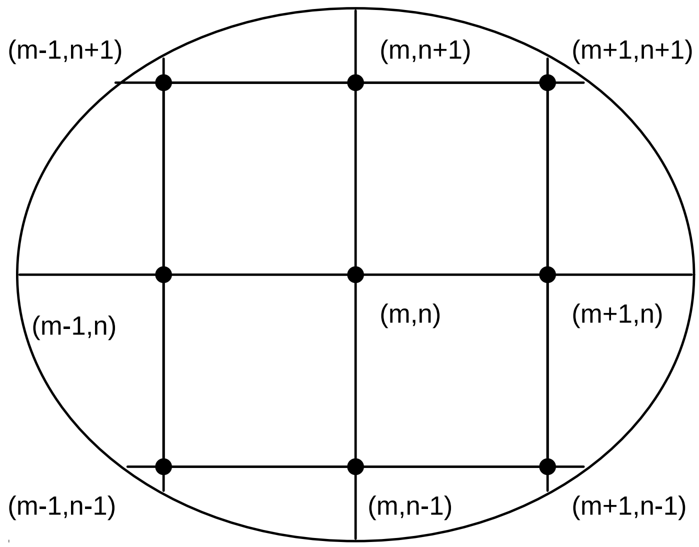

Figure 8.4: Two-dimensional bilinear finite element mesh with spacing $\Delta x = h_x$ and $\Delta y = h_y$.

where the discrete L_2 inner products are given by,

$$A^e_{ij} = \sum_{q=1}^{2} L'_i(\xi_q) L'_j(\xi_q) W_q, \qquad B^e_{ij} = \sum_{q=1}^{2} L_i(\xi_q) L_j(\xi_q) W_q \tag{8.51}$$

and ξ_q is the quadrature point and W_q the quadrature weight. In these expressions the prime on the shape functions denotes differentiation. For (2×2) Gaussian quadrature, the inner products are exactly integrated. For Lobatto quadrature, B^e_{ij} is underintegrated and diagonal, i.e. $B^e_{ij} = \delta_{ij} W_j$.

Finite element difference relations are obtained by assembling a patch of four bilinear elements as illustrated in Figure 8.4. The result is the difference stencil associated with the interior node $\phi_{m,n} = \phi^h(mh_x, nh_y)|\mathbb{R}^2_h \mapsto \mathbb{C}$.

$$\boxed{F(k) = S\phi_{m,n} - \gamma k^2 M \phi_{m,n} = 0} \tag{8.52}$$

where S and M are the two-dimensional linear difference operators emanating from the assembled stiffness (discrete Laplacian) and mass tensors respectively.

$$S = \sum_{p,q=-1}^{1} s_{pq} E_x^p E_y^q = S_x + S_y \tag{8.53}$$

$$S_x = -\frac{1}{h_x^2}(1 + \frac{\epsilon}{6}\delta_y^2)\delta_x^2 \tag{8.54}$$

$$S_y = -\frac{1}{h_y^2}(1 + \frac{\epsilon}{6}\delta_x^2)\delta_y^2 \tag{8.55}$$

$$M = \sum_{p,q=-1}^{1} m_{pq} E_x^p E_y^q = M_x \times M_y \tag{8.56}$$

$$M_x = (1 + \frac{\epsilon}{6}\delta_x^2) \tag{8.57}$$

$$M_y = (1 + \frac{\epsilon}{6}\delta_y^2) \tag{8.58}$$

The directional shift operators are defined by,

$$E_x^p \phi_{m,n} = \phi_{m+p,n} \qquad \text{and} \qquad E_y^q \phi_{m,n} = \phi_{m,n+q} \tag{8.59}$$

and the central difference operators are defined by,

$$\delta_x^2 \phi_{m,n} = \phi_{m-1,n} - 2\phi_{m,n} + \phi_{m+1,n} \tag{8.60}$$

$$\delta_y^2 \phi_{m,n} = \phi_{m,n-1} - 2\phi_{m,n} + \phi_{m,n+1} \tag{8.61}$$

The ϵ is a general quadrature parameter equal to 1 for exact Gaussian quadrature and 0 for Lobatto quadrature. The mass operator M is referred to as consistent when $\epsilon = 1$ and lumped when $\epsilon = 0$. Expressions for the bilinear stiffness and mass stencils $[s_{pq}]$ and $[m_{pq}]$ defined for the interior node (m, n) using consistent mass are given by,

$$[s_{pq}] = -\frac{1}{6h_x^2}\begin{bmatrix} 1 & -2 & 1 \\ 4 & -8 & 4 \\ 1 & -2 & 1 \end{bmatrix} - \frac{1}{6h_y^2}\begin{bmatrix} 1 & 4 & 1 \\ -2 & -8 & -2 \\ 1 & 4 & 1 \end{bmatrix}$$

$$[m_{pq}] = \frac{1}{36}\begin{bmatrix} 1 & 4 & 1 \\ 4 & 16 & 4 \\ 1 & 4 & 1 \end{bmatrix}$$

8.6 GLS Dispersion Relations

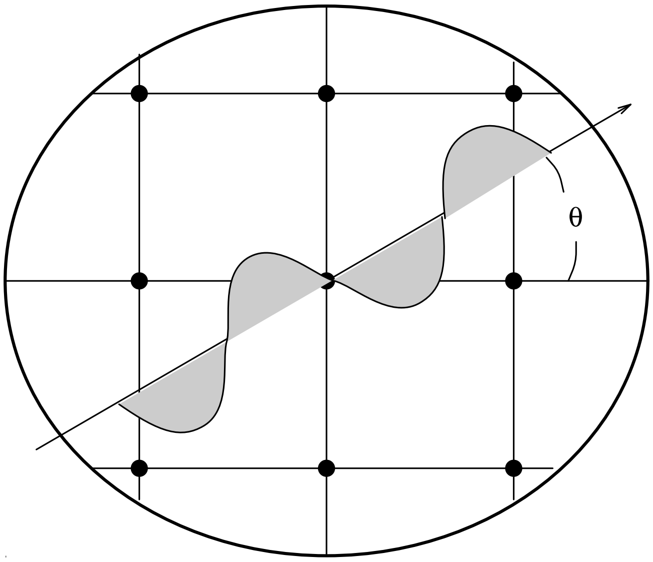

Figure 8.5: Direction of plane-wave with angle θ measured relative to mesh lines

The GLS finite element dispersion relations are obtained by assuming a plane-wave solution propagating at an arbitrary angle relative to the mesh lines,

$$\phi_{m,n} = \mathrm{e}^{i(k_x^h h_x m + k_y^h h_y n)} \tag{8.62}$$

with $i = \sqrt{-1}$. In the above, the directional wave vector components are denoted $k_x^h = k^h \cos\theta$ and $k_y^h = k^h \sin\theta$ with numerical wavenumber k^h. The normal is oriented at angle θ relative to mesh lines, see Figure 8.5. Substituting (8.62) into (8.52) results in the following GLS dispersion relation,

$$\boxed{\tilde{F}(k, k_x^h, k_y^h) = \tilde{S} - \gamma k^2 \tilde{M} = 0} \tag{8.63}$$

This equation describes the relationship between the continuous wavenumber $k = \omega/c$ and the finite element discrete wave vector components k_x^h and k_y^h. In this relation, $\tilde{S}$ and $\tilde{M}$ represent the discrete Fourier transforms of the linear difference operators S and M respectively. Expressions for these transformed stiffness and mass operators are given by,

$$\tilde{S}(k_x^h h_x, k_y^h h_y) = \sum_{p,q=-1}^{1} s_{pq} \mathrm{e}^{i(k_x^h h_x p + k_y^h h_y q)} = \mathbf{1}_y \bar{k}_x^2 + \mathbf{1}_x \bar{k}_y^2 \tag{8.64}$$

$$\tilde{M}(k_x^h h_x, k_y^h h_y) = \sum_{p,q=-1}^{1} m_{pq} \mathrm{e}^{i(k_x^h h_x p + k_y^h h_y q)} = \mathbf{1}_x \mathbf{1}_y \tag{8.65}$$

with notation,

$$\bar{k}_x^2 = 2(1 - f_x)/h_x^2 \qquad \text{and} \qquad \bar{k}_y^2 = 2(1 - f_y)/h_y^2 \tag{8.66}$$

$$\begin{aligned} f_x &= \cos(k_x^h h_x) = \cos(k^h h_x \cos\theta) \\ f_y &= \cos(k_y^h h_y) = \cos(k^h h_y \sin\theta) \end{aligned}$$

$$\mathbf{1}_x = 1 - \frac{\epsilon}{6}(\bar{k}_x h_x)^2 \qquad \text{and} \qquad \mathbf{1}_y = 1 - \frac{\epsilon}{6}(\bar{k}_y h_y)^2 \tag{8.67}$$

For a detailed description of the discrete Fourier transform applied to linear difference equations, see Vichnevetsky and Bowles [1982]. The characteristic equation (8.63) describes the nonlinear relationship between the continuous wavenumber $k = \omega/c$ and the finite element discrete wave vector components k_x^h and k_y^h. Written in the alternate form,

$$\gamma k^2 = D^h(k^h, \theta), \qquad D^h = \tilde{S}/\tilde{M} \tag{8.68}$$

it is clear that the dispersion relation depends on both the magnitude of the discrete wavenumber $k^h := |k^h|$ and the orientation of the wavevector θ.

$$|k^h| = \sqrt{(k_x^h)^2 + (k_y^h)^2} \tag{8.69}$$

$$\theta = \tan^{-1}(k_y^h / k_x^h) \tag{8.70}$$

8.7 Selection of an optimal GLS mesh parameter

The optimal least-squares mesh parameter τ is obtained by requiring the phase to be exact, i.e. $k = k^h$ for any choice of wave vector angle $\theta = \theta_o$. This requirement is met by replacing k^h with the exact wavenumber, $k = \omega/c$, in the GLS finite element dispersion relation (8.68), restricting $h_x = h_y = h$, and solving for γ. With this design criteria, the optimal τ is defined as,

$$\boxed{\tau k^2 := 1 - \frac{\tilde{S}(kh, \theta_o)}{k^2 \tilde{M}(kh, \theta_o)}} \tag{8.71}$$

where $\tilde{S}$ and $\tilde{M}$ are defined in (8.64) through (8.67) with k^h replaced with $k = \omega/c$. In particular, for exact 2×2 Gaussian integration, the expression for the optimal GLS mesh parameter is,

$$\boxed{\tau k^2 = 1 - \frac{6(4 - f_x - f_y - 2 f_x f_y)}{(kh)^2 (2 + f_x)(2 + f_y)}} \tag{8.72}$$

Selecting $\theta_0 = 0$, (8.71) specializes to,

$$\tau k^2 := 1 - \frac{6(1 - \cos kh)}{(kh)^2 (3 - \epsilon(1 - \cos kh))} \tag{8.73}$$

which yields exact phase for plane-waves directed along uniform mesh lines. When $\epsilon = 1$ this definition specializes to the GLS parameter derived by Harari and Hughes [1991b] in one-dimension. For comparison the GLS mesh parameter τ defined in (8.72), with $\epsilon = 1$, designed to give exact phase for plane-waves oriented along $\theta = 0$ (denoted τ_0) and $\theta = 22.5$ (denoted $\tau_{22.5}$) are plotted in Figure 8.6. For reference, $kh/\pi = 0.2$ represents a mesh with ten elements per wavelength. In this range, the two τ parameters compared are nearly identical and close to zero. Thus, when there are more than ten elements per wavelength, the least-squares contribution has only a small effect on the Galerkin solution. At $kh/\pi = 0.4$, corresponding to only five elements per wavelength, the two GLS parameters compared show a significant difference.

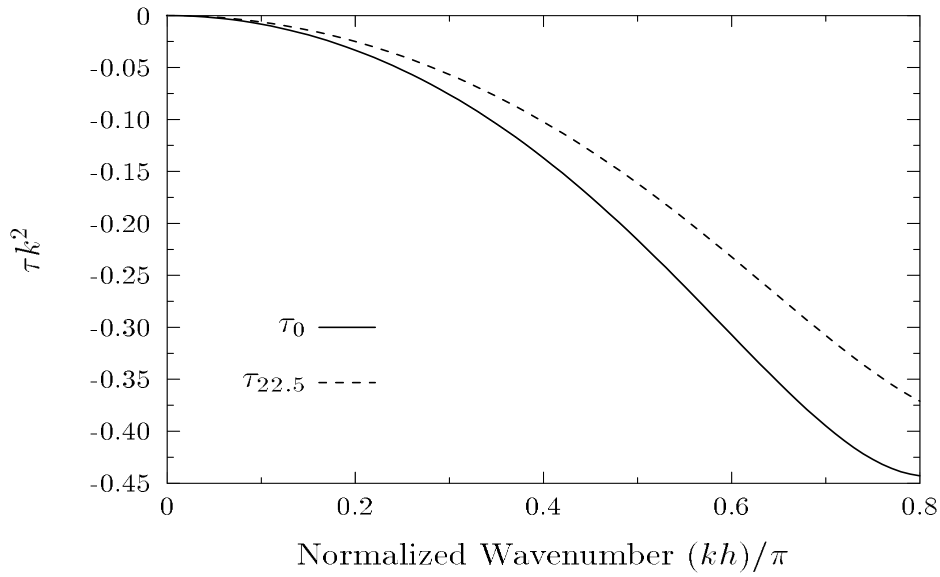

Figure 8.6: Optimal GLS parameters designed to give exact phase for plane waves directed along $\theta = 0$ (denoted τ_0), and $\theta = 22.5$ (denoted $\tau_{22.5}$).

8.7.1 GLS dispersion analysis

In this section, the performance of alternate GLS mesh parameters, based on definition (8.71), with different choices of θ_o and ϵ are examined. The accuracy of the numerical solution is assessed in terms of the phase error defined by,

$$\mathrm{e}_p(k^h, \theta) := \frac{k}{k^h} \tag{8.74}$$

with $\omega = kc = k^h c^h$, we can write the phase error in the alternative form $\mathrm{e}_p = c^h/c$. Exact phase corresponds to $\mathrm{e}_p = 1$. Results are plotted for plane wave solutions directed along mesh lines $\theta = 0$, and for plane wave solutions directed along mesh diagonals $\theta = 45$. Results for orientations $\theta \in]0, 45[$ are bounded by these angles.

8.7.2 Consistent mass

Dispersion curves for Galerkin $\tau = 0$ and GLS with τ_0, designed to give exact phase for plane-waves directed along $\theta = 0$ are given in Figure 8.7. Results are given for plane-waves propagating at angles $\theta = 0$, 22.5 and 45. Near the origin, the relative phase speed converges to unity $\mathrm{e}_p = 1$, but as the wavenumber increases, the phase error also increases. The Galerkin solution exhibits a phase lead $c^h/c > 1$ and the

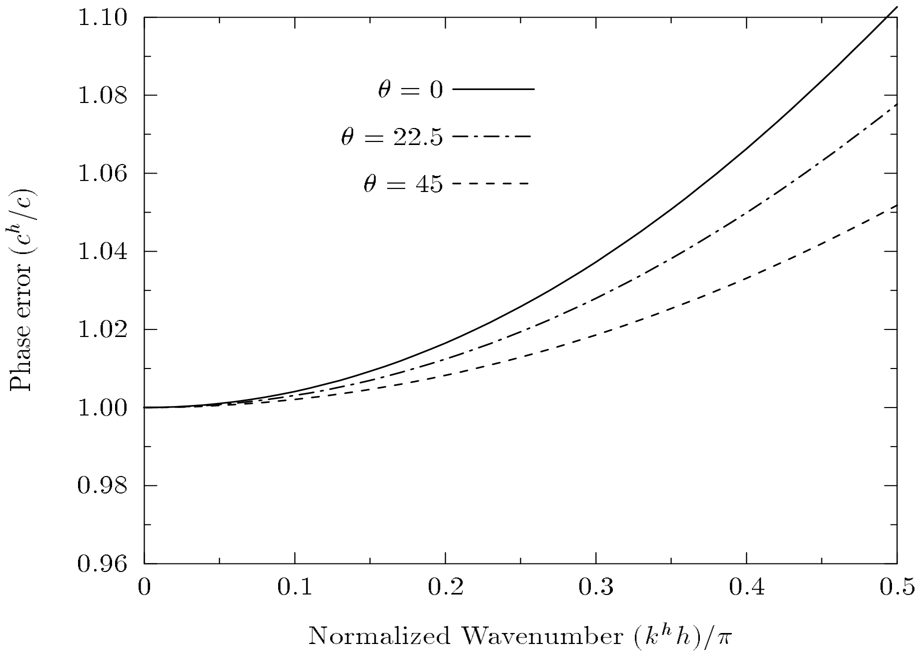

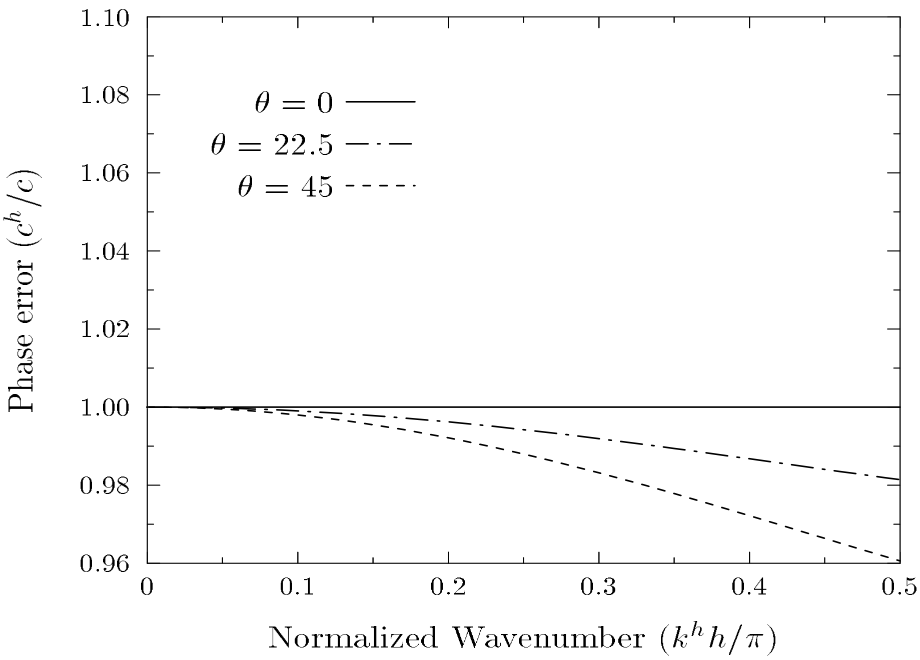

Figure 8.7: Phase error at three different angles $\theta = 0$, 22.5 and 45 using exact integration for (top) Galerkin $\tau = 0$, (bottom) GLS $\tau = \tau_0$, designed to give exact phase for $\theta = 0$.

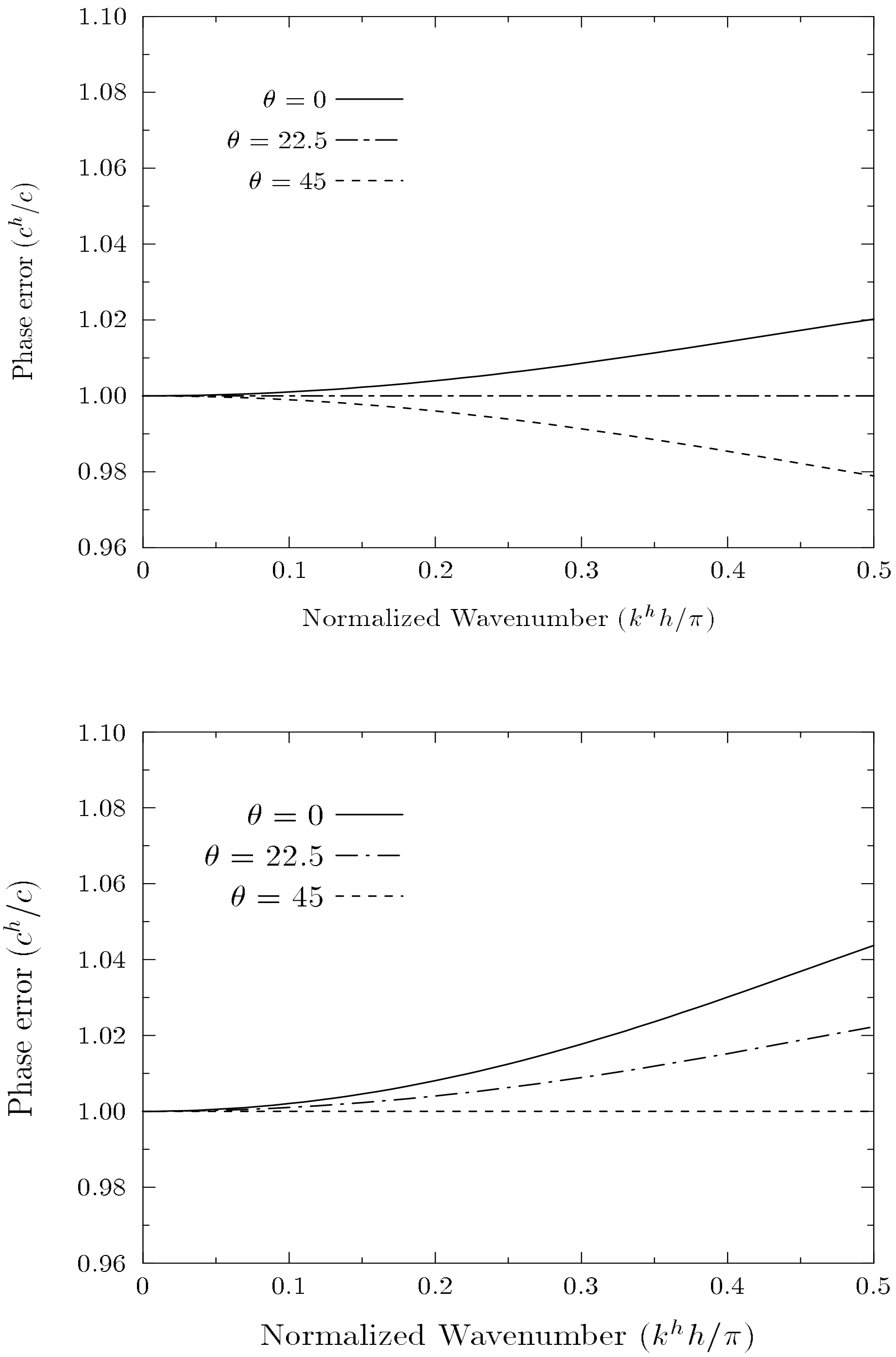

Figure 8.8: Phase error using exact integration for (top) GLS $\tau = \tau_{22.5}$, (bottom) GLS $\tau = \tau_{45}$

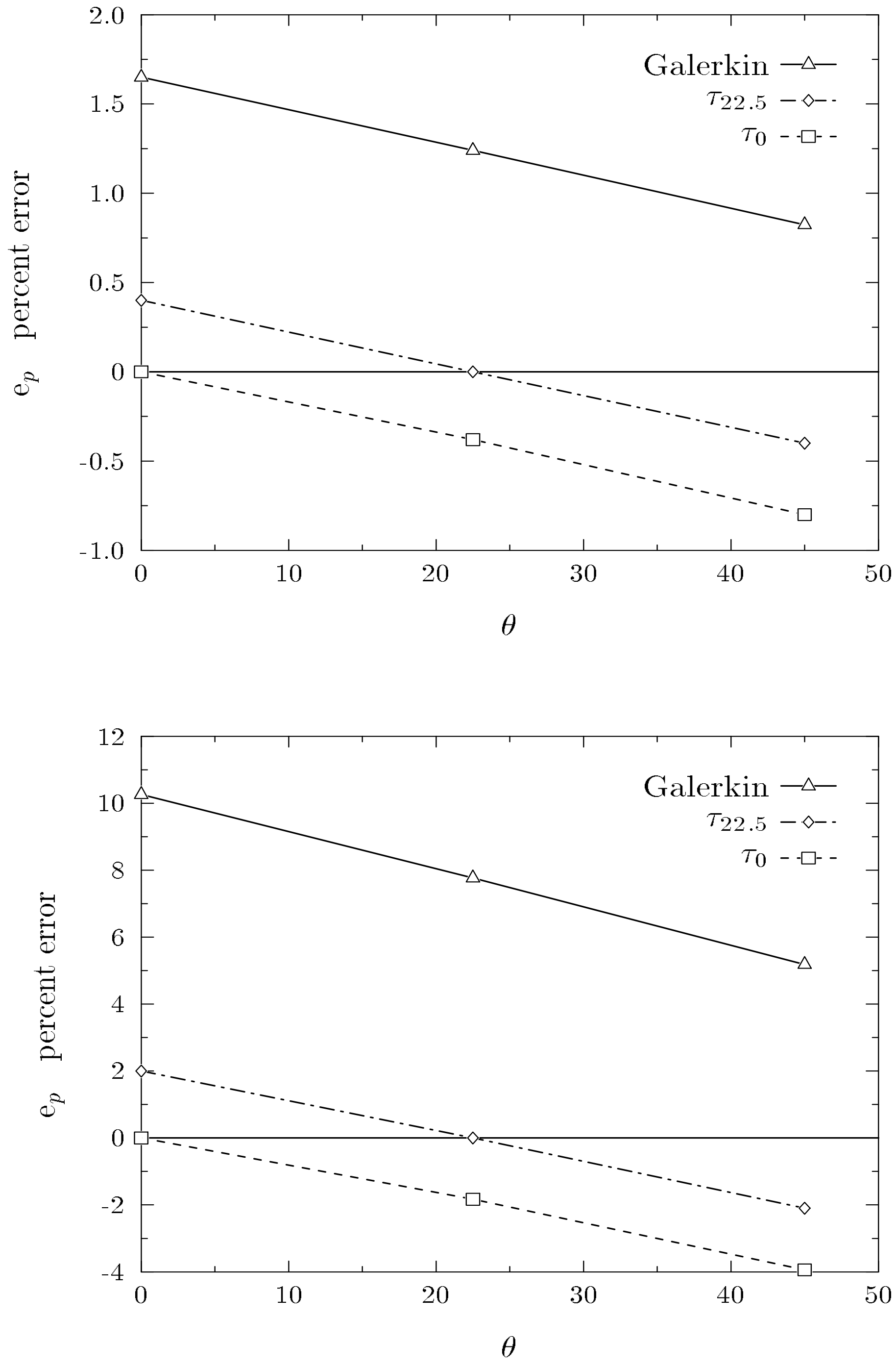

Figure 8.9: Phase error using exact integration at (top) 10 elements per wavelength, (bottom) 4 elements per wavelength.

phase error is a minimum for plane-waves directed along mesh diagonals $\theta = 45$. For a mesh refinement of ten elements per wavelength ($k^h h = .2\pi$), the maximum phase error max$|\mathrm{e}_p|$ evaluated over all angles θ is less than 2 percent. As the wavenumber is increased relative to the mesh parameter h, the phase accuracy degrades severely to max$|\mathrm{e}_p| = 10$ percent. For GLS with τ_0 and exact integration, the two-dimensional GLS dispersion relation relating the exact wavenumber $k = \omega/c$, to the discrete wavenumber k^h and angle θ is given by,

$$kh = \cos^{-1}\left\{\frac{4(f_x + f_y) + 5f_x f_y - 4}{f_x + f_y - f_x f_y + 8}\right\} \tag{8.75}$$

By design, for propagation along mesh lines $\theta = 0$ (mod 90), this relation reduces to the exact phase relationship $\mathrm{e}_p = 1$ for $kh \in (0, \pi)$. Referring to Figure 8.7, the dispersion curves for $\theta \neq 0$ exhibit a phase lag $c^h/c < 1$ with max$|\mathrm{e}_p|$ reduced to approximately 4 percent at four elements per wavelength. These two-dimensional dispersion results show how the addition of the least-squares operator, with the GLS mesh parameter τ_0 defined in (8.73), reduces the phase error over all wave vector orientations θ.

In Figure 8.8, the dispersion curves for the alternative GLS parameters, $\tau_{22.5}$ designed for exact phase at $\theta = 22.5$, and τ_{45} designed for exact phase at $\theta = 45$ are compared. For τ_{45}, the maximum phase error is still approximately 4 percent but is now reflected about the exact solution $c^h/c = 1$ such that there is a phase lead $c^h/c > 1$. By choosing the GLS parameter $\tau_{22.5}$, corresponding to exact phase for $\theta = 22.5$, the envelope of the dispersion curves is centered around the exact result $c^h/c = 1$. As a result, the GLS solution exhibits a maximum possible error $|\mathrm{e}_p|$ of only 2 percent at four elements per wavelength as compared to 10 percent for Galerkin. At ten elements per wavelength, GLS with $\tau_{22.5}$ has a maximum possible error of 0.5 percent, compared to 1.6 percent for Galerkin. Figure 8.9 illustrates these conclusions from an alternative viewpoint. In this Figure, the phase error is plotted versus the angle of wave propagation; comparisons are made with Galerkin ($\tau = 0$) and GLS with ($\tau_{22.5}$) and (τ_0) at ten elements per wavelength (top), and four elements per wavelength (bottom). These results clearly show that the solution with $\tau_{22.5}$ gives exact phase for propagation angles $\theta = 22.5$, while the solution with τ_0 gives exact phase for propagation angles $\theta = 0$. The phase error for GLS with τ_0 is a minimum (exact) at $\theta = 0$, and then increases to a maximum of 4 percent at $\theta = 45$. Phase accuracy is increased for $\tau_{22.5}$, where the maximum error is only 2 percent at $\theta = 0$ and $\theta = 45$.

In conclusion, firstly, it is clear that the least-squares addition with τ defined by (8.71) substantially improves the phase accuracy of the finite element solution for any choice of wave vector orientation θ. Secondly, we find that when the direction of wave-propagation is not known *a priori*, or when it is varying over the mesh, as will generally be the case, then $\tau_{22.5}$ is optimal.

8.7.3 Diagonal mass

The effectiveness of the Galerkin/Least-Squares method when using a lumped mass approximation (Lobotto quadrature) is examined by setting $\epsilon = 0$ in (8.73), with the result

$$\tau k^2 = 1 - \frac{2(1 - \cos kh)}{(kh)^2} \tag{8.76}$$

The two-dimensional GLS dispersion relation in this case is,

$$kh = \cos^{-1}\{(f_x + f_y + 2 f_x f_y - 1)/3\} \tag{8.77}$$

Figure 8.10 plots dispersion curves using a lumped mass approximation for Galerkin and GLS with the τ defined in (8.76). These results confirm that the least-squares addition is effective for improving the phase accuracy of Galerkin solutions even when approximate quadrature rules are used to integrate the mass operator.

8.8 Numerical Studies

A number of numerical studies are conducted to verify the improved accuracy of the GLS method and assess the performance of alternate GLS mesh parameters.

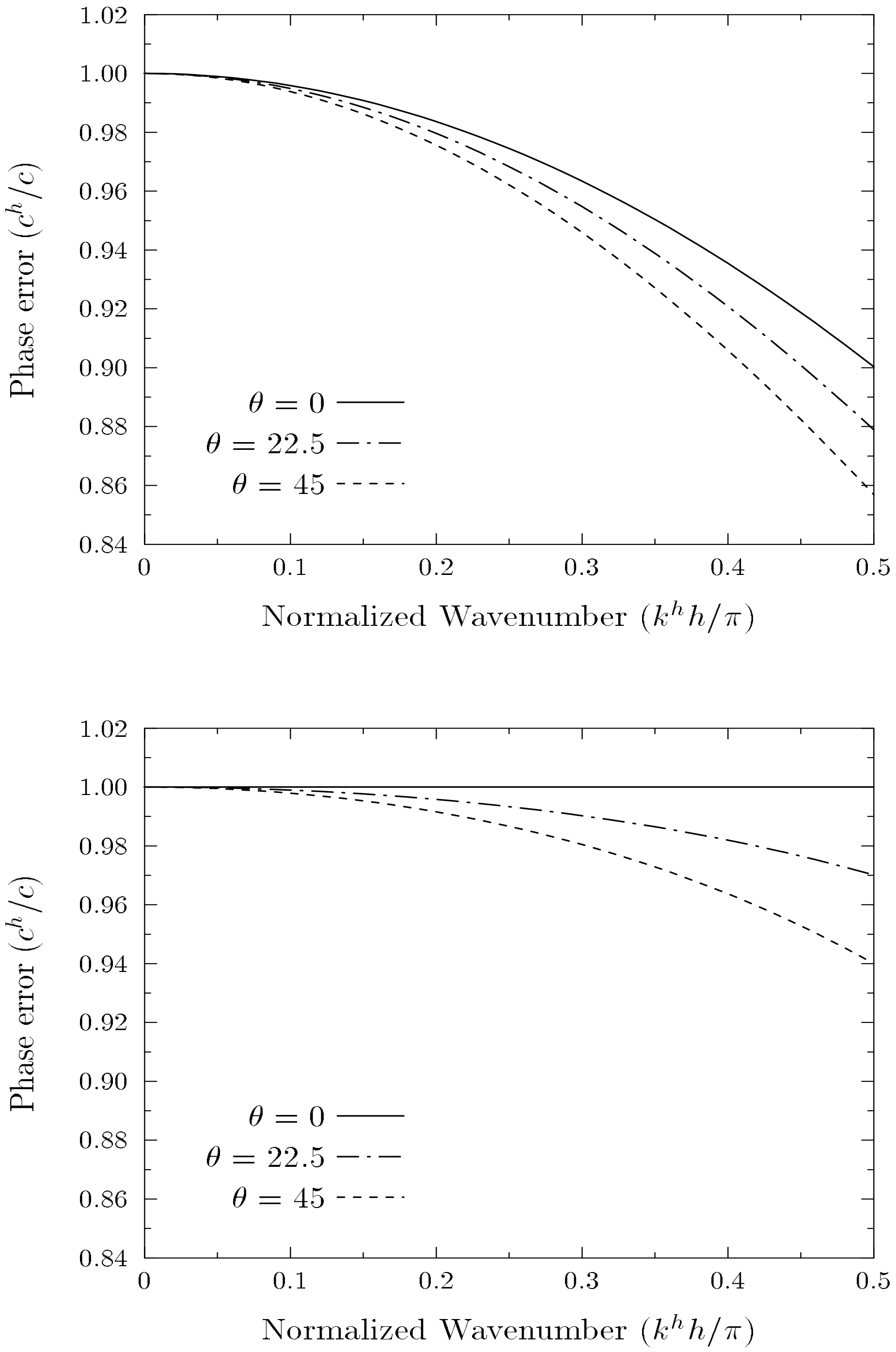

Figure 8.10: Phase error using diagonal mass approximation, $\epsilon = 0$, (top) Galerkin ($\tau = 0$) (bottom) GLS ($\tau = \tau_0$), designed for exact phase for $\theta = 0$.

8.8.1 Green's function for a rectangular domain

In this first example, consider the problem of finding the Green's function $\phi : \bar{\Omega} \to \mathbb{R}$ with homogeneous Dirichlet boundary conditions within a square domain.

$$(\nabla^2 + k^2)\phi(x, y) = -\delta(x - x_0, y - y_0) \qquad \text{in } \Omega \tag{8.78}$$

$$\phi(0, y) = \phi(L, y) = \phi(x, 0) = \phi(x, L) = 0 \tag{8.79}$$

where L is the side length. The solution to this problem is composed of a series of reflected waves which give rise to complicated standing wave patterns, see THOMPSON AND PINSKY [1993d].

This problem is numerically solved by the Galerkin/Least-Squares method using a uniform mesh of 20×20 bilinear quadrilateral elements. All calculations are performed with 2×2 Gauss integration with $kL = 5\pi/3$. The source is located in the upper right quadrant $(x_0, y_0) = (0.8L, 0.8L)$. In the upper left corner of Figure 8.11 the elevated contours of the exact series solution interpolated with the mesh employed is illustrated. In the figures that accompany this result, the contours of the exact, Galerkin and GLS ($\tau_{22.5}$) solutions are shown respectively. The solution profile for a cut located at $y = 0.2L$ is given in Figure 8.12. The L_2 norm of the error evaluated over all nodal points excluding the source node is computed as,

$$||e||^2 = \sum_m \sum_n (\phi^h_{mn} - \phi(x_m, y_n))^2 \tag{8.80}$$

The computed values of $||e||$ for Galerkin and GLS using the mesh parameters τ_0 and $\tau_{22.5}$ are:

$$\begin{aligned} \text{Galerkin} &= 0.691 \\ \text{GLS}(\tau_0) &= 0.240 \\ \text{GLS}(\tau_{22.5}) &= 0.148 \end{aligned}$$

Results of this numerical example indicate that the additional least-squares operator with the family of mesh parameters τ defined in (8.71) improves the accuracy of the Galerkin solution. However, for problems where waves are directed in arbitrary directions in $\mathbb{R}^2$, use of the GLS parameter $\tau_{22.5}$ is more accurate than the use of τ_0. These results substantiate the conclusions drawn from the multi-dimensional dispersion analysis of the previous section: If the predominant direction θ, is known *a priori*, then the optimal mesh parameter can be calculated from (8.71). However, for general problems where waves are directed in arbitrary directions in $\mathbb{R}^2$, use of the GLS parameter $\tau_{22.5}$ is more accurate than the use of τ_0.

8.8.2 Plane-wave propagation in a waveguide

Next, consider the problem of plane-wave propagation along a waveguide. The set-up for this problem is the same as given in (8.38) through (8.40), but now with the finite element mesh rotated at 45 degrees relative to the rectangular boundaries, see Figure 8.13. This example illustrates that for problems where the direction of wave propagation is known *a priori*, in this case along the x-axis, the optimum GLS parameter τ can be calculated from (8.71). For this mesh and loading, the greatest accuracy is obtained by choosing τ such that $\theta_o = 45$ since the mesh lines are rotated by 45 degrees to the direction of propagation. The GLS solution to this problem is illustrated in Figure 8.14. For comparison, the Galerkin and GLS solutions using τ_{45}; exact for waves directed along $\theta = 45$ relative to mesh lines and $\tau_{22.5}$; exact for waves directed along $\theta = 22.5$ are also shown in this Figure. From this result we observe that the GLS solution with τ_{45} is very close to the nodal interpolate of the exact solution. The solution is not perfectly nodally exact for this mesh due to the presence of linear triangular elements used near the boundaries. Results for the alternative GLS parameter $\tau_{22.5}$ also exhibit significantly improved phase accuracy when compared to Galerkin.

8.8.3 Effects of mesh distortion

In studies by Bazant and Celep [1978,1982], finite element solutions over non-uniform meshes exhibit reflections at mesh discontinuities that can cause increased amplitude and phase errors. Although undistorted (uniform) meshes tend to minimize errors due to reflection at mesh discontinuities, it is often desirable to employ unstructured meshes in an adaptive scheme to capture gradients in the solution amplitude near for example irregular surfaces or source drivers. To investigate the effects

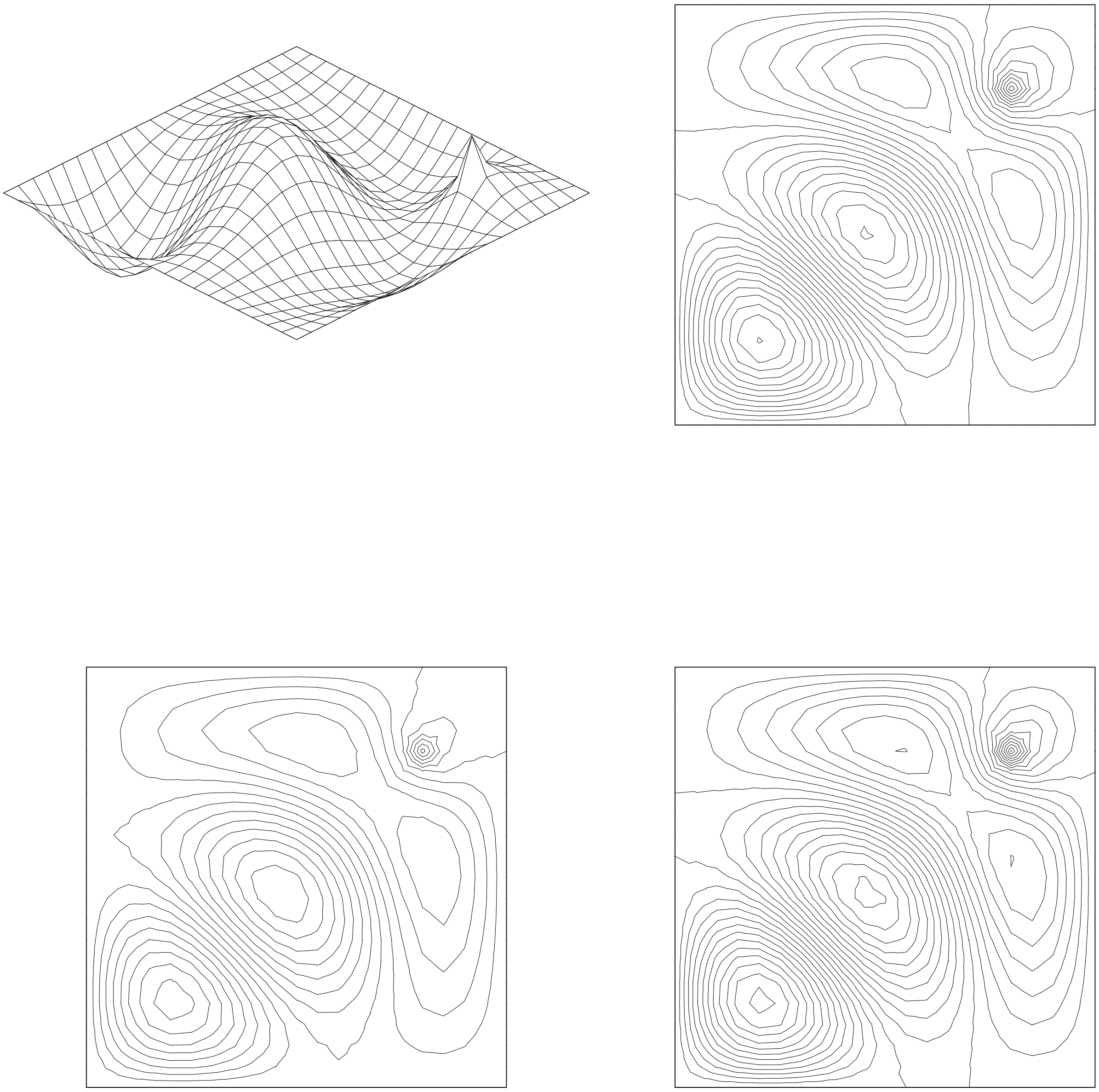

Figure 8.11: Contours for point source located in upper right quadrant of a uniform mesh of (20×20) bilinear elements, at $kL = 5\pi/3$. (Upper left) Elevated contours for exact series solution. (Upper right) Contours of exact solution, (Bottom left) Galerkin, (Bottom right) Galerkin/Least-Squares

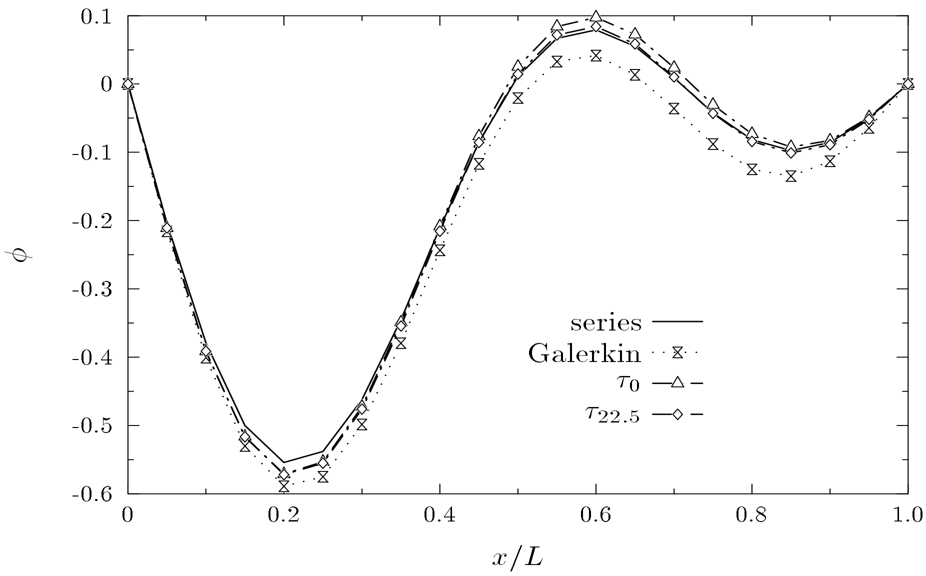

Figure 8.12: Point source located in upper right quadrant: Solution profile along x–axis for fixed $y/L = 0.2$

of mesh distortion on the Galerkin/Least-Squares solution, the uniform mesh used in the previous example is distorted such that the element area remains fixed, see Figure 8.15. For this problem, the element length h is chosen to be the square-root of the element area. In order to compare results with the nodes spaced at uniform points, the projection algorithm described in JANSEN [1992] is used to linearly interpolate the unstructured nodes to the structured nodes. Figure 8.16 shows that while the GLS numerical solution with the distorted mesh is no longer nodally exact, it it remarkably accurate. This example illustrates that at least for a quisi-uniform discretization of distorted elements, the GLS method performs optimally. However, further studies need to be performed in order to assess the accuracy and stability of the GLS technology to truly unstructured meshes with no uniformity in the mesh.

8.8.4 Radiation from an infinite cylinder

Currently there is intense interest in the application of analytical and numerical techniques to model exterior wave propagation problems such as the radiation and scattering of acoustic waves from geometrically complex structures. In this example, consider

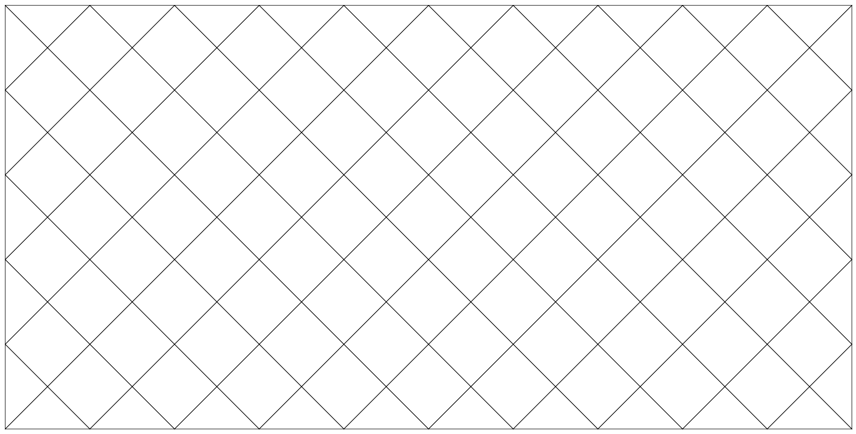

Figure 8.13: Rotated finite element mesh of linear quadrilateral elements and linear triangular elements for waveguide problem.

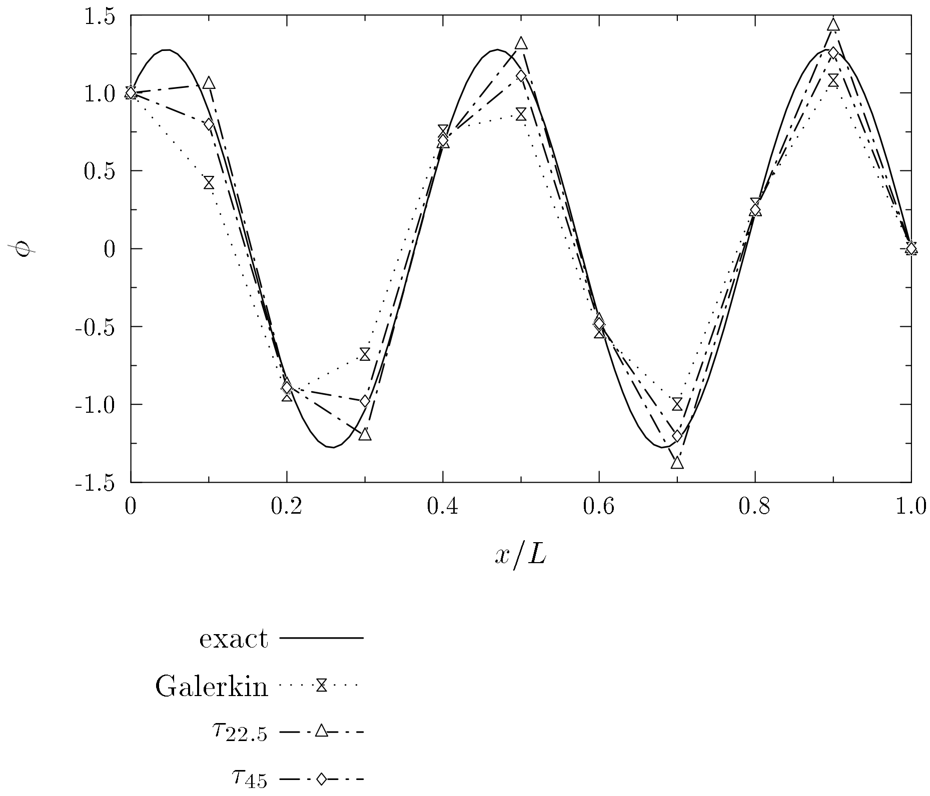

Figure 8.14: Waveguide problem with rotated mesh and plane-wave solution directed along x-axis; $kh = \pi/3$, six elements per wavelength.

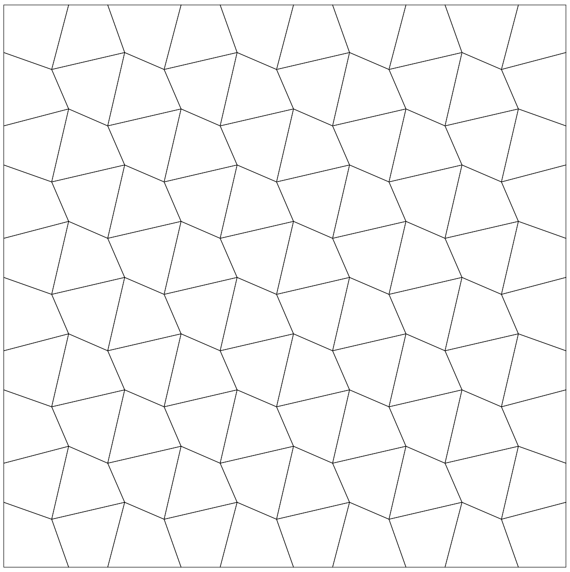

Figure 8.15: The computational domain for a square waveguide with length L, discretized by a distorted mesh of 10×10 bilinear quadrilateral elements.

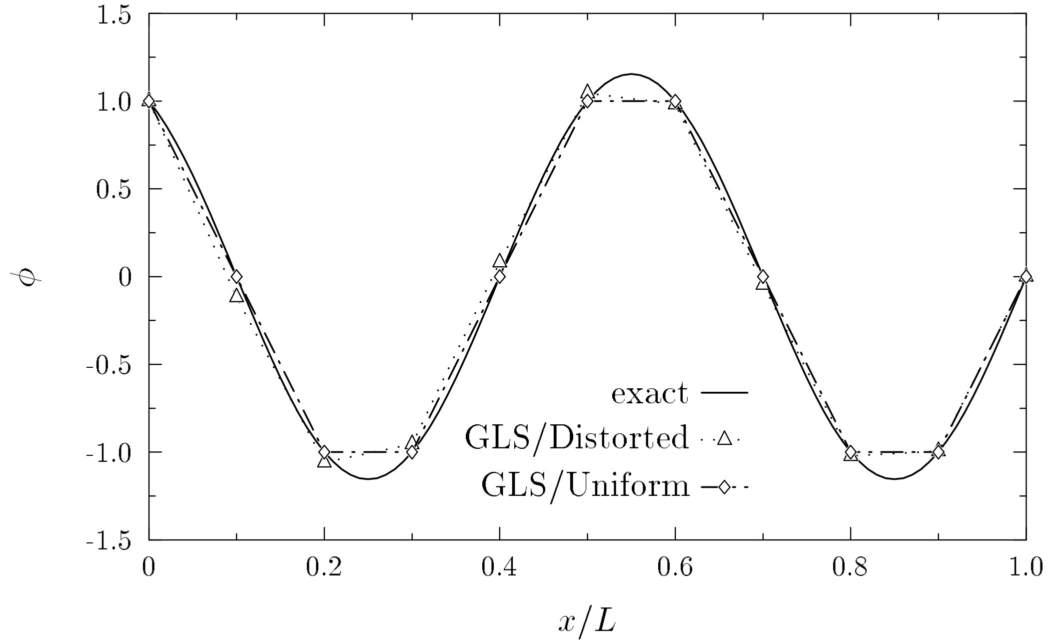

Figure 8.16: Waveguide problem with plane-wave solution directed along x-direction; comparing uniform and distorted meshes, for $kh = \pi/3$, six elements per wavelength:

the problem of non-uniform radiation from a rigid infinite cylinder of radius a. By increasing the circumferential harmonic loading on the surface of the cylinder, the response of individual modes on the performance of the numerical solution is examined. For this exterior problem, the solution $\phi : \mathcal{R} = \{a \leq r < \infty, 0 \leq \theta < 2\pi\} \rightarrow \mathbb{C}$, is sought such that,

$$(\nabla^2 + k^2)\phi(r,\theta) = 0 \qquad \text{in } \mathcal{R} \tag{8.81}$$

$$\phi(a,\theta) = \cos n\theta \tag{8.82}$$

$$\lim_{r\rightarrow\infty} \sqrt{r}(\phi,_r - ik\phi) = 0 \tag{8.83}$$

The exact solution to this problem is $H_n(kr)\cos n\theta / H_n(ka)$ where H_n are Hankel functions of the first kind of order n.

This problem is solved by the GLS finite element method by truncating the infinite domain at a finite distance from the cylinder with an artificial boundary. A non-reflecting boundary condition representing the impedance of the exterior domain is then prescribed at this artificial boundary. Let the artificial boundary to be a circle of radius R. The problem defined over the bounded domain Ω is then:
Find $\phi : \Omega = \{a \leq r \leq R, 0 \leq \theta < 2\pi\} \rightarrow \mathbb{C}$, such that

$$(\nabla^2 + k^2)\phi(r,\theta) = 0 \qquad \text{in } \Omega \tag{8.84}$$

$$\phi(a,\theta) = \cos n\theta \tag{8.85}$$

$$\phi,_r(R,\theta) = \mathbb{S}\phi(R,\theta) \tag{8.86}$$

where the last equation is the non-reflecting boundary condition expressed through the Dirichlet-to-Neumann (DtN) mapping $\mathbb{S}$. The exact DtN map $\mathbb{S}$, is expressed as the infinite series,

$$\mathbb{S}\phi = \sum_{n=0}^{\infty} \alpha_n \int_0^{2\pi} \cos n(\theta - \theta')\phi(R,\phi')d\phi' \tag{8.87}$$

where the impedance coefficients are defined as,

$$\alpha_n(kR) := \frac{\varepsilon_n k}{\pi}\frac{H_n'(kR)}{H_n(kR)} \tag{8.88}$$

and ε_n is equal to 1/2 for $n = 0$ and 1 otherwise. This non-local non-reflecting boundary condition in the frequency domain was used earlier in Chap. 5, as a starting point for the derivation of local boundary conditions in the time domain. Here we implement this nonlocal DtN condition directly as a natural boundary condition in the GLS variational formulation for the Helmholtz equation. Further details pertaining to implementation of the DtN boundary condition in a finite element formulation are given in Keller and Givoli [1989] and Givoli and Keller [1989].

For this example the positioning of the truncation boundary is set at $R = 2a$ with the resulting computational domain discretized by 3×32 bilinear quadrilateral elements as shown in the upper left had corner of Figure 8.17. In the following calculations the geometrically non-dimensionalized wavenumber is set at $ka = \pi$ (the wavelength is equal to the diameter of the cylinder). With the finite element mesh employed, this value corresponds to a resolution of six elements per wavelength in the radial direction. All calculations employ 2×2 Gaussian integration and 8 terms in the DtN series.

For the first harmonic (breathing mode $n = 0$), the exact solution is a simple cylindrical wave which has the character of a radially decaying plane-wave. For the radially uniform mesh employed, this problem reduces to a one dimensional problem with radial coordinate r. Taking h to be the element length in the r-direction, Harari and Hughes [1992c] have shown that the GLS parameter τ_0 is optimal in this case.

In this work, the higher-order circumferential harmonics $n = 1$ through $n = 4$ are investigated in order to further validate the accuracy of the GLS method for more complex non-uniform radiation patterns. In the upper left corner of Figure 8.17 the contours of the imaginary part of the exact solution for the loading $\cos\theta$, nodally interpolated by the mesh employed is shown. The contours of the imaginary parts of the Galerkin and GLS solutions are shown in the accompaning figures, where comparisons are made to the exact solution which is denoted by the overlay of dotted contours. Figure 8.18 shows the profile of the solution evaluated on the DtN boundary $r = R$ for modes $n = 1$ through $n = 3$. The GLS solution was calculated using both τ_0 and $\tau_{22.5}$ defined previously.

For mode $n = 1$, the improvement of the GLS solutions in comparison to the Galerkin solution is significant. We also observe that in this case, τ_0 is superior to $\tau_{22.5}$. As the circumferential mode is increased to $n = 2$, the improvement to the GLS

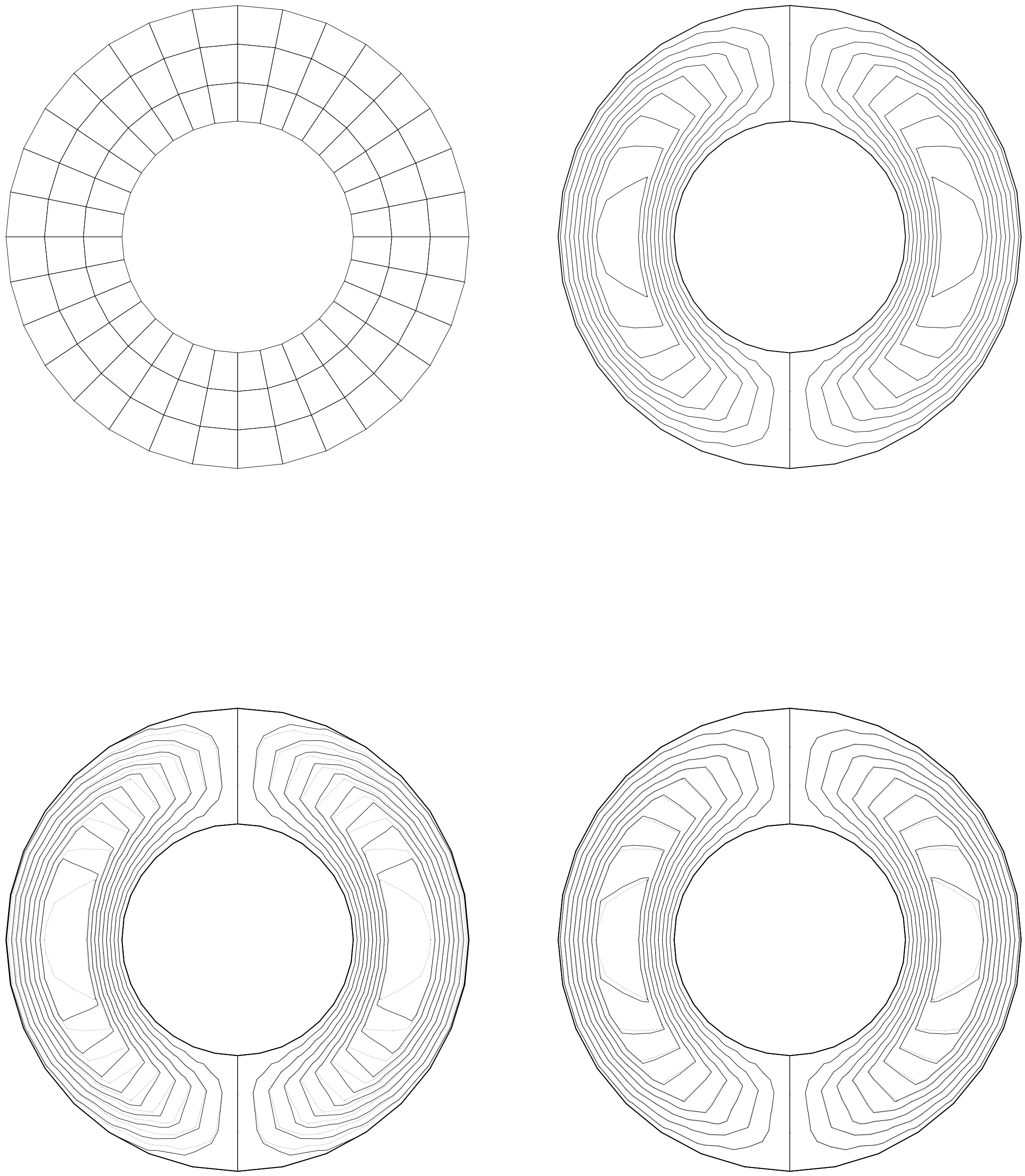

Figure 8.17: Harmonic radiation with mode ($n = 1$) and $ka = \pi$: (Upper left) Computational domain for a cylinder with radius a, and truncation boundary $R = 2a$. (top right) Exact solution (bottom left) Galerkin solution (bottom right) Galerkin/Least-Squares with $\tau_{22.5}$

solution is again significant, however in this case, the GLS solution using either τ_0 or $\tau_{22.5}$ are nearly identical. The use of τ_0 slightly under-estimates the exact solution while the use of $\tau_{22.5}$ slightly over-estimates the exact solution. For mode $n = 3$, the improvement of the GLS solutions in comparison to the Galerkin solution is again clearly shown. However, in this case the use of $\tau_{22.5}$ gives the most accurate solution and is barely distinguishable from the exact solution. Results for mode $n = 4$ are given in THOMPSON AND PINSKY [1993d].

The results of this study indicate that for this particular problem, for low modes $n = 0, 1$, the radiated energy of the cylindrical waves are best resolved by the GLS parameter τ_0, designed to improve dispersion errors for plane-waves directed along radial rays, while for higher modes $n = 3, 4$, the alternative GLS parameter $\tau_{22.5}$ designed for arbitrary directional wave vectors performs better. In more general settings such as radiation from a source located on a geometrically complex structure, the radiation pattern may be complex and difficult to predict a-priori. For these more general problems, a radially uniform mesh may not be possible and unstructured meshes must be used. In the case of unstructured meshes, it is expected that $\tau_{22.5}$ would give the best results, at least in a global sense. Further numerical studies need to be performed in order to verify this hypothesis.

8.9 Extensions of GLS

8.9.1 Three-dimensional elements

The selection of an optimal GLS parameter in three-dimensions is a simple extension of the two dimensional case. Consider a uniform mesh of trilinear 8-node brick elements with element sides h. The optimal τ in this case is,

$$\boxed{\tau k^2 := 1 - \frac{\tilde{S}(kh, \theta, \varphi)}{(kh)^2 \tilde{M}(kh, \theta, \varphi)}} \tag{8.89}$$

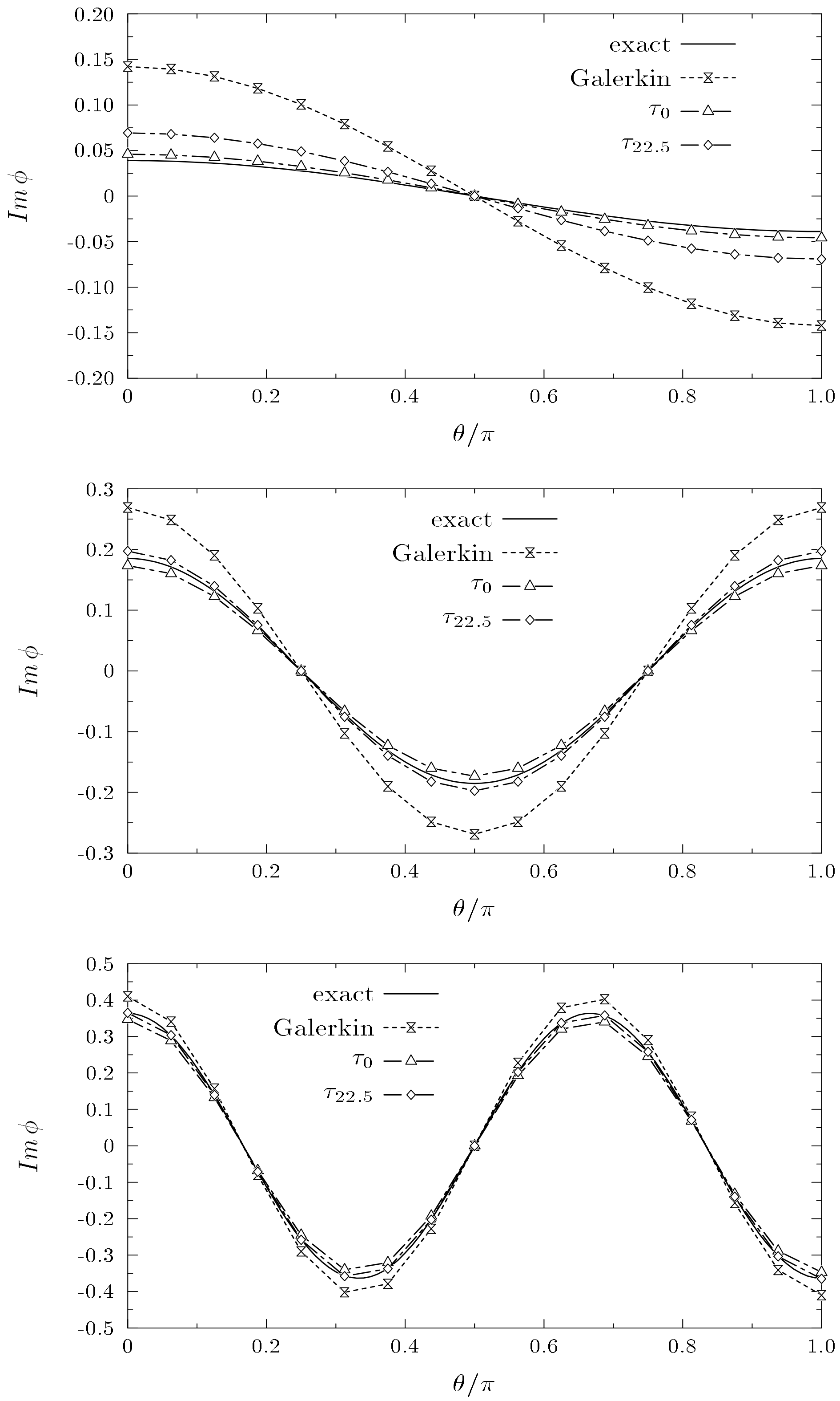

Figure 8.18: Harmonic radiation from a cylinder with $ka = \pi$. Solution plotted along the truncation boundary $R = 2a$. From top to bottom, mode $n = 1$, 2, 3

where $\tilde{S}$ and $\tilde{M}$ are the three-dimensional Fourier transforms of the stiffness and mass difference stencils respectively,

$$\tilde{S} = \mathbf{1}_y\mathbf{1}_z\bar{k}_x^2 + \mathbf{1}_x\mathbf{1}_z\bar{k}_y^2 + \mathbf{1}_x\mathbf{1}_y\bar{k}_z^2 \qquad \text{and} \qquad \tilde{M} = \mathbf{1}_x\mathbf{1}_y\mathbf{1}_z \tag{8.90}$$

$$\bar{k}_x^2 = 2(1-f_x) \qquad \text{and} \qquad \bar{k}_y^2 = 2(1-f_y) \qquad \text{and} \qquad \bar{k}_z^2 = 2(1-f_z) \tag{8.91}$$

$$\begin{aligned} f_x &= \cos(k_x h) = \cos(kh\cos\theta\sin\varphi) \\ f_y &= \cos(k_y h) = \cos(kh\sin\theta\sin\varphi) \\ f_z &= \cos(k_z h) = \cos(kh\cos\varphi) \end{aligned}$$

with polar angles $\theta \in [0, 2\pi]$ and meridional angles $\varphi \in [0, \pi]$ measured relative to mesh axis. For $\varphi = 0 \bmod 90$, (8.89) specializes to the two-dimensional case (8.71). Further details for the three-dimensional case will be published in a follow-up paper to Thompson and Pinsky [1993d].

8.9.2 Generalized Galerkin Least Squares

Alterative variants on the theme of adding least squares terms to the usual Galerkin method are possible. Consider the following Generalized Galerkin/Least-Squares (GGLS) method in $\mathbb{R}^2$, where the added least-squares term is in the form of the gradient of the residual:

$$A_{GGLS}(w^h, \phi^h) \equiv A(w^h, \phi^h) + \sum_{e=1}^{n_{el}} \int_{\Omega^e} \boldsymbol{\tau}\nabla(\mathcal{L}w^h)\cdot\nabla(\mathcal{L}\phi^h)d\Omega \tag{8.92}$$

$$L_{GGLS}(w^h) \equiv L(w^h) - \sum_{e=1}^{n_{el}} \int_{\Omega^e} \boldsymbol{\tau}\nabla(\mathcal{L}w^h)\cdot\nabla f d\Omega \tag{8.93}$$

where $\mathcal{L}\phi^h = \phi^h_{,xx} + \phi^h_{,yy} + k^2\phi^h$ and $\boldsymbol{\tau} = \text{diag}(\tau_x, \tau_y)$ is a diagonal matrix of local parameters. Note that consistency is preserved since the exact solution satisfies the gradient of the Helmholtz equation. Setting $\tau_x = \tau_y = \tau$, the method reverts to the Galerkin Gradient Least Squares (G∇LS) method originally proposed by Franca and Dutra Do Carmo [1989], see also Harari [1991a] and Grosh and Pinsky

[1993b]. For bilinear elements and $f = 0$, the dispersion relations for this method are,

$$(kh)^2 \mathbf{1}_x \mathbf{1}_y = (1 + \tau_x k^4) \mathbf{1}_y \bar{k}_x^2 + (1 + \tau_y k^4) \mathbf{1}_x \bar{k}_y^2 \tag{8.94}$$

Restricting $\tau_x = \tau_y = \tau$, the GGLS dispersion relation reverts to,

$$(1 + \tau k^4)^{-1} (kh)^2 = \tilde{S} / \tilde{M} \tag{8.95}$$

which has the same form as equation (8.63) with $\gamma = (1 + \tau k^4)^{-1}$ and the optimal GGLS parameter is given by,

$$\boxed{\tau k^4 := \frac{(kh)^2 \tilde{M}(kh, \theta_0)}{\tilde{S}(kh, \theta_0)} - 1} \tag{8.96}$$

Examining (8.95) we conclude that for bilinear elements on a uniform grid with $f = 0$, the phase accuracy for GGLS with $\tau_x = \tau_y$ is identical to GLS over all wave vector orientations, and no advantage results. This observation was also made by Harari [1991a] for the one-dimensional case.

8.9.3 Biquadratic elements

While the 4-node bilinear discretizations represent popular element families due to their computational efficiency, higher-order elements such as biquadratic interpolations offer special advantages when solving the Helmholtz equation in two-dimensions. Higher-order elements better approximate the geometric curvature of a model description, and for time-harmonic wave solutions to the Helmholtz equation, increased phase accuracy will be realized for the same number of degrees of freedom as compared to low-order elements. In this section, the extension of the Galerkin/Least-Squares method for the Helmholtz equation to higher-order interpolations is presented.

As a point of departure we first consider the dispersive properties of high-order elements based on the Galerkin formulation for the Helmholtz equation.

Consider a uniform mesh of biquadratic ($\mathcal{P}^2 \times \mathcal{P}^2$) elements with length $h = 2\Delta x = 2\Delta y$. For simplicity, consider the Galerkin method where $\tau = 0$. By assembling a patch of four elements as shown in Figure 8.19, we identify four different difference

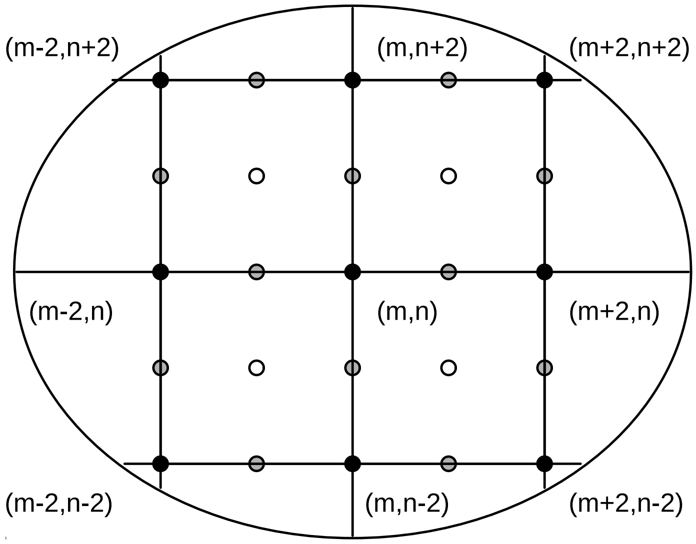

Figure 8.19: Two-dimensional biquadratic finite element mesh with corner, edge, and internal nodes.

stencils, each having the form,

$$\boxed{\sum_{p,q}(s_{pq} - \frac{(kh)^2}{10}m_{pq})E_x^p E_y^q \phi_{m,n} = 0} \tag{8.97}$$

These four stencils are associated with the following nodes where the range on the sum (p, q) is indicated.

$(\phi_{m,n})$	corner nodes	$(p,q) \in$	$\{-2,2\} \times \{-2,2\}$
$(\phi_{m+1,n})$	x-direction edge nodes	$(p,q) \in$	$\{0,2\} \times \{-2,2\}$
$(\phi_{m,n+1})$	y-direction edge nodes	$(p,q) \in$	$\{-2,2\} \times \{0,2\}$
$(\phi_{m+1,n+1})$	interior nodes	$(p,q) \in$	$\{0,2\} \times \{0,2\}$

Expressions for the difference coefficients $[s_{pq}]$ and $[m_{pq}]$ for consistent mass follow:

1. Corner Nodes

$$[s_{pq}] = \begin{bmatrix} 1 & -2 & -8 & -2 & 1 \\ -2 & 4 & 16 & 4 & -2 \\ -8 & 16 & 64 & 16 & -8 \\ -2 & 4 & 16 & 4 & -2 \\ 1 & -2 & -8 & -2 & 1 \end{bmatrix}; \quad [m_{pq}] = 2 \begin{bmatrix} -1 & 5 & -3 & 5 & -1 \\ 5 & -16 & -18 & -16 & 5 \\ -3 & -18 & 112 & -18 & -3 \\ 5 & -16 & -18 & -16 & 5 \\ -1 & 5 & -3 & 5 & -1 \end{bmatrix}$$

2. Side Nodes

$$[s_{pq}] = \begin{bmatrix} 5 & 0 & 5 \\ -16 & -48 & -16 \\ -18 & 176 & -18 \\ -16 & -48 & -16 \\ 5 & 0 & 5 \end{bmatrix}; \qquad [m_{pq}] = \begin{bmatrix} -1 & -8 & -1 \\ 2 & 16 & 2 \\ 8 & 64 & 8 \\ 2 & 16 & 2 \\ -1 & -8 & -1 \end{bmatrix}$$

3. Interior Nodes

$$[s_{pq}] = 8 \begin{bmatrix} -1 & -3 & -1 \\ -3 & 32 & -3 \\ -1 & -3 & -1 \end{bmatrix}; \qquad [m_{pq}] = \begin{bmatrix} 1 & 8 & 1 \\ 8 & 64 & 8 \\ 1 & 8 & 1 \end{bmatrix}$$

For the case of biquadratic elements, the numerical solutions are allowed to assume four different amplitudes corresponding to each of the four different stencils,

$$\begin{aligned} \phi_{m,n} &= A_1 \mu_x^m \mu_y^n \\ \phi_{m+1,n} &= A_2 \mu_x^{m+1} \mu_y^n \\ \phi_{m,n+1} &= A_3 \mu_x^m \mu_y^{n+1} \\ \phi_{m+1,n+1} &= A_4 \mu_x^{m+1} \mu_y^{n+1} \end{aligned} \tag{8.98}$$

where

$$\mu_x = \mathrm{e}^{ik_x^h \Delta x} \qquad \text{and} \qquad \mu_y = \mathrm{e}^{ik_y^h \Delta y} \tag{8.99}$$

The constants A_1 and A_4 represent amplitudes at the corner and the interior nodes of the element, while A_2 and A_3 denote the amplitudes at the edges parallel to the x and y axis respectively. Substituting the above discrete solutions into each recurrence stencil yields the characteristic matrix equations,

$$\boxed{[\tilde{\boldsymbol{S}} - \frac{(kh)^2}{10}\tilde{\boldsymbol{M}}]\boldsymbol{A} = 0} \tag{8.100}$$

where $\tilde{\boldsymbol{S}}$ and $\tilde{\boldsymbol{M}}$ are symmetric (4×4) characteristic matrices depending on $(k_x^h h)$ and $(k_y^h h)$, and $\boldsymbol{A} \in \mathbb{R}^4$ is the column of amplitudes. The characteristic functions $[\tilde{S}_{ij}]$ and $[\tilde{M}_{ij}]$ for consistent mass are as follows:

$$\begin{aligned}
\tilde{S}_{11} &= 56 - 2f_1 f_2 - 3f_1 - 3f_2 & \tilde{M}_{11} &= 16 - f_1 f_2 - 4f_1 - 4f_2 \\
\tilde{S}_{12} &= 10g_1 f_2 - 18g_1 & \tilde{M}_{12} &= -2g_1 f_2 + 8g_1 \\
\tilde{S}_{13} &= 10f_1 g_2 - 18g_2 & \tilde{M}_{13} &= -2f_1 g_2 + 8g_2 \\
\tilde{S}_{14} &= -32g_1 g_2 & \tilde{M}_{14} &= 4g_1 g_2 \\
\tilde{S}_{22} &= 88 & \tilde{M}_{22} &= 32 - 8f_2 \\
\tilde{S}_{23} &= -32g_1 g_2 & \tilde{M}_{23} &= 4g_1 g_2 \\
\tilde{S}_{24} &= -48g_2 & \tilde{M}_{24} &= 16g_2 \\
\tilde{S}_{33} &= 88 & \tilde{M}_{33} &= 32 - 8f_1 \\
\tilde{S}_{34} &= -48g_1 & \tilde{M}_{34} &= 16g_1 \\
\tilde{S}_{44} &= 128 & \tilde{M}_{44} &= 64
\end{aligned}$$

where

$$f_1 = \cos(k_x^h h) \qquad g_1 = \cos(k_x^h h/2)$$

$$f_2 = \cos(k_y^h h) \qquad g_2 = \cos(k_y^h h/2)$$

The dispersion relation is obtained by setting the determinant of this characteristic equation system to zero. For biquadratic elements, there are two frequency ranges (branches) where waves are allowed to propagate with pure real wavenumbers. Figure 8.20 shows surface plots of the relative phase speed $c^h/c = k/k^h$ as a function of the normalized wavenumber components $0 < k_x^h h/\pi < 1$ and $0 < k_y^h h/\pi < 1$ corresponding to the lower branch surface. For propagation along mesh lines $\theta = 0$

mod 90, these two-dimensional dispersion relations reduce to the one-dimensional relations derived in THOMPSON AND PINSKY [1993b]. Comparing these results to the dispersion surfaces for bilinear elements, it is clear that biquadratic discretizations exhibit less phase error for the same number of nodes per wavelength.

8.9.4 Optimal GLS parameter for quadratic elements

For a nonzero GLS parameter $\tau \neq 0$, additional equations are added to the Galerkin equations as prescribed by (8.34). The optimal definition of τ_{quad} using quadratic $p = 2$ basis functions for plane-waves propagating along mesh lines, has been reported in THOMPSON AND PINSKY [1993c,1993d]. With this assumption, the problem reduces to one-dimension and the Laplacian operator is interpreted as $\nabla^2\phi = \phi_{,xx}$. Application of the discrete Fourier transform to these equations, and requiring that the phase be exact in the x-direction, $k_x^h = k$, leads to the definition of τ_{quad}. By substituting the exact wave number into the finite element dispersion relation for quadratic elements, a quadratic equation for the optimal value of τ is obtained. Defining the nondimensional parameters $\alpha := kh$, and $\hat{\tau} := \tau k^2$, this equation is given by,

$$c_2\hat{\tau}^2 + c_1\hat{\tau} + c_0 = 0 \tag{8.101}$$

where

$$\begin{aligned}
c_0(\alpha) &= -240(1-\cos\alpha)\alpha^2 + 8(13+2\cos\alpha)\alpha^4 + (-3+\cos\alpha)\alpha^6 \\
c_1(\alpha) &= -2880(1-\cos\alpha) + 1440\alpha^2 + 24(-6+\cos\alpha)\alpha^4 + 2(3-\cos\alpha)\alpha^6 \\
c_2(\alpha) &= -240(1-\cos\alpha)\alpha^2 + 40(1-\cos\alpha)\alpha^4 + (-3+\cos\alpha)\alpha^6
\end{aligned}$$

The optimal GLS parameter τ_{quad} is obtained by solving this quadratic equation, i.e.

$$\boxed{\tau k^2 = \frac{-c_1 \pm \sqrt{c_1^2 - 4c_0c_2}}{2c_2}} \tag{8.102}$$

For quadratic elements, there are two frequency ranges where waves are allowed to propagate with real wavenumbers. In the above expression, the minus sign is used

Figure 8.20: Surface plot of phase error $e_p = (c^h/c)$ vs. normalized wave vector components $(k_x^h h/\pi)$ and $(k_y^h h/\pi)$ for biquadratic elements with $\tau = 0$: (a) exact integration (b) diagonal mass matrix (lobatto quadrature)

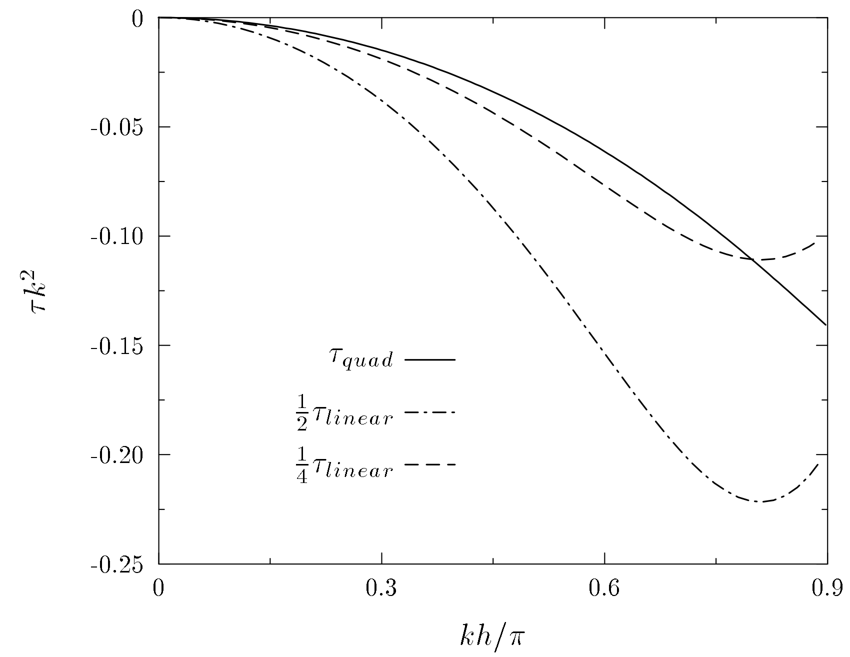

Figure 8.21: GLS mesh parameter τ_{quad} for quadratic interpolation compared to estimates based on fractions of the linear τ_{linear}.

for the range $0 < kh < \pi$ while a plus sign is used for the range $\pi < kh < 2\pi$, where 2π is the limit of resolution for quadratic elements. At $kh = \pi$, there exists a discontinuity in the value of τ_{quad}. This phenomena is related to the so-called 'stopping bands' present in high-order finite element discretizations where allowed waves possess amplitude attenuation; further discussions related to this phenomena are given in the complex wavenumber analysis performed in the next Chapter. Figure 8.21 plots τ_{quad} together with simple approximations based on fractions of the GLS parameter derived earlier for linear interpolations in the operating range of two elements per wavelength or greater. A practical estimate, useful for computation is $0.25\tau_{linear}$.

8.10 Summary and Conclusions

In this Chapter we have presented a Galerkin/Least-Squares (GLS) finite element method for multi-dimensional wave propagation governed by the Helmholtz equation. The GLS parameter τ is designed from the criterion that numerical phase error be reduced in the primary direction of wave propagation. Results from a multi-dimensional discrete Fourier analysis of the GLS method indicate that the additional least-squares operator improves the accuracy of the Galerkin solution over all wave vector orientations. Accurate GLS solutions are maintained for as little as six linear elements per wavelength compared to the limit of ten elements per wavelength required for well resolved Galerkin solutions.

A number of alternative GLS parameters were derived for general numerical integration rules such as Gaussian and Lobatto quadrature. Results from the dispersion analysis indicate that phase accuracy and directional properties associated with GLS using either exact integration, or diagonal mass approximations, are significantly improved when compared to Galerkin.

Numerical examples of plane waves traveling along a two-dimensional waveguide with uniform, rotated, and distorted mesh orientations verify that as the wavenumber, normalized with respect to the element size, is increased, the degradation in phase accuracy present in the Galerkin solution is reduced and in some cases eliminated by the proper choice of the GLS parameter τ. GLS solutions for the Green's function in the interior of simple rectangular domains demonstrates the improved performance compared to the standard Galerkin method where multiple reflections are present. These results validate our conclusion that for problems where waves are directed in arbitrary directions, use of the GLS parameter $\tau_{22.5}$ defined in (8.71) with $\theta_o = 22.5$, is more accurate than the use of τ_0, designed to give exact phase for one-dimensional solutions.

By increasing the circumferential harmonics for a radiating cylindrical model, the response of individual modes on the performance of the numerical solutions has been investigated. Results indicate that for low modes, the radiated energy of the cylindrical waves are best resolved by the GLS parameter τ_0, designed to improve dispersion errors for plane-waves directed along the radial rays, while for higher modes, the alternate GLS parameter $\tau_{22.5}$, designed for arbitrary directional wave vectors performs optimally.

Optimal GLS parameters for the Helmholtz equation in $\mathbb{R}^3$ are also reported. Detailed derivations and dispersive properties for trilinear finite element discretizations will be published in a subsequent manuscript. The extension to a Generalized Galerkin/Least-Squares (GGLS) method has also been investigated; dispersion results show that for bilinear elements on a uniform grid, the phase accuracy for GGLS is the same as GLS over all wave vector orientations. The dispersion properties of biquadratic finite element discretizations has also been examined. Results show that for well resolved waves, biquadratic elements exhibit significantly less phase error compared to bilinear elements for the same number of nodes per wavelength. The extension of the GLS method to higher-order interpolations has also been indicated. The optimum GLS mesh parameter for quadratic elements is given. GLS finite elements for time-harmonic wave propagation using higher-order basis functions require that a suitable definition of τ be obtained for each spectral order p. In this work, it was shown that GLS parameters for elements with basis functions of high spectral order p can be approximated by simple fractions of low-order GLS parameters. In particular, for quadratic elements ($p = 2$), the value $\tau = .25\tau_{linear}$ proves to be a useful estimate.

Chapter 9

Complex Wavenumber Fourier Analysis of Hierarchic P-Version and Spectral Finite Elements

In recent years, there has been a resurgence of interest in the use of hierarchical p-version finite element and spectral elements to obtain high-resolution numerical solutions for wave propagation problems. In this chapter we show that high-order finite element discretizations of the wave equation display frequency bands where the solutions are harmonic decaying waves. In these so called 'stopping' bands, the solutions are not purely propagating (real wavenumbers) but are attenuated (complex wavenumbers). In this work, the standard dispersion analysis technique is extended to include complex wavenumbers. This new complex wavenumber Fourier analysis technique is then used to examine the dispersion and attenuation characteristics of high-order finite element discretizations. Three types of high-order elements are considered: hierarchic p-version elements with Legendre basis functions; new hierarchic Fourier elements with sinusoidal basis functions, and spectral elements with Lagrange interpolation in conjunction with Gauss-Lobatto quadrature. Practical guidelines are reported for phase and amplitude accuracy in terms of the spectral order and the number of elements per wavelength. Results from this analysis provide a guide for the design of p- and hp-version adaptive schemes, high-order preconditioners for iterative solution methods, and the selection of optimal Galerkin/Least-Squares (GLS) mesh parameters for elements using high-order basis functions.

9.1 Background

Computational methods for solving vibration and wave propagation problems introduce errors which distort the physical nature of the computed wave motion. Describing those errors by invoking concepts which originated in mathematical physics, such as dispersion and amplitude attenuation has provided a greater understanding of the numerical methods. In this respect, Fourier analysis has provided an indispensable tool for measuring the accuracy of wave propagation traveling through a finite element spatial discretization of a continuum. Previous researchers in this area have generally restricted themselves to studying the ability of the finite element spatial discretization to admit purely propagating wave solutions. This type of analysis amounts to a discrete Fourier synthesis of the finite element method with pure real wavenumbers. The information obtained from real wavenumber Fourier analysis has been used by by several researchers to study the accuracy of finite element discretizations. Some examples are the works of Belytschko and Mindle [1980a], Mindle and Belytschko [1983] and Jasti [1992] where the effect of various mass approximation techniques on the accuracy of Bernoulli-Euler and Timoshenko beam elements were considered. Underwood [1974] used real wavenumber analysis to study axisymmetric shells and rings, while Park and Flaggs [1984,1985] applied this technique to study shear locking and spurious modes found in Reissner/Mindlin plate elements. Real wavenumber Fourier analysis has also been used to study the convergence rates of equation solving algorithms, e.g Lotstedt and Gustafsson [1993].

While discretizations based on elements with linear basis functions represent popular element families due to their computational efficiency, higher-order elements such as quadratic interpolations offer special advantages when solving wave propagation problems. Higher-order elements better approximate the geometric curvature of a model description, and it is shown in this work that increased phase accuracy may be realized by employing higher-order interpolation fields.

To date, most of the effort in the study of the dispersive characteristics of finite element discretization has been limited to low-order elements. The most notable exception is the real wavenumber dispersion analysis of a quadratic bar element performed by Belytschko and Mullen [1978]. In this study, the dispersion analysis revealed the existence of a ‘stopping’ band in the frequency spectrum of quadratic elements, where solutions in this frequency range decay exponentially. The ramifications of these stopping bands in the context of finite element analysis were not fully understood, although there is some discussion in Belytschko and Mullen [1978] and Abboud and Pinsky [1992]. In order to obtain finite element dispersion relations for high-order finite element discretizations and interpret the solution within the 'stopping' bands, the traditional approach to finite element Fourier analysis must be extended. The standard approach seeks real frequencies as a function of real wavenumber.

In Thompson and Pinsky [1993a,1993b] the technique of complex wavenumber Fourier analysis is used to examine the accuracy of various high-order finite element discretizations. Complex wavenumber Fourier analysis is discussed in the context of periodic structures in Brillouin [1953]. In this approach the standard Fourier analysis technique is extended to include all wavenumbers satisfying the finite element dispersion relation, either real, imaginary or complex. The complex wavenumber may correspond to either a propagating wave (real wavenumber), evanescent wave (imaginary wavenumber), or a harmonic decaying wave (complex wavenumber). This extension of the usual procedure involves only a slight modification to the standard Fourier analysis yet allows for a complete characterization of the 'stopping' band phenomena found in higher order finite element discretizations – a characterization that has previously escaped other analysts.

Other applications of complex wavenumber Fourier analysis include the works of Harari and Hughes [1991a,b] where amplitude errors caused by purely imaginary wavenumbers found in the dispersion relation for linear finite element discretizations are examined. This type of analysis can also be used to investigate other systems where complex wavenumbers are present, such as periodic composite structures Silva [1991] and the study of the subsonic, leaky and evanescent waves present in the finite element dispersion relations for fluid-loaded plates Jasti [1992],Grosh and Pinsky [1993a].

In recent years, there has been a resurgence of interest in elements of high degree, see for example Babuska and Suri [1990] and Maday and Patera [1989]. In p–refinement the effects of numerical dispersion can be minimized by increasing the spectral order p of the finite element interpolation functions, while holding the number of elements constant. In contrast, standard h-refinement is achieved by holding the spectral order fixed while increasing the number of elements. The h- and p-versions are just special applications of the finite element method, which allows changing the mesh concurrently with increasing the spectral order p; this general approach is called the hp-version. The complex Fourier analysis performed in this thesis will characterize the accuracy in terms of both h and p refinements over the entire range of complex wavenumbers. Three different p–extensions are considered: (a) Hierarchic Legendre basis functions, (b) Hierarchic Fourier basis functions, and (c) Lagrange interpolations together with Lobatto quadrature.

Results from this analysis provides a guide for adaptive solution schemes in the form of an *a priori* error estimate. For example, the dispersion error determined from the analysis of high-order methods could be used as a measure for selecting the required spectral order and mesh size at a given frequency in an adaptive solution. Results from the analysis can also be used to design efficient high order preconditioners for iterative solution techniques such as those used in Babuska, et al. [1991], Barragy and Carey [1991], and Deville and Mund [1992].

9.2 Overview

In Section 9.3 the analytic Fourier analysis of the continuous problem in one-dimension is reviewed. The resulting analytic dispersion curves will serve as a basis for comparison to the discrete dispersion curves obtained from a complex wavenumber Fourier synthesis of high-order finite element discretizations. Finite element matrix equations arising from the use of high-order basis functions are given in Section 9.4. In Section 9.5 we extend the standard finite element dispersion analysis to include complex wavenumbers in order to obtain the complex valued roots of the finite element dispersion relation for the three alternative basis functions considered. Results of the dispersion and attenuation analysis are reported in Section 9.6. Of particular interest is the presence of complex wavenumber bands (stopping bands) that occur in these high-order elements and the determination of their practical significance. In Section 9.7 a direct connection is established between the results from the Fourier analysis and the results obtained from the solution of a simple canonical boundary-value problem. We also indicate how information obtained from the Fourier analysis can be used as a tool to help improve the eigenmodes from a vibration problem through a simple post-processing exercise.

9.3 Fourier analysis of the Continuous Problem

Consider the steady-state response, ϕ for the one-dimensional reduced wave (Helmholtz) equation,

$$\frac{d^2\phi(x)}{dx^2} + \frac{\omega^2}{c^2}\phi(x) = f \tag{9.1}$$

where c is the wave speed, and f is the forcing function. with assumed time dependence $\mathrm{e}^{-i\omega t}$; and ω is the circular frequency. The Fourier analysis of the reduced wave equation is accomplished by transforming the problem from the spatial (x) domain to the wavenumber domain (k) by seeking complex exponential solutions for ϕ of the form,

$$\phi(x) = A\mathrm{e}^{ikx} \tag{9.2}$$

with constant amplitude $|\phi| = A$. We interpret the spatial contribution to the wave solution as the integrand of the Fourier transformation in which the wavenumber k represents the continuous spatial frequency with wavelength $2\pi/k$. The complex Fourier transform is defined as,

$$\tilde{F}(k) := \frac{1}{\sqrt{2\pi}}\int_{-\infty}^{\infty} F(x)\mathrm{e}^{-ikx}\, dx \tag{9.3}$$

Substituting the complex exponential solution (9.2) into the homogeneous form of (9.1), or equivalently applying the complex Fourier transform (9.3), we obtain its characteristic equation in the nondimensional form,

$$\boxed{(kh)^2 = (\omega h/c)^2} \tag{9.4}$$

where h is a problem dependent characteristic length. The properties of the solutions to (9.4) are: (a) The nondimensional wavenumber (kh) is linearly proportional to the nondimensional frequency $(\omega h/c)$ over all frequencies, and (b) The wavenumbers occur in pairs $\pm kh$ of purely real numbers corresponding to propagating free waves in both $\pm x$ directions. With c constant, the phase velocity is independent of frequency and the medium is nondispersive.

In contrast to the continuum problem, we will find that finite element solutions have a dispersive character. Many naturally occurring discrete systems exhibit similar dispersive properties. Examples include periodic lattices of polyatomic molecules studied by Brillouin [1953], and periodic composite structures studied by Silva [1991] and others.

9.4 High-order Finite Element Discretizations

In this section we describe a discrete Fourier transform counterpart to the analytical Fourier transform (9.3). It will be applied to the finite element discretization of the continuous problem in one-dimension, in order to obtain a characteristic equation relating frequency and wavenumber. Since the wavenumbers obtained through the discrete Fourier transform are in general complex, we are able to obtain real, imaginary or complex wavenumber solutions. The analysis is demonstrated for the one-dimensional Helmholtz equation, however results obtained from studying this equation are useful for multi-dimensional discretizations where spatial variations and wave propagation are restricted to one dimension. For Fourier analysis, we are interested in the infinite domain $\Omega = (-\infty, \infty)$, so that no end-point boundary conditions are considered.

Consider the higher-order finite element approximation of the solution,

$$\boxed{\phi^h(\xi) = \sum_{a=1}^{p+1} N_a(\xi)\phi_a \qquad \xi \in [-1,1]} \tag{9.5}$$

where $N_a(\xi)$ are shape functions with compact support defined in the local element coordinate ξ, and p is the spectral order. Three different finite element approximations are considered : (1) Hierarchic Legendre shape functions, (2) New Hierarchic Fourier shape functions, and (3) Lagrange shape functions in conjunction with Lobatto quadrature.

Upon introducing the higher-order interpolations defined in (9.5) into the Galerkin/least-squares variational equation for this one-dimensional problem we obtain the following symmetric element impedance matrix,

$$\boldsymbol{s}^e = [s^e_{ab}] \in \mathbb{R}^{(p+1)\times(p+1)} \qquad a, b = 1 : p+1 \tag{9.6}$$

$$\boxed{\boldsymbol{s}^e = \boldsymbol{k}^e - (1 - \tau k^2)k^2 \boldsymbol{m}^e + \tau \hat{\boldsymbol{k}}^e + \tau k^2 \bar{\boldsymbol{k}}^e} \tag{9.7}$$

where $k = \omega/c$ and

$$\begin{aligned} k^e_{ab} &= (N_{a,x}\,,\, N_{b,x})_{\Omega_e} \\ m^e_{ab} &= (N_a\,,\, N_b)_{\Omega_e} \\ \hat{k}^e_{ab} &= (N_{a,xx}\,,\, N_{b,xx})_{\Omega_e} \\ \bar{k}^e_{ab} &= (N_{a,xx}\,,\, N_b)_{\Omega_e} + (N_a, N_{b,xx})_{\Omega_e} \end{aligned}$$

and the L_2 inner product is defined as,

$$(N_a\,,\, N_b)_{\Omega_e} = \frac{h}{2}\int_{-1}^{1} N_a N_b d\xi \tag{9.8}$$

where h is the element length. In the above expressions, $\boldsymbol{k}^e$ and $\boldsymbol{m}^e$ are the local stiffness and mass matrices emanating from the Galerkin formulation, while the matrices $\hat{\boldsymbol{k}}^e$ and $\bar{\boldsymbol{k}}^e$ are additional contributions obtained from the Least-Squares terms.

9.4.1 P-Version Hierarchic Legendre Elements

Let $\mathcal{S}^p \subset H^1$ be the finite element subspace of continuous piecewise polynomials of degree p denoted by $\mathcal{P}^p$.

$$\mathcal{S}^p = \{\phi | \phi \in C^o(\Omega), \phi \in \mathcal{P}^p(\Omega_e)\}$$

The basis functions used in the p-version finite element method are obtained by starting with the standard linear nodal shape functions,

$$N_a(\xi) = \frac{1}{2}(1 + \xi_a \xi) \qquad a = 1, 2 \tag{9.9}$$

and then adding in a hierarchical fashion internal shape functions defined in terms of integrals of Legendre polynomials.

$$\boxed{N_a(\xi) := \frac{1}{||P_{a-2}||} \int_{-1}^{\xi} P_{a-2}(\xi')d\xi', \qquad a = 3, 4, \cdots, p+1} \tag{9.10}$$

with the norm of the Legendre polynomial,

$$||P_{a-2}||^2 = \frac{2}{2a-3} \tag{9.11}$$

These functions are constructed such that $N_a(\pm 1) = 0$. As a result of this property the variables $\phi_1 = \phi^h(-1)$ and $\phi_2 = \phi^h(1)$ define discrete nodal variables, while the values $\phi_a, a \geq 3$ compose a set of internal variables. The derivatives of these hierarchical functions form an orthonormal basis with the property,

$$\int_{-1}^{1} \frac{dN_a}{d\xi}\frac{dN_b}{d\xi} d\xi = \delta_{ab} \qquad a, b = 3 : p+1 \tag{9.12}$$

As a result of this orthogonality property, the local element stiffness matrix is diagonal beyond $a > 2$. For example, for $p = 6$, the symmetric hierarchical element stiffness matrix is,

$$\boldsymbol{k} = \boldsymbol{k}^T = \frac{1}{h} \begin{bmatrix} 1 & -1 & 0 & 0 & 0 & 0 & 0 \\ & 1 & 0 & 0 & 0 & 0 & 0 \\ & & 2 & 0 & 0 & 0 & 0 \\ & & & 2 & 0 & 0 & 0 \\ & & & & 2 & 0 & 0 \\ & & & & & 2 & 0 \\ & & & & & & 2 \end{bmatrix} \tag{9.13}$$

The hierarchical mass matrix in this case is,

$$\boldsymbol{m} = \boldsymbol{m}^T = \frac{h}{6}\begin{bmatrix} 2 & 1 & -\frac{3}{\sqrt{6}} & \frac{1}{\sqrt{10}} & 0 & 0 & 0 \\ & 2 & -\frac{3}{\sqrt{6}} & -\frac{1}{\sqrt{10}} & 0 & 0 & 0 \\ & & \frac{6}{5} & 0 & -\frac{3}{5\sqrt{21}} & 0 & 0 \\ & & & \frac{2}{7} & 0 & -\frac{3}{7\sqrt{45}} & 0 \\ & & & & \frac{2}{15} & 0 & -\frac{1}{3\sqrt{77}} \\ & & & & & \frac{6}{77} & 0 \\ & & & & & & \frac{2}{39} \end{bmatrix} \tag{9.14}$$

For $p \geq 2$ the diagonal mass coefficients are,

$$m^e_{aa} = \frac{h}{(2a-1)(2a-5)}, \qquad a \geq 3 \tag{9.15}$$

The off-diagonal terms are zero for $p \geq 2$, except:

$$m^e_{a,a+2} = m^e_{a+2,a} = \frac{-h}{2(2a-1)\sqrt{(2a-3)(2a+1)}} \qquad a \geq 3 \tag{9.16}$$

Note that the upper left (2×2) partition is the standard linear $(p = 1)$ element matrix. The element matrices are hierarchic in the sense that the matrix corresponding to $\mathcal{S}^p$ is embedded in the matrix corresponding to $\mathcal{S}^{p+1}$.

9.4.2 New Hierarchic Fourier Elements

Examining the propagating solution to the Helmholtz problem, I have hypothesized that the introduction of trigonometric basis functions should be a better approximation to the complex exponential solution, compared to the polynomial interpolation used in the Legendre based elements. In this case consider hierarchic elements that start with the standard linear nodal shape functions defined in (9.9) and then add to these in a hierarchical manner internal shape functions defined in terms of the Fourier modes,

$$\boxed{N_a(\xi) = \frac{2}{(a-2)\pi}\sin((a-2)(1+\xi)\pi/2) \qquad a = 3, 4, \cdots, p+1} \tag{9.17}$$

These functions satisfy $N_a(\pm 1) = 0$ and the orthogonality properties,

$$\int_{-1}^{1} N_a N_b d\xi = \frac{2}{(a-2)\pi}\delta_{ab}; \qquad \int_{-1}^{1} \frac{dN_a}{d\xi}\frac{dN_b}{d\xi} d\xi = \delta_{ab} \tag{9.18}$$

As a result of this normalization, the local element stiffness matrix is identical to the stiffness matrix obtained with the Legendre polynomial based elements. However, the use of Fourier modes changes the mass matrix. For $p \geq 2$ the diagonal mass coefficients in this case are,

$$m^e_{aa} = \frac{2h}{(a-2)^2\pi^2}, \qquad a \geq 3 \tag{9.19}$$

The off-diagonal terms are zero except for the first two rows (columns),

$$m^e_{1a} = m^e_{a1} = m^e_{aa}, \qquad a \geq 3 \tag{9.20}$$

$$m^e_{2a} = m^e_{a2} = (-1)^{a+1} m^e_{aa}, \qquad a \geq 3 \tag{9.21}$$

For example, the hierarchical element mass matrix for $p = 6$ is,

$$\boldsymbol{m} = \boldsymbol{m}^T = \frac{h}{6\pi^2}\begin{bmatrix} 2\pi^2 & \pi^2 & 12 & 3 & \frac{4}{3} & \frac{3}{4} & \frac{12}{25} \\ & 2\pi^2 & 12 & -3 & \frac{4}{3} & -\frac{3}{4} & \frac{12}{25} \\ & & 12 & 0 & 0 & 0 & 0 \\ & & & 3 & 0 & 0 & 0 \\ & & & & \frac{4}{3} & 0 & 0 \\ & & & & & \frac{3}{4} & 0 \\ & & & & & & \frac{12}{25} \end{bmatrix} \tag{9.22}$$

Comparing this mass matrix to the mass matrix using Legendre polynomials; the effect of using Fourier modes is to change the hierarchical terms in the mass matrix from a tri-diagonal matrix, to a diagonal matrix with a full block of coupling terms in the first two rows (columns).

9.4.3 Spectral elements

Higher-order elements based on Lagrange interpolation polynomials in conjunction with Gauss-Lobotto quadrature lead to the so-called 'spectral elements' when used with a high spectral order p, see e.g. PATERA [1984], MADAY AND PATERA [1989], and FISCHER AND PATERA [1991]. These spectral elements are designed to combine the geometric flexibility of the standard finite element techniques with the rapid convergence rate of global spectral schemes. For a general overview of spectral methods see VOIGHT et al. [1984] and CANUTO et al. [1988].

In the spectral element method, the solution variable ϕ^h is expanded within each element in terms of high-order Lagrangian interpolants, $N_a(\xi) \in \mathcal{P}^p$:

$$\{N_a(\xi) \in \mathcal{P}^p,\, N_a(\xi_b) = \delta_{ab}\ \forall a, b \in \{1, \cdots, p+1\}\} \tag{9.23}$$

evaluated at $p+1$ Gauss-Lobatto points such that $\xi_1 = -1$ and $\xi_{p+1} = 1$, with the other points being obtained as the roots of the derivative of the Legendre polynomials. Gauss-Lobatto points ξ_a, and their corresponding weight factors W_a can be found in tables SZABO AND BABUSKA [1991], or computed directly from subroutine libraries see CANUTO et al. [1988]. In this case, the solution variables are all nodal values, $\phi_a = \phi^h(\xi_a)$, and the basis is not hierarchical. The local matrices for these elements are,

$$k^e_{ab} = \frac{2}{h}\sum_{q=1}^{p+1} N'_a(\xi_q) N'_b(\xi_q) W_q \tag{9.24}$$

$$m^e_{ab} = \frac{h}{2}\sum_{q=1}^{p+1} N_a(\xi_q) N_b(\xi_q) W_q = \frac{h}{2}\,\delta_{ab}\, W_a \tag{9.25}$$

$$\hat{k}^e_{ab} = \frac{8}{h^3}\sum_{q=1}^{p+1} N''_a(\xi_q) N''_b(\xi_q) W_q \tag{9.26}$$

$$\bar{k}^e_{ab} = \frac{2}{h}\sum_{q=1}^{p+1} N''_a(\xi_q) N_b(\xi_q) W_q + \frac{2}{h}\sum_{q=1}^{p+1} N_a(\xi_q) N''_b(\xi_q) W_q \tag{9.27}$$

By choice of Gauss-Lobatto quadrature, the elemental mass matrix is underintegrated and diagonal.

$$\boldsymbol{m} = \boldsymbol{m}^T = \frac{h}{2}\mathrm{diag}(W_a), \qquad a = 1, 2, \cdots, p+1 \tag{9.28}$$

9.5 Complex Wavenumber Fourier Analysis

In this section a complex wavenumber Fourier analysis technique is developed to investigate the dispersive and attenuation properties of higher-order finite elements. The method employs only a minor modification to the technique of real wavenumber analysis but is completely general, and can accommodate any finite element discretization and spectral order. In the present analysis, attention is restricted to Galerkin discretizations with $\tau = 0$.

9.5.1 The Schur Complement

Before the assembly of the finite element equations, for hierarchical elements, it is necessary to decouple the degrees of freedom associated with the interior of the element domain from the element dynamic stiffness (impedance) matrix. This process of condensation reduces the system of dynamic equations to nodal (physical) variables only. This is a necessary prelude to the discrete Fourier transform, where complex exponential solutions are assumed at discrete nodes (sampling points).

The frequency dependent dynamic stiffness matrix $\boldsymbol{s}^e$ is partitioned into the following matrix block form,

$$\boldsymbol{s}^e = \begin{bmatrix} \boldsymbol{s}_{11} & \boldsymbol{s}_{12} \\ \boldsymbol{s}_{12}^T & \boldsymbol{s}_{22} \end{bmatrix} \in \mathbb{R}^{(p+1)\times(p+1)} \tag{9.29}$$

The matrix partition $\boldsymbol{s}_{22} \in \mathbb{R}^{(p-1)\times(p-1)}$ corresponds to interactions among internal shape functions, $\boldsymbol{s}_{12} \in \mathbb{R}^{2\times(p-1)}$ is the coupling matrix partition due to interactions between internal shape functions and nodal shape functions, and finally, $\boldsymbol{s}_{11} \in \mathbb{R}^{2\times 2}$ corresponds to interactions among the nodal shape functions N_1 and N_2. Using the Schur complement,

$$\boldsymbol{g}^e = \boldsymbol{s}_{11} - \boldsymbol{s}_{12}\boldsymbol{s}_{22}^{-1}\boldsymbol{s}_{12}^T, \qquad \boldsymbol{g}^e \in \mathbb{R}^{2\times 2} \tag{9.30}$$

We obtain the condensed element dynamic stiffness $\boldsymbol{g}^e$ that couples only the two element nodal (i.e. physical) degrees of freedom. For $p \geq 2$ we obtain $\boldsymbol{g}^e$ symbolically using Mathematica, (WOLFRAM [1991]). Consider an infinite uniform mesh with equal element lengths h. Assembly of the condensed element dynamic stiffness matrices results in a tridiagonal system of linear equations of the form:

$$\boldsymbol{G}\boldsymbol{\phi} = 0, \qquad \boldsymbol{G} = \mathop{\mathbf{A}}_{e=1}^{n_{el}} \boldsymbol{g}^e \tag{9.31}$$

where $\boldsymbol{\phi}$ is the displacement solution vector, and $\mathop{\mathbf{A}}_{e=1}^{n_{el}}$ is the assembly operator. For present purposes, no source terms are included. The nth equation of this tridiagonal system is a stencil of the form:

$$\boxed{G_1(\alpha)\phi_{n-1} - 2G_2(\alpha)\phi_n + G_1(\alpha)\phi_{n+1} = 0} \tag{9.32}$$

All other equations are a repetition of this stencil. In this difference stencil, the coefficients $G_1(\alpha)$ and $G_2(\alpha)$ are polynomials of degree $2p$ in the nondimensional frequency:

$$\boxed{\alpha = \omega h/c} \tag{9.33}$$

For linear elements ($p = 1$), we recover the difference coefficients of standard consistent and diagonal mass finite element approximations,

$$G_1(\alpha) = 1 + \epsilon\alpha^2/6, \qquad G_2(\alpha) = 1 - (3-\epsilon)\alpha^2/6 \tag{9.34}$$

The constant ϵ is a mass approximation parameter equal to 1 for exactly integrated (consistent) mass, and 0 for Lobatto integrated (diagonal) mass.

The structure of the stencil is seen by writing (9.32) in the difference operator form,

$$\boxed{F(\alpha)\phi_n = 0} \tag{9.35}$$

where,

$$F(\alpha) = \sum_{j=-1}^{1} F_j(\alpha)E_j \tag{9.36}$$

is a second order linear difference operator and E_j is a shift operator with the property

$E_j \phi_n = \phi_{n+j}$. The symmetric frequency dependent coefficients are,

$$\begin{aligned} F_1(\alpha) &= G_1(\alpha) = F_{-1}(\alpha) \\ F_0(\alpha) &= -2G_2(\alpha) \end{aligned}$$

9.5.2 Characteristic equation for high-order elements

In analogy with (9.2), an exponential solution to (9.35) is assumed having the form:

$$\phi_n = A\mathrm{e}^{ik^h x_n}, \quad x_n = nh \tag{9.37}$$

where $k^h \in \mathbb{C}$ is the complex valued numerical wavenumber and $i = \sqrt{-1}$. Substitution of (9.37) into (9.35) results in the characteristic function,

$$\tilde{F}(\alpha, \beta) = \sum_{j=-1}^{1} F_j(\alpha)\mathrm{e}^{ij\beta} = 0 \tag{9.38}$$

where $\tilde{F}(\alpha, \beta)$ may be identified as the discrete Fourier transform of the linear difference operator F, α is the normalized frequency, and β is the normalized discrete wavenumber:

$$\boxed{\beta = k^h h} \tag{9.39}$$

Due to the symmetric form of ($F_1 = F_{-1}$), we find that $\tilde{F}$ is an even function resulting in the wavenumber-frequency relation,

$$\boxed{\cos(\beta) = \lambda(\alpha)} \tag{9.40}$$

where

$$\lambda(\alpha) := \frac{G_2(\alpha)}{G_1(\alpha)} \tag{9.41}$$

and the real spectrum of β is periodic in 2π with aliasing, $\beta = \beta + 2\pi m$; $m \in \mathbb{Z}$.

At this point, we depart from the standard finite element dispersion technique in which real frequency roots of (9.40) are sought for a given real wavenumber. Instead, we seek all the wavenumber roots of (9.40) for a given real frequency. The complex roots $\beta \in \mathbb{C}$, of (9.40) are found using the complex arc cosine (Churchill et al.

[1976]),

$$\boxed{Re(\beta) + iIm(\beta) = -i\ln(\lambda(\alpha) + i\sqrt{1-(\lambda(\alpha))^2})} \tag{9.42}$$

It is noted that the amplitude of the discrete nodal solution is,

$$|\phi_n| = |A|\mathrm{e}^{-Im(\beta)n} \tag{9.43}$$

where the imaginary part $Im(\beta)$ is seen to be an attenuation parameter.

9.6 Dispersion and Attenuation Results

In this section we discuss the complex wavenumbers that arise from the Fourier analysis of high-order finite elements up to spectral order $p = 5$. It will be shown that the finite element characteristic equation (9.40) admits pure real wavenumbers, (propagating solutions) only when the frequency falls within a finite number of bands called passing bands. The number of passing bands is equal to the spectral order p of the elements in the mesh. In addition it will be shown that there are p stopping bands where the wavenumbers are complex. The results in this section apply to Galerkin finite element discretizations with $\tau = 0$.

9.6.1 Low-order elements

For $p = 1$ there is only one passing band where the wavenumber is purely real. For frequencies lower than a limiting frequency called the cut-off frequency we obtain real solutions for β. The cut-off frequency for consistent mass is $\alpha_{max} = \sqrt{12}$ and for diagonal mass $\alpha_{max} = 2$. In the complex wavenumber plane, for frequencies below the cut-off, then $|\lambda| < 1$, and the characteristic equation is satisfied by,

$$Re(\beta) = \cos^{-1}(\lambda), \quad \text{and} \qquad Im(\beta) = 0 \tag{9.44}$$

For higher frequencies β is complex, since above the cut-off frequency, $|\lambda| > 1$, and the characteristic equation is satisfied by,

$$Re(\beta) = \pi, \quad \text{and} \qquad Im(\beta) = \cosh^{-1}(\lambda) \tag{9.45}$$

Figure 9.1 plots the frequency dependence of the real (propagating) and imaginary (decaying) components of the complex numerical wavenumber $k^h \in \mathbb{C}$. The real wavenumber corresponding to the cut-off frequency is called the spatial resolution limit. For $p = 1$, the limit of spatial resolution is two elements per wavelength or $Re(\beta) = \pi$. For frequencies between 0 and α_{max}, β is real, and for frequencies above the cut-off, the real part of the discrete wavenumber stays constant at $Re(\beta) = \pi$, while the imaginary part of the discrete wavenumber increases rapidly.

As a result, the amplitude from node to node along the mesh stays constant until the frequency reaches the cut-off. Above the cut-off the amplitude decays exponentially along the mesh,

$$\left|\frac{\phi_{n+1}}{\phi_n}\right| = \begin{cases} 1 & \alpha < \alpha_{max} \\ \mathrm{e}^{-Im(\beta)} & \alpha > \alpha_{max} \end{cases}$$

This illustrates how the finite element mesh acts as a low-pass filter analogous to discrete signal processing of data; allowing propagation of all frequencies up to the cut-off frequency, while strongly attenuating frequencies above the cut-off frequency; see Thompson and Pinsky [1993a,b] for a plot of this amplitude spectrum.

9.6.2 Higher-order elements

For a uniform mesh of p–version finite elements with spectral order ($p = 2$), the frequency dependence of the real and imaginary parts of $k^h \in \mathbb{C}$ are plotted in Figure 9.2. In this case, there are two passing bands: one for frequencies between $0 < \alpha < \alpha_1$ and one for frequencies between $\alpha_2 < \alpha < \alpha_{max}$. Within these bands, there is a purely propagating solution with $|\lambda| < 1$ and the characteristic equation is satisfied by,

$$Re(\beta) = \cos^{-1}(\lambda), \quad \text{and} \qquad Im(\beta) = 0 \tag{9.46}$$

The dispersion curve in the lower passing band is called the acoustical branch and the upper passing band is referred to as the optical branch. These designations arise from the analogous branches found in a diatomic crystal lattice where the frequencies in the lower branch are of the same order of magnitude as acoustical or subsonic vibrations, and frequencies in the upper branch are of the order of magnitude of infrared frequencies, see Brillouin [1953]. For our discussions, we use these designations for the different branches, but attach no physical significance to their names.

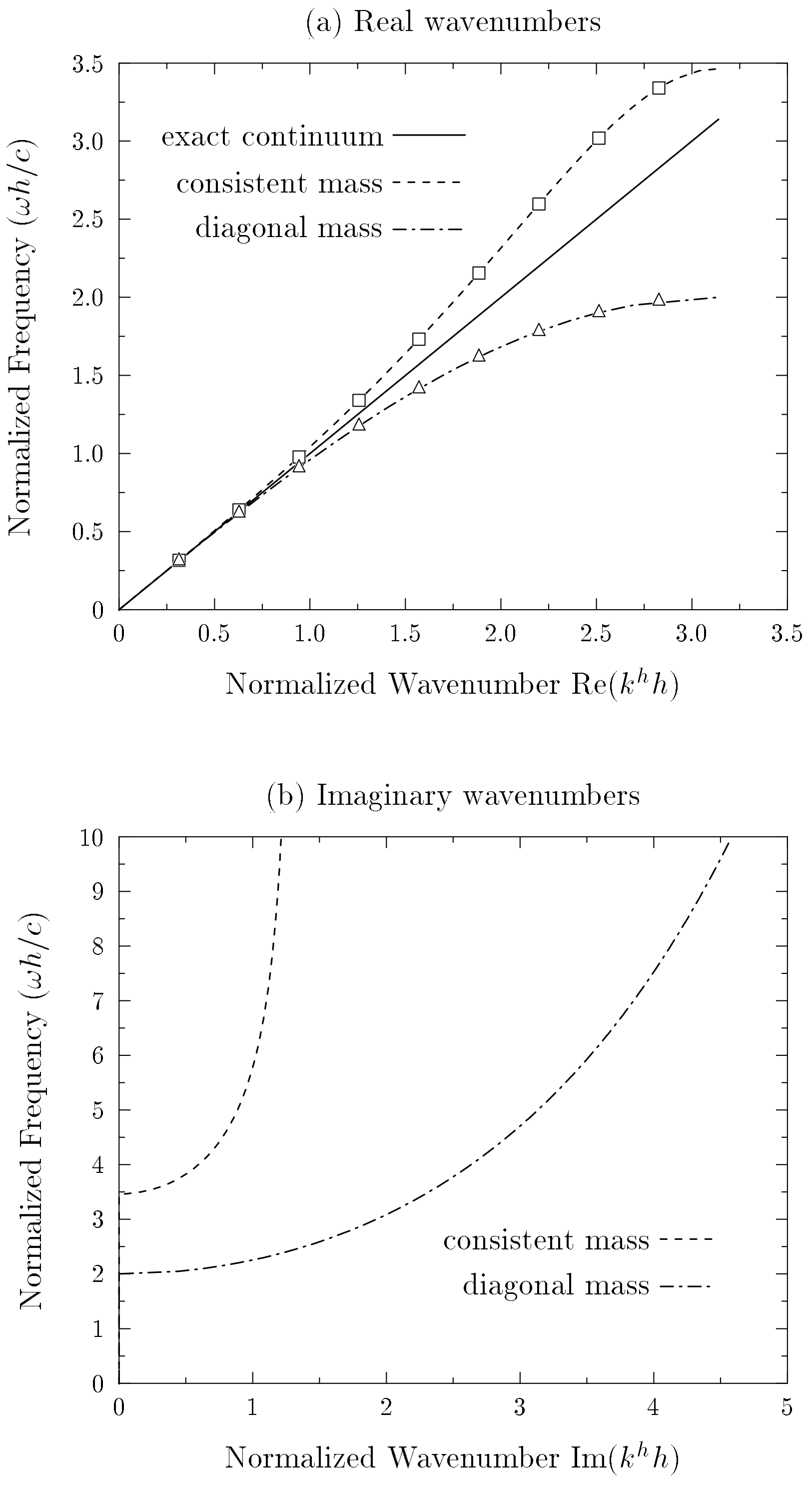

Figure 9.1: Frequency spectrum comparing linear finite element approximations obtained from Galerkin method: (a) Real wavenumbers, (b) Imaginary wavenumbers

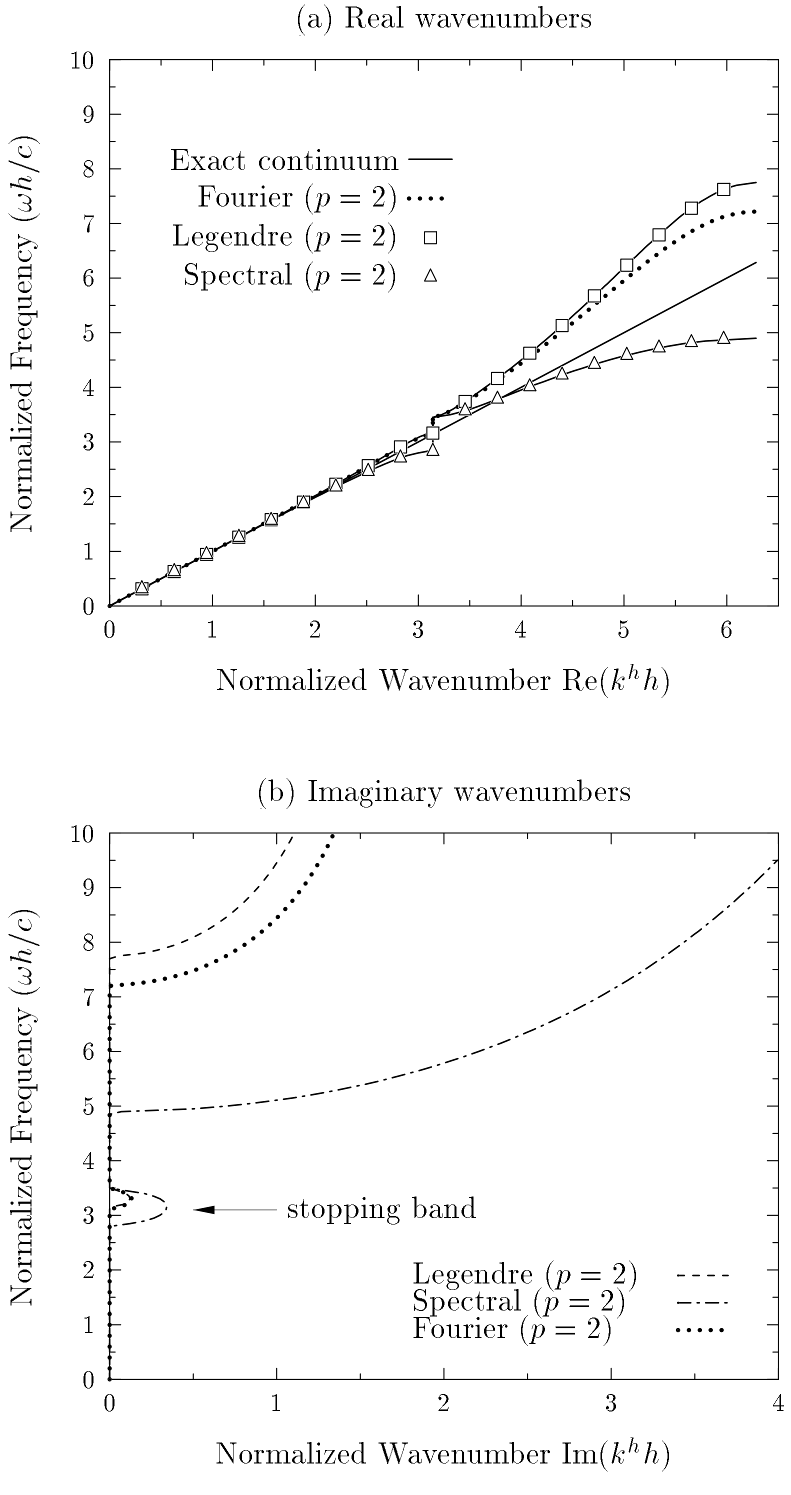

Figure 9.2: Frequency spectrum comparing quadratic finite element approximations obtained from Galerkin method: (a) Real wavenumbers, (b) Imaginary wavenumbers

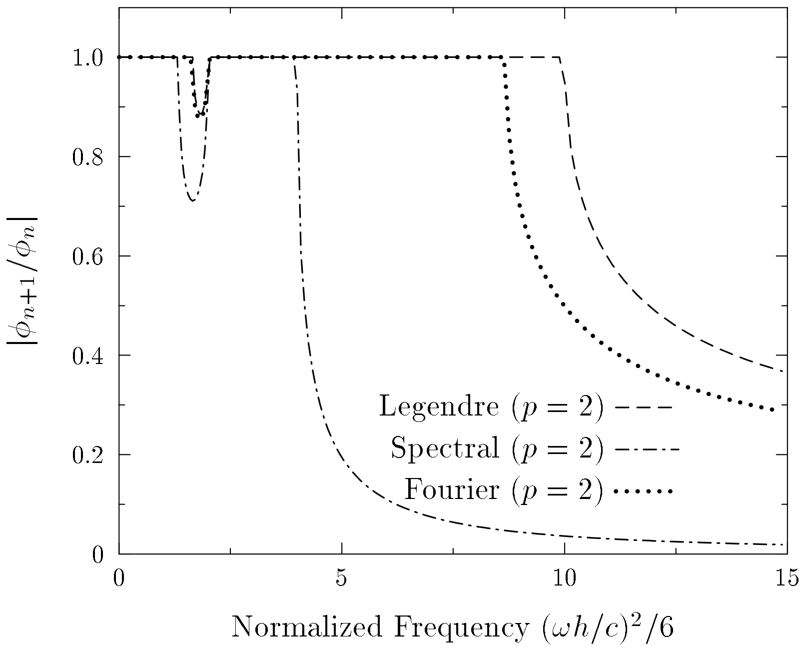

Figure 9.3: Amplitude spectrum for quadratic elements

In the frequency range between these two passing passing bands, $\alpha_1 \leq \alpha \leq \alpha_2$, there is one frequency band where the numerical wavenumbers are complex. In this band, $|\lambda| > 1$ and the characteristic equation is satisfied by,

$$Re(\beta) = \pi, \quad \text{and} \qquad Im(\beta) = \cosh^{-1}(-\lambda) \tag{9.47}$$

This complex wavenumber band is called a stopping band because in this frequency range, the real part of the wavenumber is constant and the imaginary component results in an attenuated wave solution with an amplitude decay proportional to the exponential of the imaginary wavenumber.

Above the cut-off frequency, $\alpha > \alpha_{max}$, $\lambda > 1$ and the characteristic equation is satisfied by,

$$Re(\beta) = 2\pi, \quad \text{and} \qquad Im(\beta) = \cosh^{-1}(\lambda) \tag{9.48}$$

In this case, the solution propagates with a fixed wavelength equal to the limit of resolution – one quadratic element per wavelength or $Re(\beta) = 2\pi$ with strong exponential amplitude decay from node to node along the mesh.

The amplitude spectrum for $p = 2$ is plotted in Figure 9.3. The amplitude ratio is constant in the first passing band (acoustical branch) up to the complex wavenumber band where the imaginary wavenumber components produce an amplitude decay. In the stopping band, the amplitude is attenuated until a minimum is reached and then increases back up to the exact ratio of one. The amplitude ratio continues to be exact throughout the second passing band (optical branch) until it reaches the cut-off where it is strongly attenuated. The cutoff frequency for the Spectral element falls well below that of the Legendre and Fourier elements.

Again invoking the signal processing analogy, the character of this amplitude spectrum illustrates how the p–version finite element mesh acts as a band-pass filter – allowing propagation of all frequencies in the passing bands, while weakly attenuating frequencies in the complex wavenumber band, and strongly attenuating frequencies above the cut-off frequency.

As the spectral order is increased to $p = 3$, the spatial resolution limit extends to $Re(\beta) = 3\pi$. Figure 9.4 shows that there are 3 passing and 3 stopping bands present in the frequency spectrum. The first complex wavenumber band occurs when $Re(\beta) = \pi$. The frequency range for the first stopping band is very small and appears as a small perturbation in the frequency curve for the imaginary wavenumber component at approximately $\alpha = \pi$, see Figure 9.4. The second stopping band occurs when the real wavenumber component reaches 2π and is much larger, with large imaginary wavenumber components present.

As a result of these complex wavenumber bands, we observe the amplitude attenuation characteristics shown in Figure 9.5(top). The amplitude ratio is again constant in the passing bands up to the first complex wavenumber band, where there is a very small attenuation loss. Isolating this frequency region in Figure 9.5(bottom), we observe that the maximum amplitude error is only 2.5 percent for the Spectral elements and only 1 percent for Legendre and Fourier elements. Thus in this first complex wavenumber region waves propagate with constant wavenumber $Re(\beta)$ and only a very small amplitude decay. The amplitude attenuation in the second complex frequency band is very large and in practice the element size h should be chosen to avoid this nondimensional frequency range.

These observations are extended to higher spectral orders as well. Results for spectral orders $p = 4$ and $p = 5$ are shown in Figure 9.6. For nondimensional frequencies up to $\alpha = (p-2)\pi$, the dispersion curves approximate the exact line with slope one. As the nondimensional frequency increases, the Legendre and Spectral

(a) Real wavenumbers

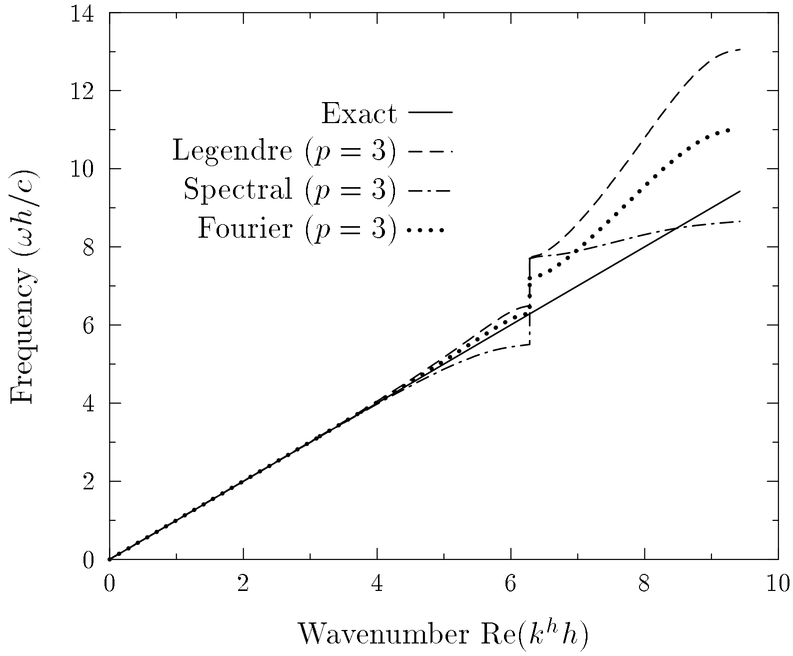

(b) Imaginary wavenumbers

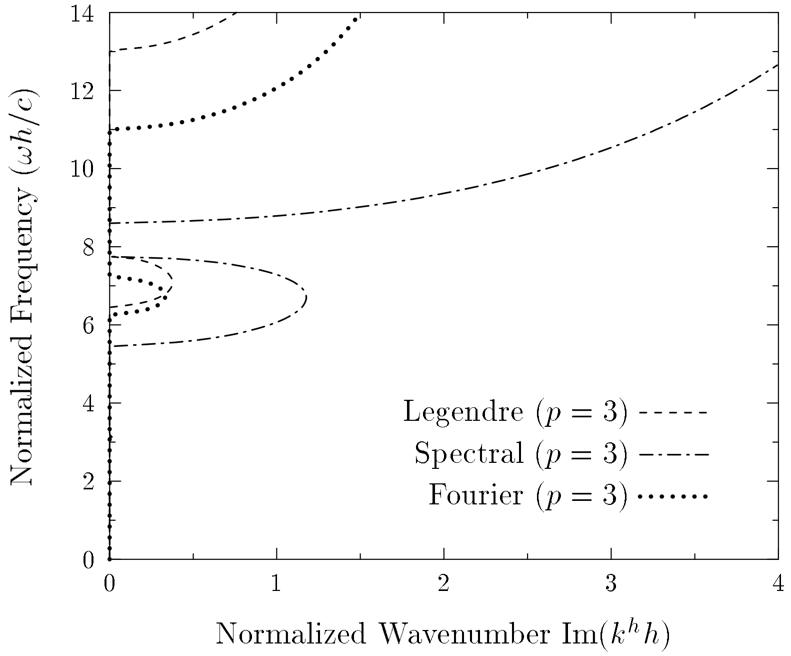

Figure 9.4: Frequency spectrum comparing cubic finite element approximations obtained from the Galerkin method: (a) Real wavenumbers, (b) Imaginary wavenumbers

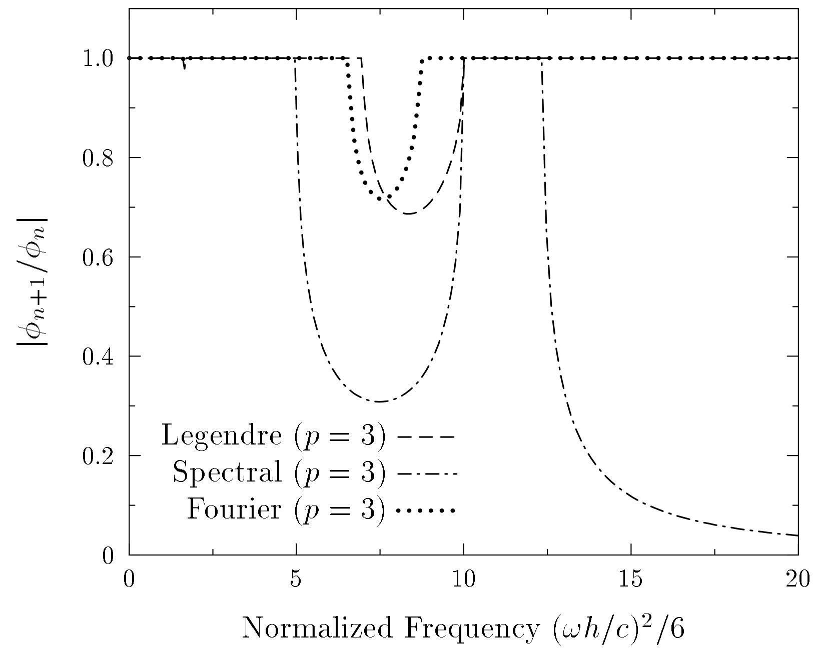

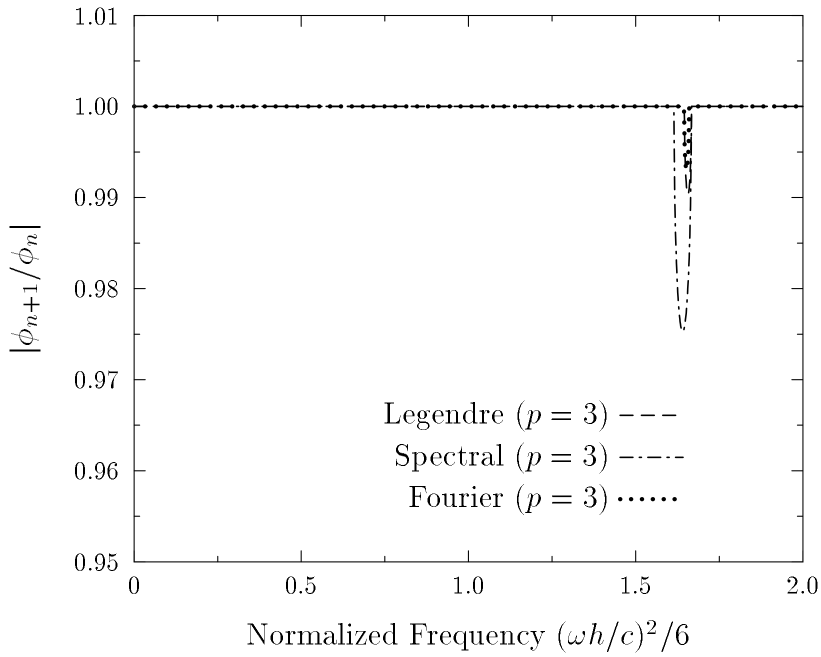

Figure 9.5: (Top): Amplitude spectrum for cubic elements. (Bottom): Isolation of amplitude spectrum near first complex wavenumber band.

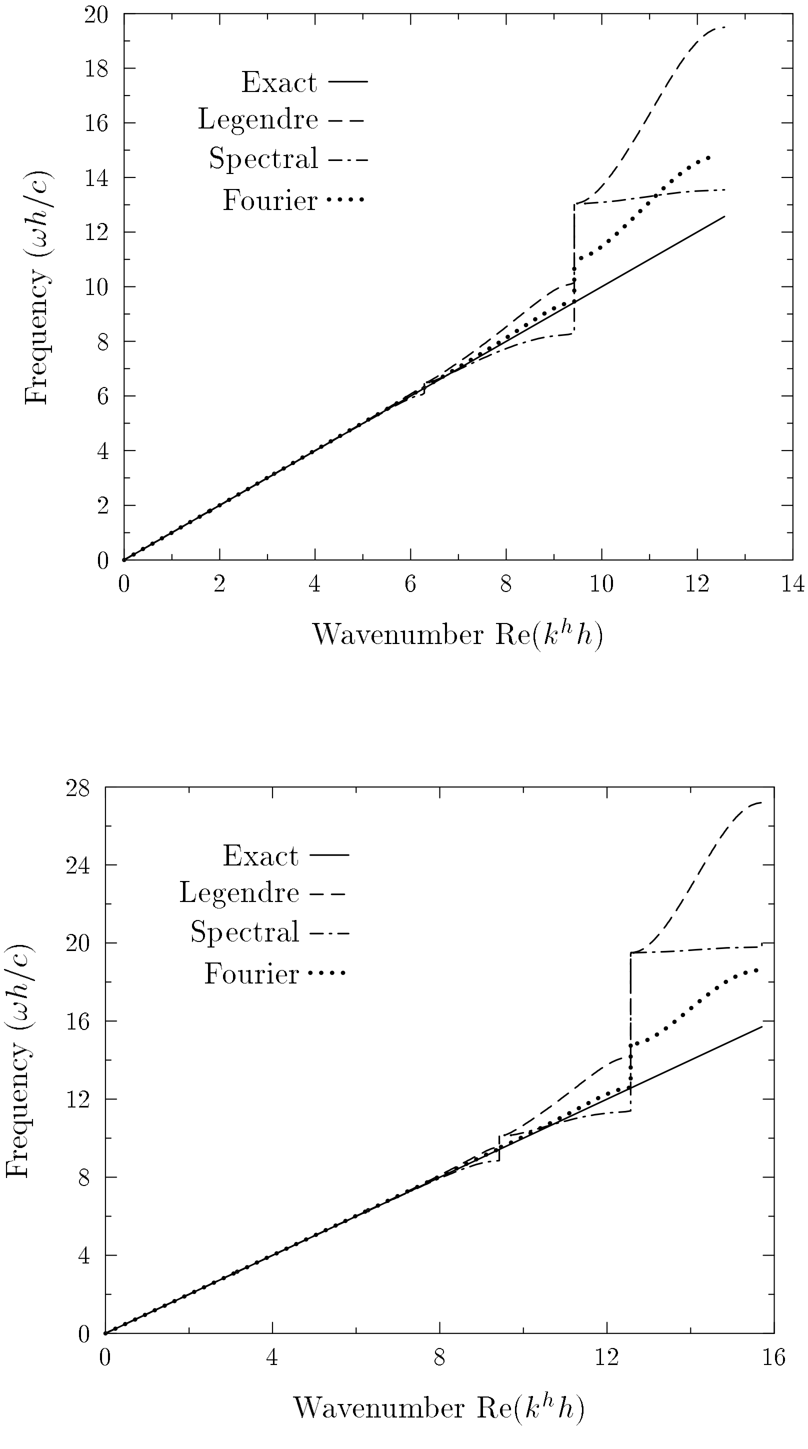

Figure 9.6: Frequency spectrum for spectral orders, (Top): $p = 4$ (Bottom): $p = 5$. Results shown for real wavenumbers only.

elements exhibit loss of accuracy in the upper two optical branches. In contrast, the Fourier element maintains accuracy up to $\alpha = (p-1)\pi$.

In conclusion, the following dispersive properties are observed: (1) There are p passing bands and p stopping bands, (2) the limit of resolution occurs at $Re(\beta) = \pi p$. In addition, *the amplitude attenuation in the first few complex wavenumber (stopping) bands is very small and converges in the limit of large spectral orders to the exact amplitude ratio of one. Thus for large spectral orders the first few stopping bands are not of practical significance.* As a general trend we observe that the amplitude error is greater for the Spectral elements than the Legendre and Fourier elements and the cutoff for Spectral elements always occurs before that of Legendre elements.

9.6.3 Analysis of phase error

Figure 9.7 shows the phase accuracy of the Galerkin finite element approximation versus a nondimensional real wavenumber ($\beta/\pi p$). The wavenumber is divided by the spectral order p to obtain an equitable comparison between the methods with the same number of degrees of freedom per wavelength. Throughout the acoustic branch, the phase error converges to the exact solution as the spectral order is increased. Clearly, in the practical range $0 \le k^h h/\pi p \le .5$ the higher-order p–type elements exhibit increased accuracy compared to low-order finite elements, for the same number of degrees of freedom. In the optical branches, the dispersive errors increase. The use of trigonometric shape functions in the Fourier elements decreases the phase error found in the optical branch as compared to the Legendre case.

The spectral convergence rate of the phase error is observed by fixing the nondimensional wavenumber at $kh/p = \pi/5$. This wavenumber corresponds to ten elements per wavelength divided by the spectral order. The results are given in Table 9.1 for Legendre and Spectral elements up to order $p = 5$. Results for Fourier elements are similar to Legendre elements.

The convergence rate of p–type elements is investigated further by examining the phase as the number of solution variables per wavelength is increased. For example for $p = 1$ a Taylor series expansion of the dispersion relation (9.40) gives,

$$k^h h = \alpha \pm \frac{(\alpha)^3}{24} + \frac{3(\alpha)^5}{640} \pm \mathcal{O}(\alpha)^7 \qquad (9.49)$$

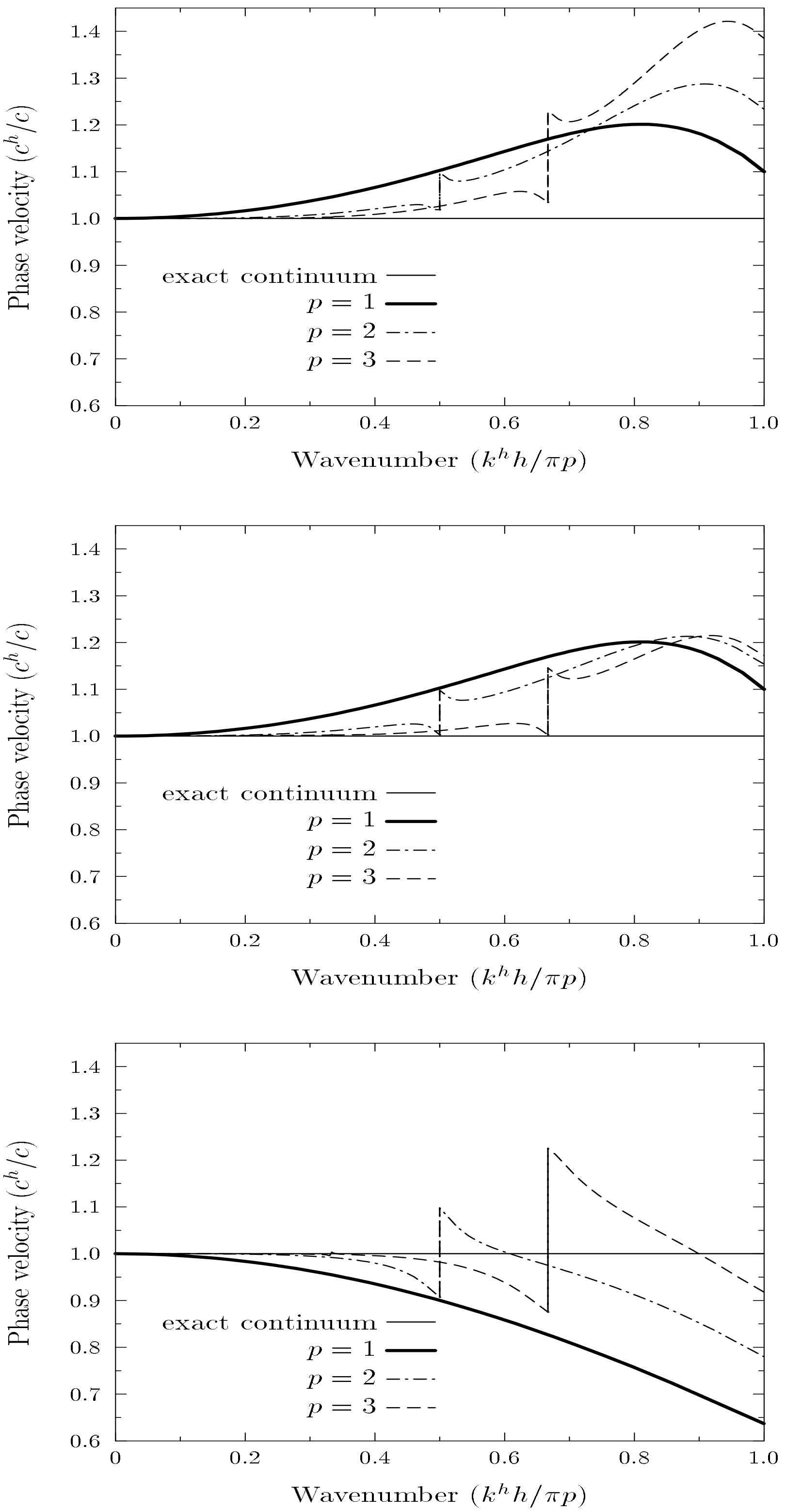

Figure 9.7: Phase velocity error for spectral orders $p = 1, 2, 3$. (top) Legendre basis, (middle) Trigonometric basis, (bottom) Spectral basis.

Table 9.1: Phase error (percent) for fixed $kh/p = \pi/5$

p	Legendre	Spectral
1	1.60e-00	-1.69e-00
2	1.59e-01	-9.17e-02
3	1.96e-02	-7.50e-03
4	2.63e-03	-9.60e-04
5	3.69e-04	6.58e-03

where the plus sign is for diagonal mass and the minus sign for consistent mass. From this expansion it is found that the finite element nodal solution is locally second order accurate. In general, in the range of resolution, the phase error for spectral order p is of the order,

$$\frac{k^h}{k} - 1 = \mathcal{O}(kh)^{2p} \tag{9.50}$$

with the nodal solution,

$$\boxed{\phi_n = A\mathrm{e}^{ikx_n[1 \pm \mathcal{O}(kh)^{2p}]}} \tag{9.51}$$

This result is verified for spectral orders of $p = 1, 2, 3$ in Figure 9.8, where the slope of the lines show the rate of convergence of the phase error to be $2p$. For reference, we note that 10 elements per wavelength corresponds to -1.0 on the abscissa of this plot.

9.6.4 Analysis of attenuation

Although the amplitude from node to node is exact for frequencies within the passing bands, it is possible for the high-order finite element solution to exhibit amplitude attenuation at points internal to physical nodes. Analysis of amplitude attenuation at points internal to the physical nodes is investigated by examining quadratic elements of order $p = 2$. In this case, the dynamic stiffness matrix is assembled without condensation and the internal variable is written in terms of the center point. The resulting stencils related to equations n and $n \pm 1/2$ are of the form,

$$S(\alpha) = 0 \tag{9.52}$$

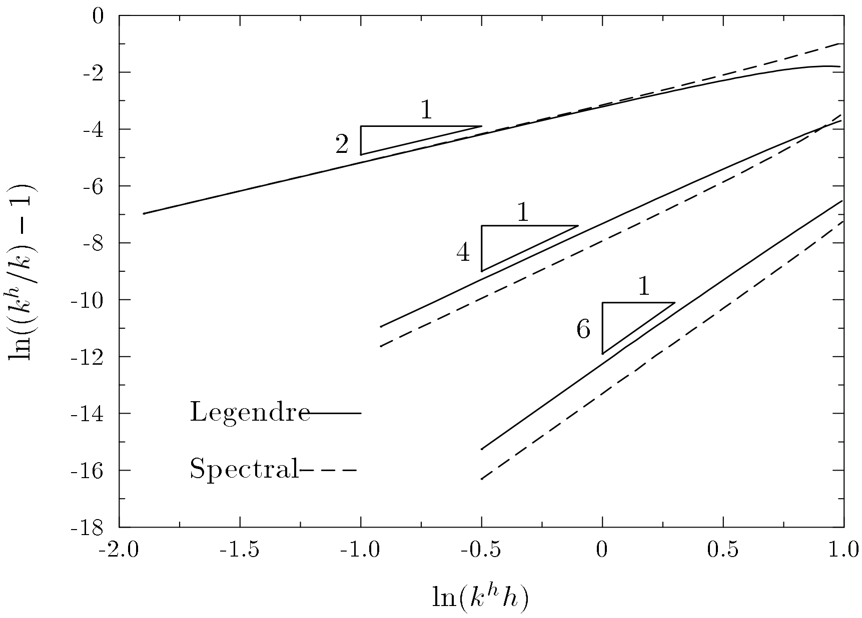

Figure 9.8: Convergence of phase error with polynomial orders $p = 1, 2, 3$.

where

$$S(\alpha) := (K - \alpha^2 M) \tag{9.53}$$

and K and M are (2×5) stiffness and mass coefficient matrices, with solution vector,

$$\boldsymbol{\phi}^T = \begin{pmatrix} \phi_{n-1} & \phi_{n-1/2} & \phi_n & \phi_{n+1/2} & \phi_{n+1} \end{pmatrix} \tag{9.54}$$

Allowing for different amplitudes at the exterior nodes n, and element center nodes $n \pm 1/2$ we assume the complex exponential solutions,

$$\phi_n = A_1 \mathrm{e}^{i\beta(n)} \tag{9.55}$$

$$\phi_{n+1/2} = A_2 \mathrm{e}^{i\beta(n+1/2)} \tag{9.56}$$

Substitution of the above two solutions into (9.52) results in the symmetric characteristic matrix,

$$\widetilde{S}(\alpha, \beta) = \begin{bmatrix} \widetilde{S}_{11} & \widetilde{S}_{12} \\ \widetilde{S}_{12} & \widetilde{S}_{22} \end{bmatrix} \begin{Bmatrix} A_1 \\ A_2 \end{Bmatrix} = \mathbf{0} \tag{9.57}$$

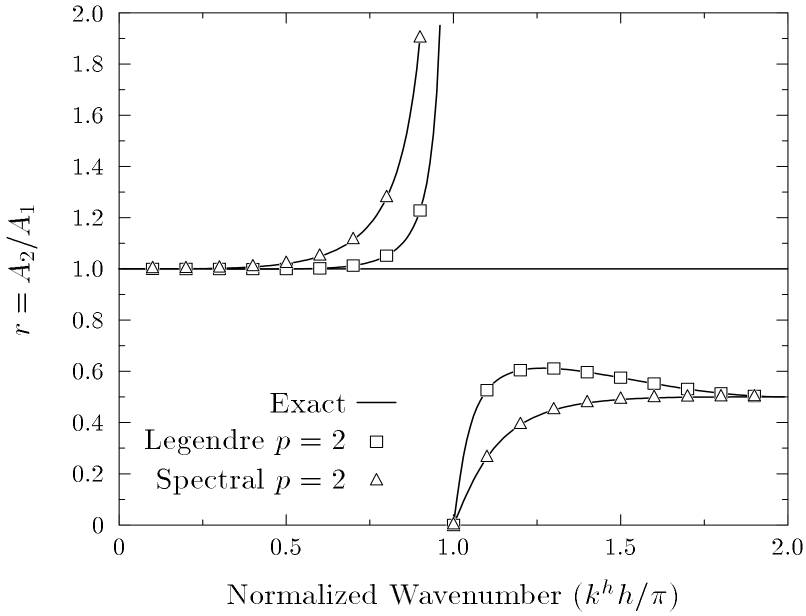

Figure 9.9: Amplitude spectrum for quadratic elements at interior nodes

Solving this system, the amplitude ratio $r = A_2/A_1$ is,

$$r(\alpha, \beta) = -\frac{\widetilde{S}_{12}(\alpha, \beta)}{\widetilde{S}_{22}(\alpha, \beta)} = -\frac{\widetilde{S}_{11}(\alpha, \beta)}{\widetilde{S}_{12}(\alpha, \beta)} \tag{9.58}$$

Note that the dispersion relation found earlier in (9.40) is obtained by setting the characteristic matrix to zero, $\det\widetilde{S} = \widetilde{F}(\alpha, \beta) = 0$.

Figure 9.9 shows the amplitude ratio $r = A_2/A_1$ plotted as a function of wavenumber. The curves lying above the ratio of one are acoustical branches, while those below are optical branches. In the range $0 \leq \beta \leq 2\pi/3$, the amplitudes are nearly equal to the exact value of one. Near the stopping band, $\beta = \pi$, r increases rapidly. At $\beta = \pi$, the amplitude ratio skips to the optical branch where it assumes the value zero. In the optical branch the ratio tends to the limit $r = 0.5$. The physical interpretation of this result is discussed at length in BRILLOUIN [1953]: Here we emphasis that two alternative interpretations are possible: (i) Referring to (9.56), the solution for the finite element mesh can be represented as *two waves*, one propagating along the exterior nodes n, and the other propagating along the interior points $n \pm 1/2$. (ii) An alternative representation is a *single wave* propagating through both interior and exterior points,

$$\phi_m = C_+ e^{i(\bar{\beta})m} + C_- e^{i(\bar{\beta}-\pi)m} \tag{9.59}$$

where $\beta = 2\bar{\beta}$ and $C_+ = (A_1 + A_2)/2$ and $C_- = (A_1 - A_2)/2$. This solution describes the superposition of two waves propagating in opposite directions with wavenumbers $\bar{\beta}$ to the right and $\bar{\beta} - \pi$ to the left. The wave propagating to the right is partially reflected as it traverses each node, thus giving rise to a solution that consists of both a transmitted and a reflected wave component. The physical significance of this result is that while the amplitude is exact from node to node for frequencies within passing bands, the reflected wave component causes amplitude attenuation at internal points.

For quadratic Legendre elements, amplitude attenuation is insignificant for $k^h h < 2\pi/3$ (three elements per wavelength), while for quadratic Spectral elements amplitude attenuation is insignificant for $k^h h < \pi/2$ (four elements per wavelength). Results for Fourier elements are similar to the Legendre elements.

9.7 Frequency response spectrum

The role that complex wavenumbers play in the practical solution of physical boundary value problems is revealed in the time-harmonic solution for the Helmholtz equation with Dirichlet boundary conditions $\phi(0) = \bar{\phi}$ and $\phi(L) = 0$, where L is the length of the domain. After discretizing with N uniformly spaced elements of length h, it can be shown that the finite element solution is,

$$\phi^h(x_n, \omega) = \bar{\phi}\frac{\sin(k^h(L - x_n))}{\sin(k^h L)} \qquad n = 0 : N \tag{9.60}$$

where k^h is the numerical wavenumber defined in (9.40) and $L = Nh$ and $x_n = nh$. The important point here is that this wave solution consists of the same numerical wavenumbers present for the infinite domain found by our Fourier analysis except that both outgoing and incoming waves are present.

The existence of the cut-off frequency and stopping bands for the example problem is exposed from the frequency response spectrum. Figure 9.10 shows the frequency response at the midnode for a uniform mesh of ten quadratic ($p = 2$) elements.

$$R(\omega) = \phi^h(x_5, \omega)/\bar{\phi} \tag{9.61}$$

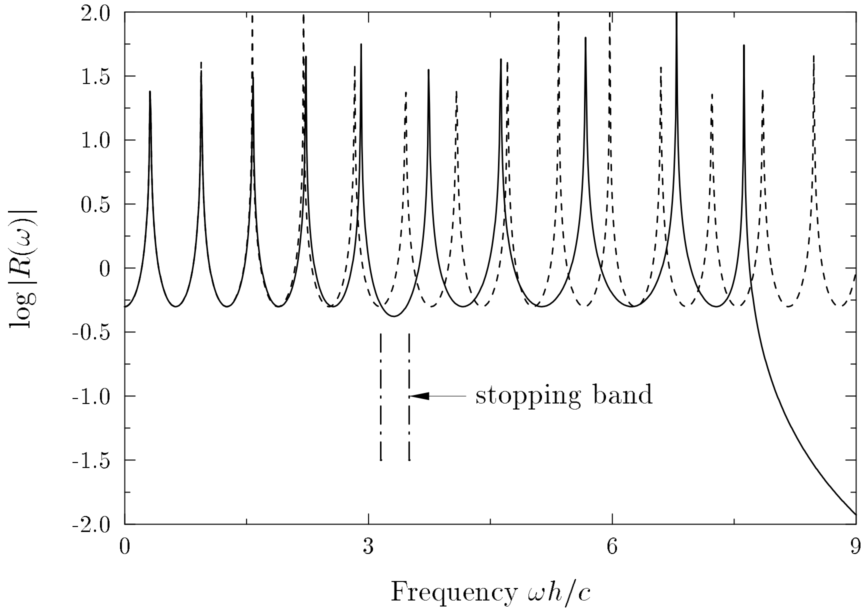

Figure 9.10: Frequency response spectrum for example problem using 10 quadratic Legendre elements.

The sharp peaks indicate the position of the resonant frequencies of the vibration problem. Accurate results are obtained throughout the acoustic branch while considerable errors are present in the optical branch. The existence of the stopping band (complex wavenumber band) is evident by the decrease in amplitude response at $(\omega h/c) \approx \pi$.

In Figure 9.11, the response for a frequency in the stopping band is plotted. It is clear that the response has a propagating component fixed at $Re(k^h h) = \pi$ corresponding to two elements per wavelength, while the imaginary component manifests itself in the amplitude decay. Further results can be found in Thompson and Pinsky [1993a,b].

9.7.1 Discrete eigenvalues

For the example problem, the exact eigenmodes $k_j = j\pi/L, j = 1, 2, \cdots \infty$ are linearly proportional to the eigenvalues through the characteristic relation $\omega_j h/c = k_j h$. It can be shown that the real eigenmodes for a uniform mesh of finite elements of any spectral order are,

$$k_j^h = j\pi/L \qquad\qquad j = 1 : pN - 1 \tag{9.62}$$

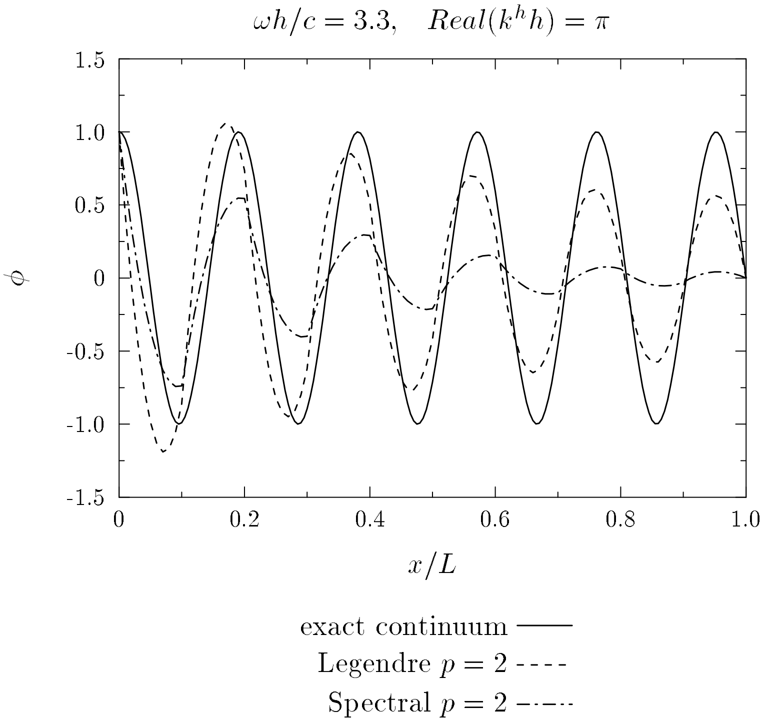

Figure 9.11: Harmonic decaying wave solution for example problem for a driving frequency in the stopping (complex wavenumber) band.

Thus the eigenmodes for the finite element mesh are exact, up to the number of free variables $(pN-1)$ present in the mesh. Discrete eigenvalues $\omega_j h/c$ are calculated from the dispersion relation (9.40) in which real frequency roots are sought for the given real eigenmodes $k_j h$. The result is a characteristic polynomial in $\alpha_j = \omega_j h/c$ of order $2p$.

$$\sum_{l=0}^{p} c_l \alpha_j^{2l} = 0 \tag{9.63}$$

For quadratic Legendre elements, the characteristic equation and its roots are,

$$\boxed{c_o + c_1\alpha_j^2 + c_2\alpha_j^4 = 0} \tag{9.64}$$

where

$$\begin{aligned} c_0(k_j h) &= 20(1-\cos k_j h) \\ c_1(k_j h) &= -2(13+2\cos k_j h)/3 \end{aligned}$$

$$c_2(k_j h) \quad = \quad (3 - \cos k_j h)/12$$

$$\left(\frac{\omega_j h}{c}\right)_1^2 \quad = \quad \frac{-c_1 - \sqrt{c_1^2 - 4c_0 c_2}}{2c_2} \tag{9.65}$$

$$\left(\frac{\omega_j h}{c}\right)_2^2 \quad = \quad \frac{-c_1 + \sqrt{c_1^2 - 4c_0 c_2}}{2c_2} \tag{9.66}$$

For a uniform mesh with $N = 10$ quadratic elements, there are nineteen discrete frequencies corresponding to nineteen active degrees-of-freedom. These frequencies are calculated from (9.65) and (9.66) and are plotted as tick marks on the dispersion curves in Figure 9.2a. We note that the second root (9.66) corresponds to the upper branch (optical branch). At the stopping band $k_j h = \pi$, there is a discontinuity in the frequency/wavenumber relation, where there are two possible choices for the roots. Eigenfrequencies in the range between these roots are skipped over. From numerical results, it was found that the eigenfrequency occupies the lowest energy mode at this wavenumber and falls on the smaller of the two roots. The discrete eigenfrequencies fall exactly on these dispersion curves; below the cut-off frequency and outside the stopping band. These results demonstrate that the real part of the complex wavenumber Fourier analysis accurately predicts the discrete eigenfrequency spectrum.

9.7.2 Post-processing of eigenmodes

The eigenvectors for the example problem are,

$$\sin(k_j x_n) = \sin(j\pi x_n/L) \qquad j = 1 : pN - 1 \tag{9.67}$$

Comparing this result to the analytical eigenfunctions, the eigenvectors are nodally exact for all spectral orders. Figure 9.12 shows an example of mode j=18 representing a wavenumber in the upper optical branch of a uniform mesh of ten quadratic elements. At the nodal points n, the amplitude A_1 is exact, whereas at the intermediate points $n \pm 1/2$ the amplitude A_2 is given by the ratio $r = A_2/A_1$ defined earlier in Figure 9.9. For mode $j = 18$, there are two aliased wave solutions, one passing through each set of points n and $n \pm 1/2$,

$$\phi_n = A_1 \sin(\beta_2 n) \qquad n = 0 : N \tag{9.68}$$

$$\phi_{n+1/2} = A_2 \sin(\beta_2(n + 1/2)) \qquad n = 0 : N - 1 \tag{9.69}$$

where $\beta_2 = (2\pi - \beta_{18}) = \pi/5$, see Figure 9.13.

Using information obtained from the complex Fourier analysis, mode shapes for higher-order elements can be processed in order to isolate individual wave components. By superposition of these wave components, a single wave solution can be constructed with a global sinusoidal interpolation. The global sinusoidal interpolation of nodal data improves the representation of the eigenmode at inter-nodal points.

For example, for mode $j = 18$, by applying a discrete sine transformation Bellanger [1989] with sample points ϕ_m, i.e.

$$w_j = \frac{1}{N} \sum_{m=1}^{2N-1} \phi_m \sin(\frac{jm\pi}{2N}), \qquad j = 1 : 2N - 1 \tag{9.70}$$

we find that the only nonzero wave amplitudes are w_2 and w_{18} illustrated in Figure 9.14. Using the inverse sine transform,

$$\phi_m = \sum_{j=1}^{2N-1} w_j \sin(\frac{jm\pi}{2N}) = w_2 \sin(\frac{m\pi}{10}) + w_{18} \sin(\frac{9m\pi}{10}) \tag{9.71}$$

we then superimpose these two wave components to form the single wave constructed from the sinusoidal interpolation,

$$\boxed{\phi(x) = \sum_{j=1}^{2N-1} w_j \sin(\frac{j\pi x}{L})} \tag{9.72}$$

see Figure 9.15. Comparing this interpolated solution to the imaginary part of (9.59) we recognize the two wave amplitudes as $w_2 = C_+$ and $w_{18} = C_-$. Although the amplitude of the sinusoidal interpolation of the eigenmode is attenuated, the post-processed eigenmode better represents the exact sinusoidal mode shape – compare Figure 9.12 and 9.15.

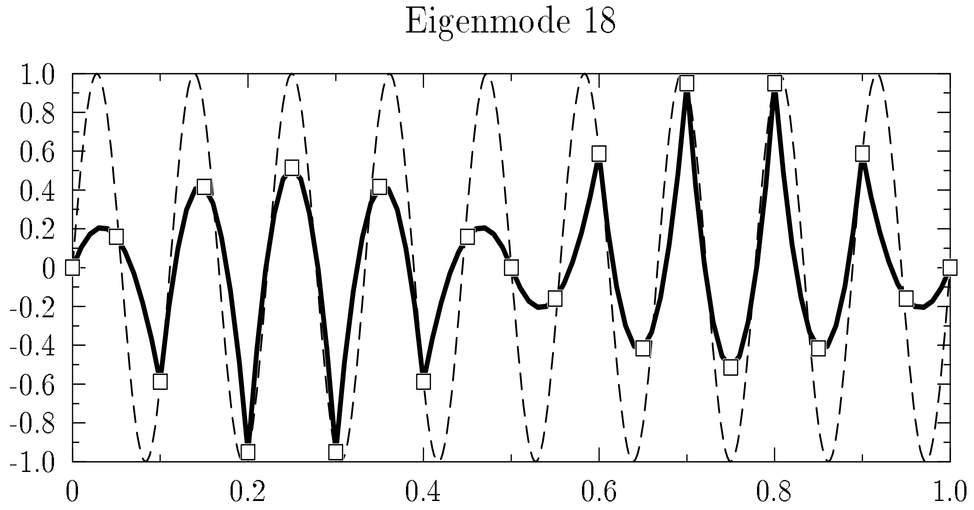

Figure 9.12: Mode shape $j = 18$ for uniform discretization of ten quadratic Legendre elements. The dashed curve denotes the exact mode while the solid line denotes the approximate mode interpolated with quadratic shape functions. The square tick marks denote nodal values.

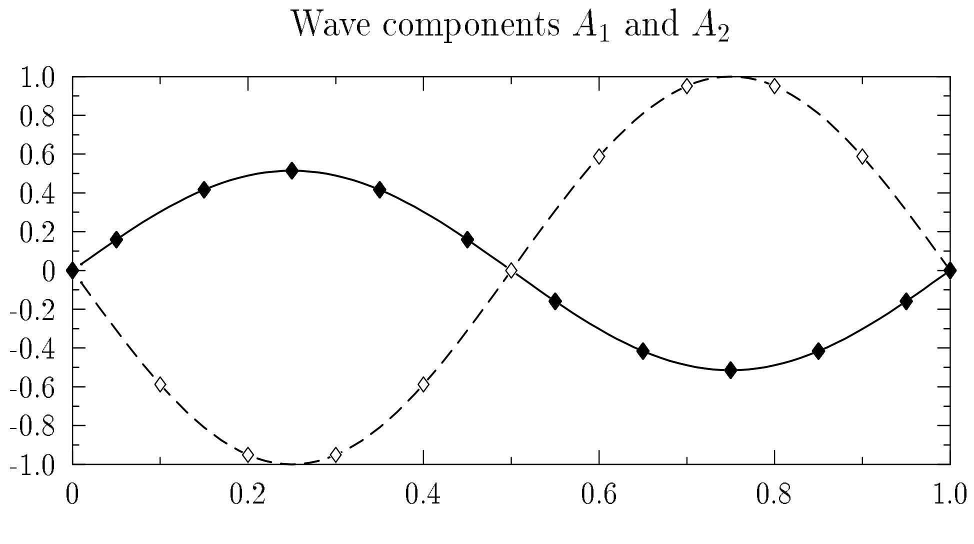

Figure 9.13: Two aliased wave solutions for mode $j = 18$; one passing through each set of points n and $n \pm 1/2$. Dashed curve indicates wave component A_1 while the solid curve indicates A_2.

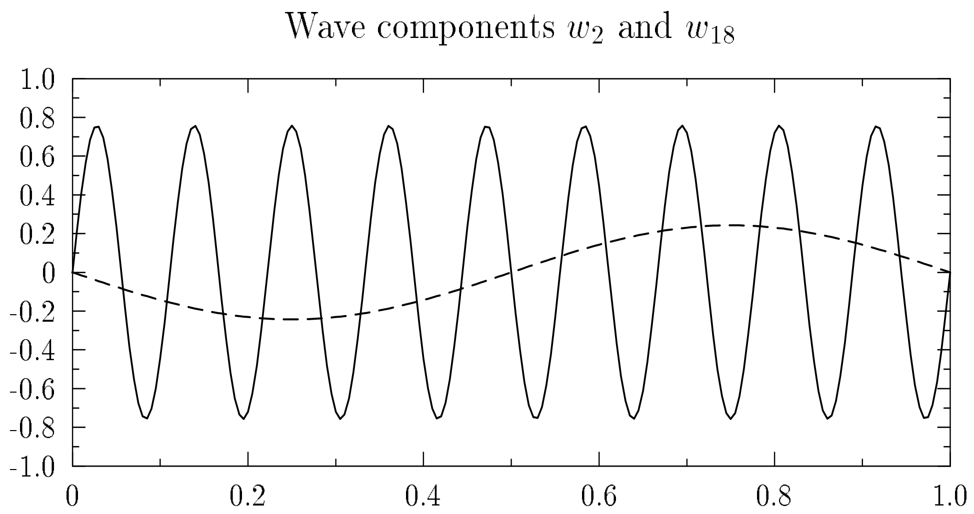

Figure 9.14: Two wave components obtained from discrete sine transform of mode $j = 18$. Dashed curve indicates wave component w_2. Solid curve indicates w_{18}.

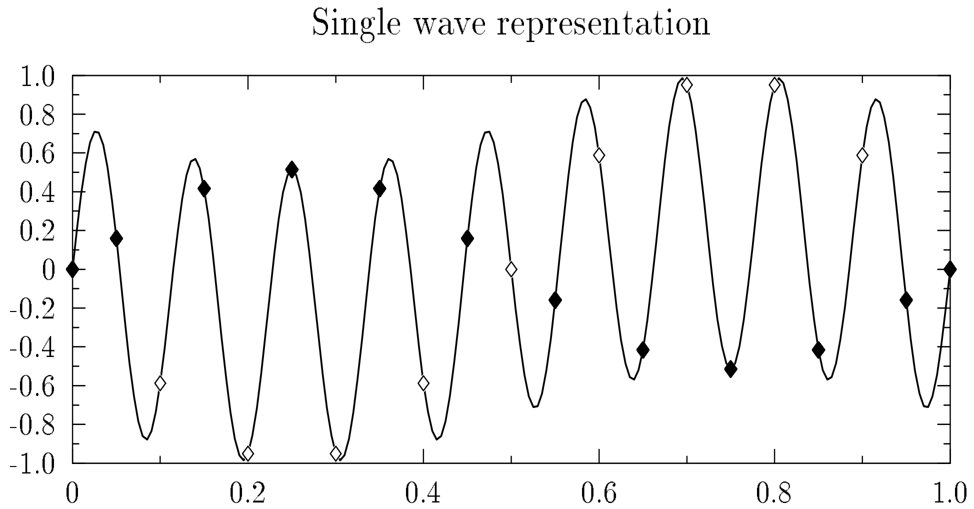

Figure 9.15: Processed mode shape: Sinusoidal interpolation for mode $j = 18$.

9.8 Summary and Conclusions

In this chapter we have shown that high-order finite element discretizations display frequency bands where the solutions are harmonic decaying waves. In these so called 'stopping' bands, the solutions are not purely propagating (real wavenumbers) but are attenuated (complex wavenumbers). In order to interpret the solution within the stopping bands the standard finite element dispersion analysis technique has been extended to include complex wavenumbers. By allowing for complex wavenumbers, a complete characterization of the stopping bands in the frequency spectrum of high-order finite element discretizations has been obtained.

The most important conclusions from this study are summarized as follows:

1. There are p stopping bands present in the dispersion curves of p–type elements

2. For large spectral orders p, the width of the first few stopping bands are very small and the amplitude attenuation is minimal. Thus for high-order finite element basis functions, the first few stopping bands are not of practical significance.

3. High-order elements display increased phase accuracy compared to low-order elements for the same number of degrees of freedom. For example, for linear elements ($p = 1$), a practical limit on phase accuracy is to require at least ten elements per wavelength. For quadratic elements ($p = 2$), as few as three quadratic elements per wavelength are required to obtain accurate phase. For a spectral order of ($p = 3$), only two elements per wavelength are needed to maintain phase accuracy. To resolve waves with increased accuracy while maintaining only two elements per wavelength, spectral orders of ($p \geq 4$) are recommended.

4. For well resolved waves, spectral elements using Lagrange interpolation in conjunction with Lobatto quadrature give improved convergence rates for phase error when compared to hierarchic elements with either Legendre or Fourier basis functions.

5. For nondimensional frequencies extending beyond the recommended limits, both dispersion and amplitude attenuation errors increase the most for spectral elements.

6. For nondimensional frequencies in the upper branches of the frequency spectrum, hierarchic p-type elements with Legendre basis exhibit improved amplitude accuracy over the spectral elements, while the new hierarchic Fourier elements exhibit improved accuracy for both amplitude and phase.

A study of the closed form solution for a canonical steady-state vibration problem demonstrated the role complex wavenumbers play in the finite element solution of boundary value problems. Frequency response results clearly display the existence of the cut-off frequency and stopping bands present in the finite element solution. The important point here is that finite element solutions to vibration problems are composed of the same numerical wavenumbers found in the complex Fourier analysis except that both outgoing and incoming waves are present. In addition there is a direct connection between the dispersion curves (real part of the complex wavenumber characteristic relation) and the discrete eigenvalue spectrum for the vibration problem. In this case, all eigenmodes correspond to real wavenumbers, and thus the real eigenvalues (eigenfrequencies) all fall below the cut-off frequency and outside the stopping bands.

In the later part of this chapter we have shown how p–type finite element solutions to vibration problems can be post-processed using information obtained from the complex wavenumber Fourier analysis. Complex wavenumber analysis allows for the determination of the underlying component waves. By superposition of these wave components through a sinusoidal interpolation, a better approximation for the mode shape at inter-nodal points can be constructed. This process demonstrates how results from a complex wavenumber Fourier analysis can be used as a tool to help improve finite element solutions to vibration problems.

Chapter 10

Conclusions

Considerable progress has been made in the development of stabilized space-time finite element methods for problems that can be written as a system of first-order equations. The equations governing classical structural acoustics can be converted to first-order hyperbolic form and these methods are thus immediately applicable. However, in this approach, the coupled state vector consists of a large number of solution variables resulting in a computationally uneconomical formulation.

In this thesis a direct approach is taken where space-time finite element methods are developed for structural acoustics based on the natural framework of second-order hyperbolic equations for elastodynamics and the acoustic wave equation. Recently, Hughes and Hulbert [1988] and Hulbert and Hughes [1990] have successfully generalized time-discontinuous space-time finite element methods developed for first-order systems to the second-order hyperbolic equations of elastodynamics. In this thesis, the formulation is extended to the fluid-structure interaction problem in exterior domains where both the elastic structure and acoustic fluid are posed in second-order hyperbolic form. The formulation employs a finite computational fluid domain surrounding the structure and incorporates local time-dependent non-reflecting boundary conditions on the fluid truncation boundary. Non-reflecting boundary conditions are incorporated as 'natural' boundary conditions in the space-time variational equation, i.e. they are enforced weakly in both space and time. Throughout the development, energy estimates derived for the coupled fluid-structure system in the continuum setting were used as a guide for the design of stable and accurate space-time methods.

For the coupled equations, scalar velocity potential was chosen as the solution variable for the acoustic fluid, while the displacement vector was chosen as the primary solution variable for the elastic body. As a consequence of this choice of variables, the coupled space-time variational equations for the fluid and structure give rise to a globally symmetric form, which in the context of the space-time finite element formulation, leads to a positive form of matrix equations and enables us to prove the unconditional stability and convergence of the method. For additional stability, least-squares operators based on local residuals of the Euler-Lagrange equations for the coupled system, including the non-reflecting boundary conditions, were incorporated into the space-time formulation.

New local time-dependent non-reflecting boundary conditions have been developed for the three-dimensional wave equation which are exact for the first N spherical harmonics for outgoing waves. The development of these boundary conditions began with the truncated Dirichlet-to-Neumann (DtN) map in the frequency domain. Time-dependent boundary conditions were obtained by an inverse Fourier transform. In addition, it has been demonstrated that a local in time counterpart exists for the spatially nonlocal and frequency dependent DtN map. The result is a new sequence of non-reflecting boundary conditions which are local in time yet retain the nonlocal spatial integral. The advantage of this sequence is that when implemented in the time-discontinuous formulation, standard C^0 continuous space-time interpolations may be used. It is this special property which offers the greatest potential for implementation of high-order boundary conditions beyond second-order. Numerical results for some canonical transient radiation and scattering problems demonstrated the improved accuracy that results from the use of high-order non-reflecting boundary conditions within the space-time finite element formulation.

Motivated by the success of Harari and Hughes [1991a,1991b,1992c] in applying Galerkin/Least-Squares (GLS) technology to the Helmholtz equation in the frequency domain, a comprehensive Fourier analysis of these methods in multi-dimensions has been performed. This lead directly to the design of new GLS mesh parameters that exhibit dramatically improved phase accuracy for wave propagation in multi-dimensions. For the case where the direction of the wave is known, the optimal mesh parameter is obtained explicitly. For general problems where waves are directed in arbitrary directions, an optimal GLS parameter is obtained which minimizes phase error over all possible wave directions. Several numerical examples are given which demonstrate the superiority of the new methods over the standard Galerkin method. The optimum GLS parameter is given for both linear and quadratic interpolation functions.

We have shown that high-order finite element discretizations display frequency bands where the solutions take the form of harmonic decaying waves. In these 'stopping' bands, the solutions are not purely propagating (real wavenumbers) but are attenuated (complex wavenumbers). In order to interpret the solution within the stopping bands, the standard finite element dispersion analysis technique has been extended to include complex wavenumbers. By allowing for complex wavenumbers, a complete characterization of the stopping bands in the frequency spectrum of hierarchical p-version and spectral finite element discretizations has been obtained. The most important conclusions from this study are:

1. High-order elements display increased phase accuracy compared to low-order elements for the same number of degrees of freedom.

2. For large spectral orders, the width of the first few stopping bands are very small and the amplitude attenuation is minimal. Thus for high-order finite element discretizations, the first few stopping bands in the frequency spectrum are not of practical significance.

3. For well resolved waves, spectral elements using Lagrange interpolation in conjunction with Lobatto quadrature show slightly improved phase accuracy compared to hierarchic finite elements. For frequencies extending beyond the limit of resolution, both dispersion and amplitude attenuation errors increase the most for spectral elements.

10.1 Future Directions

Having laid the foundation for the application of space-time finite element methods for fluid-structure interaction in exterior domains, there remains several areas for further development that would help bring the ideas presented here to their full potential. The following areas of future research are suggested:

1. The space-time finite element approach advocated in this thesis provides a powerful framework for unified and simultaneous spatial and temporal adaptivity of the discretization. This is especially useful in the application of adaptive solution strategies for transient structural acoustics, in which both spatial and temporal enhancement can efficiently capture waves propagating along space-time characteristics. Further research efforts are needed to develop efficient and accurate local error indicators to drive the implementation of adaptive strategies for the exterior structural acoustics problem incorporating non-reflecting boundaries.

2. Investigate the use of fractional-step (staggered) solution algorithms for the coupled structural acoustics problem. In this approach, a modular computer implementation could be used with separate fluid and structural analyzers interfaced through the coupling terms. The integration process could then be carried out in alternating stages: The solution of either the fluid or the structural system would be advanced first, then the other system would be solved following a time extrapolation of the coupling terms as forcing functions. It is anticipated that as a result of the firm mathematical framework inherent in the time-discontinuous Galerkin finite element method presented in this work, a staggered (fractional-step) space-time method can be obtained which inherits the stability and accuracy of the underlying method.

3. Investigate the use of predictor-multicorrector algorithms that take advantage of the positive form of the matrix equations arising from the space-time formulation for structural acoustics. Predictor-multicorrector strategies reduce the coupled system of equations to a sequence of smaller systems within each space-time slab, where iterative strategies such as Generalized Minimum Residual (GMRES) algorithms may be used for their solution.

4. Perform a Fourier analysis of the space-time methods in order to characterize the spatial and temporal dispersion and amplitude attenuation properties of time-discontinuous GLS methods. Results from this analysis could be used as a guide to help design improved intrinsic time-scale parameters.

Bibliography

[1] ABBOUD,N.N. [1990]: A Mixed finite element formulation for the transient and harmonic exterior fluid-structure interaction problem. *Ph.D. Dissertation*, Stanford University, Stanford, California., August 1990.

[2] ABBOUD, N.N.; PINSKY, P.M. [1992]: Finite element dispersion analysis for the three-dimensional second-order scalar wave equation. *Int. J. Numer. Meth. Eng.* 35, 1183-1218.

[3] ACHENBACH, J.D. [1987]: Wave Propagation in Elastic Solids. North - Holland.

[4] ARMERO, F. [1993]: Numerical analysis of dissipative dynamical systems in solid and fluid mechanics with a special emphasis on coupled problems, Ph.D. Dissertation, Stanford University, Nov. 1993.

[5] AZIZ, A.K.; KELLOGG, R.B., AND STEPHENS [1988]: A two point boundary value problem with a rapidly oscillating solution *Numer. Math.* 53, 107-121.

[6] ALVIN, K.F.; PARK, K.C. [1991]: Frequency-window tailoring of finite element models for vibration and acoustics analysis. In: Keltie, R.F. (ed): *Structural acoustics.* vol. NCA-vol.12/AMD-vol.128, pp. 117-128. ASME.

[7] AMINI,S.; HARRIS, P.J. [1990]: A comparison between various boundary integral formulations of the exterior acoustics problem. *Comp. Meth. in Appl. Mech. Eng.* 84, 59-75.

[8] BABUSKA, I.; CRAIG, A.; MANDEL, J.; PITKARANTA, J. [1991]: Efficient preconditioning for the p-version finite element method in two-dimensions. *SIAM J. Num. Anal.* 28, 624-661.

[9] Babuska, I.; Suri, M. [1990]: The p- and h-p versions of the finite element method, an overview. *Comp. Meth. in Appl. Mech. Eng.* 80, 5-26.

[10] Barragy,E.; Carey,G.F. [1991]: Preconditioners for high degree elements. *Comp. Meth. in Appl. Mech. Eng.* 93, 97-110.

[11] Bathe, K.J.; Hahn, W. [1979]: On transient analysis of fluid-structure systems, *Comput. Struct.* 10, 383-391.

[12] Bayliss, A.; Turkel, E. [1980]: Radiation boundary conditions for wave-like equations. *Commun. Pure Appl. Math.*, 33, 707-725.

[13] Bayliss, A.; Gunzburger, M.; Turkel, E. [1982] Boundary conditions for the numerical solution of elliptic equations in exterior regions, *SIAM J. Appl. Math.* 42, 430-451.

[14] Bayliss,A.; Goldstein,C.I.; Turkel,E. [1983]: An iterative method for the Helmholtz equation. *J. Comp. Phys.* 49, 443-457.

[15] Bayliss,A.; Goldstein,C.I.; Turkel,E. [1985a]: The numerical solution of the Helmholtz equation for wave propagation problems in underwater acoustics. *Comp. and Maths. with Appls.* 11, 655-665.

[16] Bayliss,A.; Goldstein,C.I.; Turkel,E. [1985b]: On accuracy conditions for the numerical computation of waves. *J. Comp. Phys.* 59, 396-404.

[17] Bazant,Z.P. [1978]: Spurious reflection of elastic waves in nonuniform finite element grids. *Comp. and Maths. with Appls.* 16, 91-100.

[18] Bazant,Z.P.; Celep,Z. [1982]: Spurious reflection of elastic waves in nonuniform meshes of constant and linear strain finite elements. *Computers and Structures* 15, 451-459.

[19] Bellanger,M. [1989]: Digital Processing of Signals. John Wiley and Sons.

[20] Belytschko,T.B.; Mullen,R. [1978]: On dispersive properties of finite element solutions. In: Miklowitz, J. (ed): *Modern problems in elastic wave propagation*, pp. 67-82.

[21] Belytschko,T.B.; Mindle,W.L. [1980a]: Flexural wave propagation behavior of lumped mass approximations. *Computers and Structures.* 12, 805-812.

[22] Belytschko,T.B. [1980b] Fluid-structure interaction, *Comput. Struct.* 12, 459-469.

[23] Burnett, D. [1993]: A 3-D acoustic infinite element based on a generalized multipole expansion, submitted: *J. Acoust. Soc. Am.*

[24] Brillouin,L. [1953]: Wave propagation in periodic structures. Dover.

[25] Burton, A.J.; Miller, G.F. [1971] The application of integral equation methods to the numerical solution of some exterior boundary value problems, *Proc. R. Soc. London.* Ser. A 323, 201-210.

[26] Canuto,C.; Hussaini,M.Y.;Quarternoni,A.; Zang,T.A. [1988]: Spectral methods in fluid dynamics. Springer-Verlag.

[27] Chertock, G. [1970]: Transient flexural vibrations of ship-like structures exposed to underwater explosion. *J. Acoust. Soc. Am.* 48, 170-180.

[28] Churchill,R.V.; Brown,J.W.; Verhey,R.F. [1976]: Complex variables and applications. McGraw-Hill.

[29] Copley, L.G. [1968]: Fundamental results concerning integral representations in acoustic radiation, *J. Acoust. Soc. Am.* 44, 28-32.

[30] Craggs, A. [1971]: The transient response of a coupled plate-acoustic system using plate and acoustic finite elements, *J. Sound Vib.* 15, 509-528.

[31] Crighton, D.G. [1989] The 1988 Rayleigh medal lecture: Fluid Loading - The interaction between sound and vibration, *J. Sound Vib.* 133, 1-27.

[32] Deville,M.O.; Mund,E.H. [1992]: Fourier analysis of finite element preconditioned collocation schemes. *SIAM J. Sci. Stat. Comp.* 13,596-610.

[33] Douglas Jr., J.; Santos, J.E., Sheen, D., and Schreiyer [1993]: Frequency domain treatment of one-dimensional scalar waves. *Mathematical Models and Methods in Applied Sciences*, Vol. 3, No. 2, 171-194.

[34] Engquist, B.; Majda, A. [1977] Absorbing boundary conditions for the numerical simulation of waves, *Math. Comput.* 31, 629-652.

[35] Engquist, B.; Majda, A. [1979] Radiation boundary conditions for acoustic and elastic calculations, *Commun. Pure Appl. Math.* 32, 313-357.

[36] Eriksson,K.; Johnson,C. [1991]: Adaptive finite element methods for linear parabolic problems *SIAM J. Numer. Anal.* 28, 43-77.

[37] Everstine, G.C. [1981]: A symmetric potential formulation for fluid-structure interaction, *J. Sound Vib.* 79, 157-160.

[38] Everstine, G.C.;Henderson, F.M. [1990]: Coupled finite element/boundary element approach for fluid-structure interaction, *J. Acoust. Soc. Am.* 87, 1938-1947.

[39] Felippa, C.A. [1980]: Top-down derivation of doubly asymptotic approximation for fluid-structure interaction analysis, in Innovative Numerical Analysis for the Applied Engineering Sciences, U. P. of Virginia, City, Vol. 46, 79-88.

[40] Felippa, C.A.; Deruntz, J.A. [1984]: Finite element analysis of shock-induced hull cavitation, *Comput. Methods Appl. Mech. Eng.* 44, 297-337.

[41] Fischer,P.F.; Patera,A.T. [1991]: Parallel spectral element methods for the incompressible Navier-Stokes equations. In: Supercomputing, pp. 71-143. ASME.

[42] Franca,L.P.; Dutra Do Carmo,E.G. [1989]: The Galerkin gradient least-squares method. *Comput. Meths. Appl. Mech. Engrg.* 74, 41-54.

[43] Friberg,O.; Moller,P. [1987]: An adaptive procedure for eigenvalue problems using the hierarchical finite element method. *Int. J. Num. Meth. Ing.* 24, 319-335.

[44] Fried, I. [1979]: Accuracy of string element mass matrix. *Comp. Meth. in Appl. Mech. Eng.* 20, 317-321.

[45] Geers, T.L. [1971]: Residual potential and approximate methods for three-dimensional fluid-structure interaction problem, *J. Acoust. Soc. Am.* 49, 1505-1510.

[46] Geers, T.L. [1978]: Doubly asymptotic approximation methods for transient motions of submerged structures. *J. Acoust. Soc. Am.* 64, 1500-1508.

[47] Givoli, D. [1988]: A Finite Element Method for Large Domain Problems, Ph.D. Dissertation, Stanford University.

[48] Givoli,D.; Keller,J.B. [1989]: A finite element method for large domains. *Comp. Meth. in Appl. Mech. Eng.* 76, 41-66.

[49] Givoli,D.; Keller,J.B. [1990]: Non-reflecting boundary conditions for elastic waves. *Wave Motion*, 12, 261-279.

[50] Givoli,D. [1991]: Non-reflecting boundary conditions: A review. *J. Comput. Phys.*, 94, 1-29.

[51] Givoli,D. [1992]: A spatially exact non-reflecting boundary condition for time dependent problems. *Comp. Meth. in Appl. Mech. Eng.* 95, 97-113.

[52] Gladwell, G.M.L. [1966]: A variational formulation of damped acousto-structural vibration problems, *J. Sound Vib.* 4, 172-186.

[53] Goldstein,C.I. [1982]: A finite element method for solving Holmholtz type equations in waveguides and other unbounded domains. *Math. Comput.* 39, 303-324.

[54] Goldstein,C.I. [1986]: The weak element method applied to Helmholtz type equations. *Appl. Numer. Math.* 2, 409-426.

[55] Goudreau,G.L., Taylor,R.L. [1973]: Evaluation of numerical integration methods in elastodynamics. *Comp. Meth. in Appl. Mech. Eng.* 2, 69-97.

[56] Graff,K.F. [1975]: Wave Motion in Elastic Solids, Dover Publications.

[57] Grosh,K.; Pinsky,P.M. [1993a]: Complex wavenumber finite element dispersion analysis of Galerkin and Galerkin Least Squares methods for fluid-loaded plates. In press (accepted) *Comp. Meth. in Appl. Mech. Eng.*

[58] Grosh,K.; Pinsky,P.M. [1993b]: New generalized Galerkin least squares finite element methods for wave propagation in Timoshenko beams. Ch. 25 *Mathematical and Numerical Aspects of Wave propagation*, (R. Kleinman, et al., Eds.), SIAM 1993.

[59] Grote,M.; Keller,J.B. [1994]: Exact non-reflecting boundary conditions for the time-dependent wave equation. Accepted: SIAM J. of Appl. Math.

[60] Harari,I. [1991a]: Computational methods for problems of acoustics with particular reference to exterior domains. *Ph.D. Dissertation*, Stanford University, Stanford, California.

[61] Harari.I.; Hughes,T.J.R. [1991b]: Finite element methods for the Helmholtz equation in an exterior domain: Model problems. *Comp. Meth. in Appl. Mech. Eng.* 87, 59-96.

[62] Harari.I.; Hughes,T.J.R. [1992a]: A cost comparison of boundary element and finite element methods for problems of time-harmonic acoustics. *Comp. Meth. in Appl. Mech. Eng.* 97, 77-102.

[63] Harari.I.; Hughes,T.J.R. [1992b]: Analysis of continuous formulations underlying the computation of time-harmonic acoustics in exterior domains. *Comp. Meth. in Appl. Mech. Eng.* 97, 103-124.

[64] Harari.I.; Hughes,T.J.R. [1992c]: Galerkin/least-squares finite element methods for the reduced wave equation with non-reflecting boundary conditions in unbounded domains, *Comp. Meth. in Appl. Mech. Eng.* 98, 411-454.

[65] Hilber,H.M.; Hughes,T.J.R.; Taylor,R.L. [1977]: Improved numerical dissipation for time integration algorithms in structural dynamics. *Earthquake Eng. and Struct. Dynamics*, 5, 283-292.

[66] Huang, G.C.; Everstine, G.C.; Wang, Y.F. [1977]: Retarded potential techniques for the analysis of submerged structures impinged by weak shock waves, in Computational Methods for Fluid-Structure Interaction Problems, edited by T. Belytschko and T. L. Geers, ASME, New York, Vol. AMD 26, 83-93.

[67] Hughes,T.J.R.; Brooks, A.N. [1979]: A multi-dimensional upwind scheme with no crosswind diffusion. In: Hughes,T.J.R. (ed): Finite Element Methods for Convection Dominated Flows, AMD Vol. 34 (ASME, New York), 19-35.

[68] Hughes, T.J.R. [1987a] The Finite Element Method: Linear Static and Dynamic Finite Element Analysis, Prentice-Hall, Englewood Cliffs, NJ.

[69] Hughes,T.J.R. [1987b]: Recent progress in the development and understanding of SUPG methods with special reference to the compressible Euler and Navier-Stokes equations. *Int. J. for Numer. Meth. in Fluids* 7, 1261-1275.

[70] Hughes,T.J.R.; Hulbert,G.M. [1988]: Space-time finite element methods for elastodynamics: Formulations and error estimates. *Comp. Meth. in Appl. Mech. Eng.* 66, 339-363.

[71] Hughes,T.J.R.; Franca,L.P.; Hulbert,G.M. [1989]: A new finite element formulation for computational fluid dynamics: VIII. The galerkin least squares method for advective-diffusive equations. *Comp. Meth. in Appl. Mech. Eng.* 73, 173-189.

[72] Hulbert,G.M. [1989]: Space-time finite element methods for second-order hyperbolic equations. *Ph.D. Dissertation*, Stanford University, Stanford, California.

[73] Hulbert,G.M.; Hughes,T.J.R. [1990]: Space-time finite element methods for second-order hyperbolic equations. *Comp. Meth. in Appl. Mech. Eng.* 84, 327-348.

[74] Hulbert,G.M. [1992]: Discontinuity-capturing operators for elastodynamics. *Comp. Meth. in Appl. Mech. Eng.* 96, 409-426.

[75] Jansen,K.; Shakib,F; and Hughes, T.J.R. [1992]: Fast projection algorithm for unstructured meshes. in *Computational nonlinear mechanics in aerospace engineering*, editor S.N. Atluri, Vol. 146, Ch. 5, AIAA.

[76] Jasti,R. [1992]: Mixed shell finite elements with applications in structural acoustics. *Ph.D. Thesis*, Stanford University, Stanford, California.

[77] Jeans, R.A.; Mathews, I.C. [1990]: Solution of fluid-structure interaction problems using a coupled finite element and variational boundary element technique, *J. Acoust. Soc. Am.* 88, 2459-2466.

[78] Johan,Z.; Hughes,T.J.R.; Shakib,F. [1991]: A globally convergent matrix-free algorithm for implicit time-marching schemes arising in finite element analysis in fluids. *Comp. Meth. in Appl. Mech. Eng.* 87, 281-304.

[79] Johnson,C.; Navert,U.; Pitkaranta,J. [1984]: Finite element methods for linear hyperbolic problems. *Comput. Meths. Appl. Mech. Engrg.* 45, 285-312.

[80] Johnson,C. [1986]: Numerical Solutions of Partial Differential Equations by the Finite Element Method. Cambridge Univ. Press.

[81] Johnson,C. [1993]: Discontinuous Galerkin finite element methods for second order hyperbolic problems. *Comput. Meths. Appl. Mech. Engrg.* 107, 117-129.

[82] Junger,M.C [1975]: Radiation and scattering by submerged elastic structures. *J. Acoust. Soc. Am.* 57, 1318-1326.

[83] Junger, M.C.; Feit, D. [1986] Sound, Structures and Their Interaction, M.I.T. Press, Cambridge, MA.

[84] Karp, S.N. [1961] A convergent farfield expansion for two-dimensional radiation functions, *Commun. Pure Appl. Math.* XIV, 427-434.

[85] Keller,J.B. [1962]: Geometrical theory of diffraction. *J. Opt. Soc. Am.* 52, 116-130.

[86] Keller,J.B.; Givoli,D. [1989]: Exact non-reflecting boundary conditions. *J. Comp. Phys.* 82, 172-192.

[87] Lesaint, P.; Raviart, P.A. [1974]: On a finite element method for solving the neutron transport equation. in: C. de Boor (ed.), *Mathematical Aspects of Finite Elements in Partial Differential Equations*, Academic press, New York, pp. 89-123.

[88] Lighthill, J. [1978]: Waves in Fluids, Cambridge University Press.

[89] LOTSTEDT,P. ; GUSTAFSSON, B. [1993] Fourier analysis of multigrid methods for general systems of partial differential equations. *Mathematics of Computation* Vol. 60, No. 202, 473-493.

[90] LU, Y.P. [1980]: The application of retarded potential techniques to submerged dynamic structural systems, in Proceedings of the 2nd International Symposium Innovative Numerical Analysis for the Applied Engineering Sciences, edited by R. P. Shaw and W. Pilkey, 59-68.

[91] MACCAMY,R.C.; MARIN,S.P. [1980]: A finite element method for exterior interface problems. *Int. J. Math. and Math. Sci.* 3, 311-350.

[92] MADAY,Y.; PATERA,A.T. [1989]: Spectral element methods for the incompressible Navier-Stokes equations. In: Noor,A.K.; Oden,J.T. (ed): State-of-the-art surveys on computational mechanics. PP. 71-143, ASME.

[93] MANSUR, W.J.; BREBBIA, C.A. [1982]: Formulation of the boundary element method for transient problems governed by the scalar wave equation, *Appl. Math. Modelling*, 6, 307-311.

[94] MANSUR, W.J.; BREBBIA, C.A. [1984]: Further developments on the solution of the transient scalar wave equation, in Topics in Boundary Element Research, edited by C. A. Brebbia, Vol. 2, Springer Verlag, Berlin.

[95] MARIEM, J.B.; HAMDI, M.A. [1987] A new boundary finite element method for fluid-structure interaction problems, *Int. J. Num. Methods Eng.* 24, 1251-1267.

[96] MATHEWS, I.C. [1986]: Numerical techniques for three dimensional steady-state fluid-structure interaction, *J. Acoust. Soc. Am.* 79, 1317-1325.

[97] MINDLE,W.L.; BELYTSCHKO,T. [1983]: A study of shear factors in reduced-selective integration Mindlin beam elements. *Computers and Structures.* 17, 339-344.

[98] MINDLIN,R.D.; BLEICH, H.H. [1953]: Response of an elastic cylindrical shell to a transverse, step shock wave. *J. Appl. Mech.* Vol. 20, 189-195.

[99] MULLEN,R.; BELYTSCHKO,T. [1982]: Dispersion analysis of finite element semidiscretizations of the two-dimensional wave equation. *Int. J. Numer. Meth. Engng.* 18, 11-29.

[100] NEILSON, H.C.; EVERSTINE, G.C.; WANG, Y.F. [1981]: Transient response of a submerged fluid-coupled double-walled shell structure to a pressure pulse, *J. Acoust. Soc. Am.* 70, 1776-1782.

[101] NICOLAS VULLIERME, B. [1989]: A contribution to doubly asymptotic approximations: An operator top-down derivation, in Numerical Technology in Acoustic Radiation, ASME, New York, Vol. 6, 7-13.

[102] PARK,K.C. [1980]: Partitioned transient analysis procedures for coupled field problems: stability. *J. Appl. Mech.* 47, 370-376.

[103] PARK,K.C.; FELIPPA [1980]: Partitioned transient analysis procedures for coupled field problems: accuracy analysis. *J. Appl. Mech.* 47, 919-926.

[104] PARK,K.C.; FLAGGS,D.L. [1984]: A Fourier analysis of spurious mechanisms and locking in the finite element method. *Comp. Meth. in Appl. Mech. Eng.* 46, 65-81.

[105] PARK,K.C.; FLAGGS,D.L. [1985]: A symbolic Fourier synthesis of a one-point integrated quadrilateral plate element. *Comp. Meth. in Appl. Mech. Eng.* 48, 805-812.

[106] PARK,K.C.; JENSEN,D.J. [1989]: A systematic determination of lumped and improved consistent mass matrices for vibration analysis. AIAA Paper No. 89-1335.

[107] PATERA,A.T. [1984]: A spectral element method for fluid dynamics: Laminar flow in a channel expansion. *J. Comp. Phys.* 54, 468-488.

[108] PIASZCZYK C.M.; KLOSNER, J.M. [1984]: Acoustic radiation from vibrating surfaces at characteristic frequencies, *J. Acoust. Soc. Am.* 75, 363-375.

[109] PINSKY, P.M.; ABBOUD, N.N. [1990]: Transient finite element analysis of the exterior structural acoustic problem, *ASME J. Vib. Acoust.* 112, 245-256.

[110] Pinsky,P.M.; Abboud,N.N. [1991a]: Finite element solution of the transient exterior structural acoustics problem based on the use of radially asymptotic boundary operators. *Comp. Meth. in Appl. Mech. Eng.* 85, pp. 311-348.

[111] Pinsky,P.M.;
Thompson,L.L. [1991b]: Accuracy of local non-reflecting boundary conditions for time-dependent structural acoustics. NCA-Vol.12/AMD-Vol.128, *Structural Acoustics*, ASME 1991 153-160.

[112] Pinsky,P.M.; Thompson,L.L. and Abboud,N.N. [1992]: Local high-order radiation boundary conditions for the two-dimensional time-dependent structural acoustics problem. *J. Acoust. Soc. Am.* 91 (3), pp. 1320-1335.

[113] Reed, W.H; Hill, T.R. [1973]: Triangular mesh methods for the neutron transport equations. *Report LA-UR-73-479*, Los Alamos Scientific Laboratory, Los Alamos.

[114] Ruzicka, G.C.; Geers, T.L. [1989]: Transient response analysis of multiple-submerged structures, *Finite Elements Anal. Design*, 6, 153-172.

[115] Safjan, A.; Demkowicz, L.; Oden, J.T. [1991]: Adaptive finite element methods for hyperbolic systems with applications to acoustics. *Int. J. for Numer. Meth. in Engin.* 32, 677-707.

[116] Schenck, H.A. [1968]: Improved integral formulation for acoustic radiation problems, *J. Acoust. Soc. Am.* 44, 41-58.

[117] Shakib,F.; Hughes,T.J.R.; Johan,Z. [1989]: A multi-element group preconditioned GMRES algorithm for nonsymmetric systems arising in finite element analysis. *Comp. Meth. in Appl. Mech. Eng.* 75, 415-456.

[118] Shakib,F.; Hughes,T.J.R. [1991a]: A new finite element formulation for computational fluid dynamics: IX. Fourier analysis of space-time Galerkin/least-squares algorithms. *Comp. Meth. in Appl. Mech. Eng.* 87, 35-58.

[119] Shakib,F.; Hughes,T.J.R.; Johan,Z. [1991b]: A new finite element formulation for computational fluid dynamics: X. The compressible Euler and Navier-Stokes equations. *Comp. Meth. in Appl. Mech. Eng.* 89, 141-219.

[120] Silva,M.A.G. [1991]: Study of pass and stop bands of some periodic composites. *Acustica.* 75, 62-68.

[121] Sommerfeld, A. [1964]: Partial Differential Equations in Physics. Academic, New York.

[122] Szabo,B.; Babuska I. [1991]: Finite element analysis. John Wiley and Sons.

[123] Thompson,L.L.; Pinsky,P.M. [1993a]: Complex wavenumber Fourier analysis of Hierarchic p-version and spectral elements. SUDAM Report No. 93-1, Stanford University, January, 1993.

[124] Thompson,L.L.; Pinsky,P.M. [1993b]: Complex wavenumber Fourier analysis of the p-version finite element method. *Computational Mechanics*, Vol. 13, No. 4, 255-275.

[125] Thompson,L.L.; Pinsky,P.M. [1993c]: A multi-dimensional Galerkin/Least-Squares finite element method for time-harmonic wave propagation. in *Second International Conference on Mathematical and Numerical Aspects of Wave Propagation*, edited by R. Kleinman, et. al. SIAM, Chapter 47, 444-451.

[126] Thompson,L.L.; Pinsky,P.M. [1993d]: A Galerkin/least-squares finite element method for the two-dimensional helmholtz equation. Accepted March 1993 (In Press): *Int. J. Num. Meth. Eng.*.

[127] Thompson,L.L.; Pinsky, P.M. [1993e]: New space-time finite element methods for fluid-structure interaction in exterior domains. in *Computational Methods for Fluid/Structure Interaction.* AMD-Vol. 178, ASME 1993, pp. 101-120.

[128] Thompson,L.L.; Pinsky, P.M. [1993f]: A space-time finite element method for transient structural acoustics. *Second U.S. National Congress on Computational Mechanics.* Washington D.C., August 16-18, 1993.

[129] Underwood,P. [1974]: Accuracy of finite difference representations for the transient response analysis of shells. *Earthquake Eng. and Struc. Dynam.* 2, 219-233.

[130] Vichnevetsky,R.; Bowles,J.B. [1982]: Fourier analysis of numerical approximations of hyperbolic equations, SIAM (Philadelphia).

[131] Voight,R.G.; Gottlieb,D; Hussaini,M.Y. [1984]: Spectral methods for partial differential equations. SIAM.

[132] Watson, G.N. [1966]: Theory of Bessel Functions, Cambridge U. P., Cambridge.

[133] Wolfram,S. [1991]: Mathematica. Addison-Wesley.

[134] Zauderer,E. [1989]: Partial Differential Equations of Applied Mathematics, Second Edition, Wiley-Interscience.

[135] Zienkiewicz, O.C.; Newton, R.E. [1969] Coupled vibrations of a structure submerged in a compressible fluid, in International Symposium on Finite Element Techniques, Univ. Stutgardt, Germany.

[136] Zienkiewicz, O.C.; Kelley D.W.; Bettess, P. [1977]: The Sommerfeld (radiation) condition on infinite domains and its modelling in numerical procedures, in the 3rd International Symposium Computational Methods and Applied Science Engineering, IRIA Laboria, Versailles, France.

[137] Zienkiewicz, O.C.; Bettess, P. [1978]: Fluid-structure dynamic interaction and wave forces: An introduction to numerical treatment, *Int. J. Num. Methods Eng.* 13, 1-16.